Technische Universität München
Fakultät für Elektrotechnik und Informationstechnik
Lehrstuhl für Nanoelektronik

Printed Sensors for the Internet of Things

Dissertation

Andreas Albrecht

Vollständiger Abdruck der von der Fakultät für Elektrotechnik und Informationstechnik der Technischen Universität München zur Erlangung des akademischen Grades eines

Doktor-Ingenieurs (Dr.-Ing.)

genehmigten Dissertation.

April 2018

TECHNISCHE UNIVERSITÄT MÜNCHEN
FAKULTÄT FÜR ELEKTROTECHNIK UND INFORMATIONSTECHNIK
LEHRSTUHL FÜR NANOELEKTRONIK

Printed Sensors for the Internet of Things

Andreas Albrecht

Vollständiger Abdruck der von der Fakultät für Elektrotechnik und Informationstechnik der Technischen Universität München zur Erlangung des akademischen Grades eines

Doktor-Ingenieurs (Dr.-Ing.)

genehmigten Dissertation.

Vorsitzender: Prof. Dr. Erwin Biebl

Prüfende der Dissertation:

1. Prof. Paolo Lugli, Ph.D.
2. Prof. Dr. Bernhard Wolfrum

Die Dissertation wurde am 17.04.2018 bei der Technischen Universität München eingereicht und durch die Fakultät Elektrotechnik und Informationstechnik am 30.07.2018 angenommen.

Abstract

The production processes from the field of Printed Electronics (PE) complement the silicon-based manufacturing with low-cost and high-throughput printing techniques. This enables cheap and lightweight electronic devices with the properties of the substrate they were printed on. These can be thin and flexible like plastic films, disposable and biodegradable like paper, or stretchable and conformable like textiles. This thesis contributes to the field of PE by presenting printed conductive patterns and sensors on flexible substrates having different properties. The overall process from design, through printing and characterization to system integration is regarded. Conductive, isolating, and sensing materials were deposited by inkjet and screen printing, as well as spray coating. We printed micro-structured conductors and dielectrics with dimensions of several tens of micrometres and layer thicknesses from nanometres to millimetres, which are all at the edge of the employed printing techniques. Intense pulsed light (IPL) curing proves to increase the electrical conductivity on temperature sensitive substrates. Conductivities ranking among the highest published for particle-based thin-films were obtained for printed metal layers and IPL-reduced metal-oxide thin-films. IPL enables conductive patterns on flexible, stretchable, and transparent plastics and papers.

The developed processes enabled us to produce mechanical, environmental, chemical, and medical sensors and design specific tools for their characterization. Among others, we produced and compare screen-printed pressure sensors that base on a change of their capacitance upon compression. They show responses of up to 400 % and sensitivities of up to 80 %/kPa, which rank highest in literature. The measurement range of five orders of magnitude covers the range necessary for human-machine interaction and is enabled by an above-logarithmic sensitivity. Additionally, we present strain sensors that consistently regain a low (1 Ω/sq) sheet resistance after relaxing from strains of up to 330 %. Representatively for the many applications in healthcare, we printed skin electrodes and used them for electrocardiography (ECG) and electrooculography (EOG). Both kinds of electrodes are integrated into ready-to-use skin patches and prove suitable for the recognition and differentiation of cardiac activities and eye movements.

We produced and characterized hybrid integrated systems that combine one or multiple of these sensors with printed antennas, printed circuit boards, and conventional surface mount devices. We show examples of security applications, small and large area force sensing, and wireless temperature and humidity sensing. Printed Electronics offers completely new designs of electronic devices and many opportunities for creative engineers and material scientists. This thesis combines both fields and takes into account many components of printed, smart, electronic systems for the Internet of Things (IoT) on any kind of substrate. Already today, printed electronics enables new and exciting designs and change the way how we make and use electronics.

Zusammenfassung

Die Produktionsprozesse aus dem Gebiet der Gedruckten Elektronik (Printed Electronics, PE) ergänzen die silizium-basierte Herstellung durch kosteneffiziente Drucktechniken mit hohem Durchsatz. Dadurch werden günstige und leichte elektronische Geräte ermöglicht, die die Eigenschaften des Mediums besitzen, auf welches sie gedruckt wurden. Dieses kann dünn und flexibel sein wie z.B. Plastikfolie, wegwerfbar und biologisch abbaubar wie Papier oder dehnbar und geschmeidig wie Stoff. Diese Dissertation leistet einen Beitrag zum Themenbereich PE und präsentiert gedruckte leitfähige Strukturen und Sensoren auf flexiblen und dehnbaren Medien mit verschiedensten Eigenschaften. Dabei wird der vollständige Prozess ausgehend vom Design, über das Drucken und Charakterisieren hin zur Systemintegration beleuchtet. Leitfähige, isolierende und sensitive Materialien wurden mittels Tintenstrahl- und Siebdruck sowie durch Sprühbeschichtung aufgebracht. Mikrostrukturierte leitfähige und dielektrische Schichten wurden mit Dimensionen einiger zehn Mikrometer und Schichtdicken zwischen Nanometern und Millimetern gedruckt, welche die Grenzen der eingesetzten Drucktechniken ausloten. Nachbehandlungen mittels intensivem, gepulstem Licht (IPL) wurden eingesetzt, um die elektrische Leitfähigkeit auf temperaturempfindlichen Medien zu erhöhen. Die erreichten Leitfähigkeiten für gedruckte Silbernanopartikelschichten und für durch IPL reduzierte Kupferoxidschichten zählen zu den höchsten bisher erzielten. IPL ermöglicht leitfähige Strukturen auf flexiblen, dehnbaren und transparenten Kunststoffen sowie auf Papier.

Die entwickelten Prozesse ermöglichten es, verschiedene mechanische, chemische und medizinische Sensoren sowie Umweltsensoren zu produzieren und speziell entworfene Instrumente für ihre Charakterisierung zu entwickeln. Unter anderem wurden siebgedruckte Drucksensoren basierend auf Kapazitätsänderungen bei Kompression gefertigt, die Sensorantworten bis zu 400 % und Empfindlichkeiten bis zu 80 %/kPa zeigen. Der Messbereich von fünf Größenordnungen deckt den für Mensch-Maschine-Kommunikation notwendigen Bereich durch eine überlogarithmische Empfindlichkeit ab. Zusätzlich werden Dehnungssensoren präsentiert, die auch nach Dehnungen von über 300 % wieder einen niedrigen (1 Ω/sq) Widerstand erreichen. Repräsentativ für die vielen Anwendungen im Gesundheitsbereich wurden Hautelektroden gedruckt und für Elektrokardiographie (EKG) und Elektrookulografie (EOG) verwendet. Beide Arten von Silberelektroden wurden in Hautpflaster integriert und haben sich als geeignet zur Erkennung und Unterscheidung von Herzaktivitäten und Augenbewegungen bewiesen.

Es wurden hybride integrierte Systeme produziert und vermessen, die einen oder mehrere der Sensoren mit gedruckten Antennen, Leiterplatten und herkömmlichen Oberflächenmontagekomponenten kombinieren. Es werden Beispiele für Sicherheitsanwendungen, klein- und großflächige Druckmessungen, sowie drahtlose Temperatur- und Feuchtigkeitsmessungen gezeigt. Gedruckte Elektronik bietet eine vollständig neue Gestaltung elektronischer Geräte und viele Möglichkeiten für kreative Ingenieure und Materialwissenschaftler. Diese Arbeit kombiniert beide Felder und berücksichtigt viele Komponenten für gedruckte, intelligente elektronische Systeme für das Internet der Dinge. Bereits heute ermöglicht gedruckte Elektronik neuartige und spannende Designs und kann die Art der Herstellung und Benutzung von Elektronik verändern.

Content

Chapter 1

Introduction

Printed electronics (PE) describe products and processes that employ printing techniques widely known for graphical printing in the manufacturing of electronics. This combination of electronic functionality and additive deposition techniques allows the fabrication of electronic devices or parts of such on a wide range of substrates. Depending on the substrate and the functional materials employed, the electronic product can feature some advantages or functionalities that are unmatched by other production methods. Printed electronics can be thin, flexible, lightweight, and produced in high-speed, cost-effective, and environmentally-friendly processes. Some products may be stretchable, transparent, large-area, bio-compatible or implantable. The involved processes are an exciting and promising, but scientifically, and technologically challenging field. Chemists, material scientists, electrical and mechanical engineers, and printing experts have to combine their experience and creativity to make this technology succeed. To complete innovations, also economic aspects have to be regarded to create product designs, a supply chain, and life-cycle management that are different to other fields of products. If this is achieved, the appearance of electronics may change fundamentally. Instead of a stiff circuit board crammed with chips, resistors, capacitors, and sockets interconnected by a sprawl of wiring, thin colourful functional layers can be printed onto flexible, bendable or even foldable or stretchable substrates. Printing techniques, new designs, and use cases can "transform the way we make and use electronics". [1]–[3]

1.1 Technology and Benefits

Silicon-based integrated circuits (ICs) require repeated thin-film depositions, baking, lithography and developing steps, and etchings, and packaging to protect the sensitive structures (see Figure 1.1). These ICs are then mounted together with thick-film devices like resistors and capacitors onto a circuit board. This features the connection between them and is often created by etching or milling a fully copper-coated glass-fibre substrate. The proportion of the functional material remaining on the final product in comparison to the employed material is low for such subtractive processes. Additive processes including printing techniques structure the functional material directly as patterns onto the substrate and require only a subsequent curing step per layer. The printing techniques employed are similar to graphical printing and many researchers and companies employ the same or only slightly modified hardware. In principle, all printing techniques from the graphical field are

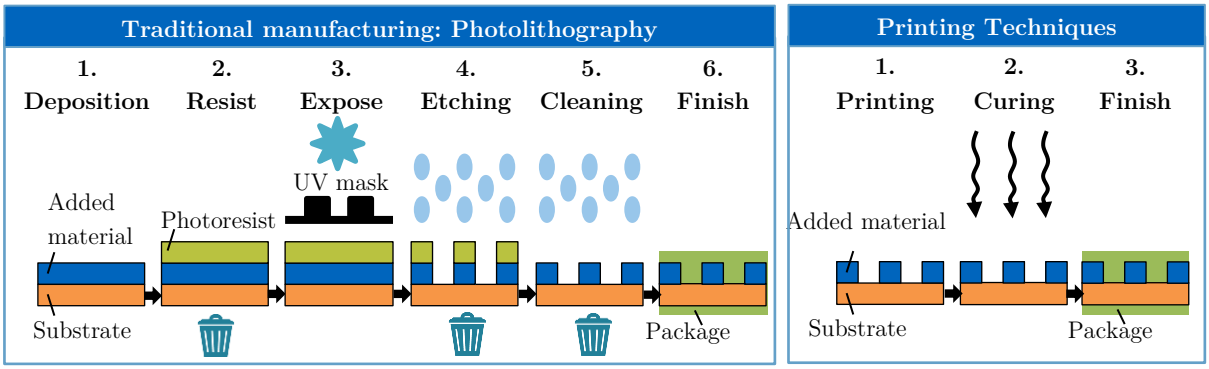

Figure 1.1. Comparison of process steps of traditional electronics manufacturing using photolithography and Printed Electronics using printing techniques. For a final product all but the last step have to be repeated multiple times.

employed. The decision is often made on basis of the investment costs, the setup costs per batch, the available functional material, and the desired properties of the thin-film or thick-film. Digital printing techniques have rather low setup costs but low throughput, whereas intaglio and relief printing techniques have a high throughput but high setup costs. All three technologies require high-tech inks and pastes. For screen printing, there are currently the most materials available and it is a simple deposition technique. These are the reasons, why it is the most used printing technique in industry at the moment. Screen printing can be used for sheet-to-sheet as well as roll-to-roll printing. Additionally, coating techniques like spray deposition and slot die coating complement the printing techniques if it comes to homogeneous thin-films over large areas. [3], [4]

The cost reduction of electronic devices has been mainly driven by reducing the space of a desired functionality on a silicon wafer. For silicon wafers, the area is the main cost factor and also defines the yield, which influences the cost again. Yet for other substrates, the area is not a crucial factor. Especially for applications that need only a few functions, the available area is big anyway or even 'bigger can be better'. The production of large-area electronics was initially driven by area-intensive applications like display, photovoltaics or large sensor matrices. Now, it expands over various other fields such as medical, sensing, flexible, and ultrathin consumer products. A major pull factor is also the integration of graphical and functional materials. [3], [5]–[7]

The combination of recent achievements in traditional graphics printing technologies like more accurate printing machines, quicker pattern generation, and optical curing techniques with the wide range of low-cost materials and new functional inks result in a printing revolution. More manufacturing platforms and printable functional materials including conductive, semi-conductive, dielectric, and electrochromic materials promise the optimization for functional printing.

1.2 Products and Trends

Printing techniques have been employed for the deposition functional materials for many groups of devices. Conductive structures have been printed on many rigid, flexible, and stretchable materials such as papers, cardboards, plastic films, textiles, glass, leather, 3-D printed structures, glass-fibre plates, and many others [3], [8], [9]. These can be used for wiring, resistors, capacitors, antennas and as electrodes for other active and passive components. Radio-frequency identification (RFID) antennas for different frequency ranges like Near Field Communication (NFC), Ultra-High Frequency (UHF) and Gigahertz communication have been printed [2], [10]–[12]. Organic solar cells, organic light emitting diodes (OLED), rectifying diodes, and organic field effect transistors are examples for more complex and partially or completely printed electronic components. [3], [4], [13], [14] The review of Tobjörk and Österbacka provides brief descriptions for several of these devices with a focus on

Figure 1.2. Several products presented in the OE-A roadmaps [15], [16] in the demonstrator phase or already on the market. Copyright by (top left to bottom right) Fraunhofer ISE, Thinfilm, Saueressig, Karl Knauer KG, SAES, Leonhard Kurz Stiftung, Enfucell, CDT, Pauline van Dongen in collaboration with Holst Centre (Photography: Liselotte Fleur), Holst Centre, DuPont, Heraeus, Plastic Logic.

paper as a substrate [2]. Energy harvesters [17]–[22] using different energy sources have been presented as well as super-capacitors and batteries [3], [23]–[25]. A large variety of mechanical, environmental, chemical, biological, and medical sensors can be found in literature, under development in companies and on the market already [26]–[31]. Other types of components include printed volatile and non-volatile memories and waveguides [32].

All these components can be combined for integrated smart systems such as RFID tags [33], smart cards [4], wireless sensor tags [34], smart textiles [35], wearable devices for sports and healthcare [36], and displays [37]. In the book of Suganuma [38], several groups of products are discussed and a guess about their future is given. In recent years, inorganic and organic light emitting diodes (LEDs) have outperformed other light sources in terms of luminous efficacy. Inorganic LEDs are compact point sources or point arrays with a small angle and a high brightness. Organic LEDs are simple multilayer stacks with a lower light intensity over a larger area that offers new and dazzle-free lighting concepts. OLEDs, electrochromic inks, thermo-active inks and electronic paper allows flexible and bendable displays on many kinds of substrates. Organic and printed photovoltaic cells can be integrated into windows and other surfaces with the option of adapting the colour and transparency to the desired location and allow a combination of design and energy generation in devices and buildings. Integrated smart systems are increasingly employed in logistics for good tracing, food monitoring as well as in sports, fitness, and healthcare applications. Often, these include sensors for environmental (temperature, humidity, gas or ion concentrations) and biological (glucose, DNA) factors, mechanical movement and forces (touch, weight, pressure, explosion), and light (photodiodes). The communication occurs by a wired connection or by a printed antenna. Such smart systems form a large part of connected devices in the Internet of Things (IoT).

1.3 Internet of Things

The Internet of Things (IoT) was coined in the last decade and is a hypernym for the many network protocols that interconnect an increasing number of small electronic devices, the things. Currently, we see many things that are enhanced in their functionality by some kind of electronic circuit including communication channels to host systems. These things can be sensors, identification tags, packages, and other daily objects. The new functionality on these can simplify the remote readout, validation, authorization, and life cycle management. Examples are environmental sensors in smart homes, medical sensors in wearables, public transportation and event tickets, identification tags in the automotive industry, and systems for energy management. Most conventional electronic devices as laptops, smartphones, televisions, lamps, speakers, and others are mainly electronics in a package for protection and sometimes also design. In contrast, the before mentioned things are objects that may work without electronics but can benefit from electronics. This means that the design process of these is different. Instead of designing a package around electronics, it is necessary to design electronics within or on an object. Most electronic production processes are not suitable for such an approach. Printing techniques are already employed to enhance the surface of electronic devices for design reasons and are able to realize electronic functionality, too. This enables a large range of new electronic things that can be identified, measured, recorded, and controlled. Furthermore, printing techniques can drive the decrease in size as the functionality is achieved in thin films that can be combined or covered with graphical elements.

1.4 Scope and Outline of the Thesis

The scope of this thesis is the investigation of two of the most used printing techniques, inkjet-printing and screen-printing for the production of printed electronic sensor systems. Their main components, wiring, sensors, communication means, passive components, and computing units are regarded. The focus of the thesis lies on the first three. Conductive wiring is the essential element of every electronic application and must fulfil a high conductivity and a defined pattern. With printed electrodes, other materials can be combined to form sensors. We created sensors for mechanical, environmental, chemical, biological and medical parameters. These are integrated into systems together with wire-based and wireless communication protocols. Passive components are widely covered in literature and are excluded from this work as well as the computing units because the computing power of silicon ICs are unmatched by printed electronics.

The thesis structures according to the workflow of printed electronics as shown in the diagram in Figure 1.3. After the introduction given in this chapter, the basics of processing technologies for printed electronics are discussed in Chapter 2. An overview of printing and coating techniques is given and a detailed evaluation of inkjet and screen printing is given as well as a short description of spray coating. All involved components such as printing equipment, functional materials, substrates and processing steps are described through experimental results. Chapter 3 focuses on electrically conductive patterns on flexible and stretchable substrates. Different curing techniques are described and results from experiments with thermal and photonic sintering by intense pulsed light are presented. Chapter 4 describes the production of sensors based on the results of the previous two chapters. Sensor electrodes as well as sensors for strain, force and pressure, temperature and humidity, for chemical and biological substances, and for medical parameters are presented. These sensors were combined to hybrid sensing systems for the Internet of Things that are covered in Chapter 5. Such systems are based on an imprinted substrate with at least one sensor and a communication channel such as an antenna. Then, they are assembled with surface mount devices such as resistors, LEDs, capacitor and microprocessors. Therefore, antennas, printed circuit boards and their assembly

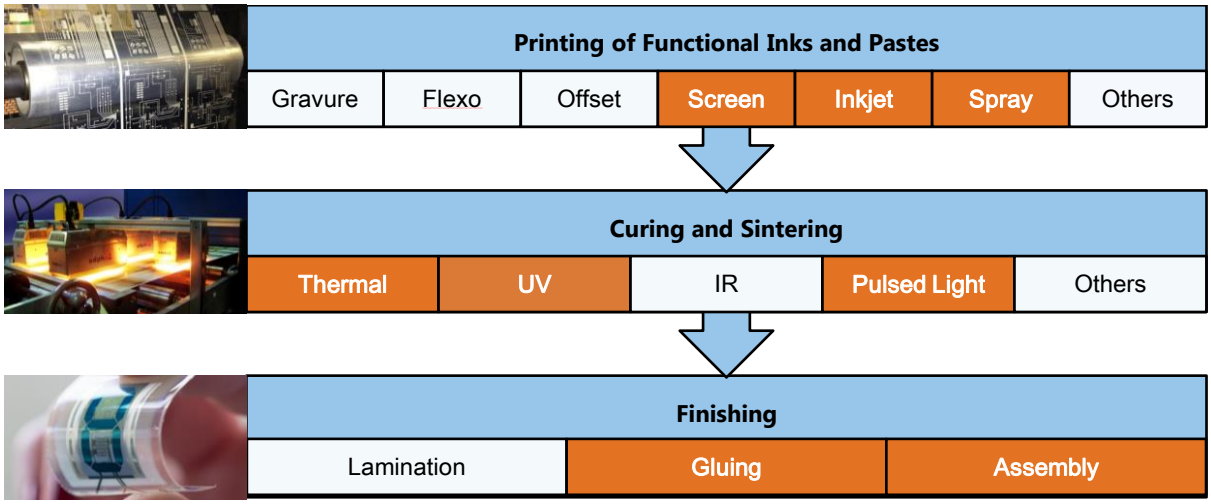

Figure 1.3. Workflow of printed electronics. Each step may be repeated several times to achieve a final product. The orange marked techniques were used during the work on this thesis. Images reproduced with permission of: Printed Electronics Now, WhatTheyThink, Holst Centre

are discussed in detail. Chapter 6 summarizes the thesis, highlights the main conclusions, and gives an outlook on future work in the field of printed electronics.

Chapter 2

Processing Technologies for Printed Electronics

Printed Electronics (PE) are produced by printing techniques, which have distinct advantages for certain applications. The design of the processes requires making decisions on the employed printing technique, the hardware, and the pre-processing and post-processing of the substrates and on inks or pastes. This chapter gives an overview of all production steps with commercial equipment, substrates, inks, pastes. The first section describes several printing and coating techniques in general and with a focus on printed electronics. The next three sections focus on the three methods employed during the work of this thesis: Inkjet printing, screen printing, and spray deposition. Inkjet printing (Section 2.2) is a digital and non-contact printing technique that can be used for simple prototyping and is easily scalable. Screen printing (2.3) is a much more popular technique already used in industrial processes and many printable materials are available but requires patterning of a screen. Spray deposition (2.4) is a coating technique to cover large areas homogeneously at a high speed but only allows coarse patterning. A summary of the chapter is given in the concluding Section 2.5.

2.1 Common Printing and Coating Techniques

Inspired by the high speed, the low cost, and the wide distribution of printing techniques in many industrial areas, more and more researchers and companies adopt them for the production of printed electronics. Some requirements of printed electronics are different from other areas like graphical printing. A clear impression of a line to a human eye is achieved at widths above 50 µm and most printers are limited to this printing resolution, which is approximately 600 dots per inch (DPI). For the visual impression, it is unimportant whether the line is composed of separate drops or a continuous line. The first is often used for graphical printing to not mix adjacent colours. For functional printing, the second is usually a requirement and the edge contours are crucial. For example, conductive lines must be continuous and homogeneous in width to allow a flow of current at an equally low resistance throughout the line. Next to a continuous line, also the film thickness and its roughness are important criteria for printed electronics, as they influence the functionality. In the graphical

field, multi-layer printing of different materials is avoided or only used to create an impression of a mixed colour. In functional printing, it is often required to deposit multiple layers on top of each other with a high control over the thickness and roughness. For example, an insulating layer between two conductive layers has to be thick enough to compensate the roughness of the bottom layer and homogeneous enough to avoid pin holes. At the same time, it should be thin at the edges to facilitate a printing across the step. [2], [3], [7], [38]

Table 2.2 gives a short overview of characteristics of the printing process of five important technologies, the commonly smallest feature sizes, and the type of ink used. The minimum features size refers to the diameter of the diameter of the thinnest line or dot that can be printed using this technique. The print speed describes the length of the substrate material that can be printed within one minute. The print speed of most printing techniques is independent of the width of the material. Some techniques have rather wide ranges because of many differences in technology. Wet film thickness refers to the thickness of the printed film after printing and before drying after a single pass. Each technique can only be used with a specific viscosity of the inks and pastes. The given values are a common range for industrial applications, yet laboratory scale printing machines can reach parameters out of the given ranges. [2], [3], [23]

In the following, we present several printing and coating techniques that all have in common that material is transferred to a surface by mechanical force or hydrodynamic stress [23]. We differentiate between printing and coating according to the definition of Nisato [23] that printing can be defined as the reproduction of patterns. Thus, subsection 2.1.1 describes intaglio, relief, mask-based, and digital printing techniques. Techniques that are rather suitable for coating large areas and offer only coarse patterning are listed under the coating techniques in subsection 2.1.2.

2.1.1 Printing Techniques

Gravure Printing transfers ink from an ink reservoir (ink pan) to the substrate by tiny engraved cells on the printing cylinder that are filled with ink and release it on contact with the substrate as shown in Figure 2.1a. The print pattern is composed of a matrix of dots which are each engraved as a dent or cell. The engraved cells define the print pattern. The recessed image is engraved into a plated and polished copper layer by chemical etching, electromechanical engraving, or laser engraving. To avoid squeezing of the ink, the cells must be disconnected by a thin wall. The size, shape, and depth of the cells play key roles in controlling the quantity of transferred ink and controlling the quality of the printed patterns. The print cylinder is bathed partially in ink to fill all cells. Excessive ink on the surface of the cylinder is wiped away by a doctoral blade. In contact with the substrate, the cells release the ink. The release is the most important step of the printing process and depends on many properties of the cells and the ink. The surface energy of the plate and the substrate, as

Table 2.1. Comparison of printing techniques used for printed electronics. Adapted from [2].

Printing technique	Print speed [m/min]	Minimum feature size [µm]	Wet film thickness [µm]	Ink viscosity [cP]
Flexographic	50 – 500	30 – 75	0.5 – 8	50 – 500
Gravure	20 – 1000	20 – 75	0.1 – 5	50 – 200
Offset	15 – 1000	20 – 50	0.5 – 2	20 000 – 100 000
Screen	10 – 100	50 – 100	3 – 100	500 – 50 000
Inkjet	1 – 100	20 – 50	0.3 – 20	1 – 40

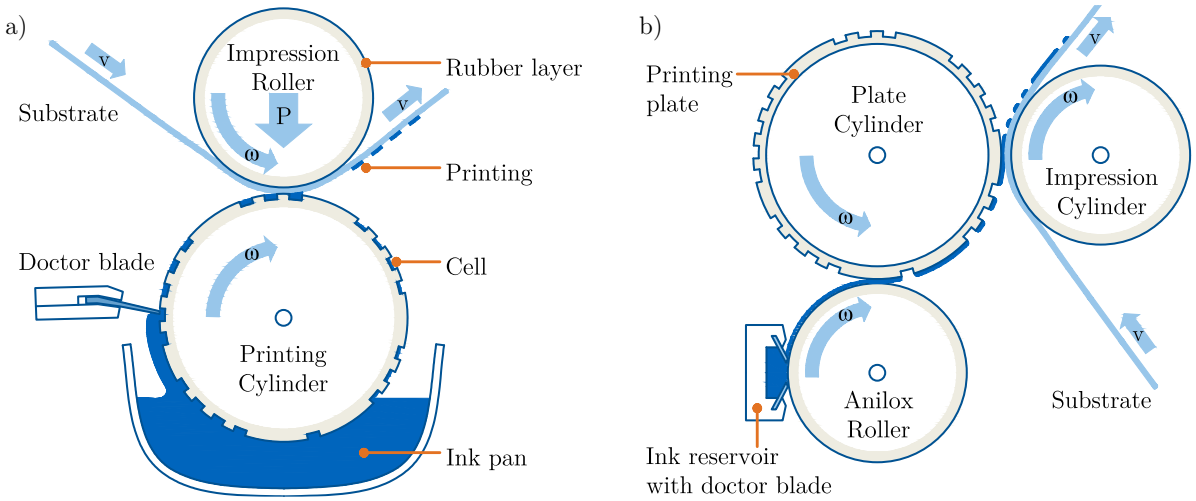

Figure 2.1. Simplified schematics of gravure and flexographic printing. Real printers possess additional rollers. a) Schematic of gravure printing. The ink is transferred by the engraved cells of the printing cylinder onto the substrate. b) Schematic of flexographic printing. The anilox roller transports ink to the raised image on the flexographic plate wrapped around the plate cylinder from where it is transferred to the substrate on contact.

well as the surface tension and viscosity of the ink, play a major role. The goal is to transfer all the ink in the cells onto the substrate. This requires a high impression pressure between the printing and the impression cylinders. Once on the substrate, the ink from the individual disconnected cells must be able to flow to form a homogeneous film. The surface energies of the ink and the substrate's surface must match. [3], [4], [23], [38]

The advantages of gravure printing are the high throughput possible in roll-to-roll processes and a repeatable quality over the long lifetime of the printing cylinder with millions of prints without deterioration. The engraved structure offers high control over the ink volume and allows thickness variations within the pattern. Common printed films are about 1 µm thick, but more than 5 µm is also possible. The primary disadvantage of this printing technique is the high plate making cost. Gravure printing is unattractive for prototyping and small batches. Usually, gravure printing is only possible at high speed. This requires a lot of material and substrate for testing new configurations and possesses the danger to produce a lot of trash in a short time if something goes wrong. The storage and transport of cylinders are difficult because of their weight. Gravure printing is only possible on flexible substrates because of the high impression pressure. If the substrate's stability or smoothness is not sufficient to transfer the ink, this can be overcome by an offset roll that is added inbetween the printing cylinder and the impression cylinder. This picks up the image and transfers it to the substrate that can also be of a curved shape, e.g. a plastic cup. [4]

Gravure printing is mainly used for highest print volumes and throughputs that are required for magazines, packaging, and decorative plastic films. It is also used for high quality and unforgeable objects like banknotes, stamps, and other securities. In the field of printed electronics, gravure printing has been used for conductors, antennas, capacitors, and organic electronics such as transistors, solar cells and light emitting diodes. Many references to gravure printed electronic devices can be found in the reviews of Yun [7], Tobjörk and Österbacka [2], and Zheng [3].

Flexographic Printing is a relief or letterpress printing technique with the pattern raised on a plate. The flexographic plates are usually made from a cheap and flexible photopolymer and are patterned by photolithography. The pattern can be replicated from a negative master plate or produced by exposure to ultra-violet (UV) light. The replica is either removed from the water-soluble photopolymer after the print pattern was cross-linked by UV light or it is formed by selectively crosslinking a liquid photopolymer through a mask. The structured plates are then wrapped around a cylinder as shown in Figure 2.1b. The ink is first homogeneously applied from an ink reservoir to an anilox roller that is micro-structured with tiny cells. Excessive ink is wiped off by a doctor blade

and the ink in the cells is transferred on contact with the flexographic plate onto the plate cylinder. Only the raised print pattern is covered with ink and then transferred to the substrate. The two transfer steps require a high matching of all surface energies and the surface tension of the ink. As the flexographic plate has to be pressed onto the substrate to some extent, ink is squeezed out towards the sides. A typical error is the so-called halo effect that distorts the edges of the printed pattern. One method to avoid this is the use of only a small amount of ink. With flexographic printing, layer thicknesses of several tens of nanometres to a few micrometres are printed. [3], [39]

The advantages of flexographic printing are the low initial costs of the plate and the smaller modification costs by producing a new plate compared to gravure printing. With the elastic plate, it is easier to print directly on rigid and rough surfaces and a lower printing pressure is necessary. Thin printing layers with sharp edges and smooth surfaces can be obtained by inks that are slightly more viscous than for gravure printing. This allows a higher loading with particles or other functional material. The thin layers can be also a disadvantage, for example at printing highly-conductive wiring, which requires a certain film thickness. Solvent-based inks often used in functional printing may lead to a swelling of the flexographic plate and deteriorate the printing over time or destroy the plate. The lifetime of the elastic flexographic plate is rather short from a few days when in use to only a few months if not used. The swelling and change of the properties of the surface can increase the tendency for halos or interrupt printed lines. [3], [39]

Flexographic printing has been mainly used in literature to print one or two functional layers for electronic devices. This includes the printing of conductive patterns for the electrodes of field-effect transistors, solar cells, and displays as well as for RFID tags and other types of antennas. [2], [3], [7]

Offset (Lithography) Printing bases on an image cylinder on which the binary pattern is reproduced by spatially varying surface energies. The image-carrying plate is usually a thin sheet of aluminium or polyester with a thickness of 40 µm to 200 µm and is wrapped around the image cylinder after structuring. The typical plates are produced as negative-working plates, but positive ones exist as well. It is first coated with a light-sensitive diazo compound or a photopolymer that can be hardened (or destroyed) by UV light. The structuring can be done with a negative (or positive) mask or without masks by computer-to-plate systems. The non-exposed areas can be washed away by water and the exposed photopolymer remains within the print pattern (or opposite). A gum solution is applied to the non-image areas of the plate that makes it ink-rejecting. Waterless plates shorten this process by having a silicone rubber coating on top of the photopolymer. During exposure, the bond between the rubber and the polymer layer is broken and the silicone in the image areas can be removed. Offset printing requires hydrophobic ink, which is a significant limitation, as no water-based inks can be used. Before printing, the image cylinder is wetted with water or another dampening solution before the ink is applied. The ink attaches to the hydrophobic surface of the inside of the pattern whereas it is repelled by a hydrophilic layer outside of the pattern. To avoid soaking of the printing substrate, a blanket cylinder is employed that transfers the ink to the substrate and absorbs the water. [4], [40]

The advantages of offset lithography printing are the avoidance of deformations of the substrate, which simplifies multi-layer printing. The lithographic process enables a rather high print resolution. The flat surface of the image cylinder does not squeeze out ink and thick layers of ink do not require large cells. The disadvantages are the plate-making process and the press setup before starting to print. The offset plates are sensitive to chemical oxidation and the non-printing areas are getting more hydrophobic. [4]

Offset lithography printing is the most common high-volume printing technology for graphics printing. Books, newspapers, advertising materials, and packages are often produced with this technique. RFID tags, solar cells, organic light emitting diodes, and organic field effect transistors or electrodes for these were printed by researchers. [2], [41], [42]

Stencil Printing and Screen Printing are two similar techniques that follow a different approach than the intaglio, relief, or offset printing techniques. For both printing techniques, a stencil or a screen, respectively, has to be produced that has openings in the shape of the pattern through which a viscous paste is pressed onto the substrate. Stencils are usually made from a thin sheet (~ 100 µm) of stainless steel that is laser-cut, etched, or milled. The main limitation is that the stencils are getting mechanically unstable if the patterns are large in at least one direction. Stabilization gutters are required then, which may lead to broken strokes in lines, which is often not desirable for functional printing. This is the reason, why stencil printing is only used for small areas like the application of solder paste on contact pads. [43]

Screen Printing is the most used printing technique in electronics manufacturing [38], [44] and will be discussed in more detail, as it was used in this thesis. Figure 2.2 shows a schematic of a flat-bed screen-printer with a mounted frame and a squeegee that presses the paste through openings in the screen. A printing substrate is put on top of the printing table under the frame, which is mounted at a "snap-off" distance away from the substrate. The frame carries a tightly stretched mesh originally made of silk, today mostly made of polyester, nylon or stainless steel. The mesh is then structured by blocking all openings in the mesh that are not needed for the reproduction of the pattern. This can be achieved in multiple ways, of which we briefly describe two different coating methods followed by two different exposure methods. Direct-emulsion coating describes the multiple application of a viscous emulsion on both sides of the screen to fill all openings, create the desired screen thickness, and smoothen the bottom (print) side of the screen. Capillary-film coating uses a water-soluble film of the desired thickness that is applied onto the print side of the water-soaked screen. Capillary forces in the mesh pull in the thin, dissolved contact surface of the film and fix it to the screen after drying. Both, emulsion and capillary film are sensitive to ultra-violet (UV) light and the coating must occur under yellow light. After coating, the coating layers are exposed selectively to UV light to harden all non-printing areas. This can be achieved by a large UV lamp and a mask that covers all printing areas or a selective hardening with UV light coupled out of a glass fibre that scans over the screen. The first is fast but requires production of a mask, the second is rather slow but allows a digital screen production. After the exposure, all non-exposed areas can be washed out with water and the screen can be mounted into a printer. The printing paste is a highly viscous material consisting of the functional material and high-boiling-point solvents or crosslinking agents. The

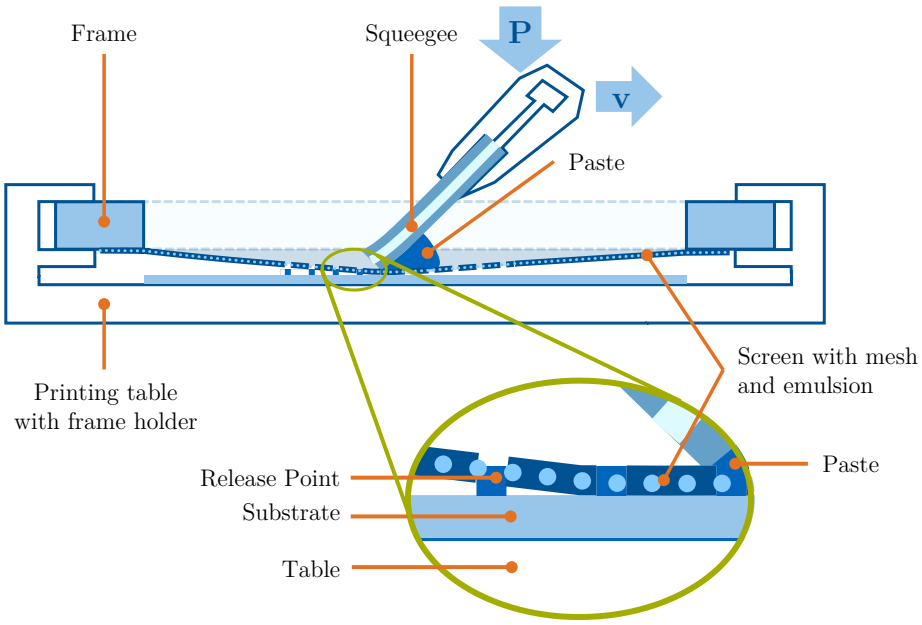

Figure 2.2. Schematic of screen printing and the required components. A screen consisting of an emulsion-coated mesh is fixed to a frame that is then put into the printer. A squeegee travels across the screen with a defined velocity v and a pressure P and presses the paste through the openings onto a substrate on a table.

functional material can be colour for graphics printing or conductive, dielectric, or sensing for functional printing. This paste is usually spread over the entire screen with a flood squeegee and then printed as shown in Figure 2.2. The print squeegee consisting of a single or multilayer rubber mounted to a holder and travels across the screen with a velocity v. A certain pressure P is exerted to deflect the screen close to or in contact with the substrate. A defined angle of about 45° to 75° is usually used to press the sharp edge of the rubber onto the screen. The deflection of the rubber under pressure has to be considered as well as the hardness and the friction on the screen. The velocity must be low enough to allow the paste to flow through the screen and achieve a proper release of the paste from the screen. At the release point, the screen is lifted up slowly while the pressure-exerting squeegee travels further. The paste in contact with the substrate is pulled out of the screen and remains on the substrate. The maximum amount of paste remaining on the substrate depends on the theoretic volume defined by the thickness of the screen, the mesh count, and the thread diameter. Only a fraction of the theoretic volume is deposited depending on the adhesive forces on the interfaces of the paste with the substrate, the threads, and the emulsion. A more technical description of screen printing can be found in the handbooks of Kipphan and Sefar [43], [45] and aspects related to printing of electronic and organic materials in the following referenced books [3], [4], [23], [38] as well as in Section 2.3.

The three unique propositions of screen printing are the wide range of substrates, the possibility to apply thick layers, and the large availability of pastes. The easy principle allows a reproduction of patterns on even, rough, and bent surfaces of various substrates, e.g. paper, cardboard, plastic, ceramics, glass, metal, and wood. The thickness of the layers can range from below 1 µm up to several hundreds of micrometres, which can only be obtained by screen, stencil-printing, and dispenser printing. Similar to the printing principle, the composition of the pastes is simple and many screen-printable pastes are commercially available. This starts in the traditional printing of colours, special visual effects, and unforgeable patterns. Additionally, a wide range of functional materials like conductive, semiconductive, and dielectric pastes exist. Some feature special properties of transparency, biodegradability, abrasion-stability and many more. The formulation of the paste is easier, as micron-sized particles are easier to obtain than nanoparticles (NPs). In the practical application, the major impact on the usability of a paste is the particle size that must be considerably smaller (max. 30 %) than the mesh opening, the curing temperature below the glass transition point of the substrate, and the cleaning agents to free the screen from paste after printing. The cost of the equipment and the pastes can be low. The disadvantages of screen printing are the low printing speed that mainly depends on the paste's viscosity and the many parameters that have to be adapted for high-precision printing. The high viscosity of screen-printing pastes often leads to rough layers. [3], [38], [43], [46]

Screen-printing is widely used for printing on paper, plastic foils, textiles, stickers, vinyl, and wood. In the field of printed electronics, thick conductive layers with a low resistance have been produced for wiring, antennas, and electrodes for sensors, solar cells, and field effect transistors [2], [23], [47], [48]. Additionally, resistors, capacitors, and more complex devices like thin-film transistors, organic solar cells and light-emitting diodes, batteries, and sensors have been shown and are in commercial production already [3], [38].

Common flat-bed screen printers have a throughput of up to 1000 copies per hour with automatic sheet feeding systems. They can be used for roll-to-roll printing if the substrate is stopped for a few seconds during the printing. To increase the throughput up to 4500 copies per hour, cylinder presses in the flat-to-bend configuration shown in Figure 2.3a have been developed. In this configuration, the horizontal position of the squeegee remains unchanged whereas the frame and the substrate are moved at the same speed below the squeegee. The substrate is fed over an impression cylinder whose curvature determines the release of the paste from the screen. When the screen is moved to the end, the squeegee is lifted and the screen and the paste on it are moved back towards the starting position. During this time, printing is not possible. In practice, this technique is often used for sheet-to-sheet

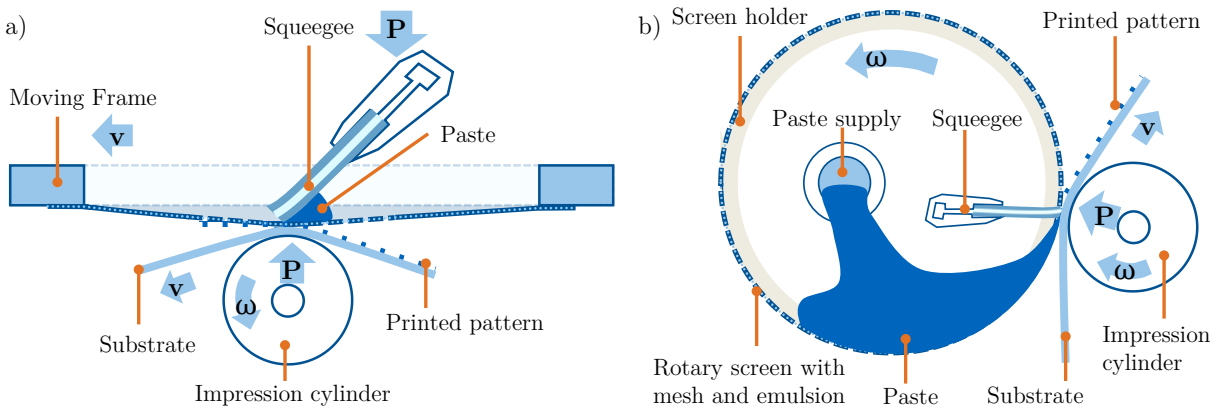

Figure 2.3 Two different roll-to-roll configurations of screen printing. a) In the flat-to-bend configuration, the screen and the substrate move at the same velocity while the squeegee remains at the same position. At the end of the screen, the squeegee is lifted and the frame is moved back to the starting position. b) In the bend-to-bend configuration, the screen is a cylinder that rotates with a speed ω, which matches to the substrate speed v while the squeegee remains at the same position.

production with a distance between the different sheets or the substrate is stopped. Multiple printing units may complement each other to continuously print in roll-to-roll printing. The flat-to-bend configuration can also be used for printing on bent objects that are rotated instead of the impression cylinder. Spherical objects can also be imprinted to a certain extent using a curved squeegee. [4], [43]

Rotary screen printing is a true roll-to-roll printing technique with a stationary squeegee and a cylindrical screen. The screen is usually a metal mesh or a specially deposited alloy to achieve a higher dimensional stability mounted onto steel rims. The paste is fed into the cylinder and pressed through the mesh onto the substrate that runs over an impression cylinder.

Inkjet Printing is a digital and non-contact printing technique. The term digital refers to the digital control over the printing process that does not require patterning of plates, cylinders or masks. A electronic controller triggers ejections of fixed quantities of ink from a nozzle towards the substrate. The inkjet printhead is not touching the substrate but is a few millimetres to a few centimetres away from it and the ink needs to travel from the nozzle across this distance. Several different implementations of inkjet printers exist with nozzle counts between one and several ten thousand nozzles. Print heads with a low number of nozzles are usually mounted on a scanning stage perpendicular to the direction of the paper transport. The print head may move once (single-pass) or multiple times (multi-pass) over the same area to increase the thickness of the printed layer or compose the pattern during multiple passes. A print head consists of a large ink reservoir or cartridge, a filtering unit, the nozzles and the actuation unit around a small ink reservoir. The actuation unit triggers a sudden, quasi-adiabatic reduction of the volume of the small ink-filled chamber. This volume reduction leads to a shock wave through the chamber towards the nozzle causing an ejection of a droplet. [23], [49]–[51] Figure 2.4 shows schematically a piezo-electric drop-on-demand print head during the droplet ejection. If no droplets are required, the print head remains inactive as seen on the left drawing. Shortly before the desired location of printing is reached, the piezo-electric actuator reduces the volume of the chamber causing an ink flow towards and out of the nozzle. When the meniscus breaks, a part of the ink is pulled back into the chamber whereas the other travels as one or multiple drops towards the substrate. Ideally, all drops merge to one drop that hits the surface at high speeds of about 1 – 25 m/s and forms a printed dot there. In the meantime, the actuator increases the volume of the chamber to refill it from a cartridge. Today, most print heads combine hundreds of nozzles into micromechanical systems to obtain a higher print speed and/or resolution. [3], [23], [50], [51]

When the droplet hits the substrate, it spreads due to its volume and speed, the ink's viscosity, and the surface energies of both the ink and the substrate or its coating. The droplet diameter can vary much between 20 µm and above 100 µm. This defines the minimal print resolution and not

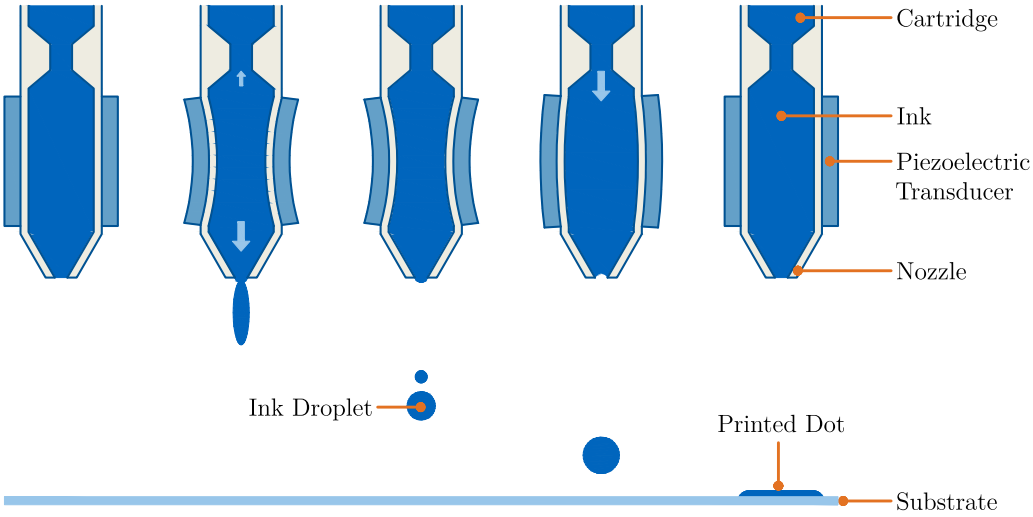

Figure 2.4. Schematic of inkjet-printing. Multiple nozzles are showing the temporal sequence of the drop ejection. The first and last transducer are in the idle position. The second shows a contraction leading to a volume reduction and a drop ejection. The meniscus breaks and the inkjet travels towards the substrate. Satellite drops merge to one drop that lands on the substrate as a much larger dot. Meanwhile, the transducer expands the volume of the chamber to refill ink from the cartridge.

directly the nozzle density, as only a few nozzles can be used to achieve high resolutions by multipass printing.

The main advantage of inkjet printing is its digital nature that allows the definition of every single printed drop and each pattern can be independent of the previous. This means a high control over the process and no changeover costs if the same ink is used. This makes inkjet printing the cheapest printing technique for low volumes and it is often used in research. Furthermore, it is easily scalable using the same print head mounted on a larger stage or using multiple print heads. Multipass printing and control over the ejected volume allow precise dosing of functional material even with a temporal resolution. The non-contact technique does not directly influence underlying printed layers because no pressure is exerted, but the high solvent content of inkjet inks is often a problem in multilayer printing. First, it leads to relatively thin dry films and second, it can dissolve previously printed layers. The low viscosity can also cause the often-encountered coffee stain effect or Marangoni effect [52], [53], which is caused by variation in the ink composition during drying because the solvent at the edges of the drop evaporates faster than in the rest of the drop. The print speed of inkjet printing is rather slow because each nozzle can only eject one drop at a time and the ejection frequency is typically limited to a few Kilohertz. High-speed printers usually combine many hundreds up to tens of thousands of nozzles to compensate this, which increases the printer cost and the complexity significantly. Another often encountered problem is nozzle clogging by dried ink or air bubbles in the chamber that were in the ink before or are sucked into through the nozzle. [51], [54], [55]

Nevertheless, inkjet printing has gained a growing interest in many areas. Consumer desktop printers mainly use inkjet printing because of it is a low-cost, reliable, quick, and convenient method for printing digital files. In industry, flexible and small volumes are commonly inkjet-printed, for example, codes, labels, wide format graphics, publications, magazines, or books on demand. Especially in the academic field, inkjet printing is used in electronics, life sciences, optics, and coatings. Electronic components like conductive lines, antennas, OLEDs, organic photovoltaics (OPV), organic thin film transistors (OTFTs), and sensors have been realized by inkjet printing. [2], [3], [23], [51], [54], [56]

2.1.2 Coating Techniques

This subsection summarizes additive manufacturing techniques that are usually employed to homogeneously coat a larger area and are only able to form patterns with additional means.

Spin Coating utilizes the balance between centrifugal and viscous forces to form smooth and homogeneous layers. A drop of the functional liquid is deposited in the centre of the substrate, which is mounted onto a spinning plate in way that the substrate and the plate have the same rotational centre. When the spinning plate is rotated, the liquid spreads over the substrate's surface by centrifugal forces. The layer thickness decreases approximately linearly with the rotational speed and approximately with the square root of density and time, which defines the centrifugal forces. A higher viscosity increases the thickness approximately with a square root relation. Excessive material is thrown off at the edges of the substrate and is usually much more than the deposited layer. [23] Spin coating is highly reproducible in lab-scale and used in semiconductor manufacturing on substrates with a diameter of up to a few tens of centimetres. Small, pin-hole-free, and homogeneous coatings can be achieved. However, small dirt particles and a rough surface can inhibit their formation on a large fraction of the substrate. Flexible substrates are commonly seen as not suitable for spin coating because they are deformed by the accelerating forces. The major disadvantage of spin coating is that it does not allow any kind of patterning and is limited to small substrates in the size of centimetres or tens thereof. Spin coating is a typical lab-scale deposition method for organic semiconductors for solar cells, light emitting diodes, and transistors which require thin and pin-hole-free coatings. [23]

Slot-die Coating is a roll-to-roll compatible coating technique that can deposit micrometre-thin layers on a large area. The die consists of a chamber into which ink is pumped precisely and without pulsation and a high-precision slot. Through this slot, the ink is flowing like a curtain onto the substrate that moves below the die. The die can be in contact to the substrate or contactless. The volume of the ink that flows through the slot and the speed of the substrate define the layer thickness. Depending on these two parameters and the viscosity of the ink, layer thicknesses between 500 nm and 500 µm can be achieved. It is possible to close certain parts of the slot and introduce a one-dimensional patterning of the substrate. [23], [56], [57] The advantage of slot-die coating is the ability to quickly coat large areas homogeneously with micrometre-thick layers. The disadvantages are mainly related to the required precision of the die. All edges must be accurate to obtain a homogeneous curtain. Such dies are expensive and easily damaged or polluted by dried ink. Slot die coating with separated slots was used to separate several stripes of organic solar cells. [3], [57]

Doctor Blading, Knife-over-Edge Coating, or **Meniscus Coating** uses a blade, knife or a roller at a precise distance to the substrate and pushes the ink over the moving substrate. The small gap and the shape of the edge defines the thickness. At slow speeds and a small gap, the meniscus of the liquid is used to precisely coat a smooth the film. In contrast to other coating techniques, doctor blading fills out uneven surfaces to some extent. If this is desirable or detrimental, depends on the application. If a roller is employed instead of a blade, the rotation speed and direction of the roller can influence the coated thickness. The advantages of doctor blading is the easy construction and low cost of the system. Therefore, small and simple system can be built that dominate the coating systems in the lab-scale size. The disadvantages are mainly related to the employed ink. The rheological behaviour of the ink is crucial and the liquid flow at the blade is complex. Small changes to the ink, for example by evaporation from the open system, can influence the thickness of the coated layer. [3]

Spray Coating is a technique that transfers tiny droplets of material across a small distance onto the surface of the substrate. It is possible to tune the process to obtain one of the following conditions. At high velocities of the carrier gas and a short distance, the solvents of the ink did not evaporate during the flight and a wet film is created on the surface. With longer distances and low-boiling-point solvents, only the dissolved material reaches the surface and no destruction of previously coated layers occur. There are also intermediate steps for deposition of droplets that dry immediately on impact on the surface. The surface of the last two operation modes is rather rough in the range of tens of nanometres due to the size of the droplets. Multiple spraying cycles over the same area with a partial dissolution of the top layers can improve this. The thickness of the sprayed film depends

mainly on the solid content of the ink and the number of spraying layers or the travel speed of the substrate moving past the nozzle. Shadow masks and stencils can be employed for structuring to some extent. [3], [58]–[60] Spray-coating is easily transferable from lab-scale to manufacturing and implementable into roll-to-roll processes. The thickness of the layers can be tuned in a wide range. The disadvantage is the atomization of the functional material into small droplets that may leave the coating machine and be inhaled by operators or deposit on other parts of the printing machine. Long, thin, and continuous lines are challenging with a shadow mask and require some tricks. Organic solar cells, light emitting diodes, thin film transistors, supercapacitors, sensors, and many other devices have been shown using spray coating. [22], [58], [61]–[63]

Evaporation Deposition is a common family of deposition techniques including physical vapour deposition (PVD) and chemical vapour deposition (CVD). The first heats a material in vacuum to the range of its boiling point and evaporated particles travel over the distance to the substrate where they condensate and form a homogeneous film. In CVD, material is deposited from a gaseous phase onto the substrate via a chemical reaction. Both techniques can achieve thicknesses starting from a few nanometres up to several micrometres and structuring can be obtained by shadow masks. The major disadvantage is the need for a vacuum chamber much larger than the size of the substrate and a lot of waste material on the walls of the chamber.

2.2 Inkjet-Printed Electronics

This section discusses the use of inkjet printing for the production of printed electronics and the main components involved: the printing equipment, the functional ink, the substrate, pre-treatment, and post-treatment techniques. Section 2.2.1 introduces some basics of inkjet-printing and its distinct advantages and disadvantages. Nowadays on the market, there are many kinds of inkjet printers from low-cost consumer printers to expensive lab printers and industrial printers. An overview of different print-head technologies is given and, exemplary, a low-cost consumer printer, a modified low-cost flat-bed printer made during the work on this thesis, and a commercial lab-scale printer are presented. Section 2.2.2 gives an overview of pre-press processes including the formation of precise patterns for inkjet printing and treatment and coatings of substrates. An overview of conductive and other functional inks that are commercially available or were synthesized during this work is given by Section 2.2.3. This section contains content from the author's publication "Inkjet Printing and Photonic Sintering of Silver and Copper Oxide Nanoparticles for Ultra-Low-Cost Conductive Patterns" [64] and is extended by findings of other inks, i.e. gold nanoparticles (Au-NPs), the conductive polymer PEDOT:PSS, and a carbon-nanotube-based ink. In Section 2.2.4, we show inkjet-printed conductive patterns on a variety of substrates including papers, polymer films, and others. Some combinations of functional inks and substrates require a treatment of the substrate before and/or after printing. Some techniques for pre-treatment and post-treatment are discussed in Section 2.2.5.

2.2.1 Technological background

The main component of each inkjet-printer is the print-head, which contains at least an ink reservoir, an actuator, and an opening through which the ink is ejected towards the substrate. Several techniques have been developed since Siemens introduced one of the first commercial inkjet-printer in 1951 [51]. Two major groups of systems can be found on the market: Continuous InkJet (CIJ) systems continuously actuate an ink-filled chamber with an opening (nozzle), through which a continuous stream of ink droplets is ejected. Drop-on-Demand (DOD) systems only form and ejects drops when required. [50], [65]

Three types of **Continuous Inkjet (CIJ)** systems are shown in Figure 2.5. All of them have in common that ink is pressed through an ink reservoir with a small opening, the nozzle, by a pump. When exiting the nozzle, the fluid stream is broken into droplets by the surface tension of the liquid. Different methods have been developed to support this breakup closer to the nozzle and achieve more regular drop sizes. [66] Most systems either employ a piezoelectric transducer or a thermal excitation.

Piezo-electric transducers reduce and expand the volume of the chamber constantly. Each sudden reduction in volume ejects one droplet through the nozzle of the chamber. CIJ systems require inks that are electrically chargeable by electrodes that are placed close to the nozzle. These electrodes charge the droplets that will be printed while leaving others uncharged as shown in Figure 2.5a or vice versa. The charge of the ink droplets is used to selectively deflect the droplets that are not needed by the second row of electrodes. The not needed droplets are collected by a gutter and, in some systems, recirculated. [8] Due to the complexity of the entire print-head, CIJ is typically used with stationary print-heads and a moving substrate. [65] In Figure 2.5, the substrate moving direction would be in perpendicular to the drawing plane. The differences between the three systems are in the possible print quality. Binary deflection systems (Figure 2.5a) only select between needed and discarded droplets and can print only binary pixel per drop. The moving substrate below the print-head allows the printing of one line of dots.

Multiple deflection systems (Figure 2.5b) can deflect drops to multiple positions on the substrate by varying the charge of the droplets in multiple steps, e.g. This deflection is typically used in the perpendicular to the substrate moving direction and allows to print multiple binary lines with only one droplet generator. This increases the printing resolution, as the spacious transducers and electrodes require a certain distance to each other. In the 1970ies, IBM licensed the technology and commercialized continuous inkjet printers as a word processing hardcopy-output. [65] The Hertz method is a method that breaks up the ink drops into a mist of small droplets. [67] By controlling the number of these droplets that reach the substrate, it is possible to print grey-scale images.

Kodak produces a third type of continuous inkjet systems, which will be called the Thermal Method here (Figure 2.5c) that employs a different drop generation mechanism. Instead of a contraction of the volume of the chamber, a constant pressurized flow of ink is exposed to varying temperatures generated by thermal actuators directly at the nozzle. The temperature variations modify the physical properties of the ink flowing out of the nozzle. These are mainly the viscosity and the surface

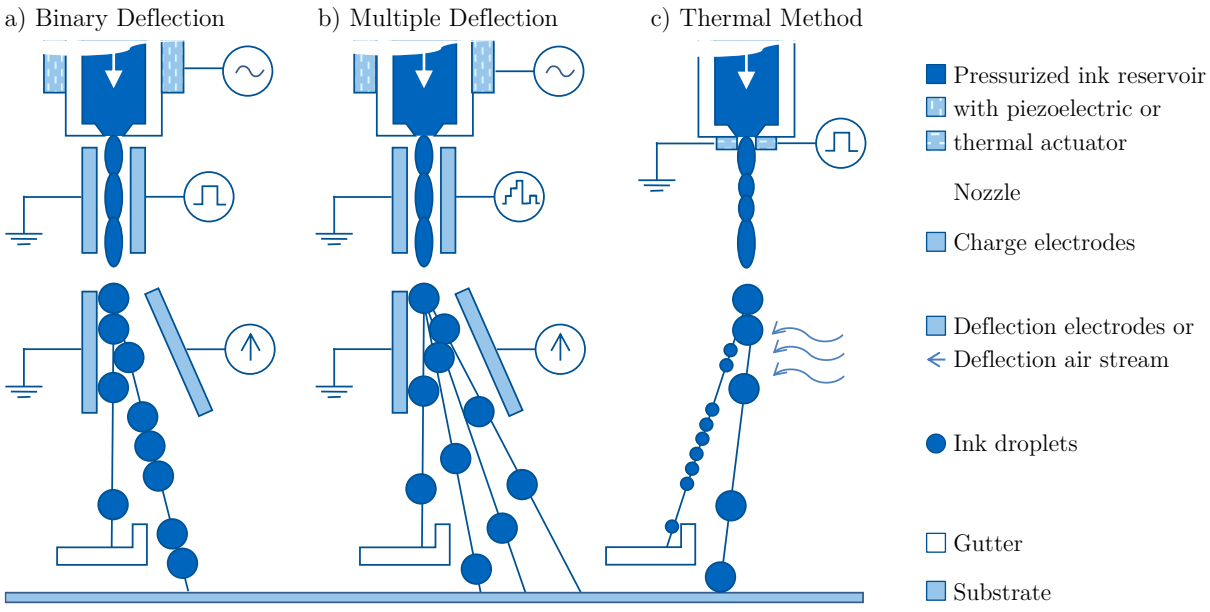

Figure 2.5. Schematic of three piezo-electric continuous inkjet technologies with labelled components. Adapted from [68] with permission from Elsevier.

tension. Periodical heating by the heater and cooling by the ink leads to local minimums of viscosity and breaks up the liquid stream periodically. This technique may replace the piezo-electric actuators and allows much more condensed dimensions and simple manufacturing processes in comparison. Still, it can be employed with charge and deflection electrodes and is also realized in Kodak systems. [69] Additionally, the Thermal Method can be used to generate drops of different size, e.g. small droplets for all not-to-be-printed pixels and large drops for the to-be-printed pixels. The smaller drops can be deflected by an air stream while the larger ones only slightly change their path of flight as shown in the central part of Figure 2.5c. A variation of the drop size can also be used to create drops of multiple steps of sizes that can be used to print grayscale pixels. [68]–[70]

CIJ systems are widely used in industrial coding, marking, and labelling because of their high speed that is compatible with the speed of packaging lines. Examples are individual codes that require digital printing, like printing small texts for serial numbers or best-before dates or tracking codes. Currently, the companies Videojet [71], Domino [72], Linx [73], and Kodak [74] are selling CIJ systems according to Ujiie et al. [68] and the companies' websites.

Drop-on-Demand (DoD) systems generate droplets only when needed. The most common mechanisms base on a volume reduction of an ink-filled chamber by a thermally induced creation of a vapour bubble or a piezo-electric deformation of at least one wall of the chamber. Both mechanisms force a droplet out of a nozzle that is travelling towards the substrate at a lower speed than CIJ systems. The number of necessary components is reduced because the systems do not require a pressured ink supply or a recirculation system. Today, most manufacturers try to integrate the DoD systems into micro-electromechanical systems (MEMS) that are partially produced with semiconductor technologies. [68]

Thermally excited DoD systems consist of an ink reservoir with at least one heater that quickly heats up a thin layer of ink close to the surface so that it forms a vapour bubble. Typically, water-based inks are used that are locally heated up to 500 °C. The vapour bubble expands to a multiple of its liquid volume and forces ink out of the nozzle. Different types of thermal DoD systems are shown in Figure 2.6, which mainly differentiate by the position and number of heaters. Roof or face shooters have the heater positioned opposite to the nozzle in the chamber, whereas side shooters have a heater on a side. Back shooters combine nozzle and heater on the nozzle's side of the reservoir. One or multiple heaters may be positioned at least partially suspended in the ink. All types, but especially the latter allow the creation of droplets of different sizes by applying different voltages to the heaters. Some printers employ a moveable member to amplify the pressure generated by the vapour bubble. [51], [68], [75] An assessment of the best type of heater configuration is difficult, as most companies only highlight the advantages of their product and the main reason for the different configurations

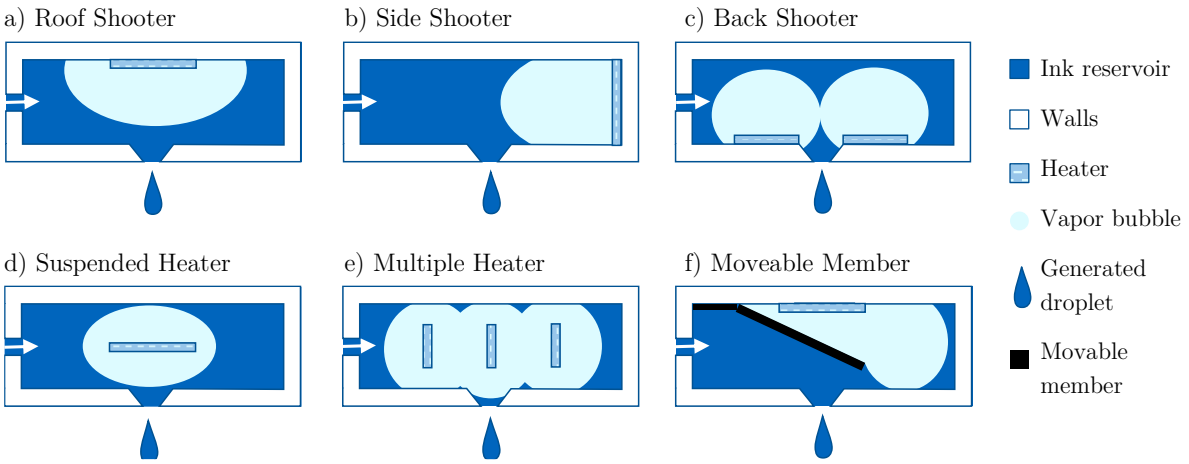

Figure 2.6. Schematics of six different types of thermally actuated drop-on-demand systems. Adapted and merged from [51], [68], [75] with permission from Elsevier.

is the circumvention of patented ones. Additionally to the position of the heater, the operation in relation to the chamber size differs among companies. Whereas most companies only heat a small fraction of the ink in the reservoir, Canon's Bubblejet technology creates vapour bubbles that empty the entire ink reservoir between the heater and the nozzle. [76] Thermal inkjet technology is used in a large proportion of desktop printers, large format printers, and industrial inkjet printers of the companies Hewlett Packard, Canon, Kyocera, Lexmark, Xerox, and Samsung. [68]

The key advantage of thermal DoD is the low manufacturing cost and easy production in semiconductor manufacturing lines, as the actuator is simply a resistive track. This allows the production of MEMS systems without or with a reduced number of assembly and gluing steps. The size of the chambers can be small and allows a high nozzle density at a low price per nozzle. Single-pass print heads can achieve a high resolution with thermal DoD. The low cost and the possibility to produce the nozzles in the same distance as the required resolution allows the construction of print heads with a few thousand nozzles at a reasonable price. Such print heads can be as wide as the substrate and print over the entire width of the substrate simultaneously instead of moving the print head over the paper. The disadvantages are primarily related to the requirements and limitations of the fluids that can be used in the ink. Non-water based inks must contain fluids that can be vaporized easily and all components must withstand high local temperatures. The functional material or colorant should not lose its functionality and not stick on the heaters surface. As many functional materials employed in printed electronics are solvent-based and post-treated with heat to create continuous and connected films, it is generally recognized that piezo-electric printers are preferred for printing electronics. [2], [50], [51], [65], [75]

Piezo-electric DoD systems base on the piezo-electric effect that describes the mechanical deformation of a polarized material on the application of an electric potential and the reverse relation. Predominantly, the ceramic lead-zirconate-titanate (PZT) is poled in a strong electric field to align previously randomly oriented groups of electric dipoles and is then applied as the actuator. In PZT, the piezoelectric effect is anisotropic and two deformation directions can be achieved. An electric field in parallel to the poling direction expands or contracts PZT in the same direction. A field perpendicular to the poling direction causes a shear deformation. [51], [65] Similar to thermal inkjet, many different versions of print head configurations exist. Figure 2.7 shows six common ones. Push mode uses the expansion of the piezo-electric material perpendicular to the poling direction when an electric field in the opposite direction is applied. Squeeze mode printer utilize a tube of piezoelectric material and an electric field in polarization direction leading to a contraction of the tube. In bend mode, the ends of the piezoelectric material are fixed and they bend towards the centre of the ink reservoir on expansion. Shear mode roof shooters employ the shear deformation in a segmented piezoelectric. Shear mode shared wall print heads use piezo-electric actuators between the chambers that can compress the volume of the two adjacent chambers. This allows a dense construction of the nozzles but not a simultaneous operation of two adjacent nozzles. In all types, some barriers obstruct the backwards flow of the ink during contraction by thin ink feed channels or a porous structure as shown in Figure 2.7f through which the ink is fed into the chamber. [49]–[51], [68], [75], [77]

Piezo-electric inkjet printers support most fluids within a given range of viscosity and surface tension making them more popular for printing of functional and heat-sensitive inks. Still, the strong compression and expansion force can lead to vaporization of the ink. Although the waveform of the excitation signal to the piezoelectric ceramics is complex, a change in the waveform allows the creation of drops with different size and speed as well as a control over satellite drops. This is especially important if a printer is applied for inks with different properties. For a successful printing, the ideal waveform must be identified and the signal strength to all nozzles adapted to reach a similar behaviour of all nozzles. Piezo-electric printers are sensitive to air bubbles in the ink that may absorb a big proportion of the volume contraction. Another disadvantage is the smaller excitation forces in comparison to thermal inkjet printers that may not be sufficient to clean clogged nozzles. The

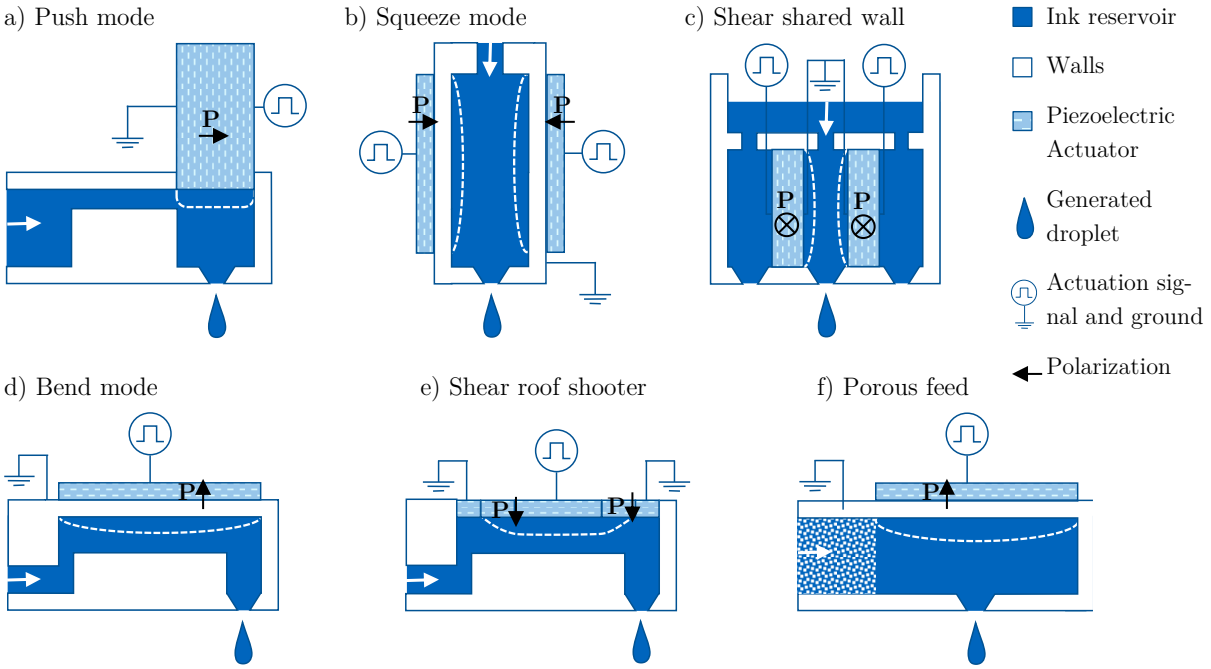

Figure 2.7. Schematics of six different types of piezo-electric actuated drop-on-demand systems. The deformation of the piezo-electric actuators or the walls of the chamber is shown by a dashed white line. Adapted and merged from [51], [68], [75] with permission from Elsevier.

required size of the ceramics puts a lower limit to the size of each chamber leading to a lower maximum nozzle density. Most printers compensate this disadvantage either by multipass printing across the same region with a small offset or multiple rows of nozzles that are slightly shifted towards each other. Multipass printing is often found in cheap consumer printers and increases significantly the time for a print. Industrial printers often employ multi-row printheads to decrease the number of passes. Page-wide, piezo-electric ones are rare because of the cost of the print head. [49]–[51], [68], [75], [77], [78] A lot of companies employ piezo-electric print heads. Among them, the most famous are Epson, Brother, Kyocera, Samsung, Toshiba, Xerox, and Konica Minolta. Ujiie et al. gives a complete overview of printhead technologies and mentions more companies [68].

Other techniques were developed and patented besides the two mostly used DoD technologies. Castrejon-Pita et al. [70], Pond [79], Caironi [78], and Ujiie [68] provide an overview of some techniques that are briefly described in the following and are schematically shown in Figure 2.8. Electrostatic DoD Inkjet bases on the electrical attraction and repulsion of charged electrodes to reduce the volume of the chamber. It is a promising approach under constant research and on the market in a few products, as such print heads can possibly be produced with semiconductor manufacturing similar to thermal print heads. Acoustic excitation of the ink can generate a drop ejection on a free surface of the ink if constructive interference is focused properly. In principle, nozzles are unnecessary, however, they are used to control the ink level. Some demonstrators of Xerox showed the practical implementations and a possible reduction of the minimum drop volume to less than 10 % as well as a smaller drop diameter in comparison to a piezo-electric printer. Electro-hydrodynamic extraction employs a high potential on an extraction electrode in front of the nozzle. The electrostatic stress can overcome the capillary tension and create droplets even from nozzle diameters below one micrometre. These droplets are then guided by an electric field towards the substrate. Park et al. inkjet-printed sub-micrometre lines [80]. The superfine inkjet technology by Murata et al. is assumed to use a modification of this concept, too. [81], [82] The concept of surface-tension-driven inkjet bases on a pre-stressed ink surface that is kept at a force slightly below the breaking point. By heating the ink around the nozzle, the surface tension can be lowered for a short time and a droplet is extracted from the nozzle and guided towards the substrate by an electrode behind the substrate.

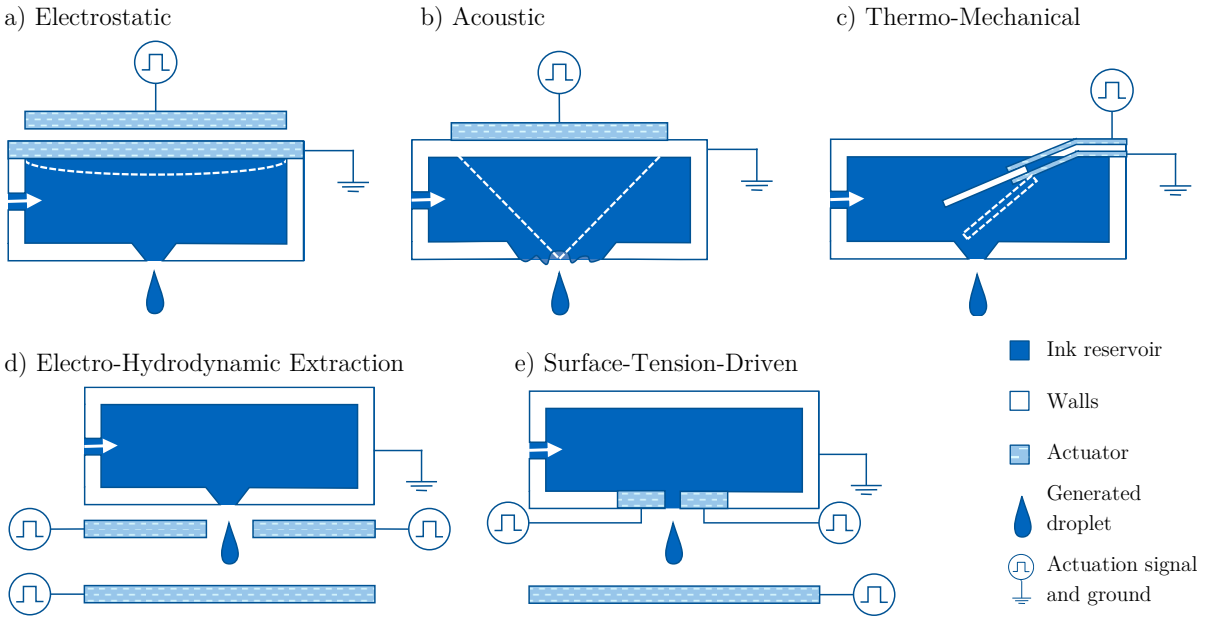

Figure 2.8. Schematics of six different types of other drop-on-demand systems. Adapted and merged from [51], [68], [75].

The main driving force for the development of optimized and new types of print-head technologies comes from the user's need to print a variety of materials at a fine resolution. Especially for functional printing like printed electronics, it is wished to print inks with a higher solid loading, which results in many cases in a higher viscosity that can only be printed with dispensers. Inkjet-systems that can print a higher viscosity are researched [83] and among others, Murata et al. claim their superfine inkjet system can print inks with a viscosity up to 10000 cP, which is comparable to screen-printing pastes. [81], [82] Another driver is the drop volume that is closely related to the thinnest possible line that can be printed. Fuji found that until the year 2005 and probably also slightly longer, the minimum drop volumes achieved in commercial inkjet printers are getting halved about every two years. [84] His data is shown together with other inkjet technologies of 2010 and before in Figure 2.9. For all inkjet systems, a drop ejection occurs when the surface tension of the ink is overcome. If only pushing forces are employed like in thermal and piezoelectric printers, drop volumes below about 1 pL are hard to achieve. [85] To the knowledge of the author, there are only few of such systems reporting drop volumes below 1 pL and none below 100 fL reported in literature until today. Acoustic drop generation seems to be able to produce about a decade smaller volumes because higher forces can be achieved, which are not counteracted by the nozzle walls [86]. However, if pulling forces are used like in the electro-hydrodynamic extraction method, it is possible to create even sub-femtolitre inkjet-printers [81], [82], [87], [88]. Such systems may allow inkjet-printed lines in the range of down to 700 nm [80]. Furthermore, research is going on in reproducibility, printing speed, variable drop-size, print-head production, and roll-to-roll integration. [38]

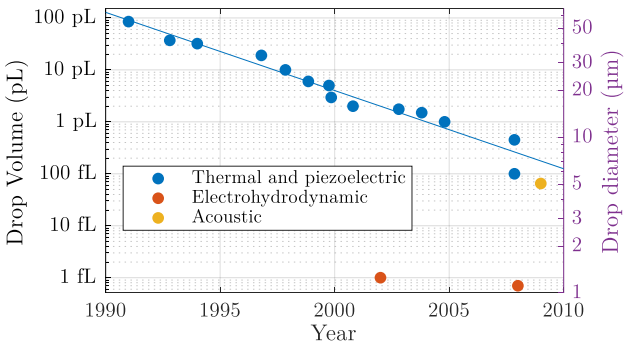

Figure 2.9. Development of the minimum drop volume and the effective drop radius from 1990 to 2010 for three different technologies. The data is acquired from [78], [80], [82], [84], [86].

During the work of this thesis, two different inkjet-printers were used. A low-cost consumer inkjet printer of Epson, which was modified to be able to print on flat substrates, and a lab-scale high-precision inkjet printer of Fujifilm Dimatix.

The low-cost consumer desktop **Inkjet Printer WF-2010** of Seiko Epson Corporation (Shinjuku, Tokyo, Japan) was used to print whenever speed was more important than print resolution and the substrate was flexible enough to be bent in the paper feed. Refillable cartridge ordered from Amazon were filled with the respective ink in the black cartridge. The printer settings of "high quality" printing on "Epson Matte" paper showed the highest resolution and coverage for most inks. The print head employs piezo-electric push-mode. The four colour printer has 180 nozzles for the black ink and 59 nozzles per colour, which are equally placed in two rows on a one-inch long nozzle plate. The resulting distance between the nozzles is 141 µm with a nozzle diameter of 25 µm as can be seen from the disassembled print head in Figure 2.10. The large nozzle distance is compensated by multi-pass printing. The multi-pass printing also increases the film thickness. The rapid printing of an A4-sized page in less than a minute leads to a formation of a homogeneous wet film on non-absorptive substrates.

During the work of the thesis, a **Flat-bed modification** of this printer shown in Figure 2.11 was built to facilitate multi-layer printing and printing on rigid substrates. The plastic cover of the printer was removed and the paper feed was sawn away. This opens the rear side of the printer for inserting substrates without bending them. The remaining parts of the printer were fixed onto a wooden plate. A moving table was constructed that moves on rails through the printer to ensure an accurate and repeatable positioning in the y-direction, which is perpendicular to the substrate moving direction. This table consists of transparent Acrylglas XT with a thickness of 10 mm and a dimension of 50 x 20 cm^2 that was precision-cut. On the sides of the table, miniature rails MMO-09N1 of Dr. Bertram Tretter GmbH (Rechberghausen, Germany) with a width of 9 mm were fixed. Three matching carriages MMN-09N1 on each side of the table were mounted onto aluminium plates at the previous position of the paper feed to ensure the horizontally move the table. The white plastic blocks on each side of the printer carry the weight of the plate before and after printing. The height of the carriages and blocks were adjusted to match exactly the paper transport cylinder in the printer. This enables the moving of the table by this cylinder and does not require another transport system. We found the pressure of the table on the cylinder to be crucial and has to be fine-tuned to avoid misalignment. The y-stage of the WF-2010 containing the print head is only fixed at four spots of which only three are required. These were unscrewed and distance holders of 10 mm were added to lift up the entire printing mechanism to be able to print on top of the table. If thicker substrates than ordinary paper has to be inserted, distance holders with suitable height need to be inserted. Finally, the cleaning station was sawn out and lifted by the same distance.

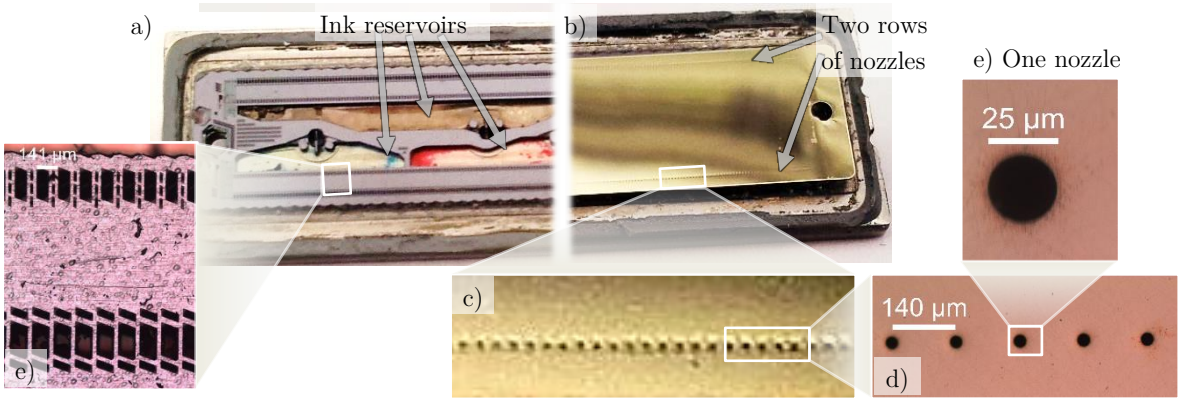

Figure 2.10. The inside of a consumer inkjet print head. a) The microstructure with reservoirs for each colour that is covered by b) the nozzle plate with two rows of 180 nozzles each. c) Magnification and d) optical microscope image of one nozzle row, which are at a distance of 1 inch/180 = 141 µm. (d) Magnification of one nozzle with a diameter of about 25 nm. e) Optical microscope image of the chambers behind the nozzles.

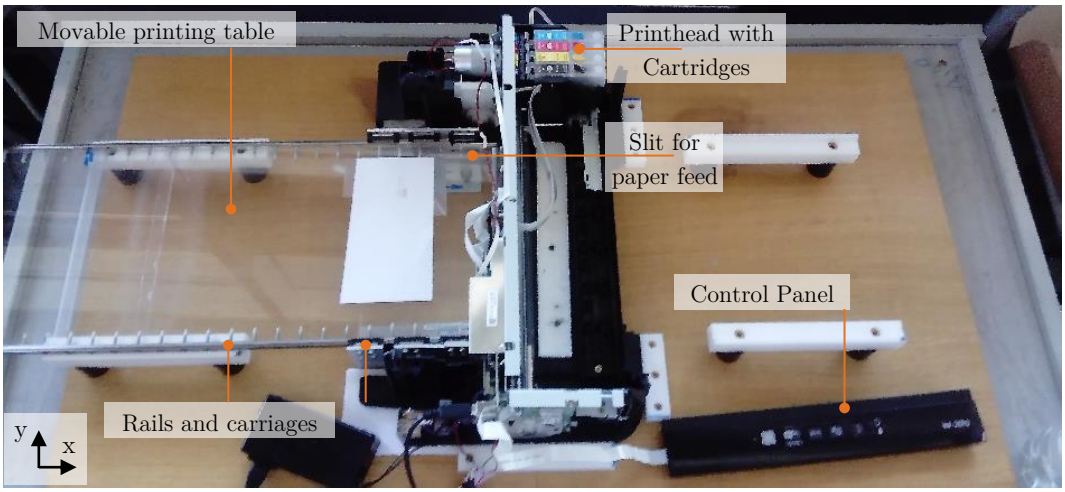

Figure 2.11. The modified WF-2010 inkjet printer that features flat-bed printing and nozzle-to-substrate distance adjustment. The cover of the printer was removed and the paper feed cut away. This opens the rear side for a new rail-guided plexiglass printing table that is moved horizontally in x-direction through the printer by the original paper transport cylinder. The additional height was compensated by lifting up the print-head rails in the y-direction by the thickness of the table.

The control button and LED panel were fixed next to the printer. To facilitate the backwards-movement of the table, a second power supply of 18 V was added. A new two-position switch allows the selection of the voltage at the x-direction linear motor. For forward movement, the signals of the printer were used whereas for backward movement, a voltage of 18 V was applied. For improved alignment in the x-direction, the paper feed switch was modified and moved to the side of the table. A slit in the table was added that has the exact length necessary to make the printer recognize a present substrate. To print on an arbitrary substrate, it has to be glued behind this slit onto the table. A document with the pattern has to prepared that possesses a distance of at least 1.5 mm to the left and right side of the document. After the first move of the print head, it is crucial to insert the flatbed table at the right moment onto the transport roller. A slight manual assistance during the transport of the table is helpful for better alignment. The movement of the table stops automatically because the rear part of the table was thinned and the contact to the transport roll is lost. After a short waiting time, the direction switch can be turned to the other position and the plate can be easily moved back to its initial position and another layer can be printed similarly.

This printer combines the advantages of rapid inkjet-printing with the ability to print on flexible as well as rigid substrates with an arbitrary thickness. Furthermore, the alignment of a second print on the same substrate is accurate in the y-direction (< 50 µm) and acceptable in the x-direction (< 300 µm). The printer is also simple to maintain. The print head can be exchanged by removing the two thicker flat-band cables, the plastic part carrying the electrical contacts to the cartridges, and then unscrewing the print head. A print head from a new WF-2010 printer can be removed with the same procedure and put in the flatbed printer.

The professional laboratory scale inkjet printer **DMP-2831 (Dimatix)** of Fujifilm Dimatix Inc (Santa Clara, CA, USA) was used for inkjet-printing high-resolution patterns or experimental inks. This printer operates in the piezo-electric squeeze mode. The employed print heads are exchangeable, can be heated up to 45 °C and have 16 nozzles with a drop volume of 10 pL or 1 pL. The print area is 21 x 26 cm^2. The printer supports substrates with a thickness up to 25 mm. The repeatability in both directions is $\pm$ 25 µm. The substrate holder is heatable up to 60 °C and uses vacuum to fix the substrate. A drop watcher helps to adjust the waveform applied to the piezoelectric material in the nozzles to form regular drops.

2.2.2 Pre-Processing

High-quality inkjet-printing requires several steps before and after the printing itself. Before printing, these are mainly the preparation of print pattern and the selection and preparation of the substrate [3]. After printing, drying and curing of the films to achieve the desired functionality without destroying neither the thin films nor the substrate.

The **Preparation of the print patterns** for inkjet-printing is the conversion of the drawing a matrix of dots that are either printed or not. The diameter of a drop is the minimum possible feature size. A single row of drops forms the thinnest printable line. In the evaluation, if the desired pattern can be printed on a specific substrate, the diameter of a single drop has to be measured. Typical drop diameters on PET are between 40 µm and 100 µm. If the dots would be placed directly at a spacing of the drop diameter, a pattern like in Figure 2.12a would be created. For graphical printing, such pattern may be desirable, because the adjacent drops do not mix. In contrast, this is not desirable for most functional printing of conductive patterns, as no continuous line is formed. A continuous line can be formed if the drop spacing is reduced below the drop diameter as Figure 2.12b-d shows. For a drop spacing slightly lower than the drop diameter, the individual drops can still be perceived, whereas, the drops merge to a continuous line for small spacing. At a certain drop spacing, typically around 50 % of the drop diameter, a homogeneous line is formed. An even smaller drop spacing leads to bulging in the line (d). Figure 2.12e shows the print pattern formation for a two-dimensional pattern with a drop spacing of 50 %, which is recommended as a starting point. If rippled edges with a frequency around the drop spacing is detected, the drop spacing has to be reduced and if bulges with a frequency considerably higher than the drop spacing are detected, the drop spacing has to be increased. In the following, we assume that the ideal drop spacing is equal to the drop radius.

With this knowledge, the binary matrix is produced from the desired print pattern. This matrix is the raster image and determines whether a drop is placed at a certain location or not. In most printers including the used Epson printer, the printer driver does this automatically. In industrial environments, raster image processing software is used to optimize the creation of a raster image. Many printers support multiple droplet sizes that can be used to improve the printing quality, e.g. place a smaller droplet at the corners of a pattern to get a sharper angle. In the following, we assume, that the printer only supports one drop size and the drop spacing is equal in both directions because these are the limitations of the Dimatix printer. As we want to use a drop spacing of about the radius of a single drop, the pixel size of the raster image is the drop radius. However, a pixel will be printed as a circle with a diameter of twice the pixel size. Figure 2.13a visualizes the printing of individual drops. All pixels that are printed as a drop are coloured in orange in contrast to the not-to-be printed pixels in beige. In the background, the resulting drop pattern is shown by blue circles. Although the raster image has a gap between the pixels, the drops are touching each other. When designing a line as shown in Figure 2.13b, a row of pixels needs to be filled and will be printed as a row of overlapping dots. On the right, the resulting line is shown, which has a width of twice the pixel size. The pixel size is indicated by an orange bar at the top and the line width by a blue bar at the bottom of the

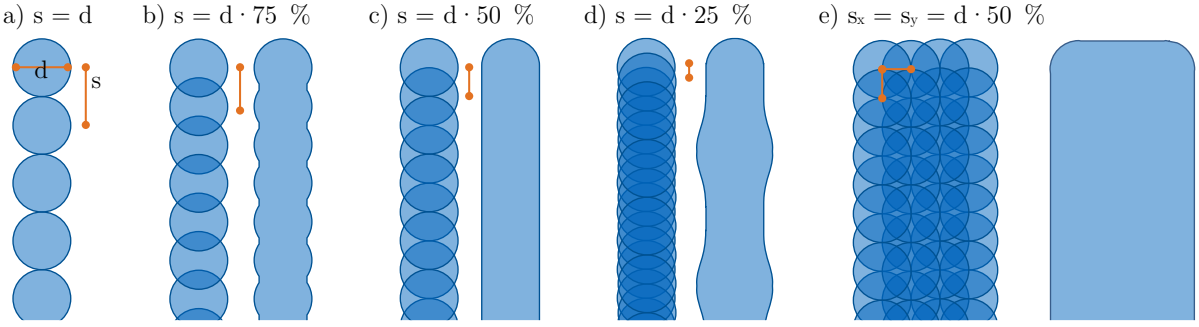

Figure 2.12. Inkjet-printed drops and resulting patterns for different drop spacing s in relation to the drop diameter d.

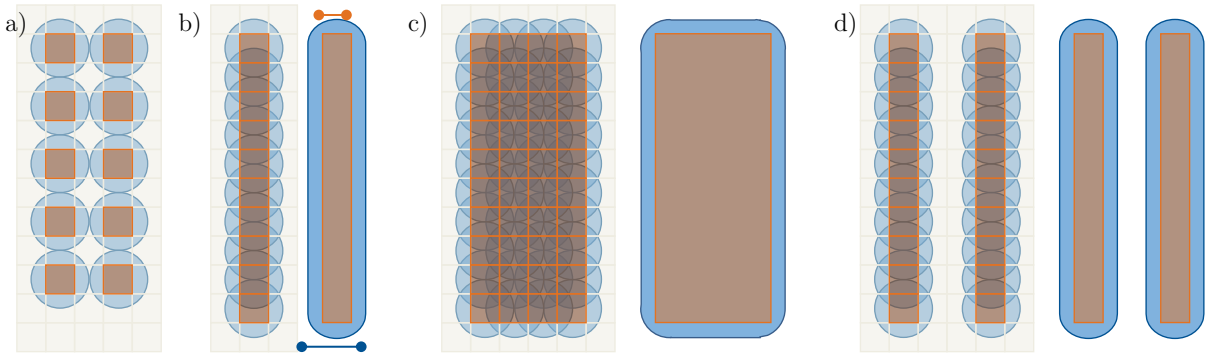

Figure 2.13. Principles of raster images for a) separate drops, b) a single line, c) a uniformly coated area, and d) closest two adjacent lines. The raster image pixels are shown in beige for non-printing pixels and orange for pixels to be printed. The drop pattern with a drop diameter of twice the pixel size is shown behind the raster images. On the right of b-d, the resulting print pattern in comparison to the raster image is shown. In b) the designed line width and the printed line width is indicated by an orange and a blue bar.

schematic. The printed line width is always one pixel-size wider than the raster image, which is also visible for a multi-column line as shown in Figure 2.13c. This means, that the distance between adjacent lines reduces by the drop diameter as well. Two lines with the smallest possible gap must have two non-printing pixels between them as shown in Figure 2.13d to be not shorted.

This behaviour has to be considered when transforming a vector graphic to a raster image. Lines that have to be printed with a defined line-width should be reduced in width by the drop radius before converting them to a raster image. In general, all edges of the print pattern have to be moved inwards by the half of the drop radius. In the following, we want to show the resulting print pattern starting from an arbitrarily shaped vector image. We chose the word “Ink” in a bold font to be our print pattern as shown by the black contour in Figure 2.14a. To compensate the line growth when printing a raster image, we move inwards all edges of the print pattern by half of the drop radius (half of one pixel). The remaining part is visualized in dark blue, while the removed part is shown in bright blue. Now, the vector image is transformed to a raster image. We chose the purely local conversion rule “print if filled by more than the threshold of 50 %”. This is a simple method that transforms strong patterns quite accurately. However, lines that are thinner than $(\sqrt{2}-1)$ times the pixel size are not printed and lines with a width between this value and $\sqrt{2}$ times the pixel size are printed depending on their position and angle and may be interrupted. Thicker lines may also be represented thicker than in the vector image by up to $\sqrt{2}$ times the pixel size. To print such lines and keep the rule simple, the threshold could be reduced, which would lead to a general widening of the pattern. More sophisticated raster image generation algorithms are using the information of neighbouring pixels as well. A review of some algorithms can be found in the work of Trier and Taxt [89].

Figure 2.14b shows the grid lines of the matrix as an overlay and the orange marked elements are chosen to be printed because they are covered by more than 50 % by the drop-gain corrected print pattern (dark blue). It can be seen that some areas are not converted accurately. For example, the right leg of the letter “n” consists only of one printed row although it has the same thickness than the other leg in the original image. This results from its position on the intersection of the pixels. Another position dependent rendering effect can be seen in the round part of the letter “k” that is converted with many corners. The pixel marked in green is filled by almost exactly 50 %. We decided to include it, but if it was slightly less, it would lead a gap between the adjacent pixels.

Figure 2.14c shows the simulation of the drop pattern when a blue drop is printed at each orange pixel. It can be seen, that the drop pattern does not represent all the features of the original image. For example, the letter “I” is just straight instead of curved. Figure 2.14d shows the resulting image after the drops merged in blue in comparison to the original image in grey. Many distortions can be

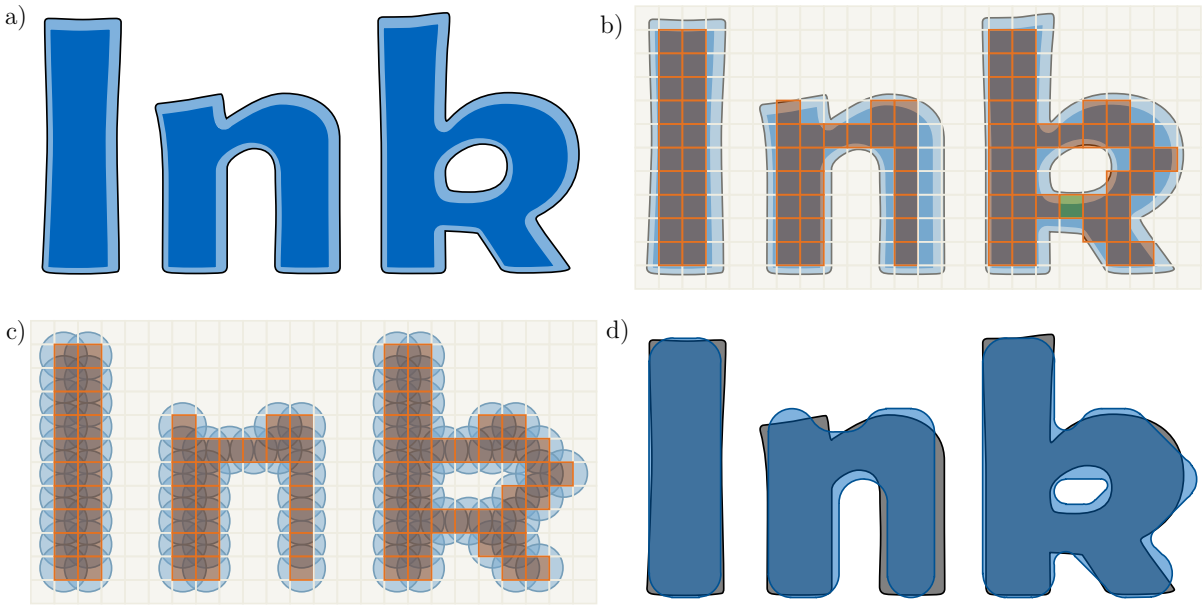

Figure 2.14. The process during the transformation of a vector graphic to a raster image. a) The work "Ink" was designed as a text and is shown as the black contour. The dark blue filling shows the remaining area after drop-size correction shown in bright blue. b) A raster overlay is added with orange showing the matrix elements that are filled more than 50 %. c) Simulation of the drops (blue) according to the raster image. d) Resulting print pattern (blue) in comparison to the designed pattern (grey).

determined. Some examples are that sharp edges at the top of the letter "I" are rounded, slight curvatures on the right leg of letter "n" are straightened, and stronger curvatures at the right of letter "k" are bulging. In general, we think, that the print result is sufficient for this example, as the work "Ink" is still readable and we could highlight the challenges of raster image processing.

The **Preparation of the substrates** surface involves changes in the wettability. When printing on substrates with a low surface energy, the contact angle of the wet ink is too high and it is favourable for the ink droplets to agglomerate to larger drops. Substrates with a low surface energy are classified as hydrophobic and low-wettable. [3] One example is silicone rubber. Figure 2.15a shows an optical microscope image of such a film that was imprinted with silver nanoparticles (Ag-NP) ink in the top-left of the image. Another microscopic image of inkjet-printed Ag-NPs on a hydrophobic, specially coated paper can be seen in Figure 2.18d on page 33. Please note that in Figure 2.15a, the ink drops are shown in darker, whereas in Figure 2.15b and Figure 2.18d, the Ag-NPs are shown brighter in comparison to the substrate. As the drops are not connected, this substrate is not suitable for inkjet-printing conductive patterns on top without pre-processing. The term hydrophobic shows that a low surface energy particularly affects aqueous inks. Several solvent inks have already a much lower surface tension, which can compensate for the lower surface energy of the substrate. On the shown silicone rubber film, the measured contact angle with water calculated by the Laplace-Young method leads to 110°. The contact angle of the Ag-NP ink with the solvent

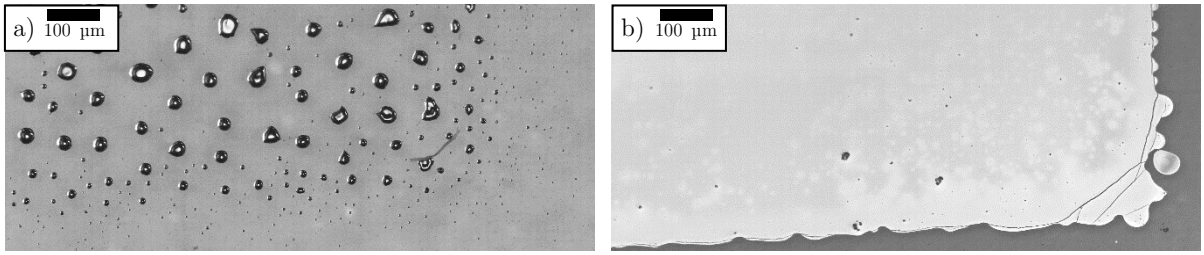

Figure 2.15. Optical microscope images of inkjet-printed and dried Ag-NPs on a silicone rubber film a) without surface treatment and b) with light oxygen plasma treatment. Please note that in the left image, the silver ink is darker than the substrate, whereas, on the right image, the ink is brighter than the substrate due to higher light reflection.

TGME lies at around 60°. Apparently, this value is still too high for the substrate to be printable. The surface energy can be increased by different treatments. Several methods have been developed to induce an oxidation of a thin layer of the substrate's surface that render the surface more hydrophilic. The second option is to apply a coating layer with a higher surface tension or a porous layer.

Surface oxidation reactions can be activated by oxygen plasma, corona treatment, UV irradiation or strong oxidizing liquids. [3], [25] These can be used to alter or homogenize the surface energy, clean the substrate, ablate a weak microscopic layer, increase the crosslinking in the surface or increase the work function of certain materials, for example, indium tin oxide (ITO) and silver. [3], [90] All surface oxidation treatment have a disadvantage, that the oxidation is partially reversible when exposed to ambient conditions. After tens of minutes, the contact angle increases and after a few hours, the original value is almost reached. [91] This process referred to "hydrophobicity recovery" is mainly caused by three effects: Materials from the bulk of the substrate diffuses to the surface replacing or covering the oxidized layer, especially if the surface is cracked already. [92] A reorganization of the polymer chains due to the rotation of groups around sigma bonds moves non-oxidized functional groups from the bulk to the surface. [92] The third are reducing reactions that can reverse the process under certain atmospheric conditions. [92]

Particularly oxygen plasma is widely used in literature and industrial processes to modify the surface of silicone rubbers and other surfaces. Other types of plasma-like argon, helium, or nitrogen have similar effects. [93] The plasma propagates several hundred nanometres under the polymer surface. It substitutes carbon atoms by oxygen atoms in the near-surface region of silicone rubbers rapidly creating irreversible, polar functional groups like hydroxyl groups. [94], [95] The newly created surface is rather silica-like (Si bonded to more than two oxygen atoms) [92] and more hydrophilic but brittle as well. A strong and long oxygen plasma treatment creates cracks in the surface of silicone rubbers due to different elastic moduli and different thermal expansion coefficients. In comparison to wet-chemical oxidation, the plasma-functionalized surfaces are more heterogeneous. This applies to the type as well as to the location of functional groups. [94], [96] The advantages of oxygen-plasma are that it is a dry process without the need for solutions and drying, the process speed is high (few to tens of seconds are sufficient) and it is applicable in industrial processing. [95] The disadvantage is, that most systems require vacuum although some companies, e.g. Tri-Star Technologies (CA, US) offer a portable plasma device without the need for a vacuum chamber. [97] Another example is the micro-plasma system µPlasmaPrint of InnoPhysics (Eindhofen, Netherlands). It has 24 electrodes in two rows with an electrode tip diameter of 50 µm and a distance of 270 µm and can be integrated into several systems, among them the laboratory inkjet printing system Pixdro of Meyer Burger (Eindhofen, Netherlands). [98], [99]

We conducted oxygen plasma treatment to the silicone rubber films to modify the wetting properties to be able to imprint them by inkjet printing. We used a Femto low-pressure plasma system of Diener electronic GmbH + Co. KG (Ebhausen, Germany) with a frequency of 13.56 MHz and a maximum power of 300 W. Typically, we used only a power of about 30 % (90 W) for 30 s – 60 s at a pressure of 0.3 mbar. To drastically reduce the power, we placed the samples inside an aluminium cage, which acts like a Faraday cage and only a minimal amount of the radio frequency is passing inside. We found that the chosen parameters are rather arbitrary and a wide range of parameters can be employed to change the wetting behaviour. Our silicone rubber films could be used for at least 30 min without significant changes of its properties. After 60 min, the ink distribution started to get less uniform.

Corona treatment is another widely used oxidation method in industry. It does not require vacuum and is more suitable for industrial manufacturing on a large scale. A high voltage is discharged in atmospheric conditions and produces a local plasma that oxidizes the surface. [3], [100] Such devices can be small, low-cost, and scalable, but have disadvantages, too. Corona treatment is only applicable

on non-conducting surfaces. It creates ozone and, thus, requires ventilation. It produces significant radio frequency noise that can affect or destroy nearby electronic systems. [100]

Ultraviolet (UV) treatments are extensively used to modify polymer surfaces, especially PDMS. Several research groups have evaluated ultraviolet light alone and in combination with the presence of ozone that may be created by ultraviolet light in air. The chemical surface changes are similar to those induces by plasma treatment: Hydroxyl groups are formed and especially when ozone is involved, a uniform silica-like layer of tens of nanometres was found. The disadvantages of UV treatments are the longer process duration of several minutes and thus about one order of magnitude higher than for plasma treatments and the creation of ozone. [90], [94] On the other side, the treatment can occur in atmospheric conditions with proper ventilation and does not require complex technology and process parameters. Shin et al. utilized ultraviolet treatments for 6 min to be able to print the same Ag-NP ink as we used during this work on silicon wafers. [101] Ultraviolet treatment has one major advantage, which is the opportunity to selectively oxidize only parts of the substrate and offer the opportunity to confine the liquid ink inside the hydrophilic areas to avoid outflow and decrease line widths. [102]

Strong oxidizing solutions and acids such as potassium dichromate solution [3], [103] or peroxymonosulfuric acid (also called piranha acid) [104] can also be used to alter the surface tension. Typically, the substrates have to be put into the solution for about 15 minutes, which is rather long in comparison to other methods. Campbell et al. showed a wet stamping process that allows modifying the surface energies only locally. [103] In general, wet processes with dangerous and explosive substances like the mentioned ones are not desirable in an industrial environment and is avoided as much as possible. [3]

The other option to change the surface properties is the **Coating of the substrate**, which can be achieved by a thin self-assembled monolayer of molecules having a hydrophobic and a hydrophilic part. Typical examples are silanes on a silicon-containing surface and thiols on metallic surfaces. [3] Adly et al. showed that a coating of silicone rubber surfaces with 3-mercaptopropyl trimethoxysilane (MPTMS) can decrease the contact angle permanently and can be treated with oxygen plasma without forming cracks [96]. Wu et al. and Park et al. showed improved wettability, too, and highlight the effect of MPTMS as an adhesion promoter for metals on silicone rubber [105]–[107]. During our experiments, it was not possible to achieve a homogeneous wettability across the entire surface of a larger PDMS film. Another coating way is a thick coating layer called primer that either has the desired surface energy or can absorb the solvent of the ink. Andersson et al. used inkAID Clear Gloss Type II for coating of polyimide and PET to improve the printing behaviour on these two materials [108]. Shin et al. used an epoxy primer to achieve well-defined patterns on Kapton and FR4 [101]. Some substrates should be coated prior to be printable, for example, plain paper and textiles. Paper is often sealed with a two-sided resin coat with polyethylene (PE) to make it impenetrable to liquids. This improves the stability, reduces corrugation upon drying and speeds up the drying after printing, as no solvent is absorbed in the base material. [50], [109] On polymer-based substrates as well as resin-coated papers, more primer layers may be applied to improve some properties of the material. Whereas for graphical printing, a higher colour range and a greater brightness are desirable, the application in functional printing requires a higher sharpness of the print and the reception for ink carriers. These properties can be achieved by coating materials like fumed and fused silica (SiO2), forms of alumina (e.g. AlO(OH), Al2O3), titanium dioxide (TiO2), calcium carbonate (CaCO3), mixtures of the before mentioned (e.g. Kaolin) and various polymers. The coatings can be categorized as swellable or porous. Organic polymers are mostly swellable and encapsulate the ink between their polymer chains while expanding. The ink is locally fixed and cannot flow, but also the drying and curing after printing are slow. Micro-, meso-, or nanoporous coatings contain small inorganic particles dispersed in a synthetic binder. After application on the substrate, a porous layer is formed that can absorb the ink quickly and let it evaporate easily. The printed layers are almost instantly dry, which

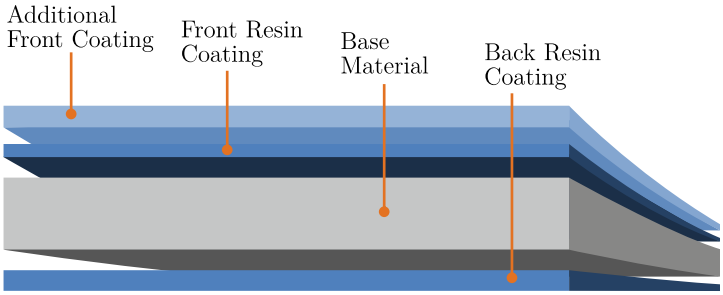

Figure 2.16. Typical composition of a coated substrate with several coatings on the front and back side.

prevents smearing. [3], [109]–[113] For functional printing, only pore sizes smaller than the particle size in the ink are desirable. For such coatings, the functional material is deposited on top of the porous layer, whereas the solvent is absorbed. Such porous coatings can be found on most glossy and semi-glossy print media such as photo papers and polymer films. Another group are reproduction films for inkjet printing photomasks for screen printing and other processes. [64] In contrast, matte photo papers and other print media shows a rather high pore size and are typically not suitable for inkjet-printing of metal NPs. Many primers can also be used to flatten such or other too rough surfaces, for example, to prepare textiles, wood, or 3D-printed objects for inkjet printing. [114] Primers are typically liquid materials that are applied by doctor blading, spraying, plating or slot-die coating. [3] Figure 2.16 shows a schematic of a coated substrate with two front coatings and a back coating. Many commercially available papers have multiple coating layers to improve parameters like mechanical stability, colour, ink reception, and gloss.

Embossing methods to create high precision microstructures are reported in the literature to create inkjet-printed line widths in the low micrometre range. Nanoimprint lithography is a tool that can produce even finer surface structuring and can influence the ink distribution on the surface. [3], [102]

2.2.3 Functional Inks

The most important rheological ink parameter for most printers is the viscosity of the ink. Viscosity is a measure that describes the resistance of fluids to deform under mechanical stress. We decided to give the viscosity values in the unit centipoise (cP), as it is most commonly used for printable materials. The corresponding standardized unit would be mPa · s and can be converted 1:1. The recommended range is from 3 cP to 15 cP for printers that only push the ink through a nozzle. The values are rather low because only weak forces can be created in the small chambers to press the ink forward. [8] Inkjet-printable inks contain a mixture of many materials that influence the viscosity. The viscosity of low-loading inks is mainly defined by the solvent mixture, whereas towards higher loading, the functional material increases the viscosity. Inks with a high loading and especially such with functional materials with a high aspect ratio like nanowires start to behave like non-Newtonian fluids. In such fluids, the viscosity depends on the shear rate, a measure for the acceleration of the liquid under pressure. The books of Nir [50], Nisato [23], Gamota [4] and Morris [115] go into more detail on rheological parameters. The viscosity of most inks decreases with temperature. A heatable ink reservoir in the print head can be used to modify the viscosity to make it printable. The possibilities are limited by the room temperature, the temperature of a possibly heated printing table in close vicinity to the print head and the evaporation rate of the ink's solvent.

The second important parameter is the surface tension and describes the capillary forces at the interfaces of the fluid with air or the substrate. [23] It must be sufficiently low to allow the ejection of a droplet from the nozzle but not too low to flow out of the nozzle by itself. On the surface of the substrate, the surface tension should be high enough to inhibit outflow of the printed areas, which increases the minimal line width and leads to distortion of the pattern. On the other hand, it should be low enough, so that the contact angle to the substrate is low and a good adhesion is reached. [8]

Typical values are 25 – 35 mN/m. To achieve a homogeneous dry film, it has to be considered that the surface tension changes with the concentration of the functional materials, which will constantly rise during drying. In a printed ink drop, the evaporation will be higher at the edges of the drop resulting in a different concentration and thus a varying surface tension. At a certain point, a lateral fluid transport from the edges to the centre or reverse will be caused by a gradient of capillary forces. This leads to an inhomogeneous deposition of functional materials and is referred to as Marangoni effect or, more figuratively, the "coffee stain effect". [23], [53], [116] Layani et al. showed, that the effect can be beneficial for certain applications as well, here a transparent conductive coating consisting only of coffee-rings of Ag-NPs [117].

Inkjet printing requires the **Functional material in a liquid form** with restrictions on the viscosity and surface tension. Most graphical and functional materials are not liquid per se and in the final product, a solid film is desirable. To form a layer after printing, the material needs to contain or be converted to a solid material. Two main approaches have been made to achieve this. In graphical printing, dye inks basing on mostly water-soluble colourants that are absorbed by a coating on the substrate. Similar approaches have been made in functional printing for many soluble materials, mostly polymers, for example, the water-soluble conductive polymer PEDOT:PSS. Organometallic inks consist of one or more metal atoms and an organic rest and are mostly soluble in water or other solvents. The second approach is the formation of particle-based inks and is employed in graphical printing as well as functional printing. Small particles of the desired functionality are encapsulated and then dispersed in a suitable solvent. In the following, we show important characteristics of inkjet inks and then show several examples of inks that we used during this thesis.

The percentage of functional material in the ink controls the layer thickness of a single print and the number of printing cycles to achieve the desired thickness. The values are typically given as solid loading in the ratio of the weight of functional materials to the weight of the ink. Common metal NP inks have solid loadings between 20 and 60 %(wt.) and polymer inks about 1 %(wt.). The large difference lies in the density of the functional material. The volume fraction of functional material in inkjet inks lies in the region of 0.5 % to 5 %(vol.). This means, that more than 95 %(vol.) are solvents, dispersants and other components of the ink that just help to make it printable and must be removed from the printed layer to achieve a high density of the functional material.

Common nozzle sizes of inkjet-printers are in the region of 10 µm to 100 µm. A general rule of thumb says that the maximum size of aggregates and accumulates should be about 100-times smaller than the nozzle diameter. This limits the particle size to NPs, which are usually defined as particles with a diameter below 100 nm. The ongoing research in nanomaterials and NPs created a variety of materials that can be created. The main challenge remains the homogeneous distribution in a suitable solvent. As most particles have a high density, e.g. metal particles, they need to be encapsulated in dispersants that are well-dissolvable. Conductive inks need to be designed also with respect to electric charging of the particles that may lead to accumulation due to electrostatic forces. [8], [23], [50] It has also be shown, that the upper limit of the particle size can be surpassed if the ink is carefully designed. In literature, examples of inkjet-printed silver nanowires and carbon nanotubes can be found that are several micrometres long but thin. [118]–[120]

For inkjet-printing, inks containing metal NPs and organic conductive materials have been used in this thesis. The rest of this section discusses the metal-containing inks based on Ag-NPs, Au-NPs, and copper-oxide NPs (CuO-NP). Figure 2.17 shows SEM images of dried thin-films of the three kinds of NP inks. Then follows a brief discussion of the used poly(3,4-ethylenedioxythiophene) polystyrene sulfonate (PEDOT:PSS) ink. Table 2.2 summarizes names all inks used for inkjet-printing.

The **Silver nanoparticle ink DGP 40LT-15C** of Advanced Nano Products (Sejong, Korea) was ordered through SigmaAldrich. The ink contains 30 – 35 %(wt.) Ag-NPs of around 50 nm diameter. These are dissolved in triethylene glycol monoethyl ether (TGME) that has a high boiling-point

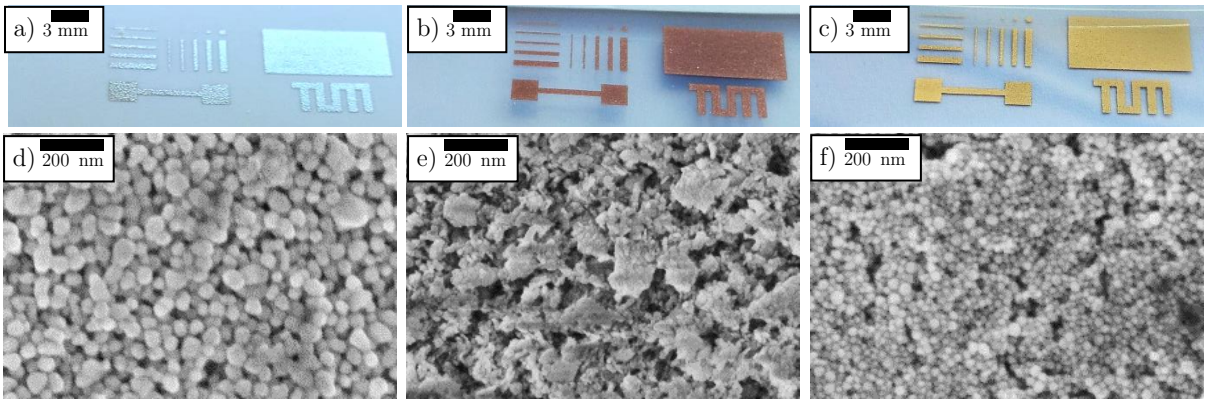

Figure 2.17. Photos and SEM images of inkjet-printed metal films with the a/d) Ag-NP ink DGP 40LT-15C, b/e) the CuO-NP ink ICI002HV (photo shows cured film), and c/f) the Au-NP ink Au-LT-20 after drying without curing.

around 250 °C according to the Open Chemistry Database [121]. The viscosity of the paste ranges from 10 cP to 17 cP depending on the temperature and age of the ink. The surface tension lies between 35 and 38 mN/m according to the datasheet [122]. The ink can be washed with polar solvents, e.g. ethanol, before drying and features a good adhesion after drying. The ink can be directly filled into printer cartridges after only strong shaking by hand. The colour of the ink is dark black with a slight green-brown tendency. The curing temperature lies between 120 °C and 150 °C leading to a specific resistivity as low as 11 µΩ·cm according to the datasheet. [122], [123]

The **Gold nanoparticle ink Au-LT-20** was purchased directly from the producer Fraunhofer ITKS (Dresden, Germany) from lot Au059. It contains 19.6 ± 0.5 %(wt.) Au-NPs dispersed in water having a viscosity of 7.3 cP at 22 °C and a surface tension of 35.1 mN/m. The recommended curing temperature lies at above 250 °C and is optimized for adhesion on PET and polyimide. According to the manufacturer, the particle size was limited to 200 nm. However, we measured a particle size of 20 nm to 40 nm as can be seen in the SEM image in Figure 2.17c. Still, a 400 nm filter should be employed while filling the cartridges.

The **Copper-oxide nanoparticle ink ICI002HV** of Novacentrix (Texas, US) was purchased through their online store. It contains 16 %(wt.) fully oxidized copper NPs of around 120 nm in diameter and is water-based. The viscosity ranges from 9 cP to 12 cP and the specific gravity is 1.21. No special preparation of the ink is necessary before printing. A nanoporous substrate is recommended by the manufacturer. After drying, the ink must be quickly processed with intense pulsed light curing such as the PulseForge tools of Novacentrix to transform the CuO to copper. The advertised resistivity is as low as 1.7x – 2.4x the bulk copper resistivity. [124]

A rough **Estimation of the density** of inkjet-printed metal NPs present on a specific area was done by cutting two non-porous films to the identical area. Both were weighted with a precision scale directly after printing Ag NP ink on one of them without drying. We used the Epson printer for this experiment because its printing duration is much shorter than the drying time of the ink. The average additional weight introduced by the printed silver was 1.19 ± 0.24 mg/cm² of printed ink. The ink

Table 2.2. List of Inks for inkjet-printing used in this work.

Material	Content (%wt.)	Name	Manufacturer	Distributor
Silver NP	30 – 35	DGP 40LT-15C	Advanced Nano Products	SigmaAldrich
Au-NP	20	Au-LT-20	Fraunhofer ITKS	-
CuO NP	16	ICI002HV	Novacentrix	-
PEDOT:PSS	0.8	Orgacon IJ-1005	Agfa	SigmaAldrich

has a density of 1.45 g/mL according to SigmaAldrich. [123] This means, that a volume of 8.19 ± 1.64 nL/mm² was applied. With the density of bulk silver of 10.49 g/mL and the silver content of the ink, 30 - 35 %(wt), the minimal film thickness that could be achieved is in the order of 368 ± 79 nm. Assuming that the Epson inkjet printer always applies the same volume of ink, the calculations can be transferred to gold and CuO. With a solid content of 19.6 ± 0.5 %(wt) gold with a density of 19.3 g/mL and mainly water as the solvent, the density should be around 1.238 ± 0.006 g/mL. With the volume from above, the amount of printed gold is about 1.97 ± 0.41 µg/mm². If it would be packed like bulk gold, the thickness would be 102 ± 21 µm. Based on the atomic weights of copper and CuO, a copper content of 12.8 %(wt.) of a density of 8.96 g/mL is assumed and a density of the ink of 1.21 g/mL was taken from the datasheet. [124] If this copper would be packed dense as bulk, it would have a height of 142 ± 28 nm.

Due to pores resulting from non-perfect packing, the real thickness is expected to be much higher. Assuming that the NPs are perfect spheres, the theoretic packing density of 74 % seems still too high. We measured the thickness of the thin films on one of the smoothest substrates T8 and found that the average film thickness is 696 nm with a roughness of 111 nm for Ag-NPs. The measured thickness can be explained by a porosity that leads to an average density of 52.9 % ± 11.4 % of the density of bulk silver, i.e. 5.55 ± 1.19 g/mL that is comparable to other literature. [5], [6] Unfortunately, we were not able to measure the thickness of the printed gold layers, because the only available substrates were too rough. Assuming the same density than for silver, we can estimate a thickness of around 193 ± 40 µm, which will be used in the following. The measured copper layer was 212 nm on the substrate T2 with a roughness of 37 nm. This results in a density of 67.0 ± 13.4 % of bulk copper, i.e. 5.97 ± 1.20 g/mL.

The PEDOT:PSS inkjet ink is Orgacon™ IJ-1005 from Agfa (Mortsel, Belgium) and was purchased through SigmaAldrich. It is water-based and contains 0.8 %(wt.) PEDOT:PSS together with 1 – 5 % ethanol and 5 – 10 % diethylene glycol. The viscosity lies between 7 cP and 12 cP at 22 °C and the surface tension is between 31 and 34 mN/m. It is advertised to have a sheet resistance of 110 Ω/sq at a transmittance of 90 % at 550 nm.

2.2.4 Substrates for Inkjet Printing

We found that the **Print quality of the metal NP inks** is mainly depending on the choice of the substrate. Thus, we show a detailed analysis of the printed silver samples and only highlight the differences of gold and copper inks later in this work. For the printing of all samples in this section, the Epson desktop printer was used. This allows the study of the drying behaviour and the rapid production of inkjet-printed layers on a large variety of substrates.

On some substrates, the Ag-NP ink immediately creates a shiny silver layer after printing. On others, heat-drying is necessary to achieve this layer. On the third group of substrates, the ink remains dark green or shows a inhomogeneous pattern. Figure 2.18 shows optical microscope images of printed areas of about 1 mm² Ag NP ink on different substrates. Another important criterion for printed electronics is the quality of printed lines. Figure 2.19 shows optical microscope images of lines with a designed width of 100 µm of Ag NP ink on a selection of substrates.

Most porous inkjet media like glossy or semi-matte inkjet photo paper or inkjet reproduction films show a print pattern like on substrate T8 in Figure 2.18a. Individual drops are perceptible and cover the entire area. The pattern looks like an inhomogeneous deposition caused by the “coffee stain effect” [52] This results from an effective and quick separation of solvent and functional material on micro- or nano-porous coated films and papers. This leads to an immediate fixing of the functional material at the place of printing and a short drying time. For colour printing, this is desirable to print different colours closely next to each other instead of mixing them. For functional printing, it

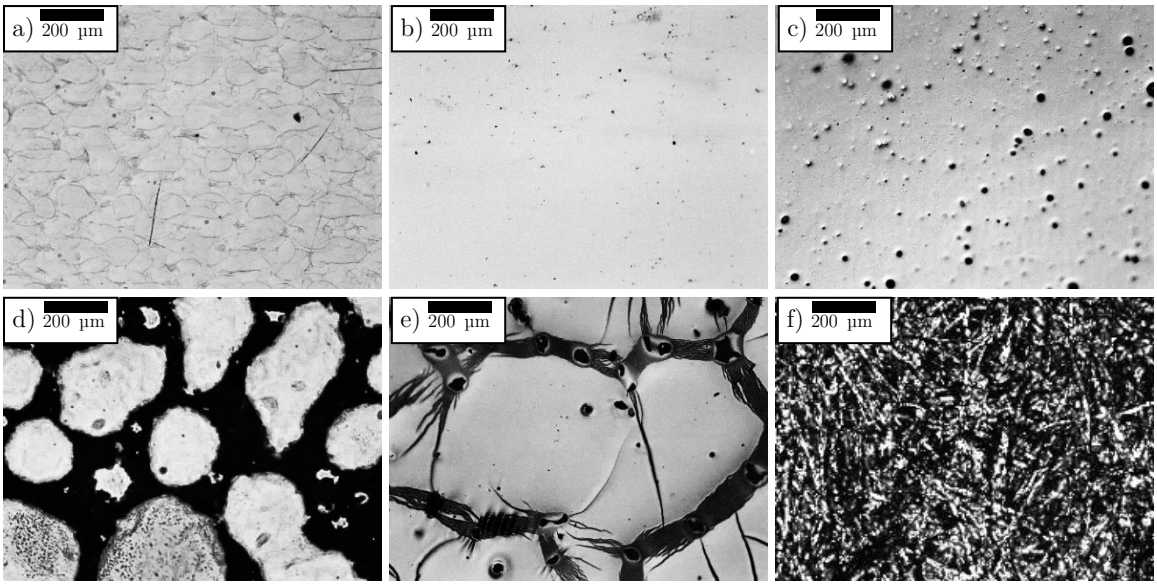

Figure 2.18. Microscope images of printed areas on different substrates: a) porous inkjet media (P9), b) smooth non-porous film (N8), and c) rough non-porous film. All these three surfaces exhibit a shiny silver layer and low sheet resistances are obtainable. d) Low-wettable substrates, e) low-adhesion substrates, and f) absorptive substrates (office paper) are not suitable for inkjet printing. The silver ink is always shown brighter than the substrate. [64]

is desirable to overlap adjacent drops to form a continuous pattern. However, the wet ink should not flow out of the desired patterns. Figure 2.19a shows a line composed of ink droplets on porous inkjet media (P9). The drop diameter is approximately 70 µm for the Epson printer. A drop gain of 50 µm was observed for all line widths, which is assumed to be related to missing dot gain compensation mechanisms in the ultra-low-cost printer. This is the reason, why the final line widths of all lines in Figure 2.19 are more than the designed 200 µm.

Figure 2.18b shows the print pattern on a smooth non-porous polymer film. No individual drops are visible as the ink remains liquid after printing and solidifies during drying. Figure 2.18c shows a rougher non-porous polymer film that is disturbed by stains of different sizes. All these three surfaces exhibit a shiny silver which is shown with a higher brightness than the substrate in the microscope images. Some non-porous media show a uniform line as depicted in Figure 2.19b. Others show some stains as can be seen in Figure 2.19c that may interrupt the continuous line if too large. The surface energy matching of ink and film, as well as the quality of the film, must be high to obtain a line with homogeneous edges. [125] A mismatch leads to an increased linewidth (Figure 2.19d) or irregular

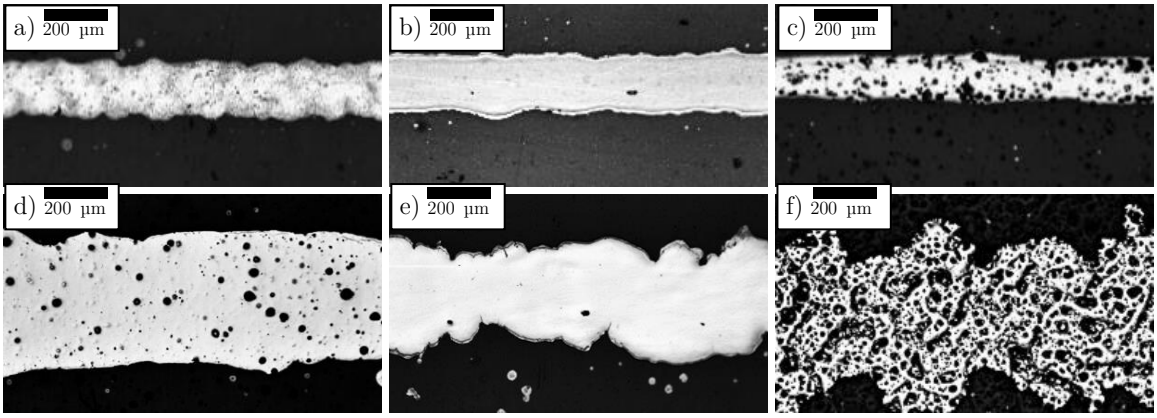

Figure 2.19. Microscope images of printed lines on different groups of substrates. a) porous inkjet media (P9), b) smooth non-porous film (M2), c) rough non-porous film, d) high-wettability substrates, e) substrates with high but irregular wettability, f) rough high-wettability substrates The silver ink is always shown brighter than the substrate. [64]

line edges with bulging or outflow of the ink as shown in Figure 2.19e. An increased roughness of the surface as seen in Figure 2.19f does not improve this behaviour.

If the wettability does not match the surface energy of the ink, dot gain may increase or the ink agglomerates to separated drops. Figure 2.18d shows a substrate with low wettability on which all printed ink flows together to isolated islands before drying. Such a film cannot be well conductive. Figure 2.18e shows a substrate on which large cracks appear after drying. It is assumed, that a combination of surface energy mismatch and a low adhesion of the ink on the substrate are the reasons for the cracking. The stains on the surface of this substrate play an important role as the starting and end points of the cracks.

Some substrates, for example, letter or copy paper, matte photographic paper, and polypropylene-based graphic films show a dry but dark surface, which presumably originates from an absorption of both the ink carrier and the metallic NPs. Figure 2.18f shows a normal office paper on which the silver only coats the surfaces of the cellulose fibres instead of forming a plain film on top. The ink penetrates the entire paper and can be even seen from the back side. Papers that show such characteristics are not suitable for inkjet-printing of metal NP inks. This includes all non-coated and matte-coated papers and polymer films that we tested.

After evaluation of the printing properties on different kinds of substrates, there are two groups of substrates that are suitable for inkjet-printing functional inks: The first are papers or films that are coated with a porous layer. Semi-glossy and glossy photo papers, glossy inkjet polymer films as well as inkjet reproduction films are counted to this classification. The second group includes non-porous polymer films or photo papers for laser printers. Here, the properties of the inks employed have to be studied to decide whether the substrate is suitable or not.

40 porous paper- and polymer-based substrates were tested in a preliminary study for inkjet printing of silver, copper, and gold inks. The paper-based substrates are a selection through all kinds of papers. Glossy, semi-matte and matte coated photo papers, fine letter paper, low-cost copy paper, and two special papers for inkjet-printed electronics were tested. The polymer-based substrates contain inkjet reproduction films, polypropylene-based graphic media, and two special films for inkjet-printed electronics. The 21 porous substrates listed in Table M.2 in the Materials and Methods section were found suitable for inkjet printing. Nine of these substrates are white paper-based (P1 to P9), ten are transparent polymer-based (T1 to T10) and two are white polymer-based (W1 and W2) substrates. All substrates have an ink-absorptive coating. The numbering of the substrates is equivalent to the author's publication on "Inkjet Printing and Photonic Sintering of Silver and Copper Oxide NPs for Ultra-Low-Cost Conductive Patterns". [64] There are also AFM images of different porous substrates shown in the supplementary information.

Inkjet-printing of metal NP layers on porous substrates creates an instantly dry layer and allows a multi-layer printing without intermediate drying until the absorption capability of the substrate is exhausted. On some substrates, a Ag-NP layer is shiny silver-coloured and immediately conductive to some extent. Drying for one hour at 65 °C, which is considerably lower than the sintering temperature, made all tested porous substrates conductive. All sheet resistances given in the following were measured with a four-point probe and the values were corrected with the boundary formulas of Smits [126]. Values down to 385 mΩ/sq were measured, which correspond to a conductivity of about 6 % of bulk silver. Figure 2.20 shows in grey the conductivity value of an approximately 700 nm thick silver layer after drying in relation to a bulk silver layer of the same thickness. The average conductivity is about 2.4 % of bulk sliver with a rather high standard deviation of 2.5 %. The CuO-NP films are dark brown and show a high resistance above 1 GΩ/sq what was expected for the non-conductive CuO. The Au-NPs were only printed on two substrates and even though they formed a shiny gold layer, they were not conductive after printing and drying and are not shown in the figure prior to sintering. This may result from encapsulants used to disperse the NPs in the film.

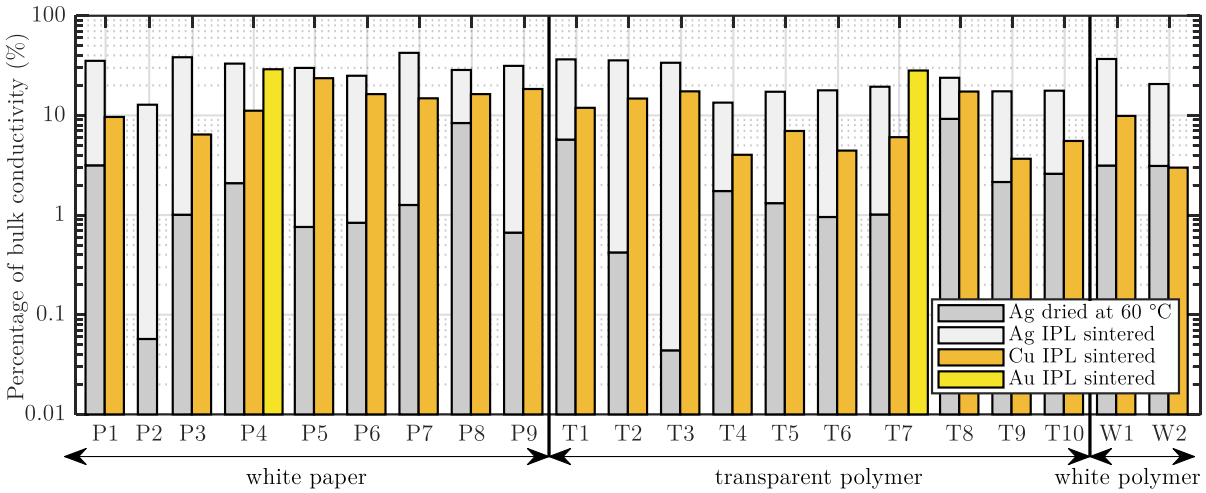

Figure 2.20. The conductivity of an inkjet-printed film of different metal NP ink on a variety of substrates after drying and after intense pulsed light (IPL) sintering in relation to the bulk conductivity of the respective metal. The list of substrates can be found in Table M.2 in the Materials and Methods section. The non-sintered Cu and Au films are neglected because they were not conductive.

Figure 2.20 also shows the **Sheet resistance of the three metal NP inks** after intense, pulsed light sintering (IPL) with the ideal parameters as identified in Section 3.1.3. Sintering is able to reduce the resistance of the silver ink by 75 % to 99 % to values as low as 55.4 mΩ/sq on substrate P7 (with some damages to the film), which corresponds to 46 % of the conductivity of bulk silver. The highest sheet resistance of 195 mΩ/sq was measured on T4, which still correspond to 13 % of the bulk conductivity in the approximately 700 nm thin film. The standard deviation of the resistance values decreased from 85 % to 40 %. All sheet measured values are shown in Figure 2.20 in bright silver bars behind the non-sintered values. Intense, pulsed light sintering converted the dark layers of the CuO ink into shiny copper-coloured layers of about 210 nm thickness with sheet resistance values down to 335 mΩ/sq on P5. This corresponds to 23 % of bulk copper conductivity. The values for the other substrates are shown together with the values for silver and gold in Figure 2.20. The gold layer was only printed on two substrates, photo paper and transparent reproduction film, and showed a consistent conductivity to the other substrates. The 193 nm thin Au-NP film showed sheet resistance values down to 435 mΩ/sq on P4, which corresponds to 29 % of the bulk conductivity.

Furthermore, 22 non-porous substrates were tested on the printing quality. The substrates included special films for printed electronics, photo papers for laser printers, laser and inkjet copy foils, and films for screen printing. Eight of them are presented here: Two are white special papers for printed electronics (N1 and N2), three are laser copy papers (N3 to N5), two are laser copy foils (M1 and M2), and one is a screen printing film (M3).

The non-porous substrates do not absorb the solvents and require drying of the samples before sintering. We heated the samples for one hour at 65 °C to evaporate the solvent but not destroy the substrates. On most substrates, the ink flows slightly and increases the line width. The dried samples mostly show a small Marangoni effect [53]. On substrate N2 with a low wettability, the ink agglomerates to drops of about 1 mm in diameter. As these are separated by gaps, no conductivity could be measured. All other paper-based substrates showed a sheet resistance of more than 100 Ω/sq, which is up to three orders of magnitude higher than on porous substrates. We assume, that the film consists still of the NPs mixed with encapsulants that inhibit a current flow. This cannot be the only explanation, as the measurements on non-coated transparent polymer films show. Sheet resistances down to 2 Ω/sq were measured, which corresponds to about 1 % of the bulk silver conductivity and is comparable to the non-sintered films on porous samples. The sheet resistance of all samples except for N2 could be reduced by multiple orders of magnitude to values down to 150 mΩ/sq, which

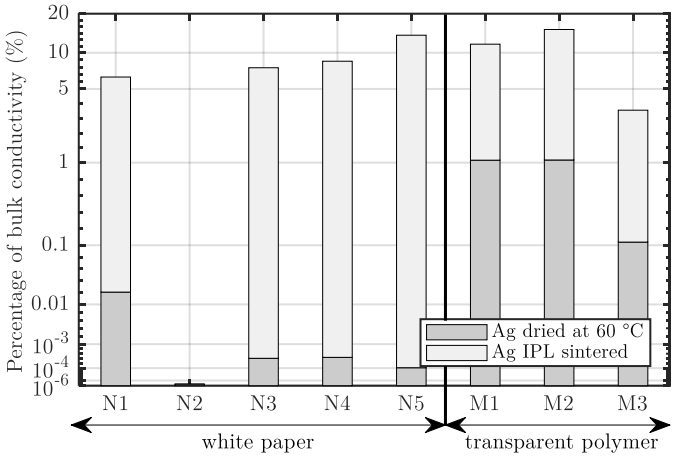

Figure 2.21. The conductivity of Ag-NP films on different non-porous substrates after drying and after intense pulsed light (IPL) sintering in relation to the bulk conductivity of the respective metal. The list of substrates can be found in the Materials and Methods Section M.2. IPL sintering was able to reduce the sheet resistance of inkjet-printed silver in all cases drastically from the dark grey to the bright grey value.

corresponds to 15 % of bulk conductivity. Figure 2.21 summarizes the conductivities of the silver film after drying (dark) and after sintering (bright).

In summary, all samples with a high conductivity have in common a shiny metal layer in the colour of the respective material. Any darker or matte layers showed a high resistivity. It was found that the creation of shiny layers mainly depends on the surface of the substrate and the separation of the ink components. Generally speaking, the ink carrier needs to be separated from the NPs to obtain the prerequisites for conductivity.

2.2.5 Post-Processing

Often, inkjet-printed film does not have the desired functionality directly after printing and some post-processing treatments are necessary to achieve it. Due to the high solvent content in inkjet inks, a separation of the functional material from the solvent mixture is necessary. Some substrates have a solvent-absorbing nanoporous layer that facilitates this separation directly during printing. Some inks are based on low-boiling point solvents that evaporate after printing such as ethanol, isopropanol or water. Other substrate and ink combinations require elevated temperatures for drying. Such drying cycles are typically rather long, especially if the temperature cannot be high because of the thermal budget of ink or substrate. After drying of the printed film, additional steps may be required to liberate its functionality. Whereas our Ag-NP ink was directly conductive after drying, the presented Au-NP ink was not and the CuO ink was not even metallic.

Particles ink inks are typically capped with organic materials that enhance the dispersion of the particles in the solvent. Such capping agents require heat or other mechanisms to get released from the particles. The recommended drying temperatures of our Ag-NP ink lies at 150 °C and the Au-NP ink at above 250 °C. When the capping agents are removed, the particles touch each other and conductivity is established.

Especially particle-based inks show a rather low density of the functional material with many pores. Conductive NP films have rather low and complex paths for charged particles to pass. Additionally, the resistance is increased by the small cross-sections at the touching point of the particles. Sintering increases the cross-sections between the particles and densifies the films. Heating in an oven is time-consuming and often not compatible with the substrate. Therefore, several other techniques have been developed like photonic heating using ultraviolet light, broadband visible light, or infrared light as constant lighting, flashes, or lasers. [44], [64], [127]–[129] These methods and others to deliver heat specifically to the functional film but not the substrate and are described in Section 3.1 in detail.

Sintering is also widely used for the formation of ceramics from particle dispersions but also for organic layers. An example is the thermal annealing of P3HT:PCBM in bulk heterojunction solar cells. The annealing strongly affects the morphology of a nanocomposite layer and improves significantly the efficiency of such solar cells. [3], [130]–[132]

Many printed films require additional chemical reactions to get the desired functionality. An example is our CuO based ink, which needs photonic curing shortly after printing to convert CuO to copper to achieve conductivity [64]. Section 3.1.4 focusses on the post-processing of this ink. Metalorganic decomposition (MOD) inks for silver and other metals contain the metal atoms in a molecule and need a decomposition by heat, light, or chemicals [54], [133], [134].

Ultraviolet curable materials are usually used for dielectrics, insulator or etch resistant layers, but can be conductive if a certain amount of conductive particles or nanowires is added. Such inks can be completely or partially solvent-free, which eliminates drying. Still, the required low viscosity of inkjet-inks may lead to outflow and distortions in the print layer. A UV curing unit directly integrated into the inkjet printer can cure the printed layer immediately and control the movement of the ink on the substrate. So far, UV curing inks are playing a minor role for inkjet inks in contrast to other printing methods, e.g. screen printing. [3]

2.3 Screen-Printed Electronics

Screen printing is one of the most common printing methods that are in use since many years in electronics manufacturing. It is used both for graphical, e.g. labels, and functional printing, e.g. conductive or isolating patterns. [38] Figure 2.22a shows a schematic of the printing process with labelled components. The main component is a screen with a mesh on which the print pattern is reproduced by covering all not-to-be-printed areas with emulsion. In Figure 2.22b, the print pattern can be seen in yellow, whereas the rest of the screen is covered by a green emulsion. A table on which the substrate is fixed by vacuum, glue or simply by gravity forms the base of each screen printer. A mechanically stable fixture holds the frame in place and withstands high shear and normal forces. A snap-off distance between the surface of the substrate and the lower side of the screen of typically a few millimetres is held.

The printing starts by dispensing paste on top of the screen at one side of the print pattern. The squeegee consisting of a single or multilayer polyurethane rubber embedded into a wooden or metal holder is used to move the paste across the print pattern. A certain pressure P is exerted by the squeegee to deform the screen until in contact with the substrate. The squeegee moves with a velocity v while maintaining this pressure and presses the paste through the openings in the screen onto the substrate. Due to the snap-off distance, the screen lifts off from the substrate slowly after the

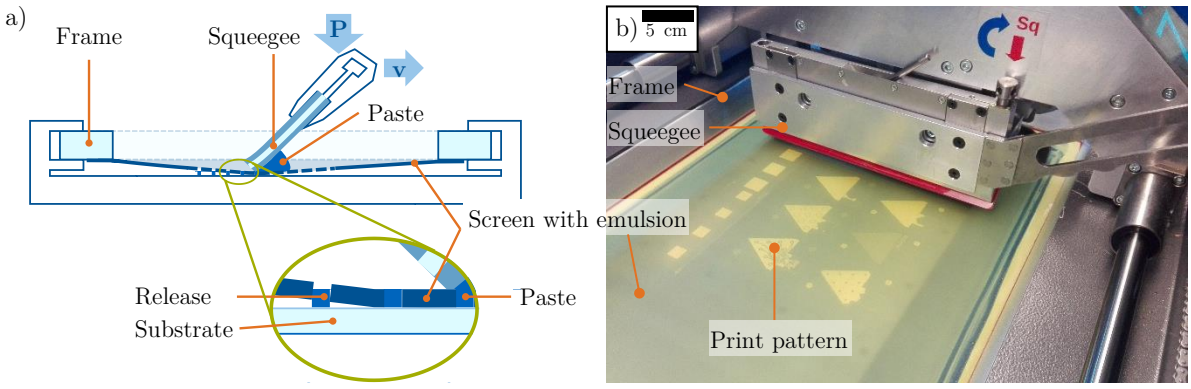

Figure 2.22. a) Schematic of screen printing with labelled components, pressure P and velocity v. b) A photo of a commercial screen-printer with mounted squeegee and screen.

squeegee passed and releases the paste from the mesh. After the release, the paste remains on the substrate at the open areas of the screen and forms a replica of the print pattern. The usually high viscosity of the paste ensures that it will not flow out even though the thickness of the wet film can be up to several tens of micrometres. The wet film needs post-treatment by heat or light to evaporate solvents and/or crosslink the printed material. [3], [23]

Figure 2.22b shows a photo of a high-precision screen-printer. A screen with a yellow mesh is mounted that is covered by green emulsion around the print patterns. A red rubber squeegee is fixed in the metal holder on the print head, which allows to lower the squeegee to a defined height before printing and can be moved parallel to the screen while maintaining a constant pressure. This squeegee moves the paste across the screen and presses it through the openings onto the substrate on the vacuum table below. Before starting a new printing cycle, a flooding blade on the other side of the print head moves back the paste towards the front and creates a thin layer of paste on the screen.

The most distinct advantage of screen printing compared to other printing methods is the possibility to achieve layer thicknesses of 3 – 4 orders of magnitude from single pass printing starting from below 100 nm [135] up to more than 150 µm as shown in this work. Especially the higher range cannot be obtained by other printing techniques. For both extreme values, the ink and the screen must fulfil certain properties that are discussed in the following. Although there is a trade-off between the layer thickness and lateral printing resolution, aspect ratios of perpendicular divided by lateral dimensions of more than 25 % can be reached and even surpassed by multi-layer printing.

2.3.1 Screen Types and Preparation

The main component of screen printing are the **Parameters of the mesh**. Originally made of silk, today's meshes are plain woven with thin threads of polyester, polyamide (nylon), or stainless steel. All three have distinct advantages and disadvantages. Polyester is much more mechanically and chemically resilient than nylon and stainless steel. Especially nylon should not be used with highly viscous pastes. Polyester is the most flexible of the three and is the most suited for printing onto uneven substrates. Nylon is the most elastic of the three and less prone to damages. However, a lower elasticity is preferred for accurate reproduction of the film, as it may lead to elongated images. Polyester and stainless steel have a long lifetime and allow high precision registration and definition. Stainless steel has the advantage, that the threads can be thinner at the same strength but is much more costly. This allows a higher number of threads with the same open area or a higher open area with the same number of threads. Due to its low flexibility, stainless steel is recommended for high-precision printing on small and flat substrates. Polyester is the most used material as it is the most economical for many applications. [136], [137]

The most common meshes are made by weaving monofilament threads of the chosen material. Thus, the two directions on the mesh are different. In the warp direction, the threads were straightened and in the weft direction, the threads are woven up and down between the warp threads. Typically, a 1:1 weaving is employed, meaning that the weft threads are going up and down after each warp thread. Other weaving types like 2:2 describe the numbers of warp threads after which the weft thread is woven up and down, respectively. The weaving makes the mesh direction-dependent. Especially the different stretchability can lead to different mesh parameters in both directions when the mesh is stretched and fixed onto the frame. Figure 2.23a shows a schematic of an ideally woven mesh with two weft and five warp threads. Brighter sections of the threads indicate that these are located on top of another thread shown in darker colour. The most important criteria for a mesh are indicated in the figure. The thread diameters d_e and d_a may vary between wefts and warps. Depending on the stretching forces, the real opening widths w_e and w_a may be different from the indicated values in the datasheets. From these four values, the open area a_0 can be calculated according to Eq. 2.1 and is typically given in percent.

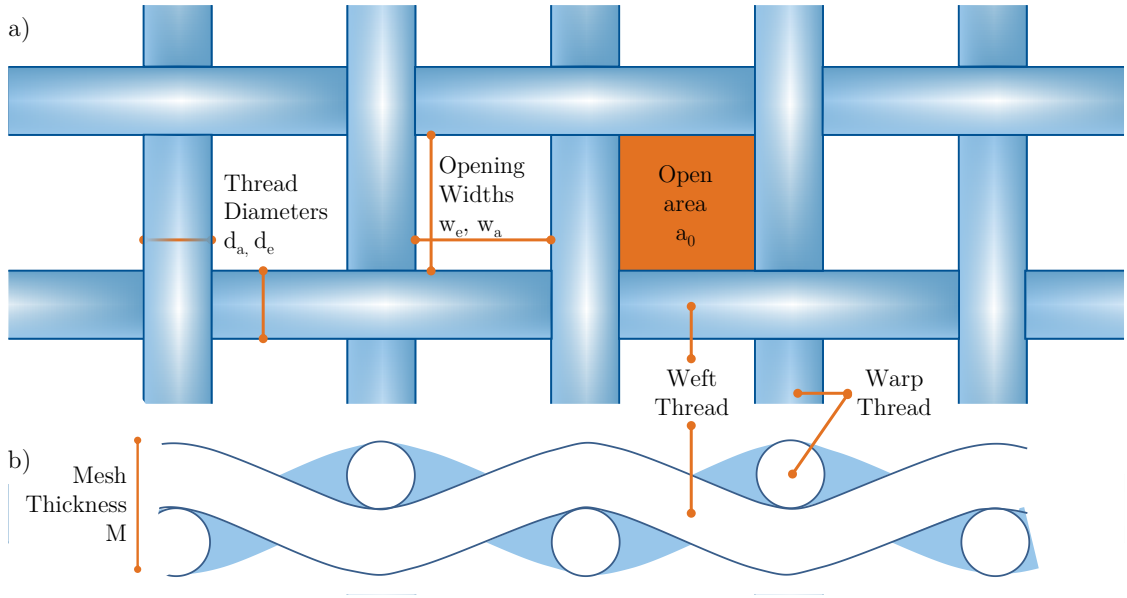

Figure 2.23. Schematic a) top view and b) side view on a 1:1 woven mesh with definitions of the important mesh parameters.

$$a_0 = \frac{w_a \cdot w_e}{(w_a + d_a) \cdot (w_e + d_e)} \cdot 100\ \% \qquad \text{Eq. 2.1}$$

Figure 2.23b shows the side view of the mesh showing the threads in viewing direction as white circles and the first thread in the paper plane in white. The second thread in the paper plane is shown in bright blue. The thickness of the mesh is formed by the addition of the thicknesses of the wefts and warps. However, real meshes are typically hot calendared to melt together the thread intersections to stabilize the mesh. A rough estimation of the mesh thickness is about 80 % of twice the nominal diameter for regular polyester meshes. The mesh thickness and the open area defines the thickness of the wet film. As the paste can only pass through the openings of the mesh and all excessive paste on top of the screen is removed by the squeegee, an estimation of the wet film thickness t can be calculated from Eq. 2.2. Some books [137] suggest the use of twice the thread diameter as an approximation as well. Anyway, the exact theoretical value should include the round profile of the threads and the weaving geometry. In reality, the paste's viscosity and release behaviour also play a role and, thus, this value can only give an estimation.

$$t = a_0 \cdot M \approx a_0 \cdot 1.6d \qquad \text{Eq. 2.2}$$

Meshes are typically characterized by a combination of two numbers, e.g. 140/355-30 Y PW. The first two numbers indicate the mesh counts meaning the number of threads per centimetre and per inch. In this thesis, we will only use the mesh count per centimetre and have converted other numbers if necessary. The second value gives the nominal thread diameter. Additional letters may indicate the colour of the mesh with Y for yellow and W for white and the weave type with PW standing for plain weave (1:1) and TW for twill weave (1:2 or 2:2). Table 2.3 shows typically parameter ranges for polyester and stainless steel meshes. The first indicated values shows an example for a fine mesh, the second a typical value (in bold), and the third stands for a coarse mesh. The second assumes a rather fine print typically used for printed electronics. It can be seen that stainless steel allows much thinner threads at approximately the same mesh count. This can lead to a higher open area of about two thirds. However, steel meshes are about ten times more expensive than polyester meshes.

When selecting a mesh, the opening width should be at least three to five times larger than the size of the largest particle dispersed in the paste. This puts a minimum on the mesh count and the thickness that can be printed. Finer meshes are typically more suitable for printing fine structures and coarser meshes are used for thick layers. Generally, it is recommended to employ a mesh with

Table 2.3. Typical parameter ranges of polyester and stainless steel meshes. The mesh count is given as a decreasing range to start all parameters with values of finest mesh, then indicate a typical value (bold) and end with the coarsest. Values are taken from the product datasheet of Sefar [45] and from [4].

Material		Polyester	Stainless Steel	Unit
Count	n	180 – **120** – 24	200 – **130** – 12	
Thread diameter	d	27 – **40** – 140	18 – **23** – 160	µm
Opening width	w	22 – **47** – 270	46 – **56** – 680	µm
Open area	a_0	15 – **30** – 55	42 – **50** – 65	%
Mesh thickness	M	43 – **65** – 250	25 – **50** – 300	µm
Max. tension	F	15 – **20** – 25	15 – **20** – 50	N/cm
Colour		White/Yellow	Silver	
Appr. cost ratio		1	10	

opening widths below half of the smallest feature of the print pattern. This limitation may be overcome with a special coating of emulsion and for certain types of paste. [45]

The mesh is fixed onto a frame, which can consist of wood, aluminium, steel or other materials. Wood is typically used in the low-quality graphics printing and steel for high-precision printing. The most economical and most stable per weight is aluminium. Various types of profiles are in use starting with a rectangular or trapezoidal shapes. The profiles are welded at the corners while ensuring a high degree of alignment among the four profiles. Finally, the welding edges are ground to form a flat surface. The mesh is stretched with clamps at a high pressure applied by pneumatic systems. It is brought in contact with the mesh and an adhesive is applied to the bottom of the frame to bond frame and mesh. After curing the adhesive, the mesh is cut around the outer edges of the frame and should be labelled with mesh count and thread diameter. To avoid differences in tension, typically a much larger piece of mesh is stretched and only the central region is used. [4], [137]

For the preparation of the structuring of the screen, an **Emulsion or capillary film** is brought onto the screen across the entire surface. Both methods have to be conducted in a yellow-light room as the emulsion and the capillary film are sensitive to ultraviolet light. Emulsions are coated with a blade on both sides of the screen. The thickness and quality of the emulsion layer can be influenced by the selected emulsion, the number of coatings as well as the sequence of coating and intermediate drying. Single component emulsions are easy to handle and are suitable for small batches of screens. Its disadvantage is a short timeframe for application once out of the container and a low thickness. Two-component emulsions are mixed from a base component and a diazo prior to the application. Such emulsions are more resistant but excessive emulsion can only be used for some days to weeks. The number of coatings can influence the thickness of the screen and the roughness of the emulsion. Thicker emulsions can be created by multiple coating and intermediate drying cycles. The thicker the emulsion, the thicker the printed pattern will be. The emulsion also protects the threads from abrasion. Figure 2.24 shows a side view of an emulsion-coated screen. The top side of the screen is referred to as the squeegee side as this side is touched by the squeegee later. On the bottom side, the substrate will be imprinted and it is called print side. The emulsion fills the openings between the threads and smoothens the surface. A typical coating procedure of the screen is the following. At first, the print side of the screen is coated and then twice the squeegee side. The first coating assures a well-coated print side and the following coatings press emulsion of the same volume through the screen from the squeegee side to the print side. This increases the thickness of the screen D in comparison to the mesh thickness M. The additional thickness is often referred to as emulsion over

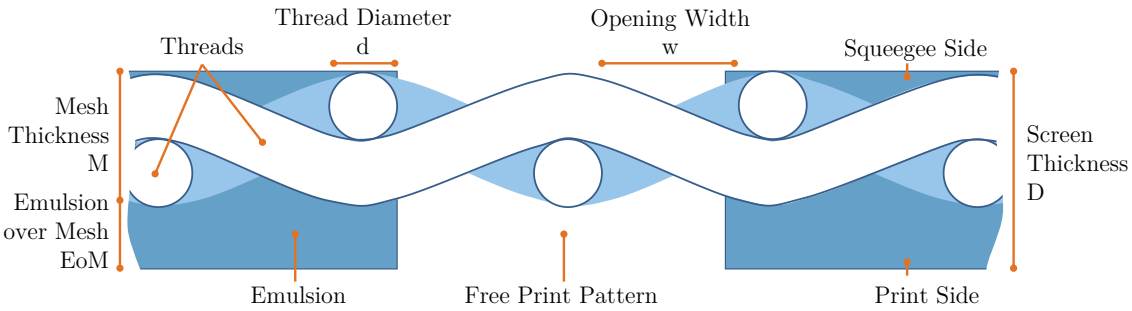

Figure 2.24. Schematic side view of an emulsion-coated screen with a free gap for the print pattern.

mesh EoM. The wet film thickness of the emulsion coated screen has to include the EoM according to Eq. 2.3.

$$t = a_0 \cdot M + EoM \approx a_0 \cdot 1.6d + EoM \qquad \text{Eq. 2.3}$$

The second option for stencil making is the use of a capillary film, which is applied to the print side onto the water-soaked mesh. The capillary film delivered with a transparent carrier polyester film is partially dissolved and drawn into the mesh by capillary forces. Capillary films show a higher uniformity on the print side as the main part of the film remains solid and no shrinkage occurs during solvent evaporation. The costs for capillary films are more than ten times higher than for direct emulsion coatings. Both, capillary film and emulsion can be washed away with water or specific solvents easily before exposure to ultraviolet light. This may be required if the final coating does not fulfil the quality expectations.

The screen needs thorough drying after coating to evaporate all remaining water and/or solvents. Then the screen is ready for exposure, which hardens the areas that are exposed to ultraviolet (UV) light while leaving unexposed areas water-soluble. Two exposure methods are in use. The cheap one uses a mask to cover the areas that should not be exposed by a large UV lamp. The mask can be printed with an inkjet or laser printer or be an optically exposed film. Typically, the resolution of the mask should be at least ten times higher than the desired feature size and the coverage must be highly opaque and pin-hole free. The mask is put with the printed side in contact with the emulsion and a UV lamp is switched on for a defined time. The second method is direct writing of the stencil with a high-precision machine. Ultra-violet light from a UV lamp or a UV-LED is coupled into a light guide. The other end of the light guide is position on an exposure head that scans over the entire screen. A shutter closes for each pixel that should not be exposed to UV light. Such systems are often referred to as computer-to-screen (CTS) systems. They allow a fully automated and mask-free exposure and are often used when the number of different patterns is high and the storage costs exceed the costs of the machines.

The emulsion or capillary film crosslinks under the influence of UV light. This leads to a hardening of the stencil and the exposed areas are not water-dissolvable anymore. In these areas, the openings of the screen are closed. The non-exposed areas are washed out with water after the exposure and are open for the ink to pass through. It is important to obtain sharp edges around the free printing patterns as shown in Figure 2.24 to avoid a flow of the paste under the closed areas and obtain an accurate reproduction of the pattern. Excessive exposure leads to the unwanted exposure of the edges of the print patterns due to scattering of the light in the emulsion or the threads. For high mesh count screens, the threads are mostly coloured yellow to reduce the scattering of UV light. The ideal exposure time is the minimum necessary time to expose the entire thickness of the film. This time can be determined with so-called exposure checker films that show the same pattern multiple times but modify the transparency of the areas outside of the patterns from 10 % to 100 %. The double of the estimated time is used to expose the screen to cover both, an under-estimation and an over-estimation. The field with the correct exposure is determined by comparing the colour of the exposed areas after washing of the film. It is recommended to use the lowest value at which the colour of the

screen is the same as on the fully exposed part of the film. The transparency value is then multiplied by the estimated time and the resulting value can be used to expose screens that were produced in the same manner. Similar approaches exist for CTS systems.

The screens used in this thesis were coated with the emulsion 1850 solo of Fotec Ag (Küsnacht, Switzerland) and produced at the laboratory of Prof. Moosheimer at the Hochschule München. The emulsion was coated once on the print side and twice at the squeegee side (1:2). The exposure box consists of a UV lamp at the ceiling and a vacuum system that presses the screen and a mask lying on top of it against a glass plate facing the lamp. The vacuum system needs about a minute to evacuate the lower part of the chamber, then a shutter at the UV lamp is opened. A photo-sensor integrates the radiation and the shutter is closed when a defined quantity of radiation was reached. In principle, such a system should be independent of the ageing of the lamp. However, between two screen production sessions for this thesis, the lamp had to be exchanged. We found, that the exposure parameters had to be approximately halved afterwards. Table 2.4 lists the exposure parameters that were found ideal with the new lamp and if no screens were yet exposed with the new lamp, the values for the old lamp are indicated with a superscript 1.

All produced screens were washed out with water at moderate pressures and thoroughly dried in a ventilation oven. The patterns were measured after exposure with a digital microscope to assess the reproduction quality of the screen. The values for a mesh count of 80 and 100 showed a slight reduction of the widths of small lines and the exposure time should be slightly reduced for future screens. Finally, the screens with an acceptable quality were hardened by exposing them to another 2000 units in the exposure chamber. This should result in a higher stability against abrasion and chemicals.

2.3.2 Comparison of Printing Equipment

During the work on this thesis, two different screen printers were employed. One is a low-cost screen printing table typically used for graphics printing on paper, foils and textiles. The other is a high-precision manual screen printer that was developed for printed electronics with highly accurate definition and a camera module for registration.

The low-cost screen printer used in this thesis is the manual screen-printing machine **FLAT-DX 200** ordered at Siebdruck Versand (Magdeburg, Germany). It consists of a 62 x 52 cm^2 printing

Table 2.4. Exposure parameters for the exposure machine at Hochschule München. During the work on this thesis, the lamp had to be exchanged, which resulted in significantly shorter exposure durations. [1]Values for the old lamp. [2]A slight overexposure was detected.

Mesh count	Coating	Value	
43	1:2	150	[1]
80	1:2	120	[2]
100	1:2	90	[2]
120	1:2	55	
140	1:2	50	
150	1:2	40	
165	1:2	35	
180	1:2	55	[1]

table and a holder with a counterweight for mounting screens and holding them while exchanging the substrate. Both are mounted on a mechanically stable steel frame. The distance between the screen and the substrate can be set at a handle on the holder. The printer with a mounted screen is shown in Figure 2.25. The entire holder can be flipped towards the right to exchange the substrate below the screen. To achieve the same distance throughout the screen, a matching spacer is needed on the other side. The screens for this printer were ordered from the same company with the screen size A3+ coated with the emulsion Fotecoat 1850 SOLO of Fotec Ag (Küsnacht, Switzerland) and developed. Squeegees with a hardness of 75 Shore and wooden handles were employed. The large area makes it possible to print large patterns. Mounting of the frames, printing and cleaning of the components is simple and time-saving. Only two of the four screws are necessary to hold the screen firmly in place if the nuts of the holder are tightly fixed. The printer costs only about 250 euros and is well suited for low-resolution printing, quick prototyping and was used by the author for educational purposes, too. The major disadvantages are the following. No vacuum system is employed making it necessary to tape the substrates onto the table to avoid sticking to the screen after printing with highly viscous pastes. Attention should be paid when flipping up the screen as a low viscous paste may run down towards the holder. The manual application of pressure on the squeegee requires experience to not deform the screen and receive a distorted image. The angle of the squeegee at the contact point to the screen has to be maintained between 45° and 75° to avoid squeezing the paste out of the desired print patterns. The alignment for multi-layer printing is challenging and can be only reliably achieved for an accuracy of about 1 mm.

The **High precision printer Nino** was built by Coruna Printed Electronics (Bettwil, Switzerland). It is a manually operated printing machine, which was designed to fit inside a glove box. During the work of this thesis, the printer was operated only in ambient conditions in a clean lab atmosphere. The printer consists of a substrate table, a screen transport system, a print head, and a camera module as shown in Figure 2.26. The substrate table has the dimensions 40 x 20 cm^2, of which the central 20 x 20 cm^2 are perforated with small holes for fixing the substrate by vacuum, Which is connected on the right side to a pump. The top of the substrate table can be moved in two directions up to 10 cm far with a position accuracy of 1 µm and rotated by ± 5°. The screens have a format of 50 x 38 cm^2 and require precisely put nuts in each corner and a high degree of planarity. Therefore, the screens used in this work were purchased directly from the producer of the printer.

On the rear side of the printer (Figure 2.26), a waggon is intended to transport the screen from the entry of the possibly existing glovebox towards a location under the print head. At the end of the waggon rail, the screen can be lifted by turning the handle on the back right of the printer. After lifting, the screen has to be mounted on the bottom side of the print head with the four screws in each corner and the screen lifter can be lowered again. The print head shown in Figure 2.27 can be moved towards the front and back on rails and has to be in the rear position while loading the screen. The print head consists of a steel frame that is additionally strengthened by an aluminium profile

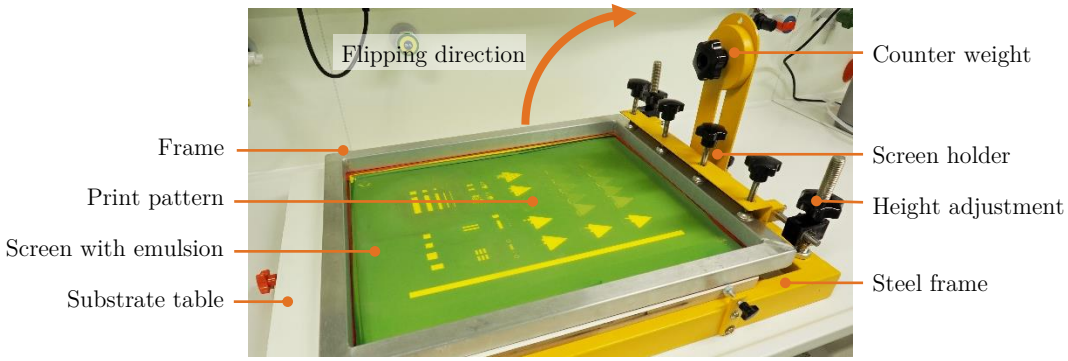

Figure 2.25. Manual screen-printing machine FLAT-DX 200 with labelled components and indicate the direction in which the frame can be flipped for exchanging the substrates.

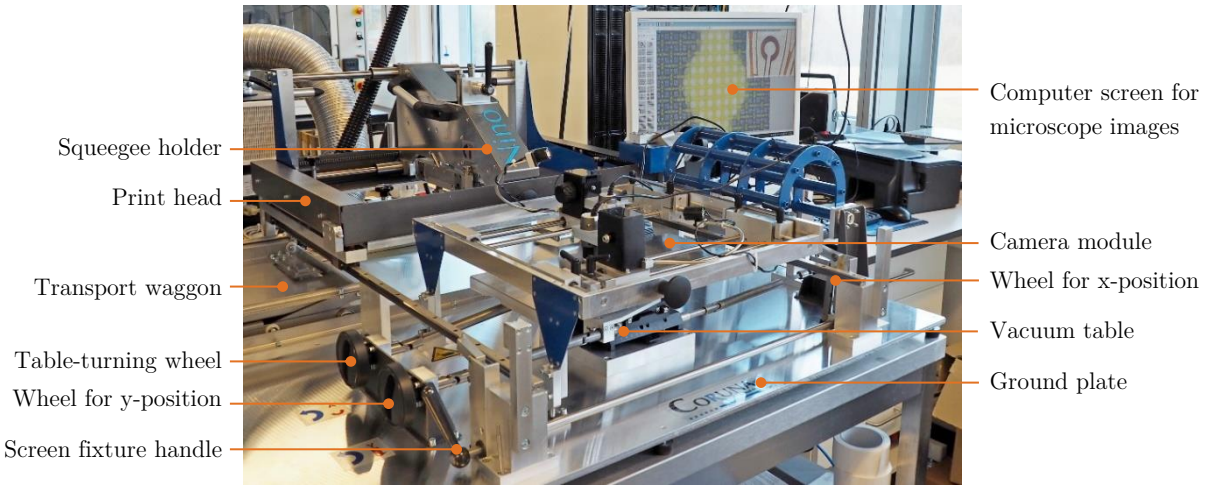

Figure 2.26. The high-precision screen printer Nino of Coruna with its main components, the print head in the back, the camera module put down, the vacuum table with the three hand wheels for each direction, and the transport waggon.

below. It is designed to be plain and stable to flatten any existing deformation of a screen. In the front position during printing, it has to be fixed with the screen fixture handle that ensures a precise positioning of the print head.

On the print head, the squeegee holder is mounted that can be moved from left to right and takes the squeegees. The print squeegee consisting of a three-layered polyurethane rubber is fixed in an aluminium holder that lasts almost to the end of the rubber and forms a rigid backbone. The aluminium holder has a handle and two knobs that need to be inserted in the designated positions in the squeegee holder. Then, the small handle on top of the squeegee is locked to fix it tightly. The print squeegee can be adjusted in its angle by a wheel next to this handle and in its height with the left of the two wheels at the top of the squeegee holder. On the other side of the squeegee holder, the flooding squeegee consisting of an aluminium blade that is formed to collect and equally distribute the paste can be mounted and its angle and height adjusted similarly. All four wheels move the squeegee by 250 µm per turn. The switch at the top of the print head allows the selection between printing (left) and flooding (right) mode by lowering the required squeegee and rising the other.

Figure 2.28 shows the camera module of the Nino printer that can be flipped down when the print head is in its rear position. It is mounted on the blue arm, which also contains the brake to inhibit accidental falling. The module contains two cameras that can be positioned in two directions. The metal frame has an axis on each side for the y-positioning on which a carriage with the x-axes is mounted. These carriages contain two fixtures. One at the outer side is holding the carriage at a

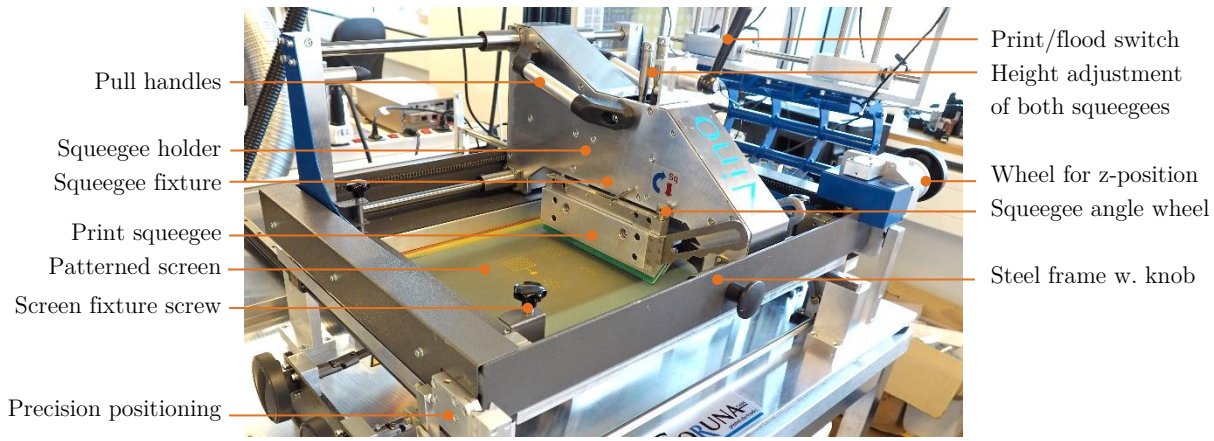

Figure 2.27. The printhead of the high-precision screen printer Nino with a mounted screen to its bottom and the squeegees in the designated positions.

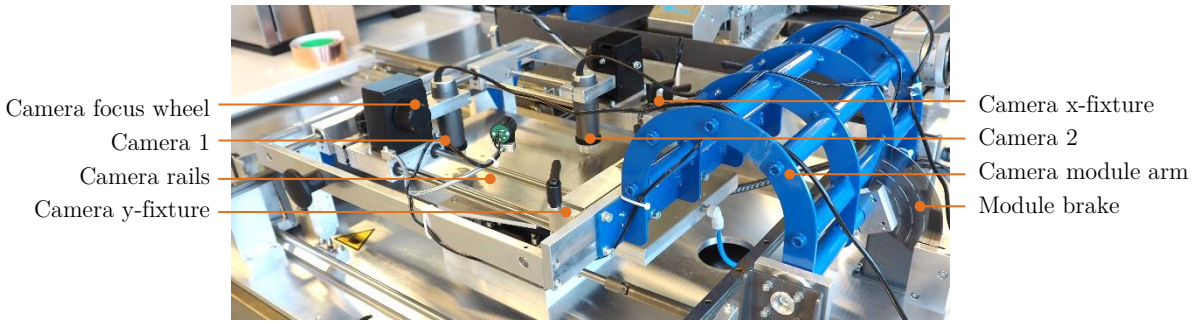

Figure 2.28. The camera module of the screen printer Nino with two cameras that can be precisely moved in two directions and tightly fixed at the desired positions.

coarse position while fine-positioning the camera whit the small wheel. Once in the desired y-position, the second fixture is tightened. On the x-axes, the camera blocks are mounted and can be precisely positioned and fixed with the same mechanism. The author exchanged the original large microscope cameras with two digital microscopes, an AM4115ZT and an AM7915MZT Dino-Lite Edge. These feature colour images at a resolution of 1.3 and 5 megapixels, respectively, and two magnification points at around 65x and 220x, which can be adjusted on the wheel directly on the microscope. Eight LED lights encircle the lens and provide a homogeneous lighting. Different caps can be used to diffuse the light or only use light from one direction. A polarizer may also help to improve the image quality. A touch sensor can be used to trigger an action in the software. This software offers the possibility to see live images of both cameras at the same time as well as previously acquired images. The front camera possesses an automated magnification reading. To obtain accurate measurements with the other camera, the magnification setting from the camera has to be read or experimentally determined with the calibration glass slide. The focus wheels of the previous microscopes may be used to focus the image and adjust the working distance of the cameras to slightly increase or decrease the magnification at the focus points.

The first task before starting to print is the precise positioning of the squeegees. Both squeegees have to be mounted on the print head without the screen. The print head is moved to the front and the selection switch put in the position to lower the print squeegee. Now, the print squeegee's height is adjusted to form a thin gap between the edge of the rubber and the table. The angle of the print squeegee has to be adjusted to get a homogenously sized gap across the entire substrate table. A stripe of paper can be used to check the thickness of the gap. After the parallelization of the print-squeegee, the print head is moved to the rear position and the screen is mounted by placing it on the transport waggon, then moving that to the end of the rail, lifting it by the designated handle, fix the screen with the four screws in the corners of the print head and lowering the transport waggon. Now, the printhead can be moved to the front again and the height adjustment of both squeegees follows. The snap-off distance between the substrate and the print side of the screen is adjusted by the z-positioning wheel. The distance is changed by 50 µm per turn of the wheel. A distance of about 1-3 mm is recommended in most cases. Then, the height of the print squeegee is adjusted with the screws on top of the squeegee holder. The ideal setting is if the squeegee presses the screen just into contact with the substrate. The flood squeegee's height and angle have to be adjusted as follows. It should be lowered onto the screen until it has only a small distance of approximately 100 µm to the squeegee side, which can be measured by moving a small piece of paper between screen and squeegee. This helps to find out if the angle of the flooding squeegee needs adjustment so that it has the same distance throughout the entire length. Now, the printer is ready to print.

The printing procedure for a multi-layer print is as follows. After cleaning and placing the substrate onto the vacuum table and closing all open holes around the substrate, the print head is moved to the front and fixed with the handle. The squeegee holder is moved to the left. After mixing the paste, it is put on the right side of the frame. The squeegee holder is moved towards the right while making

sure that the flood-squeegee does not touch the paste by moving the squeegee switch slightly to the left. Once all the paste is between the squeegees, the squeegee switch is moved completely to the right moving down the flood-squeegee. Now, the squeegee holder is moved to the left with a constant velocity depending on the ink's viscosity. Typically for low viscous inks, a higher velocity is used than for highly viscous inks. After reaching the end, the switch is turned into the printing mode and the print head is moved back to the right position. During the first printing, it may be hard to move and it is helpful to not move the switch fully to the printing position. After printing, the print head fixture is loosened and the head is moved to the back. If the print is incomplete, it is necessary to lower either the height of the print squeegee or the snap-off distance.

Once a satisfactory print is achieved and shall serve as a base for a second layer, the current printing position has to be registered. The camera module is flipped down and for each camera, all four fixtures are loosened to position the cameras on the alignment marks. On the PC, the DinoCapture software is opened. A successful connection to the cameras is established if their lights turn on and the live image appears on the screen. The magnification and other settings can be changed with the components labelled in Figure 2.29. The magnification wheel can be turned from about 50x to 230x. While turning, two magnifications can be found which lead to a sharp image. It is recommended to use the one at around 220x. The polarizer may help to decrease reflections and exchanging the transparent cap to others may improve the image quality of transparent or reflective layers. Once the focus point and the position on the alignment marks are found, the outer handles are fixed and the accurate position is adjusted with the small wheels before fixing the other two handles. It is recommended to position both live images on the screen next to each other with the DinoCapture software. The author recommends creating drawings on the live images that follow the edges of the alignment marks or other unique features and then take a snapshot. Now, the printed substrate can be post-processed, e.g. put for drying into an oven. The author finds it useful, to place the snapshots below the live images so that there are two frames with the live images and two frames with the snapshots visible on the screen. Once, the previously printed layer is dry, it should be put on approximately the same position onto the vacuum table. Now, the camera module is flipped down and the table is positioned by moving the x-, y- and angle wheels until the alignment marks appear exactly at the same position in the live image and the snapshots. Then, the camera module can be flipped up, the print head moved to the front, and a second layer should be printed exactly on top of the previous one.

Possible failures may be caused by a not fixed print head, a shrinking of the substrate in the oven, leaning on the printer while taking microscope images or other mistakes.

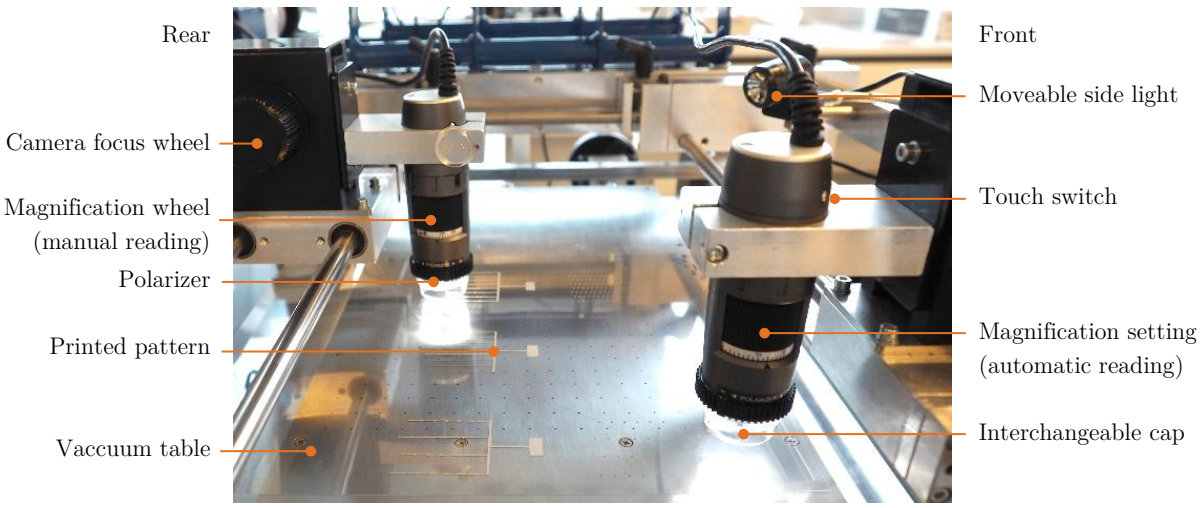

Figure 2.29. Close view on the cameras of the print module in the Nino printer.

2.3.3 Screen-Printing of Conductive Pastes

Screen-printing pastes are much less complex in comparison to inkjet inks. This section shows additional properties important for screen printing and refers to Section 2.2.3 for an introduction on the used terms. Screen-printing pastes have a three to four orders of magnitude higher viscosity than inkjet inks and are in the range of 2500 cP to 100,000 cP. The high viscosity is needed so that the paste does not flow through the mesh. Low-viscous pastes require small mesh openings. A certain viscosity is desirable so that the paste is not pressed under the emulsion and does not flow outwards of the several microns thick wet films after printing. In common screen-printing pastes, the viscosity is defined by the amount and properties of the loading with functional material. The upper limit of the viscosity is defined by the mesh opening width and the pressure applied. A too high viscosity may result in the incomplete printing of edges. [138]

The surface tension of screen-printing pastes is not as important as for inkjet inks. Still, it should be sufficiently high to keep the paste within the mesh before printing and low enough to feature a good release from the mesh after printing. It should also be higher than the surface energy of the substrate to achieve a good resolution. [138]

For screen printing, conductive pastes containing silver flakes, carbon flakes and PEDOT:PSS were used in this thesis and are summarized in Table 2.5. Six different silver pastes were used with each possessing unique properties. The first three are economic printing pastes that consist of silver particles of different size. Then follow a stretchable, an epoxy-based and a silver chloride blended paste. Figure 2.30 shows SEM images of all pastes after printing and drying.

The first of the **Silver pastes** is the silver-flakes paste Ag-510 of Applied Ink Solutions (Westborough, MA, USA) a brand of Microchem and was purchased through PrintColor (Bochum, Germany). It consists of 68 ± 2 %(wt.) silver flakes with diameters in the low micrometre range. Figure 2.30a shows these rather large flakes that vary in size across about one order of magnitude. The viscosity lies between 3400 and 4200 cP. The recommended drying time is 1.5 to 4 min at

Table 2.5. List of conductive pastes for screen-printing and stencil-printing used in this thesis.

Material	Name	Manufacturer	Distributor
Ag Flakes	Ag-510	Applied Ink Solutions (Microchem)	PrintColor
Ag Flakes	ECI 1010 E&C	Loctite (Henkel)	-
Ag NP	ECI 1011 E&C	Loctite (Henkel)	-
Stretchable Ag	CI-1036	EMS Inc	-
Ag Epoxy	CircuitWorks 60 Min.	Chemtronics	Mouser
Ag-AgCl	EDAG 6038E SS E&C	Loctite (Henkel)	-
Carbon	C-220	Applied Ink Solutions (Microchem)	PrintColor
PTC Carbon	EDAG PF 455BC E&C	Loctite (Henkel)	-
Stretchable Carbon	CI-2051	EMS Inc	-
PEDOT:PSS	EL-P3145	Orgacon (Agfa)	SigmaAldrich

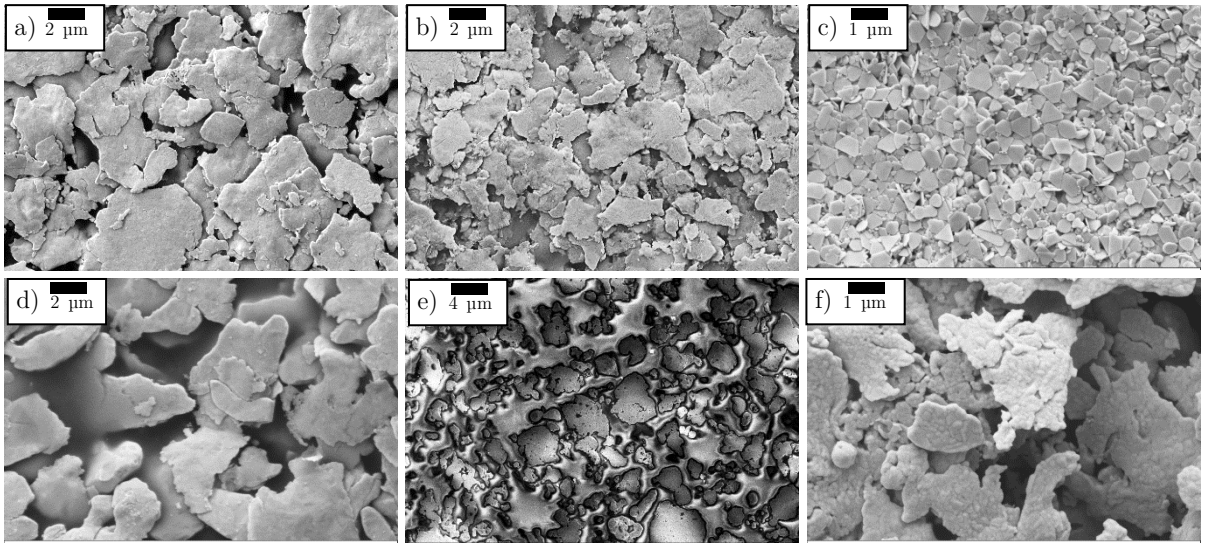

Figure 2.30. SEM images of the silver pastes a) AG-510, b) ECI 1010, c) ECI 1011, d) CI-1036, e) CW-60, and f) EDAG 6038E.

130 °C and can lead to sheet resistances down to 15 mΩ/sq in a 25.4 µm thin film. The recommended screens have a thread count between 60 and 90.

The second silver paste is the silver-flakes paste ECI 1010 E&C of Loctite (Henkel), which provided it to the author. It consists of 62 %(wt.) silver flakes with diameters of a few micrometres and smaller (Figure 2.30b). The viscosity is around 9000 cP, the density 2.1 g/ml and the theoretical coverage 10.6 m²/kg at 10 µm dry film thickness. The recommended drying cycles are either 2 min at 150 °C or 15 min at 120 °C and can lead to a sheet resistance of 7 mΩ/sq in a 25.4 µm thin film. The recommended screen has a thread count between 60 and 80.

The third silver paste is the silver NP (Ag-NP) paste ECI 1011 E&C of Loctite a brand of Henkel, which provided it generously to the author. It consists of 75.6 %(wt.) Ag-NPs with diameters in the range from tens to hundreds of nanometres. Figure 2.30c shows the flat shape of the flakes with straight edges. The viscosity is 2800 cP and lower than that of the previous paste. The density is 3 g/ml and the theoretical coverage is 8.3 m²/kg. The recommended drying cycle is 10 min at 150 °C and leads to a low sheet resistance of 5 mΩ/sq in a 25.4 µm thin film. The recommended thread count is 80 to 120.

The stretchable silver paste is CI-1036 of Engineered Materials Systems Inc. (Delaware, Ohio, USA), which provided it generously to the author. The total solid content is 69 %(wt) of particles with diameters up to tens of micrometres as can be seen in Figure 2.30d. These are not aligned as flat as in the other pastes indicating that they are hold in place by an elastic matrix that can deform. The viscosity of 12000 cP is high. Cured at 120 °C for 10 min, this paste should show a sheet resistance of 10 mΩ/sq in a 25.4 µm thin film. Screens with a thread count of 60 to 80 are recommended by the manufacturer.

The epoxy-based paste is CircuitWorks 60 Minutes Conductive Epoxy (CW-60) of Chemtronics (Kennesaw, Ga, USA) and was ordered through Mouser Electronics. It is a two-part silver epoxy which features strong mechanical bonds and high electrical conductivity after drying. The two components have to be mixed equally and can be cured at room temperature for several hours. Higher curing temperatures decrease the curing time but also decrease the viscosity. This leads to an outflow of the paste, so we recommend to cure it at room temperature. The particles shown in Figure 2.30e are rather large and embedded into a non-conductive matrix indicated as charging in the SEM image.

The silver-chloride (AgCl) paste is EDAG 6038E SS E&C of Loctite a brand of Henkel, which provided it generously to the author. It consists of a blend of silver and silver-chloride in a ratio of

9:1 and contains 66 %(wt) of solid contents. It has a high viscosity of 21000 cP and can be cured at 120 °C for 15 min or at 80 °C for 30 min resulting in a sheet resistance of less than 40 mΩ/sq in a 25.4 µm thin film. It can be printed through a screen with a mesh count between 68 and 110. From the SEM image in Figure 2.30f, it is not apparent that this paste is a mixture because all particles look the same.

Three different **Carbon-based pastes** were used: a normal screen-printable carbon paste, a paste with a high positive temperature gradient and a stretchable carbon paste. Figure 2.31 shows SEM images of all three pastes at two different magnification levels to show their composition in the micrometre and nanometre range.

The resistive carbon paste C-220 of Applied Ink Solutions (Westborough, MA, USA) a brand of Microchem and was purchased through PrintColor (Bochum, Germany). It has a solid loading of 42 %(wt.) and a viscosity of 20000 cP. After drying at 130 °C for 5 min, it shows a resistivity of 15 Ω/sq in a 25.4 µm film and can be printed through a mesh with a thread count of 60 to 90. As can be seen in Figure 2.31a, the paste consists of particles of several tens of micrometres with a nanoporous structure (Figure 2.31d)

The resistive carbon paste with a positive temperature coefficient (PTC) ECI 8001 E&C of Loctite a brand of Henkel which provided it generously to the author. It contains 50 %(wt.) of solids at a viscosity of 6500 cP. The recommended drying cycle is 10 minutes at 120 °C. The paste then shows at a sheet resistance of 1.7 kΩ/sq in a 25.4 µm thin film at room temperature. At higher temperatures, the resistance increases slightly until it jumps to the 5.5-fold at a threshold value of around 60 °C. This behaviour is reversible and typically used for self-regulating heaters that can rapidly heat and then maintain a constant temperature. In the SEM images Figure 2.31b and e, we can see conductive nanoparticles embedded into a non-conductive material.

The stretchable carbon paste CI-2051 of Engineered Materials Systems Inc. (Delaware, Ohio, USA) which provided it generously to the author. It consists of 40 %(wt.) carbon flakes and has a viscosity that ranges from 50000 to 80000 cP. A typical sheet resistance after 10 min drying at 120 °C is 50 Ω/sq in a 25.4 µm thin film. It consists of very large carbon particles (Figure 2.31c)

We employed these inks for a variety of applications shown later in this thesis and want to present only one that is important for a wide range of sensors. We investigate screen-printing of conductive pastes for thin lines and gaps between them for the application as interdigitated electrodes. We produced a screen with the patterns shown in Figure 2.32. They were intended for use as an

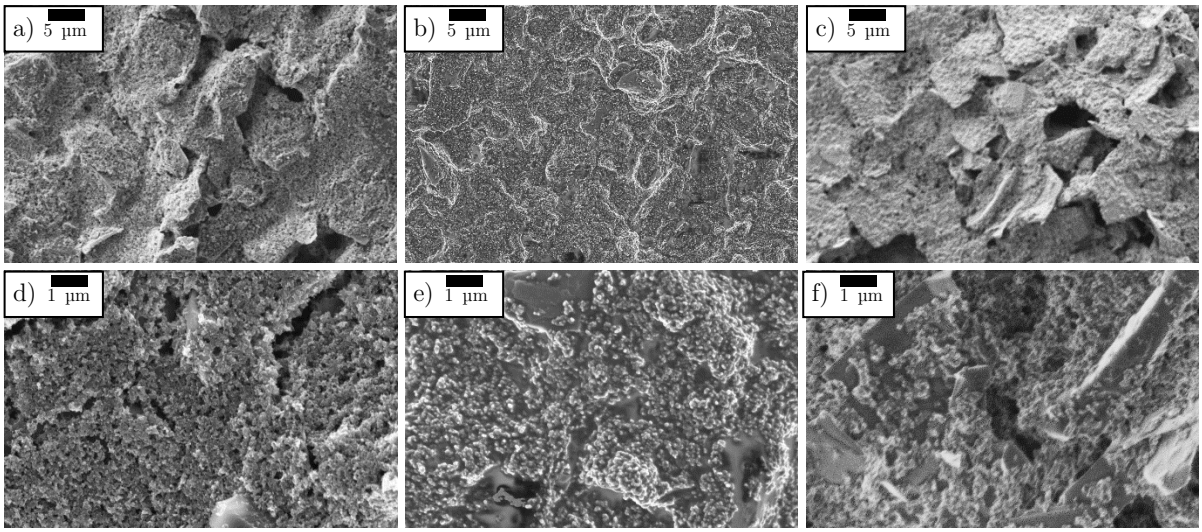

Figure 2.31. SEM images of the carbon pastes in two different magnifications a) C-220, b) EDAG PF 455BC, c) CI-2051.

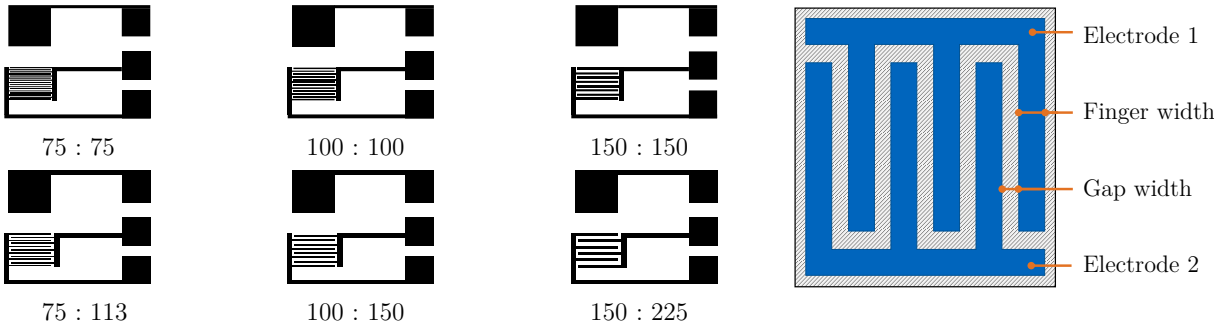

Figure 2.32. Left: Designs of the evaluated interdigitated electrodes designated for biosensing. The top row has equal finger width and distance increasing from 75 µm to 150 µm. The second row has an increased gap of 50 %. Right: The definitions of finger widths and gap widths.

electrolyte gated field effect transistor and thus consist of three electrodes. The most challenging printing task is the printing of the interdigitated electrodes (IDEs) and we designed IDEs with a finger and gap width of 75 µm, 100 µm, and 150 µm. Preliminary tests showed that our pastes rather tend to flow out. Therefore, we designed IDES with increased gaps by 25 % (not shown here), and 50 % (second row). These finger structures may be printed on top or below a semiconductive CNT layer to build thin film transistors.

We produced the screens for the patterns and show microscope images of examples in Figure 2.33 with different mesh counts of 80, 140, and 165, from left to right. The threads are clearly visible in yellow because the microscope images were taken from the squeegee side. The emulsion can be seen by a grey layer below the threads. It is apparent that for the low mesh count, the variation between the different fingers is rather large and the printing depends on the position of the emulsion-free area on the threads. In the worst case, the finger is partially blocked by the 48 µm wide threads. Therefore, it is better to use a higher mesh count. As the mesh count is increased (Figure 2.33b), the open area of the screen is reduced from 38 % to 27 %. This reduces the amount of paste, which can be even beneficial for our application as it reduces the paste flow that increases the finger width. The resistance of the printed electrodes will be rather low in comparison to the employed sensing material and is not a crucial factor. Still in this configuration, the position of the threads is deciding the printing. For example in some parts, there are two rows of openings forming the line, on others only one. This can be reduced by putting the pattern at an angle onto the screen as shown in Figure 2.33c. The 75 µm thin lines are still homogeneously patterned in the 165 mesh.

Figure 2.34 shows several of the best IDEs printed with the carbon paste C-220 on screens with two different mesh counts and design parameters. We found that for a mesh count of 140, the minimum dimensions to achieve were a gap of about 120 µm on average with a rather low edge roughness in comparison to higher mesh counts. At a mesh count of 165, the line thickness decreased slightly,

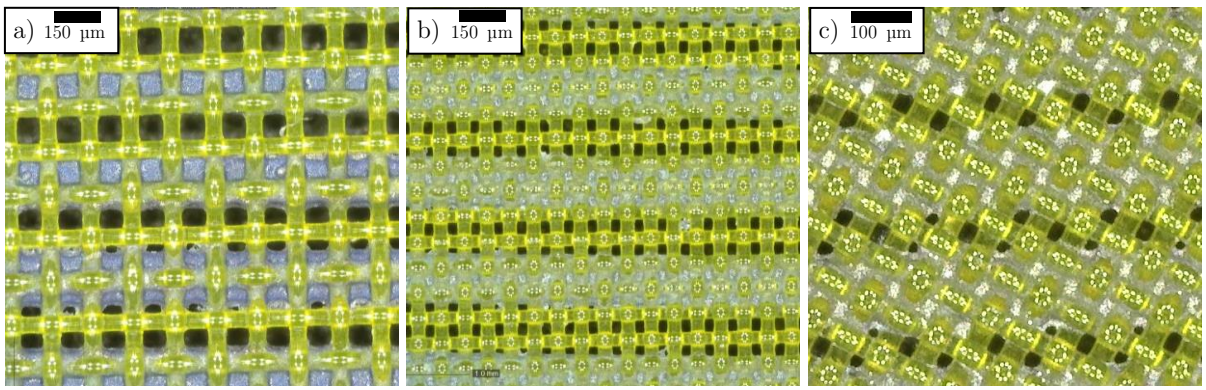

Figure 2.33. Optical microscope images of screen-printing screens with different mesh counts for printing of interdigitated electrodes seen from the print side. a) 150 µm wide fingers and gaps on an 80-mesh, b) 150 µm wide fingers and gaps on a 140-mesh, and c) 75 µm wide fingers with a 125 µm wide gap on a 165-mesh.

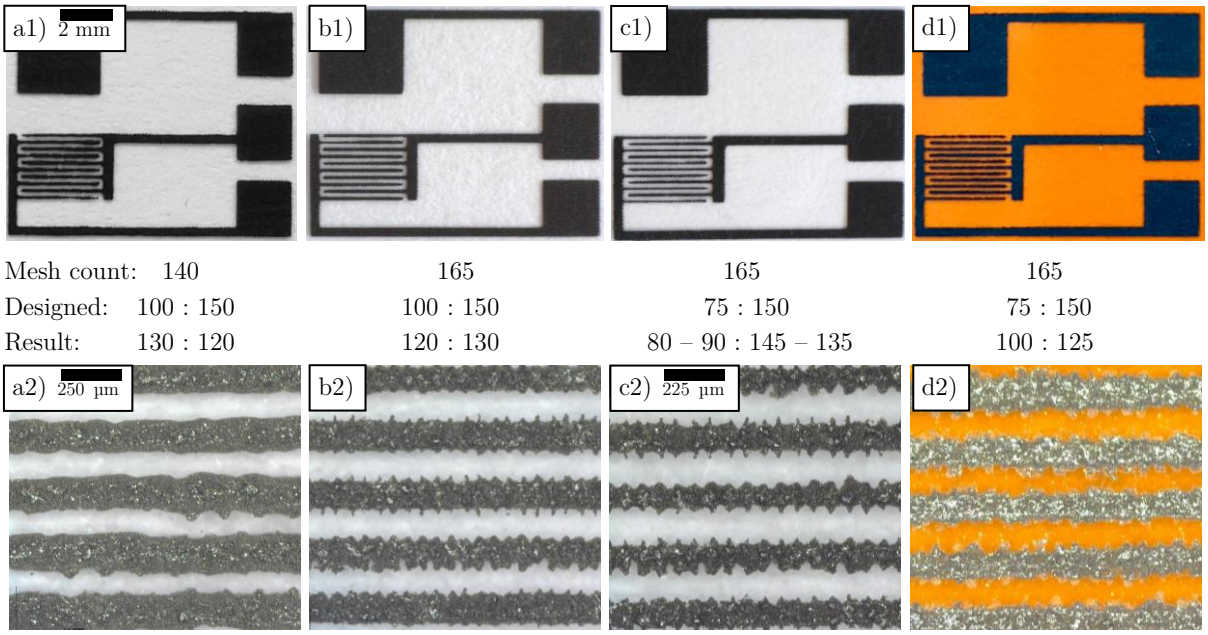

Figure 2.34. Screen-printed carbon electrodes with a magnification on the printed IDE structure, and mesh and design parameters (in µm). The carbon paste is shown dark whereas the substrate is white or orange. The scale bars are always valid for the images on the right in the same row if no other scale bar is shown.

but the edge roughness increases significantly. We assume that the particles in the C-220 carbon paste are too large and some of them start clogging the screen. The same edge roughness was found for the smaller dimensions with a finger width of only 75 µm and a designed gap of 150 µm. The fingers printed 5 µm to 15 µm larger than designed. This sample shows the potential to decrease the gap width to a lower value, as none of the fingers is close to their neighbours. Finally, we also printed the same pattern on a polyimide film and could achieve a channel length of 125 µm.

These values are still above the desired channel length of below 100 µm but the potential can be seen. For future prints, we suggest to use a high-resolution emulsion and increase its thickness to obtain more homogeneous edges.

2.3.4 Screen-Printing of Dielectric Pastes

Table 2.6 summarizes the isolating and dielectric pastes used in this thesis. We used a thermal and a UV curable isolating paste, a paste with a high dielectric permittivity, and different kinds of silicone rubber pastes.

Table 2.6. List of isolating and dielectric pastes for screen-printing and stencil-printing used in this thesis.

Material	Technique	Name	Manufacturer	Distributor
Thermal Dielectric	Screen	TD-642	Applied Ink Solutions (Microchem)	PrintColor
UV-curable Dielectric	Screen	EDAG PF 455BC E&C	Acheson (Henkel)	-
$BaTiO_3$	Screen	BT-101	Applied Ink Solutions (Microchem)	PrintColor
Silicones	Screen	Alpatec 30191 TZ Alpatec 30143 Alpaprint Clear + CAT	CHT Bezema	-

The thermal cure **Dielectric paste** TD-642 of Applied Ink Solutions (Westborough, MA, USA) a brand of Microchem was purchased through PrintColor (Bochum, Germany). It has a low viscosity of about 7000 cP and a dielectric constant of 3.65. It is available transparent or with additional blue colouring. In contrast to most dielectric or isolating pastes, it is thermally curable at 140 °C for 3 - 8 min. It can be printed with screens with a thread count of 95 – 140.

The ultra-violet (UV) light curable dielectric is EDAG PF 455BC E&C of Acheson (Henkel), which provided it generously to the author. It has 100 % solid contents at a viscosity of 13500 cP and can be cured with UV lamps of 80 – 120 W/cm with an energy density of 0.5 J/cm². The high solid loading has the advantage, that the film thickness does not shrink during post-treatments.

The barium titanate ($BaTiO_3$) paste BT-101 of Applied Ink Solutions (Westborough, MA, USA) a brand of Microchem and was purchased through PrintColor (Bochum, Germany). It consists of 67 %(wt.) of $BaTiO_3$ and possesses a dielectric constant of 35 to 40 after drying for 6 min at 130 °C. The dielectric paste is intended for use in electroluminescent lamps and displays. It has a viscosity of 10.000 cP and a screen with at least 95 threads per centimetre is necessary. To achieve a pinhole-free layer, it is recommended to print at least two layers.

Three different **Silicone pastes** were used that were generously provided to the author by CHT (Tübingen, Germany). All silicones are transparent, two-component pastes that need to be mixed before use. The A-component and the B-component have a density of 1.10 g/cm³. The two components of Alpatec 30191 TC have a viscosity of 70000 cP and 74000 cP and need to be mixed 1:1. The hardness (Shore A) is 22 and it can be stretched up to 510 %. The two components of Alpatec 30143 are less viscous with 60000 cP and 55000 cP and need to be mixed 1:1 as well. The hardness is higher (25) and it is less stretchable (300 %). Both pastes have a platinum catalyser in their A-component. The silicone paste Alpaprint Clear needs to be mixed with 2 % Alpaprint CAT, which contains the catalyser. The mixture has a high viscosity of 200000 cP – 300000 cP and results in a high hardness of 35 ° shore A. Low thread counts of 15 to 77 are recommended to print the pastes, however, it was possible to use higher thread counts to achieve a low film thicknesses.

During the comparison of the three silicone pastes, the silicone Clear was found to be hard to print because of its high viscosity. The other two are similar whereas the 30143 leads to higher film thicknesses on the same screen. This means, that a higher amount of paste is released whereas, for the other two pastes, a considerable amount of paste remains in the screen after the jump. The jump is the moment of the separation of the substrate and the screen.

The following experiments were done with a custom-made screen having a thread count of 54 and a thread diameter of 48 µm. This screen has an aperture of 55.6 %. According to the manufacturer, the emulsion added another 100 µm in height below the mesh, which leads to a total height of approximately 246 µm. The theoretical wet film thickness is then approximately 153 µm. This is in accordance with the measured thickness of the 30143 paste after curing of about 148 µm, which is shown in Figure 2.35a by a horizontal red line. It seems, that the paste contains only little solvents and the film thickness remains constant during drying and curing.

The focus of the screen-printing of silicones was to achieve patterns with a high aspect ratio between the film thickness and the diameter. Figure 2.35b shows a circular pattern that has a designed diameter of 750 µm. After printing and drying, it was found that the height of 181 µm was slightly smaller than the theoretical thickness but higher than the average value measured on the larger pattern. The width measured at a height of 5 µm was 766 µm and slightly larger than the designed diameter. This gives an aspect ratio of 0.24, which is already comparably high for screen printing. However for smaller diameters of the hills, their height changes.

For an in-depth investigation, we start with the characterization of the screen using an optical microscope. Figure 2.36a shows images of the bare screen and the emulsion-coated screen. The bare

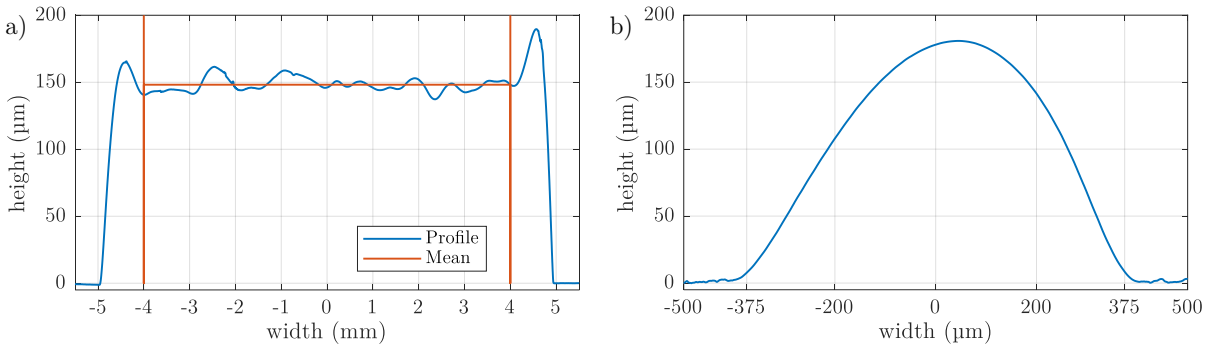

Figure 2.35. Height profile of screen-printed silicone patterns with different forms: a) A flat square of 10 mm and b) a circle with a designed diameter of 0.75 mm. The mean value (red) was calculated in the marked region of the flat profile.

screen should have a thread count of 53 and a thread diameter of 48 µm. However, we measured a thread count of 51.4 in the printing direction and 50.7 in the perpendicular direction. The measured thread diameter is 50 µm. Due to the angle of 6° of the vertical threads, the open mesh area calculates to $a_0 = \frac{147 \cdot 145}{197 \cdot 195} \approx 55.5$ %, which is only slightly smaller than the values given by the manufacturer. This would lead to a maximum wet-film thickness of 55 µm. As the measured thickness of the 10 mm square leads to an average thickness of 150 µm, we have to assume, that the thickness of the emulsion is 95 µm or that the release of the screen occurs mainly from the emulsion whereas the part of the paste in the mesh remains there after printing.

The circular openings in the emulsion shown in Figure 2.36a are accurately reproduced on the screen, without an influence of the underlying threads. The circles were designed to have the diameters of 750 µm, 600 µm, 500 µm, 400 µm, 350 µm, 300 µm, 250 µm, and 200 µm, from top left to bottom right. The measured diameters are close to the designed ones with an accuracy of ± 3 µm. Whereas for the larger circles, the diameter of the threads plays a minor role, for the smaller ones, the position of the threads within the circle is important. Circles smaller than 150 µm have a high chance to be blocked completely by a crossing of threads.

It can be seen, that especially for smaller diameters, the position of the circle on the mesh can lead to a large deviation from the average open area of 55.5 %. For circles smaller than the thread diameter, the open area can be 0, if the circle lies directly on a thread. For circles smaller than the mesh width, the open area can be up to 100 %, if the circle is placed directly in the opening. Also for larger diameters, there may be a significant deviation from the average value. We conducted a numerical simulation that calculates the open area for a large range of diameters. Figure 2.36b shows the open area in percent for diameters below 1 mm. As expected, the maximum and minimum open area start at 100 % and 0 %, respectively, for small diameters and then converges towards the average value of 55.5 %. Both values move in waves with a length of $w = \frac{10\,mm}{mesh\ count}$ because for each

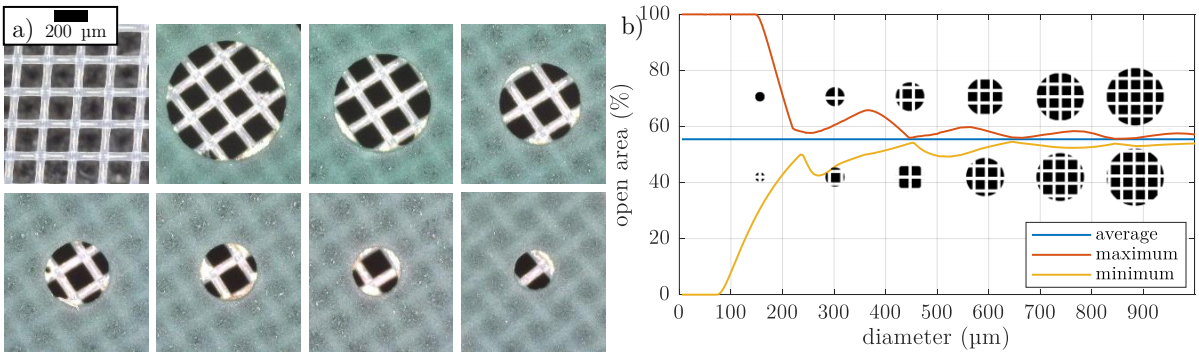

Figure 2.36. a) Optical microscope images of the bare screen and circular patterns with different diameters (from top left in µm: 750, 600, 500, 400, 350, 300, 250, and 200). b) Average, minimum and maximum open area for a screen with a mesh count of 53.

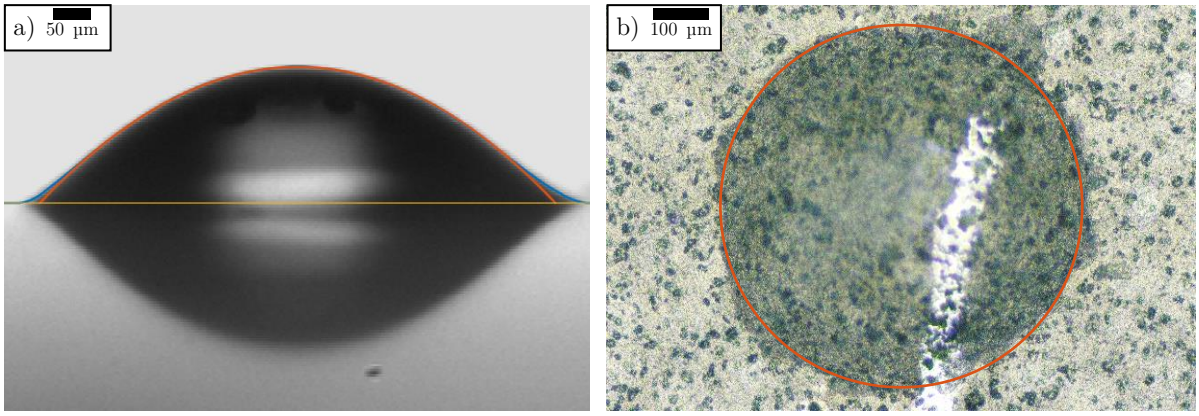

Figure 2.37. Optical microscope images of a screen-printed silicon rubber hill. a) Side view with the marked baseline (yellow), hill shape (blue) and a fitted parabola (red). b) Top view with a marked circle at the edge (red).

increment of w, one more thread is inside the circle. The small insets in Figure 2.36b show the position of the mesh for maximum and minimum open area at the top and bottom of the curves, respectively. For small diameters, it is favourable to place the circle in an opening and detrimental on a thread crossing. For increasing diameters, these two positions alternate between being favourable and detrimental. In between, some other positions may be favourable as well.

The circles on the designed pattern do not print as cylinders but as hills as the optical microscope image of the printed dots from the side in Figure 2.37a show. The hills follow a paraboloidal shape with squeezed out edges in the side view. The hill is shown in dark in front of a bright background and reflects on the PET substrate below the baseline (yellow). The shape of the hill is marked in blue and a fitted parabola is shown in red. The hill printed on top of a silver layer seen from the top in the microscope image (Figure 2.37b) shows that it is almost round as the red marked circle shows.

The paraboidal shape was confirmed by surface profiles (blue) in Figure 2.38 show. The profiles were measured with a contact profilometer on circles printed on top of the previously screen-printed silver. We found that the measured curves look similar for all measurement directions. A diameter of at least 175 µm was necessary to release paste during printing. For smaller patterns, the paste remained completely inside the screen. With increasing diameter from 200 µm to 750 µm, the height increases from 37 µm to 183 µm. The cross-section profile of the hills follows almost exactly a parabola for all measured profiles. Fitted parabolic curves onto the part of the measured profile that is 3 µm above the substrate are shown in red in Figure 2.38. The fitted parabolic curves follow the measured values closely and have almost the same peak height. At the bottom, some pillars are squeezed out of the designed pattern. At the top, a slight shift towards the measurement direction was found independently from which direction the measurement was conducted. Apparently, the slight pressure that the stylus exerts onto the hill bends the pillar slightly. Without mechanical stress, the profile should follow even more a parabola as can be seen in the microscope images.

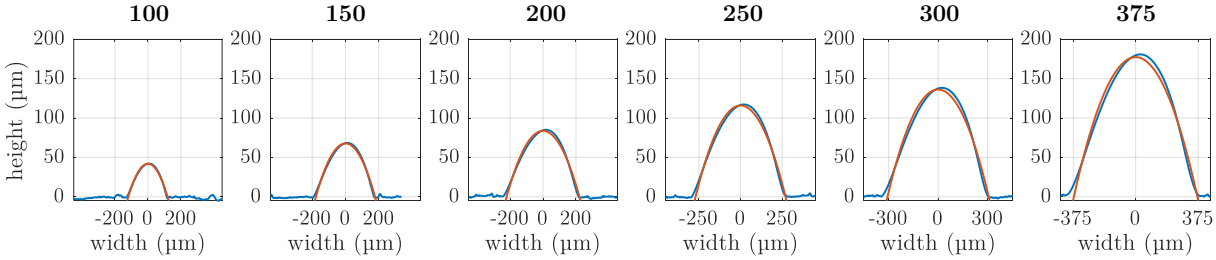

Figure 2.38. Height profiles (blue) of screen-printed silicone circles with varying radius with a fitted parabolic curve (red).

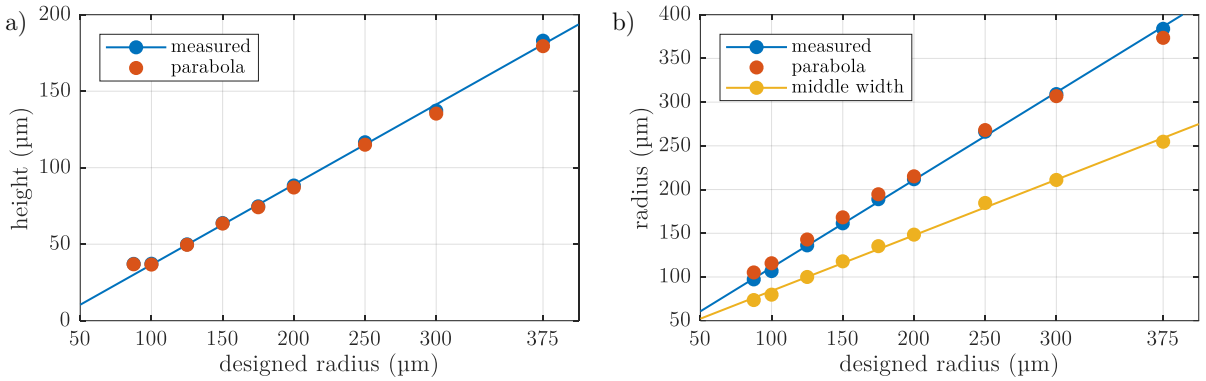

Figure 2.39. a) The maximum height of screen-printed silicone circles (blue) with fitted line and peak of the fitted parabola (red) with varying diameter. b) Bottom width (blue) and width at half maximum (yellow) of the measured profiles with fitted lines and width of the parabola (red).

Figure 2.39a shows that the height of the hills increases linearly with the radius at a slope of 0.52 and an offset of -16 µm (Eq. 2.4). The only exception is the smallest hill with a diameter of 175 µm that is as high as the 200 µm hill. The width of the printed hill is approximately 11 µm more than the designed pattern. It seems that the hills are pressed out of the designed pattern. We evaluated the width at half of the peak height for all diameters. This is only about 90 % of the expected value of $1/\sqrt{2}$ of the bottom width. The height and the width of the hills follow linear relations and, thus, the aspect ratio of height divided by the diameter h/2r is linear, too. Figure 2.40 shows this relation which is between 17.4 % and 23.8 % linearly depending on the measured radius. Eq. 2.4 summarize the formulas for the height h and the radii r and r_{hm} at the bottom and at half the maximum height, respectively, and the aspect ratios h/2r depending on the designed radius r_d.

$$
\begin{aligned}
h &= 0.524 \cdot r_d - 15.7\ \mu m \\
r &= 2r_d + 11\ \mu m \\
r_{hm} &= \frac{0.900}{\sqrt{2}} \cdot w + 13.5\ \mu m \\
\frac{h}{2r} &= r_d \cdot 20.2 \frac{\%}{mm} + 16.4\ \%
\end{aligned}
\qquad \text{Eq. 2.4}
$$

We investigated the influence of the slight mismatch of the measured curve to the parabolic approximation by calculating the cross-section area of a hill and its volume (Figure 2.41). Again, we found a good approximation by the parabola shape for the measured values.

Only the volume of the largest hill was slightly overestimated. This shows that the squeezed out edges of the hills do not contribute significantly to the cross-section area and the volume. These investigations show that a sensor built with such hills screen-printed with silicone paste can be modelled by a paraboloid shape. The linear relations between the height and the designed radius may help to find an ideal combination for the desired application. The squeezed out edges may be neglected as they don't play a big role for the filled area nor the entire volume of paste.

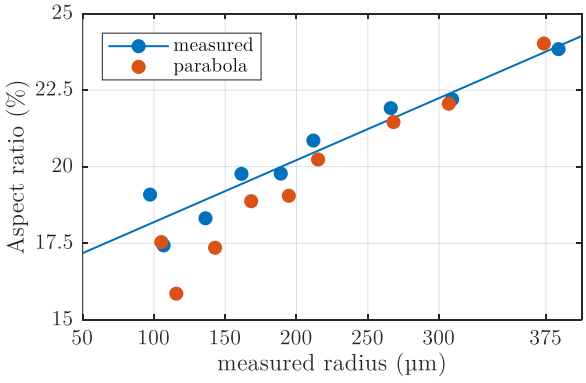

Figure 2.40. Aspect ratios between pillar height and radius r depending on the measured radius.

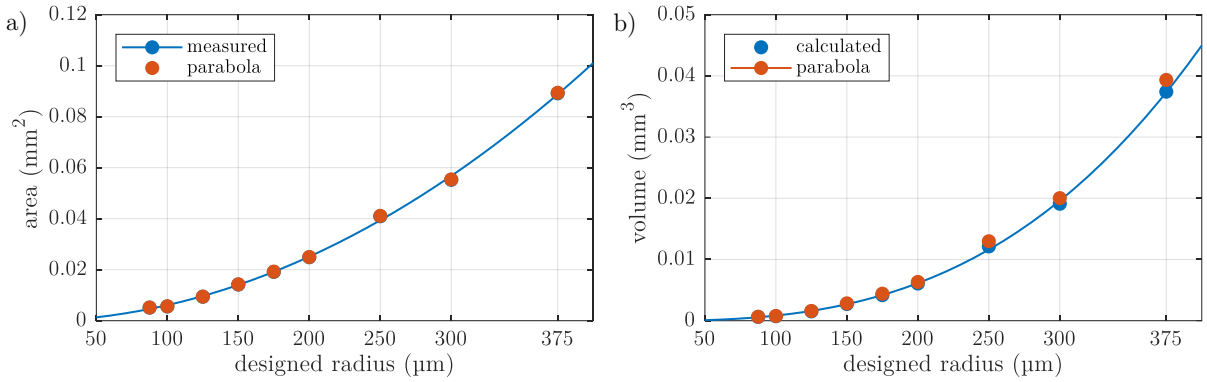

Figure 2.41. a) The cross-section area and b) volume of a hill by integration (blue) with a fitted quadratic curves and of the fitted parabola (red) with varying diameter.

2.3.5 Multi-Layer Screen Printing

Among all printing techniques, screen printing is the most suitable one for multilayer printing. Neither high pressures nor much solvent are involved that can harm previously printed layers. Still, it is an ongoing field of research and development. Especially height differences in the underlying layers can influence the printing behaviour significantly, large particles can pin through underlying layers, and still, most pastes consist of a large amount of solvent. The simplest multilayer stack is printing of an isolator on. In continuation of the previous subsection, Figure 2.42 shows a 3D profilometer study about the reproducibility of the printing on PET and previously screen-printed layers. Here, we found an accurate hill formation independently of the underground. The hills with a radius of about 250 µm showed all a height of about 110 µm on the PET and about the same height with respect to the silver layer.

Another example is alternating isolating and conductive layers, which are needed, for example, for printed circuit boards. Figure 2.43 shows one of the circuits developed during the thesis. On the left, the first printed conductive layer is shown. Then an isolator was applied with three wet-on-dry printing cycles and finally another conductive layer. We found that at least three layers of the thermal curable paste are required to not form any shorts between the layers. Each layer must be dried and the substrate aligned again to be able to print the next layer at exactly the same location. Figure 2.44 shows the layer stack in more detail and indicates the step that occurs when a printed layer from the top reaches over the edges of a lower-lying layer. The step height is the crucial point and the conductive paste must be well applied to achieve a conducting path across the step.

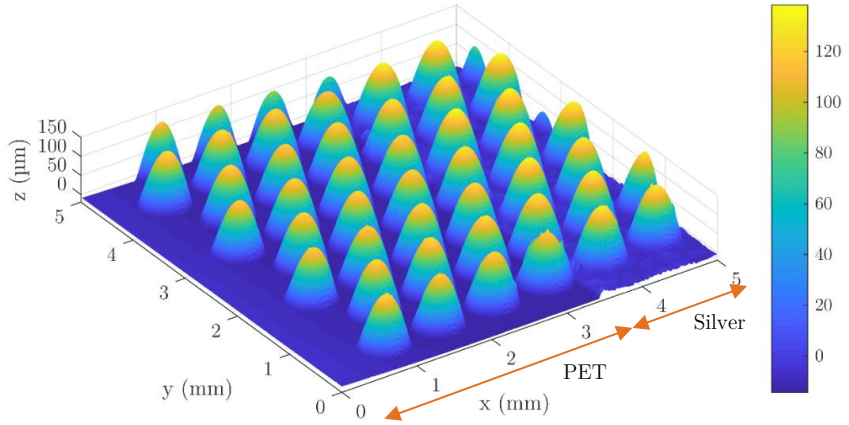

Figure 2.42. 3D profile of the silicone rubber hills printed on PET (x < 3.3 mm) and on previously screen-printed silver (x > 3.3 mm) with above 110 µm high pillars. The radius is about 250 µm and the centre-to-centre distance 750 µm.

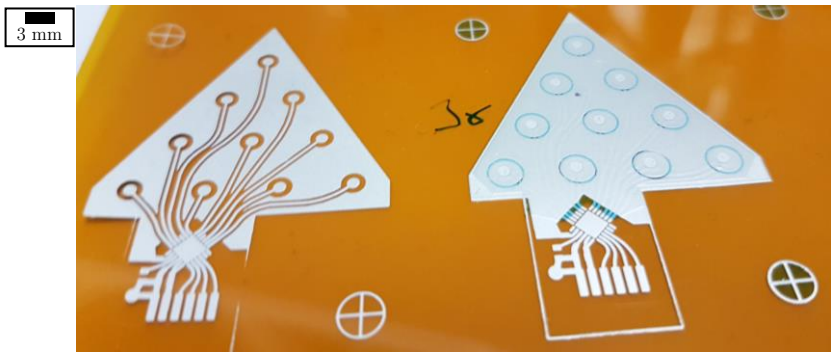

Figure 2.43. Left: The first screen-printed layer of a printed circuit on polyimide film. The second layer is the blue dielectric that covers the entire triangle with exception of the ten circles. Right: The second screen-printed layer of the printed circuit.

We found that alignment of multiple layers especially on PET is not that easy. With the manual screen printer, alignment is only possible with an accuracy of about 1 mm. With the Nino screen printer, much higher accuracies can be achieved. However, when transferring a sample between both printers, we found that for an identical pattern, the pattern was stretched randomly. We found that a stretching is likely on the manual screen printer due to pressure variations of the operator. Too strong pressure stretches the screen by a few hundreds of micrometres. Another crucial point is the shrinking of substrates during drying. Especially the PET, which is a Melinex 506 of DuPont, shrinks significantly within the first minutes at temperatures above 80 °C. Figure 2.45a shows the shrinkage of PET and polyimide (Kapton HN of DuPont). Whereas PET shrinks by about 0.3 % during the first five minutes at 100 °C, it does not shrink much afterwards anymore (0.32 % after 10 min). The maximum temperature that the PET can withstand without visible damages was found to be about 120 °C. Kapton shrinks only little and rather at higher temperatures. We found that both substrates do not shrink even more after putting them in an oven for 40 min or more. This is highly recommended to achieve accurate multilayer printing.

In the following, we want to present our multilayer printing for the vibration sensors described in Section 4.2.5. This work highlights several aspects of multilayer printing. Our goal was to print pillars of one millimetre in diameter as high as possible. Therefore, repeated printing, drying, and alignment cycles were necessary. We printed with three different pastes, the silver pastes Ag 1010 and the Ag 1011, and the carbon paste C 220. Figure 2.45b shows the average heights that were achieved after the indicated number of layers measured with the surface profilometer. The almost linear increase in all lines shows that the printing is repeatable even for a high number of layers. The pastes printed with the mesh count of 80 (indicated in brackets in the legend) showed a higher thickness than for a mesh count of 100 because the opening is higher. We could achieve almost similar heights with all silver pastes and decided to stop at 50 µm because the repeated drying and printing is time-consuming. The carbon paste dried quickly and we were not able to print more than four layers without clogging the screen.

The dots were printed on the patterns shown in Figure 2.46. The figure shows photographs of three samples that were printed with different screens or pastes. All pillars have a diameter of 1 mm on the screen and are only slightly (< 5 %) deviating after printing. All of them were printed seven

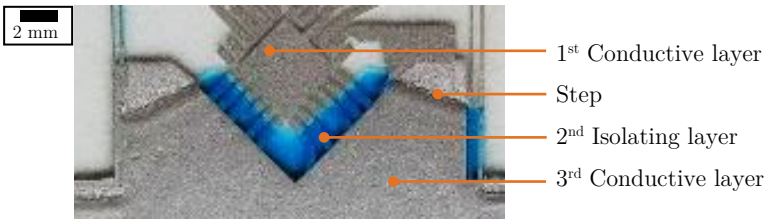

Figure 2.44. a) Printed bottom layer (silver) of a PCB with isolation layer (blue). b) Magnification of a Section of the final print showing some distinct differences to conventional PCBs.

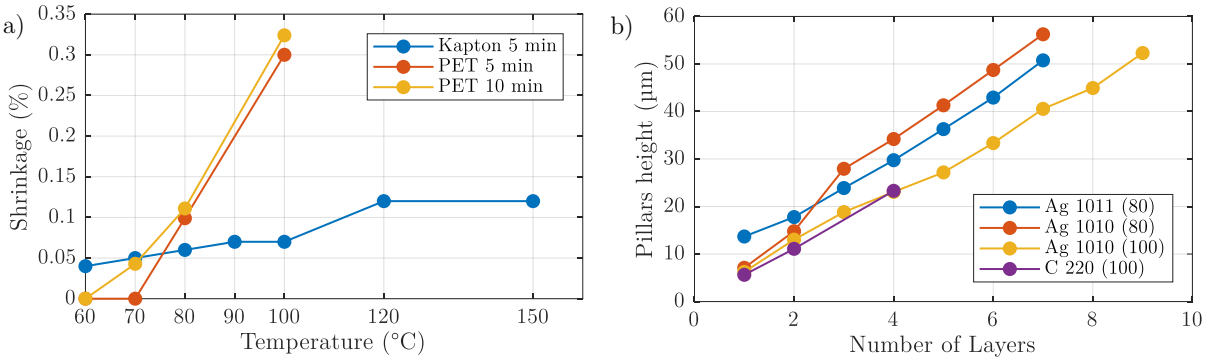

Figure 2.45. a) Shrinkage of PET and Kapton after being exposed to a certain temperature for 5 min or 10 min. b) The average height for multilayer printing with different silver (Ag 1011 and Ag 1010) and a carbon paste (C 220) through screens with a mesh count of 80 or 100 as indicated in brackets in the legend.

times with intermediate drying at 100 °C. The first and the second are printed with the silver paste ECI 1010 and a different mesh count, namely 100 and 80. The second and third are printed with the same screen, but a different paste. The third one was printed with the nanoflakes paste ECI 1011. Microscope images of all three show already a major difference especially in the choice of paste. Whereas the 1011 paste looks rather smooth with pronounced edges, the 1010 paste is rough.

Figure 2.47 shows 3D surface topographies of the two different silver pastes and confirm the optical impression of a different roughness of the pillars. Both pillars have a similar average height of 60.9 µm and 61.4 µm, respectively, but vary in their maximum heights of 133 µm and 111 µm. For the future, we recommend the Ag 1011 paste for multilayer printing because it results in much smoother surfaces. A screen with a higher open area and a higher emulsion thickness may reduce the number of printing cycles to achieve a certain height. We also want to evaluate epoxy-based and UV-curable pastes that are solvent-free and their height does not shrink after printing.

We could show several examples of multilayer screen-printing for dielectric and conductive materials. This is a basic requirement for printing of sensors and smart systems as we present them in the next chapters of this thesis. In the next section, we continue with the opposite side of the thickness range of printed films: deposition of films in the nanometre range.

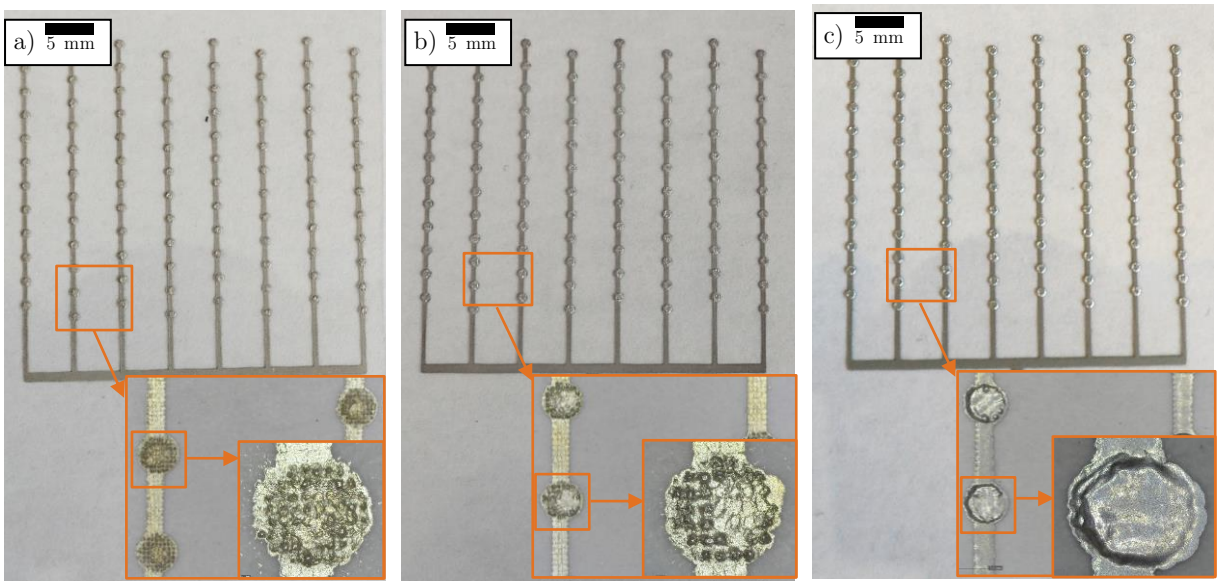

Figure 2.46. Photos and microscope images (insets) of screen-printed multilayer pillars printed with a) Ag 1010 through a 100-mesh, b) Ag 1010 through an 80-mesh, and c) Ag 1011 through an 80-mesh. The diameter of the pillars is designed to 1 mm and is only slightly larger after printing.

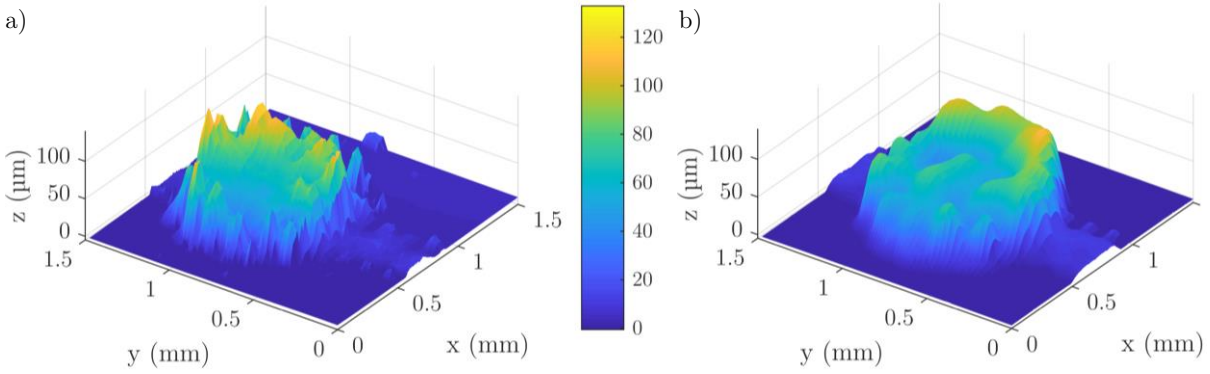

Figure 2.47. The roughness of the hills depending on the employed paste. a) Ag 1010, b) Ag 1011. The colour bar applies to both graphs.

2.4 Spray Coating

Spray deposition is a technology that can be used for surface coating with graphical as well as functional materials. In comparison to the printing techniques presented in the previous sections, spray deposition was only minor used during this thesis. Thus, only a brief description of the technology, a selection of conductive inks that are also transparent, and a low-cost approach for patterning is described. The focus is on the applications for thin-film thermocouples and the sensing layers of chemical and biochemical sensors described in Sections 4.3.1, 4.4.2, and 4.4.3, respectively. For a complete description and evaluation of spray deposition, the author refers to literature [59], [139], [140] and other theses at the same department by, among others, Alaa Abdellah [59], Ahmed Abdelhalim [60], Aniello Falco [58], Marco Bobinger [141], and Florin Loghin.

2.4.1 Technological Background and State of the Art

Gas-assisted spray deposition relies on a high-speed stream of a carrier gas, which can be air for most graphical applications or nitrogen for most functional applications. The gas stream passes a material nozzle that feeds the functional ink by gravity or pressure into the stream. The difference in velocity of the gas stream and material feed leads to a breaking of the liquid of the ink into fine droplets. This process is referred to as atomization. The size of the generated droplets depends on the nozzle diameter and fluid properties like viscosity, surface tension, and density. [139] The gas flow in the centre of the stream is fast and more material is deposited there with a radial gradient. To achieve a homogeneous coating over a large area, the nozzle most move in rows and columns with a defined distance to compensate the gradients. Figure 2.48 shows the spraying process schematically. Ink is fed through an ink reservoir into the chamber, where it is atomized by the carrier gas and expelled from the nozzle towards the substrate. The spray stream consists of droplets of varying size that form a film on the surface of the substrate. By moving the nozzle across the substrate, a homogeneous coating can be achieved.

A wide expertise in spray deposition is available from the surface coating that is used in various industries. A variety of simple and low-cost spray guns are available as well as fully automated atomizing systems with sample holders able to move in multiple dimensions and are still affordable in comparison to other equipment necessary to deposit thin-films and organic materials. [59] An example is the fully automated spray system that was used in this thesis. It consist of the three-dimension robot PVA350 from Werner Wirth equipped with a 781S spray valve from Nordson. We used a substrate temperature of 50 °C, an atomizing pressure 0.05 MPa, a material pressure 0.02 MPa, a deposition speed 250 mm/s and a nozzle-to-sample distance 50 mm. [142].

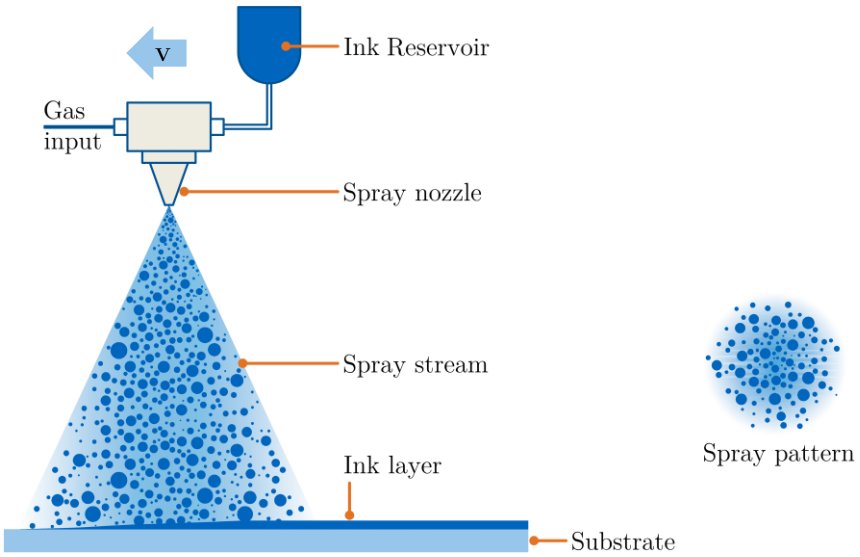

Figure 2.48. Schematic of spray deposition with the main components moving at a certain velocity v.

2.4.2 Spray Coating of Conductive Inks

During this thesis, three different transparent conductive inks for spray-coating were used that are listed in Table 2.7. The silver nanowires (AgNWs) were ECD0X3 of Ras Materials. 1 g AgNWs was diluted in the as-purchased form with 14 g of isopropyl alcohol (IPA) and 5 g of deionized water and viscously shaken. The PEDOT:PSS ink bases on Clevios PH1000 purchased from Heraeus. 1 g was diluted in 4 g deionized water and 10 mg of the wetting agent Dynol 604 purchase from Sigma Aldrich and 200 mg ethylene glycol was added and then sonicated with a Branson Sonifier S-450D for 30 s to disperse agglomerates. Ethylene glycol was frequently reported to increase the conductivity of PEDOT:PSS layers. [143] The CNT-ink bases on the 90 % semiconducting CNTs with the product number 773735 of Sigma Aldrich. 1 %(wt.) of the dispersing agent sodium dodecyl sulphate (SDS) purchased at Sigma Aldrich was dissolved in water and 0.03 %(wt.) of CNTs were added and sonicated for 25 min at a power of 50 %. The dispersion was then centrifuged at 15 krpm for 90 min and the top 80 % of the supernatant was separated to be used as the CNT ink. The author thanks his colleagues Marco Bobinger and Florin Loghin for the preparation of the inks.

Figure 2.49 shows SEM images of the thin films spray-deposited with the three different inks. The silver nanowires, which are shown white, are separated from each other, which shows, that agglomeration was successfully overcome. The same applies less clearly for the carbon nanotubes, which are well-dispersed with only a few bundles. Furthermore, CNTs are much more flexible than the stiff silver nanowires and entangle much more because of non-negligible Van-der-Waals forces between the CNTs. [144] PEDOT:PSS forms a partially homogeneous layer but some parts show drops with diameters in the micrometre range. This was found to be of minor importance for the optical and electrical performance.

Table 2.7. List of conductive inks for spray-deposition used in this thesis.

Material	Name	Ordered at	Mixture by weight
AgNW	ECD0X3	Ras Materials	1 : 14 : 5 AgNWs : IPA : water
PEDOT:PSS	Clevios PH1000	Heraeus	1 : 4 : 0.01 : 0.2 PEDOT:PSS : water : Dynol : EG
CNTs	773735	SigmaAldrich	1 : 33 CNTs : water

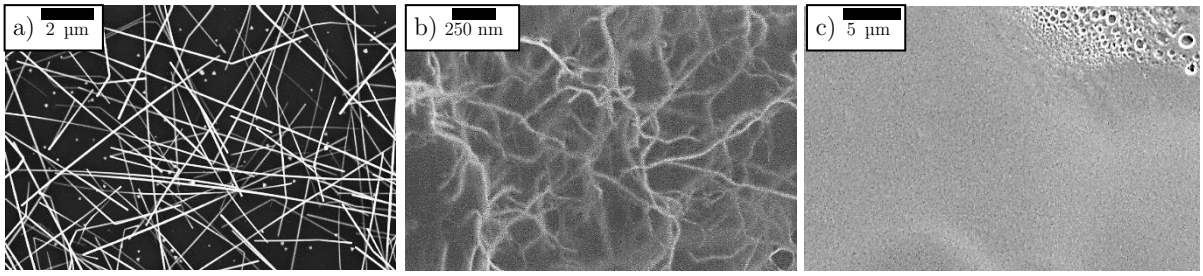

Figure 2.49. SEM images of a) randomly oriented silver nanowires, b) randomly oriented carbon nanotubes (CNTs), and c) a thin film of PEDOT:PSS.

2.4.3 Patterning

Spray-coating is a deposition technique that forms homogeneous thin films over a large area. If patterning is necessary, one needs to work with masking. One option is lift-off lithography with a photo-resist that is removed in a subsequent step after spray-deposition of the desired material. Another option is the used laser-cut masks that are placed onto the substrate. Typically, stainless steel masks are used, which are expensive to produce. During this work, much cheaper masks were laser-cut from a 100 µm thick PET film for the patterning in the millimetre range. Such masks need to lay flat on the substrate and should not move in the gas flow of the spray setup. Furthermore, a certain pattern size in the millimetre range is necessary and the larger dimension of a pattern is limited to the centimetre range.

2.5 Summary

This chapter presented an overview of additive deposition techniques from the field of printed electronics. These can be grouped into printing techniques, which are intended to form a structured pattern, and coating techniques, which are intended to deposit a homogeneous film onto a substrate. Examples of printing techniques are gravure, flexographic, offset lithography, transfer, stencil, aerosol jet, inkjet, and screen printing. The last two were studied in depth and will be used in the subsequent chapter. Coating techniques include slot-die coating, doctor blading, and spray coating.

Inkjet printing is a digital and contactless technique that allows the formation of thin patterns with an accuracy of several tens of micrometres. We presented an overview of different techniques and the two commercial and one self-made inkjet-printers used during the work on this thesis. One was a low-cost desktop inkjet printer of Epson, the second a high-price and high-precision lab scale inkjet system of Fujifilm Dimatix with control over a large range of parameters. The self-made inkjet printer consists of a part of the Epson printer but was modified to be able to print on rigid and thicker substrates and on wet substrates. Therefore, a flat table is moved through the printer on which the substrate is fixed and all rollers at the top were removed. The pattern generation for inkjet-printing is not trivial as an overlap of the drops is necessary to form continuous lines. The general approach for finding the ideal drop spacing and how to adapt the image was presented and discussed. The high volume of solvents in inkjet inks requires a substrate preconditioning and in some cases the use of coated substrates. The conditioning and coatings used during this work were explained and others were presented. The properties of inkjet inks were discussed and selected inks made from silver nanoparticles, copper-oxide nanoparticles, and gold nanoparticles were characterized optically, morphologically, and functionally. Inkjet printing on a large variety of porous and non-porous substrates was tested with the different inks and the main findings were presented. These contain the formation of a thin film and thin lines on the substrate and the resistance of the printed layers before and after intense, pulsed light sintering. On some substrates, conductivities of up to

46 % of the bulk conductivity were achieved. The section was concluded with the presentation of different post-processing techniques that apply specifically to inks for inkjet-printing and other printing techniques with low viscous inks.

Screen printing is a simple technique that is much less demanding on the paste quality and allows the printing of several micrometre thick and robust layers. The printing principle and the two screen-printers used during the work on this thesis were presented with a focus on the high-precision screen printer that possesses some major differences to other printers on the market. The most important component of screen printing is the screen that consists of a mesh with certain parameters stretched over a frame. The mesh properties and the different methods for forming a pattern on it by coating and exposure to ultraviolet light were discussed including practical experience from our own screen-making. The few important characteristics of screen printing inks were explained and the results from experiments with several silver, carbon, and dielectric pastes are shown. The major differences and scanning electron microscope images were presented and discussed. A focus of the section lies in the printing of silicone pastes to create micro-structured elastic dielectrics. Repeatable structuring and layer thicknesses of up to almost 200 µm were achieved with a single pass.

Spray coating is a method to form homogeneous thin films over a large area and was briefly discussed as far as required to understand the results of the next chapters. We spray-deposited homogeneous thin films with silver nanowires, carbon nanotubes and PEDOT:PSS to be used as transparent conductive layers in thermocouples and heaters.

In general, this chapter provided insight into two of the most used printing techniques and showed experimental results that are related directly to the printing processes. The next chapter focuses on the functionality of the printed thin films as conductive layers.

Chapter 3

Printed Conductive Structures

The basic element of every electronic device is the wiring of different components. In conventional electronics, this is usually achieved by a copper-plated circuit board that shows a low resistance. Printed conductive films usually possess a rather high resistivity and are thin. Heating of the films would reduce the resistivity significantly but the substrates like plastic films and papers have glass transition temperatures well below the required temperature. Therefore, several alternative curing and sintering techniques for printed conductive films were developed. One of them is phonic sintering with intense pulsed light (IPL) that is discussed in detail in Section 3.1 and the processing of several inkjet-printed and screen-printed metal layers is investigated. The rest of the chapter shows selected applications for printed conductive structures that exceed the use of conductive patterns just for wiring. Section 3.2 presents transparent conductive patterns with three completely different materials. Stretchable wires as discussed in Section 3.3 are an ongoing research topic. We present our work on self-recovering conductive layers of silicone rubber films that overcome the low surface energy and are over-stretching tolerant. Furthermore, the resistance of the wires does not increase significantly even after thousands of stretching cycles. The concluding Section 3.4 summarizes this chapter with the main findings.

3.1 Curing and Sintering Techniques

The low glass transition temperatures of polymer films and the low heat stability of many other materials like paper and textiles require alternatives to simple heating of the entire printed device. Such substrates are desirable for many applications because of their low cost or because they have certain properties that are appealing for the final product like transparency, biocompatibility and others. The contradiction of high temperatures in the printed films and low temperature in the substrate was solved by several groups of researchers that developed methods to selectively deliver heat to printed films. The most important techniques are discussed in the first subsection 3.1.1, and one of them, photonic or intense pulsed light (IPL) curing is explained in detail in the second subsection 3.1.2. This curing technique was used during the work on this thesis for sintering inkjet-printed silver and gold nanoparticle-based inks as well as screen-printed micro- and nano-flakes-based pastes. A drastic increase in conductivity and a significant change in morphology were found and are

presented in Section 3.1.3. IPL curing can not only be used for sintering but also to trigger certain chemical reactions, for example for the reduction of inkjet-printed copper-oxide (CuO) to plain copper with a high conductivity as shown in Section 3.1.4. Subsection 3.1.5 discusses briefly the use of IPL curing for improving the adhesion of metallic nanowires by slightly melting the surface of low-melting-point substrates like PET.

3.1.1 Overview of Curing Techniques

Many methods have been proposed and employed for sintering and curing printed layers, which consist of usually two or more steps. First, the solvents in the ink or paste must evaporate if any is present. In a second step, nanoparticles (NPs) try to reduce their surface energy by creating necks and thermal curable polymers start to entangle more due to Van-der-Waals forces. One option is heating of the entire device including the printed films and the substrate. For some sintering processes, it is desirable to achieve a quicker heating rate. Many substrates with a low glass-transition temperature possess an upper limit for the temperature. Alternative approaches to thermal curing utilize certain properties of the printed layer to absorb another energy form and only selectively heat it. Some printed materials show a much higher optical or electromagnetic absorption or show more sensitive to plasma or chemicals in comparison to the substrate. In the following, thermal, photonic including infrared, ultraviolet (UV), laser, and intense pulsed light, electrical, microwave, plasma, and chemical curing will be discussed. [120], [145]

Thermal Curing is achieved by heating the entire printed devices, which results first in an evaporation of the remaining solvent, decomposition of dispersing agents, and a formation of a binder-matrix. This reduces the particle or polymer distance and densifies the functional material. Often temperatures above 150 °C or even 300 °C are necessary to decompose organic stabilizer molecules that encapsulate the particles to prevent aggregation during printing. Such high temperatures are usually required to start sintering NPs to form conductive layers. The non-specific heating limits the compatibility of cheap polymer and paper substrates due to warping, shrinking, and gas emission at high temperatures. Large thermal expansion coefficients may also harm the printed layer by forming cracks. [2], [51], [54] Ink manufacturers advertise their products with curing temperatures as low as 120 °C, but higher temperatures are recommended to increase the conductivity. Thermal sintering is usually time consuming and requires durations of above 30 minutes, which complicate its application in high-speed and roll-to-roll processes. [51] The advantages of thermal curing is the repeatability on a wide range of heat-stable substrates and the slow process, which is beneficial for forming smooth polymer layers but can be detrimental for sintering as at low temperatures non-reversible morphology changes occur. [14]

Photonic Curing is based on the distinctly different light absorption of printed layers in comparison to the substrate. Metallic NPs absorb visible and infrared light much more than a polymer substrate or paper. The high intense light heats the metallic layer rapidly and causes an evaporation of solvents and the sintering of the material. Initially, the heat is confined within the superficial few NP layers and dissipated to neighbouring particles through small contact areas. The heat transfer leads to a rapid heating of the entire film and a formation of necks between the particles. Lasers, flash lamps, and infrared lamps have been used as light sources. If an UV-absorptive component is added to the ink or paste, UV lamps can be employed as well, which is often used for dielectrics and encapsulants. All photonic curing techniques have the advantage of being a dry and contactless process that is roll-to-roll compatible. Disadvantages of photonic curing are mainly the high absorption of the electromagnetic waves on the surface, whereas lower-lying layers only experience heating by heat transport. [145], [146]

Laser Curing is a spatially focused technique suitable for small areas and for extremely temperature-sensitive substrates. Ideally, the wavelength matches the maximum of the absorption spectra

of the printed layer. Small focus points can be achieved to cure sub-micrometre thin lines. It is possible to only cure parts of the printed layer and structure these at a higher resolution than is possible by other techniques. Non-cured layers may be removed by chemicals or not be conductive anyway. Furthermore, the laser can be used to burn away parts of the film that are not wanted. The major disadvantage is the limitation of the maximum spot size of about 40 µm for point lasers, yet line lasers partially overcome this limitation. The low speed of down to only 0.2 mm/s can mean long process durations for scanning large areas. [147], [148]

Intense Pulsed Light (IPL) Curing employs flash lamps to expose the entire area close to the lamp including the printed films and the substrate. This technique is widely employed in research as well as in production lines already. The light spectra is usually broad and covers the visible range including some parts of the UV and IR region. The distinctly high transmission of transparent films, reflection of white paper, and lower absorption of many substrates allows them to withstand high optical powers. Printed thin films of metal particles, carbon, or other coloured materials absorb light quickly and can heat to temperatures above 1000 °C. Common pulse durations are in the range of around one millisecond and only a few pulses are required. This makes IPL curing well suitable for roll-to-roll processes. Next to sintering, IPL curing can also be used to trigger chemical reactions in the film and to improve the adhesion of metal-nanowire films. [64], [149]–[151] Drawbacks of IPL curing are the high system cost and the time-consuming optimization of the parameters that are often not transferable to other substrates, inks, and stacks. [152] The next subsection elaborates the functional principle in more detail.

Infrared Light Curing uses incandescent lamps and uses the different absorption spectra of printed films and the substrate in the infrared region. The system cost is only about 10 % of IPL curing tools and it is easily scalable. It has lower running costs and can be adapted to be employed on stacks of materials. The disadvantages are mainly the larger and constantly exposed area that also heats the environment of the substrate to high temperatures and does not allow processing printed layers on heat-sensitive substrates. The employed wavelengths are usually between 0.8 µm and 4 µm and result in vibration excitation of the molecular bonds in the printed layer that causes an increase in temperature. IR curing can be used for drying and for sintering particle-based metal and oxide layers within seconds to minutes. [128], [145], [152], [153]

Ultra-violet Light Curingis mainly used for insulation, dielectric, and acid resistance layers but can be mixed with metal particles to be conductive. Furthermore, UV-curing has been applied to metal-organic decomposition inks that require an absorption outside of the visible light. UV-curable materials usually consist of one or two components that react with each other. This can be used to crosslink polymer chains to solidify liquid polymers after printing and increase their chemical stability. A disadvantage of UV curing is the degradation of most polymer substrates at low wavelengths and the generation of ozone at wavelengths below 250 nm. Therefore, filters, as well as absorbents with higher wavelengths, are researched. The later also offers the compatibility with UV-LED lamps that are much more energy efficient, smaller, do not produce ozone, and can be used to selectively expose only desired areas. Another disadvantage is the usually rather long exposure in comparison to other optical curing techniques. Still, UV curing is the most used curing technique for dielectrics in the field of printed electronics. [154], [155]

Electrical Sintering uses a directly applied or induced current flow in the film to generate Joule heating in conductive films. This technique does not affect any non-conductive substrates, but also requires some initial conductivity of the printed film. Then, the conductivity can be increased within a short time. A disadvantage is the practical implementation for arbitrary patterns, especially if the current is directly applied to the pattern as one may imagine at sintering a circular path. The generated conductive paths in the film are narrow and can carry a high current, which inhibits the sintering of other areas after one path is created. [51], [145], [156]

Microwave Curing induces heating by movement of charges in conductive materials or by dielectric losses in insulating materials induced by microwaves. This method can be applied to opaque layers as long as no Faraday isolation occurs. The absorbance of microwaves in metallic powders with nano- or microparticles is rather high but in bulk metals low, which makes it hard to achieve penetration depths higher than a few micrometres. An improvement can be the use of magnetic instead of electric microwave heating that has a large penetration depth in copper powder. Successful microwave sintering was reported for several metals but requires several minutes to a few hours. The amount of dielectric loss in an insulator can be estimated by the relation of the imaginary to the real part of the electric permittivity. Most polymer foils are rather transparent to microwaves but the same also applies to many isolating materials. The main drawback is the difficult upscaling with a homogeneous and effective absorption. Hot-spots due to overheating caused by an inhomogeneous field limit the application currently to the lab- and small-scale. [145], [157], [158]

Plasma Curing bases on ionized and highly reactive gas atoms and the reaction depends on the employed gas. Plasma can have reducing (hydrogen), oxidizing (oxygen, air) or inert (nitrogen, helium, argon) properties. Reducing plasmas are often used for the decomposition of metal salts to the plain metal. Oxidizing and inert plasmas destroy the usually organic stabilizers that encapsulate metal particles in most inks and prepare them for heat-induced diffusion processes. Plasma curing is usually time-consuming with process durations above 30 min. Long processing times lead to degradation and etching of most polymer foils. The main disadvantage is the need for vacuum in most commercial systems although some companies, e.g. Tri-Star Technologies (CA, US) offer a portable plasma device. [97] Another example is the micro-plasma system µPlasmaPrint, which can be integrated into several printing systems. [98], [99] Roll-to-roll integration will only be feasible if much more research and engineering are done to increase them in size. As metallic layers shield most plasma excitation sources as well as the reactive ions, it is expected, that plasma cured metal layers are only cured on their crust. [145], [159], [160]

Chemical Curing includes many different curing techniques mainly related to either destroy the encapsulation agents of NPs, decompose metal-organic inks, or reduce metal salts. Most methods for chemical curing of NPs only destabilize the metal-encapsulant system by detaching or dissolving organic molecules. It was found that dodecylamine dissolves in alcohols and breaks its bond to Ag-NPs. Other approaches involve the neutralization of charges that are often used to bond encapsulants to NPs. [161] Chloride containing salts like sodium (NaCl) or magnesium chloride ($MgCl_2$) added in small concentrations to the ink as well as exposure of the printed layer to hydrochloric acid (HCl) vapour were successfully used to replace encapsulants. Metal-organic inks and metal salts usually require a reduction of the metal cation to the zerovalent metal. Several precursor materials and reaction agents were proposed, demonstrated, and summarized in the review of Wünscher et al. [145] Chemical curing can achieve conductive patterns from NPs and metal-composites with simple means at room temperature. Disadvantages are the often required wet processing and subsequent drying that make chemical sintering not easily compatible with roll-to-roll printing, and possibly the exposure to vapours. [54], [145], [162]–[164]

3.1.2 Intense Pulsed Light (IPL) Curing

Intense Pulsed Light (IPL) curing is often also referred to as (photonic) flash (light) sintering and is essentially a thermal process whose heat source is the absorption of visible light. Figure 3.1 shows schematically the **Principal components**. Commonly, xenon stroboscope lamps with an emission spectrum ranging from 200 nm to 1.2 µm are used that possess a maximum in the green range and several high-intensity peaks in the IR region. Visible light is the key component as most metal NPs show intense surface Plasmon resonance bands in this region of the spectrum. Reinhold et al. found that Ag-NPs in the range of 50 nm, which is comparable to our Ag-NP inkjet ink, have a strong

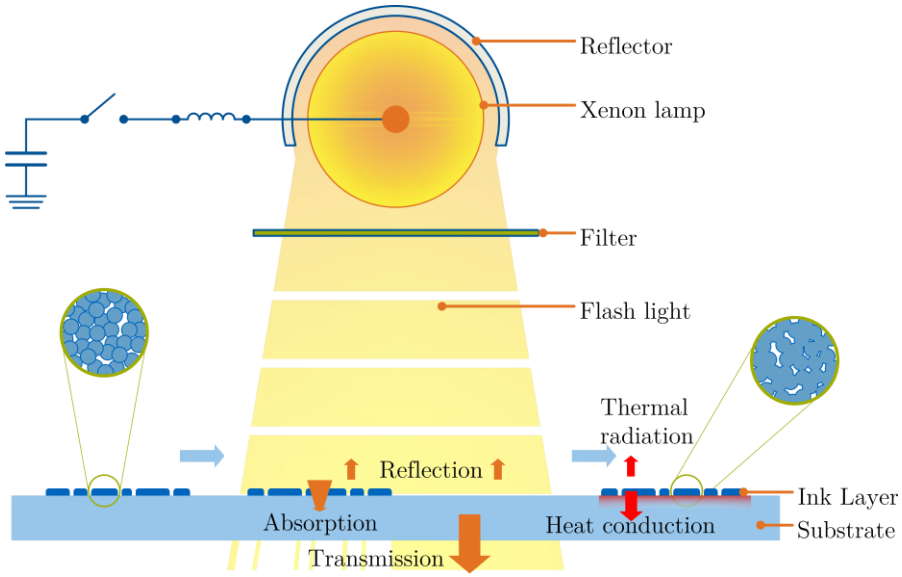

Figure 3.1. Schematic of the principle of intense, pulsed light curing of NPs including a simplified electrical circuit and the physical light paths and heat transfer. A charged capacitor is discharged over a flash lamp within a few hundred nanoseconds or microseconds. A reflector directs all light towards the substrate and a filter cuts out UV light to inhibit ozone generation. The printed film is rapidly heated, encapsulants of the NPs destroyed, and diffusion or partial melting of the particles lead to a coarsening and densification of the printed film. Finally, the film cools down as the remaining energy is transmitted as thermal radiation to the environment or towards the substrate. The interruptions of the light cone are for visualization of the pulsed nature of the visible light only whereas in real applications the flashes are approximately 8 – 9 orders of magnitude longer than the time the light requires to reach the substrate. The periods are usually even 2 – 4 orders of magnitude longer than the flashes.

absorption in the blue to purple region [165]. In contrast, glass substrates and many polymer foils have their absorption maxima rather in the UV region if no colourants are added. [145] A reflector behind the lamp redirects light emitted to other directions towards the substrate and is used to form a homogeneous light density. A filter lowers the rather small UV contribution in the emission spectrum to avoid degradation of the polymer films. Filters with a lower cut-off frequency are often employed to avoid the generation of ozone. According to the datasheet of our photonic sintering tool, about 40 % of the electrical power reaches the substrate table within a circular area of 10 centimetres in diameter. This shows an about an order of magnitude higher power conversion of electrical to optical energy compared to typical lasers. By focusing the light on the substrate table, high energy densities of 10 J/cm² can be reached. This can generate locally high temperatures of above 1000 °C within less than 1 ms [166] without the need for huge power electronics. Usually, one or multiple capacitor blocks are charged rather slowly to voltages in the between 400 V and 3 kV depending on the system. A trigger closes the connection to the lamp and quickly discharges the capacitor through the lamp. An inductor in the circuit flattens the discharge curve and produce temporally rectangular power pulses. Typical electrical power values are in the range of hundreds of kilowatts and flash durations below 3 ms. This results in electrical pulse energies of up to 2.5 kJ. [64], [145], [149], [167]

When the visible light accompanied by some fractions in the UV and IR range reaches the surface of the printed substrate, the physical processes are different between areas with and without a printed layer. On non-printed areas of transparent substrates, the main part of the light is transmitted to the other side and only small fractions are absorbed or reflected. On white substrates like paper and especially glossy photo papers, the major mechanism is reflection with a small fraction of absorption depending on the surface coating. On printed areas, the goal is to achieve an as high absorption as possible for energy-efficient curing. A small part of the incident light will be reflected, especially if reflecting gold or silver layers are sintered. Thin and porous layers may have a significant transmission as well. As the top layers of thicker films absorb the main fraction of the incident light, also lower-lying layers are exposed due to light diffusion in the typically porous layers. The Lambert-

Beer's law is applicable for most materials on the macroscopic level and the absorbed optical energy is converted to heat. The heat is either conducted into the bulk of the printed film or is dissipated to the environment. At the bottom of the printed film, a fraction of the heat is conducted towards the surface of the substrate and into the substrate. As most substrates are usually at least ten to hundred times thicker than the printed film and have a low heat conductivity, the heat transfer is limited to the surface of the substrate. Several research groups have simulated the processes in the printed layers and the surface of the substrate and in-line process monitoring has been developed. In the simulation, temperatures above 2000 °C have been predicted. In experiments, up to 1000 °C were measured in the film while the substrate temperature remained below 60 °C. [145], [147], [168]–[171]

The length of a pulse is a crucial criterion for successful curing. The pulses should be long enough to establish a thermal equilibrium in the printed layer and hold this as long as possible. The limiting factor is the time after which a certain depth of the substrate is heated to the glass transition temperature. This is usually below the establishment of the thermal equilibrium between the ink or paste and the substrate. Eq. 3.1 gives an estimation for the thermal equilibrium for a given material using the specific heat capacity c, the mass density ρ, the thickness d and the thermal conductivity κ. The heat capacity of substrate and ink is rather similar, but the higher density of the ink is more than compensated by the low thickness and the high thermal conductivity. This results in the formation of a thermal equilibrium in the printed layer within a time t_{ink} in the order of a microsecond whereas for a typical polymer foil the time $t_{substrate}$ is several tens of seconds. Therefore, suitable pulse lengths t_{pulse} can be selected between microseconds and a few milliseconds (Eq. 3.2). [145]

$$t = \frac{c \cdot \rho \cdot d^2}{4\kappa} \qquad \text{Eq. 3.1}$$

$$t_{ink} \ll t_{pulse} \ll t_{substrate} \qquad \text{Eq. 3.2}$$

Research on photonic curing has been conducted almost exclusively for silver [55], [64], [149], [168], [172] and copper [64], [147], [173]–[175] with a few publications about sintered nickel [176] and gold [177]. For the last metal, this thesis will present some new insights. The ink composition is an ongoing research field as, for example, Abbel et al. found that it has a strong influence on the sintering result. [47] Furthermore, research was conducted on the interaction of IPL curing with other previously printed layers, e.g. CNTs. Both of the major suppliers for IPL curing tools, Novacentrix (US), and Xenon Corporation (US) offer system that can produce fast microsecond pulses that can be varied in power with pauses of only a few tens of microseconds. This allows, for example, a short strong pulse that heats the film quickly followed by multiple weaker ones that keep the achieved temperature. [178]–[180] This offers much more opportunities to tune the process and optimize it for a specific ink composition and layer thickness on a specific substrate. References to research groups investigating this can be found in the outstanding review of Wünscher et al. [145] We will not discuss this in detail as our photonic sintering tool does not support these micro-flashes.

Figure 3.2 shows the **IPL curing tool Sinteron 2010-S** of Xenon Corporation (Wilmington, Massachusetts, US) that was employed for the experiments during this thesis. It consists of three main components, the blower, the power electronics rack, and the process chamber. The power electronics rack is composed of a controller, a power supply, an active control, and two pulse forming network modules. The controller at the top shows the currently set threshold voltage below which the electronics will start charging the capacitor and which can be modified with the knob. On the neighbouring display, one can read and set the pulse parameters, switch on the high voltage, and open and close the trigger. Below on the power supply, the tool can be switched on (Start) and off (Stop) and the fuses can be used to deactivate the device after using it. On the back of the rack, the main switch is positioned. The process chamber is connected via a ventilation pipe to the blower, which has to run at any time using the device and via several cables to the power rack. The process chamber contains the reflector at the top part, then the lamp housing, and the height-adjustable

Figure 3.2. Photographs of the Sinteron 2010-S of Xenon that was employed during the work on this thesis. Left: The complete setup including the power electronics rack and the blower. Right: The main component is the process chamber including the flash lamp.

substrate table with two marked rings. The height of the table was always set at 1 inch, which should give the most homogeneous light distribution according to the manufacturer. The two rings on the table mark the centre of the light exposure. Whereas within the central circle of five centimetres, the power density is rather constant (± 8 %), it reduces quickly towards the sides. On the 10 cm circle, the intensity can be as low as 50 % of the central intensity. The central intensity is approximately 0.4 %/cm² of the electrical power to the lamp.

The electrical energy to the lamp can be calculated according to Eq. 3.3 by knowing the high voltage U_{HV} and the pulse duration t_{Pulse}. The average output power only depends on the voltage.

$$E = {U_{HV}}^{2.3} \cdot 9\frac{mA}{V^{1.3}} \cdot t_{Pulse} \qquad \text{Eq. 3.3}$$

The high voltage can be set within the interval of 2.0 kV to 3.0 kV, which leads to output powers between 250 kW and 900 kW. The pulse duration can be adjusted in steps of 50 µs up to 3 ms leading to a maximum pulse energy of about 2.7 kJ. The minimum time between two pulses can be set to values starting from around 500 ms for low energies to several seconds for high energies.

It is recommended to start the blower before turning on the device because it should run at least 60 s before the first flash. Then, the blue and white fuses on the front right side have to be switched upwards and the Start button hold for a few seconds until the controller switches on. The Mode button opens the Display Mode, which shows the main parameters. The HV button switches on the high voltage after a few seconds and shows the current voltage in the red numerical display. The voltage can be regulated by the knob below between 2.0 kV and 3.0 kV. It is important to note, that this is not the current voltage at the internal capacitor block after decreasing the voltage at the provided knob. Only if a gentle clicking sound of the relays is perceivable, the shown voltage agrees with the internal voltage. If this sound is not hearable, one has to wait for the voltage to decrease or start one flash without a sample. With the pulse mode button, the sequence of pulses can be scrolled and selected. A single flash with a defined pulse length, a double flash with two different pulse lengths and a certain period, a defined number of pulses (count), and continuous (cont) flashing can be selected. The mode button at the top brings the operator into the Edit mode. Here, the pulse

parameters can be selected. These are the high voltage, which needs to be manually transferred from the displayed number on the red display and entered with the up and down arrow. With the arrow button, the next parameter can be selected, which is the pulse width (width1) that defines the pulse duration of the pulses. If the double mode is selected, the next parameter is width2, the duration of the second pulse. For all pulse modes except single, the period can be set next, which is the time between the pulses including the pulse duration itself. In count mode, the number of pulses can be set last with the count parameter. The values are automatically saved and only if the standard settings shall be changed, the Set button should be pressed. The Mode button can be used to switch to Run mode. Now the sample can be loaded into the process chamber and aligned to the middle of the circles. It is recommended to put a plain white paper on the table. We found that it reduces the variations between substrates of different size and reflectivity if the white paper reflects parts of the incident radiation back towards the reflector. Other researchers have found this, too, and investigated it in detail [181]. After the chamber is closed again, the Trigger button has to be pressed followed by the Start button. The stop button can be used to abort the process, especially for the continuous mode. For all other modes, the process stops automatically. For safety reasons, the trigger should be stopped before opening the chamber.

We recommend drying printed silver and gold layers at a low temperature (e.g. 60 °C) before conducting IPL curing, whereas sinter CuO after a short waiting time without heating. Details can be found in the following subsections.

3.1.3 Sintering of Metallic Particles

After drying of the wet films, the NPs and microparticles form a porous layer that is far from an ideal bulk layer as can be seen in Figure 2.17 and in Figure 2.30 on page 31 and 48. The polycrystalline particles possess a high conductivity comparable to the bulk material, whereas large pores and the contact area between the particles dominate the conductivity of the film. Furthermore, remaining solvent and dispersants decrease the density of the particle film and increase the resistivity. This also applies to a randomly-oriented network of silver nanowires. The small intersections at the crossings are the main cause of the resistance. If the contact areas were increased, the resistance of particles and wires would be considerably lower.

The real processes during sintering in polycrystalline layers are complicated. Thus, the following sections use theoretical assumptions and the **Geometric model** shown in Figure 3.3. First, it is assumed that the particles are perfect spheres of a certain radius r. Especially for inkjet-printed NPs, this can be quite accurate as can be seen in the SEM images of Ag-NPs in Figure 2.17a on page 31. Remaining solvent and dispersants are neglected completely. The resistance of the film mainly originates from the small cross-section of the contact region. This model may include an additional part of the resistance originating from oxidation or contamination of the particle surfaces. [14], [182], [183]

NPs possess high Van-der-Waals or electrostatic forces in regard to their surface area due to their fine particle size. Agglomeration or clustering of the particles occurs that increases the effective radius and create an initial conductivity through the small contact areas. The weak bonding between the particles marked in Figure 3.4a is susceptible and the particles can be relocated or even re-dispersed easily. This leads to a low adhesion among the particles and a high resistance. [14], [50], [184]

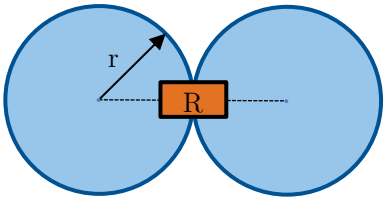

Figure 3.3. Geometric model of the NPs as perfect spheres of radius r that are touching each other and show a resistance R that mainly originates from the small contact region.

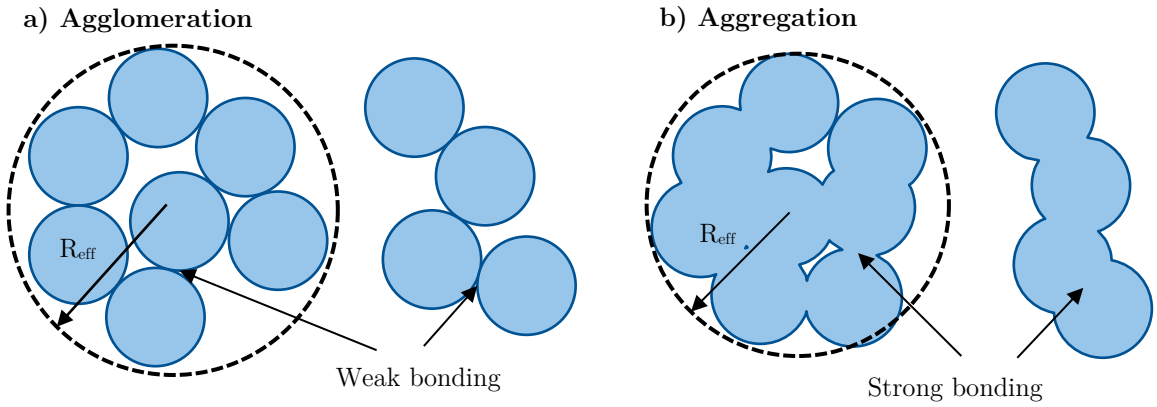

Figure 3.4. Illustration of agglomeration and aggregation and the effective radius R_{eff}. Adapted from [14].

External energy or spontaneous reactions can lead to aggregation of adjacent particles as shown in Figure 3.4b. Solid necks of a certain strength are locating the particles fixed in place by metallic force. Aggregated particles possess continuous conducting levels, which leads to a much lower resistivity. The geometric model with perfect spheres has a maximum packing density of about 74 %. Both agglomeration and aggregation disturb the relocation of a certain amount of particles leading to a lower density and larger pores than in an ideal packing. The goal of sintering is increasing the packing density as well as decreasing the resistance of the contact area between the particles.

The melting point of NPs is considerably lower than for bulk material because of the high surface-to-volume ratio and the corresponding surface area. Many works on different NPs have been done in this field showing a clear decrease for particles in the few-nanometre range. [185]–[189] Most of the works show a significant decrease in diameters below 10 nm down to a few hundred degrees Celsius for particles with a diameter of 2 nm. At higher diameters, only the short work of Asoro et al. shows a measured melting-point depression to about 600 °C for Ag-NPs with a diameter of 40 nm [185]. Kang et al. claim to have measured a melting point depression to less than 200 °C for 20 nm to 40 nm particles with differential scanning calorimetry, but at the same time gives a formula that predicts a much higher melting point [190]. We assume that during sintering, the particles used in this thesis are not melting completely but only on the surface and use other diffusion mechanisms of polycrystalline systems to reduce the surface energy. It is expected that the main cause for starting sintering is the removal of stabilizing molecules from the metal surface and atomic diffusion rather than the melting point depression. This explains that larger particles up to the micrometre range can be sintered. [145]

At the initial stage of thermal sintering, a creation and growth of necks occur between the particles. Matter is transported towards the contact area between particles. This is a favourable process that reduces the free energy of the system, mainly the free surface energy. [14] A creation of necks and, in general, a degeneration of all sharp edges and points reduces the surface area. Most of the processes require an activation energy that can be added to the system by elevated temperature, externally applied pressure or chemical reactions. At low-temperature sintering, the diffusion of the material occurs mainly from the surface of the pattern. The dominating transport mechanisms are surface diffusion (1) on the surface, by lattice diffusion (2) through the particle, or by vapour transport (3) outside of the particle. At higher temperatures, the energy is sufficient to drive significant matter transport from the grain boundaries (4, 5) and dislocate the grains (6). [14], [191], [192] Figure 3.5 illustrates the mentioned transport mechanisms for both temperature regimes. A more detailed differentiation between the different mechanisms can be found in the theses of Bai [14] and Enz [193]. According to the rapid rate sintering theory [191], it is advantageous to use a fast heating rate to bypass the low-temperature effects. They can inhibit an effective sintering even if the temperature is high later on because some bonds were already formed. However, the fast heating may induce a thermal shock to the film and introduce cracks or completely destroy the film.

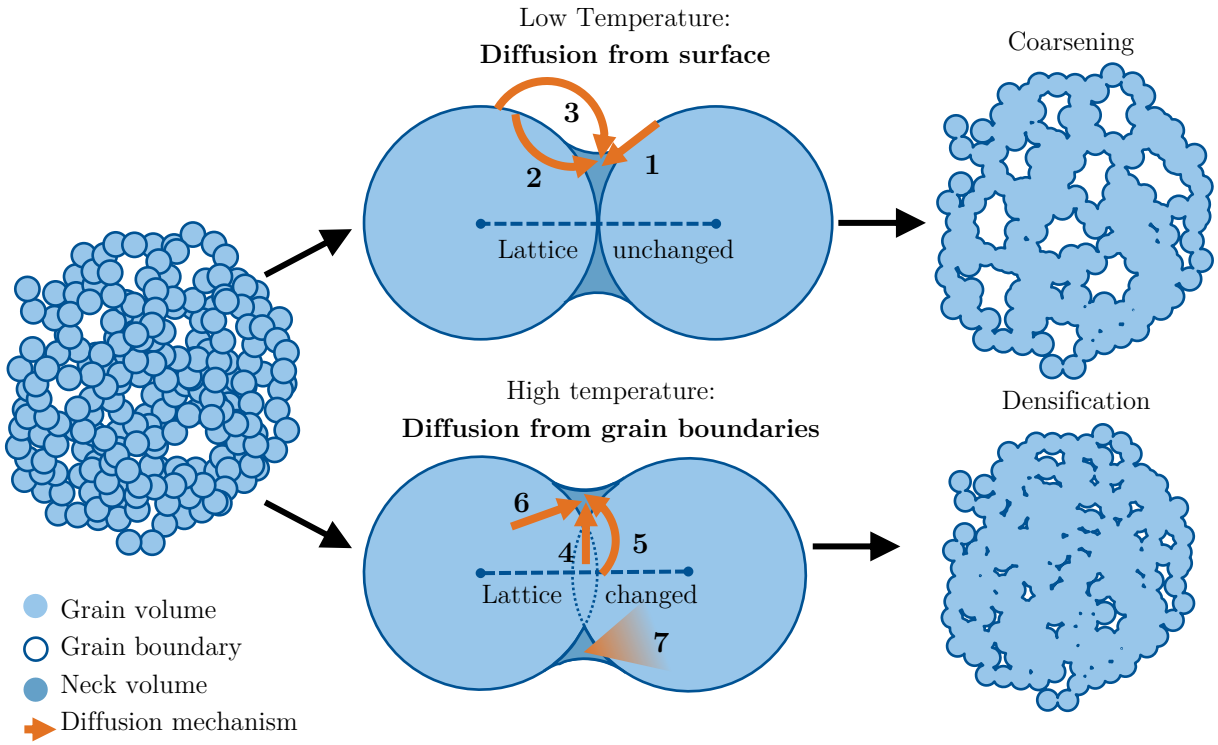

Figure 3.5. Illustration of the seven transport mechanisms (1: Surface diffusion, 2: lattice diffusion, 3: vapour transport, 4,5: grain boundary transport, 6: grain dislocation, 7: bulk-surface diffusion) and their effect on coarsening and densifying diffusion. Adapted from [14], [192].

In the following, the sintering of **Silver and gold-NPs** is investigated. The rapid photonic sintering method is used, which employs intense pulsed light to deliver the heat specifically to the printed layers. The particle geometry was investigated with a scanning electron microscope (SEM) before and after sintering and Figure 3.6 shows the recorded images. The Ag-NPs shown in Figure 3.6a were printed on substrate P7 and imaged after drying at 60 °C for 30 min. The particles are mostly round with a diameter of about 50 nm. The particle size distribution is sharp for the 50 nm range. Some aggregates of several NPs are visible as well that are around 100 nm in size and not as round as the single particles. The particle distribution is homogeneous across the surface and no cracks are visible. The pore size is rather small and the packing density is high.

After IPL sintering with two pulses of 2 ms at a voltage of 2.5 kV, the particle size increases by a factor of approximately 5 as can be seen in Figure 3.6b. Now, the size distribution is larger starting from unsintered particles of 50 nm up to 300 nm aggregates. Especially the larger grains show strong neck creation towards their neighbours. This leads to a variety of particle shapes depending on the number of neighbours. The contact area towards the neighbouring particles is increased. The grain boundaries are still visible by almost straight lines at the necks between them. The larger contact area is the main reason for a higher electrical conductivity. As discussed in Section 2.2.4, the conductivity can be increased by a factor of 10 to 1000, depending on the used substrate and up to 46 % of bulk silver. Not only the grain size increased, but also the pore size increased leading to pores of up to 150 µm. If the sintering energy and power were sufficiently low, no cracks were observed.

Figure 3.6c shows the unsintered Au-NPs inkjet-printed on substrate P4 after drying at 60 °C. The particle size is about 30 nm with a wide size distribution with particles between 20 nm and 40 nm. Some particles are even larger. These are still round, so we assume that the variation during particle growth is rather high and it is not caused by aggregation. The pore sizes between the particles are larger than for the Ag-NPs and can be as large as 100 nm. Before sintering, the Au-NP film is not conductive. The reason is not visible in the SEM images, but we assume that a thin, insulating encapsulation layer in the range of a few nanometres surrounds the NPs. After IPL sintering with a

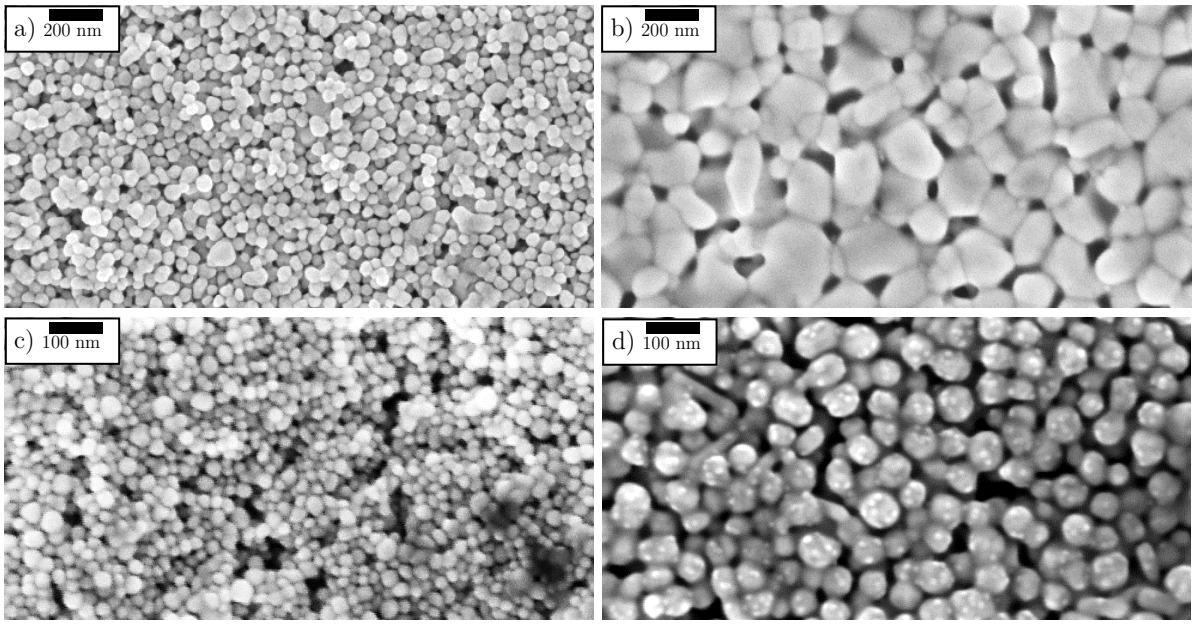

Figure 3.6. SEM images of silver NP ink on substrate P7 a) after drying without sintering and b) after sintering and Au-NP ink on substrate P4 c) after drying without sintering and d) after sintering

2.5 ms pulse at 2.5 kV, the boundaries between the particles disappear and a similar grain growth like for the Ag-NPs is visible. The main difference is the less pronounced necks between the particles. The necks are rather oriented to only one or two other particles, whereas for silver they are oriented to all adjacent particles. The behaviour of the gold electrodes will probably lead to a higher resistance in comparison. Also, the porosity is much higher than for silver. The less effective sintering results also from a difference of around 100 °C in the melting temperatures of silver and gold. Silver melts at around 960 °C and gold at 1.060 °C. Therefore, AuNPs require a higher sintering energy.

We want to discuss exemplary on these two materials how to identify the ideal sintering parameters that lower the sheet resistance as well as avoid a destruction of the thin film. The parameter set of the employed photonic sintering tool is the high voltage setting U_{HV}, the pulse duration t_{Pulse} and the number of pulses. We will discuss the sintering parameter optimization on the example of Ag-NPs first in detail and then for Au-NPs rather short, because the results are similar and we had less samples to optimize the parameters. The silver and Au-NP films regarded in the following were printed with the Epson printer on the photo paper P7 and P4, dried for 30 min at 60 °C in the oven and then sintered with varying sintering conditions. The voltage was set at five equidistant voltage levels between 2 kV and 3 kV and the pulse duration was changed in steps from 250 µs up to 3000 µs. These are the minimal and maximal allowed voltage and the maximum pulse duration.

Inkjet-Printed Ag-NPs - For each sample, the sheet resistance was measured and is shown as markers in Figure 3.7a. The five different colours indicate the sintering at different voltages which corresponds to a non-linear increase in power. At combinations of a high voltage and a long pulse duration, the samples were destroyed, which is indicated by vertical lines in the respective colour. Below these values, the samples remained conductive with lower values for higher voltages and higher pulse durations. The lowest sheet resistances of 82 mΩ/sq and 88 mΩ/sq were obtained for one pulse of 2000 µs at 2.75 kV and 2.50 kV, respectively. A clear relation between the pulse duration t_{Pulse} and the measured sheet resistance R_S was found in form of an exponentially decaying relation with offset according to Eq. 3.4. The parameters a, b, and c were chosen positive and the best fit curve for each voltage setting is drawn as a continuous lines of the same colour in Figure 3.7a.

$$R_S = a \cdot \exp(-b \cdot t_{Pulse}) + c \qquad \text{Eq. 3.4}$$

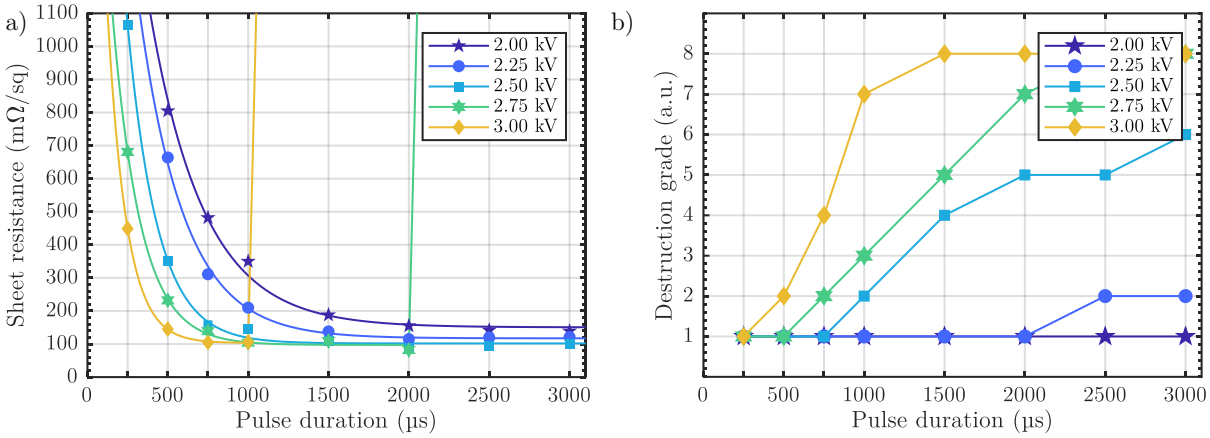

Figure 3.7. a) Sheet resistance and b) destruction grade of IPL-sintered Ag-NPs depending on the pulse duration and the lamp voltage. Adapted from [194].

At a certain pulse duration for both highest voltages, the samples were completely destroyed and the film was detached. It was impossible to measure the sheet resistance, which is shown in the figure by steep lines, e.g. for 3.00 kV at 1000 µs. Also, samples sintered at a lower power were damaged. Thus, the destruction grade of the samples was simultaneously evaluated. For the Ag-NP films, round blow-ups are the main occurrence of destruction in the film. The maximum diameter of these damages according to the third column of Table 3.1 was determined and used as a destruction criterion. It ranges from 1 to 8 and is based on visual inspection of the film after sintering. The lowest destruction grade 1 indicates visually perfectly intact structures all over the test pattern. The following destruction grades 2 – 6 indicate minor, medium, or severe damages to the patterns according to the size of the damages. Destruction level 7 is given to samples that are destroyed but still enough silver is left on the surface to measure the sheet resistance. If not enough silver is left, the samples is graded with 8.

Figure 3.7b shows the rating of each sample for different voltages and pulse durations. A clear increase of the destruction for longer pulses can be seen for high voltages, whereas sintering at low voltages allows much longer pulses without destroying the silver film. For 2.00 kV, all pulse lengths leave the pattern intact, for 2.25 kV minor damages appear above 2000 µs pulse length. For 2.50 kV, only short pulses of 750 µs and below leave the pattern intact and for higher voltages, the destruction curve is shifted further to lower pulse durations.

Table 3.1. Destruction grading for the evaluation of the destruction of inkjet-printed metal NP films after intense pulse light sintering.

Grade.	Wording	Silver	Gold	CuO
1	Visually perfect structures over the entire test pattern.			
2	Minor damages	Ø ≤ 50 µm	Ø ≤ 50 µm	w ≤ 50 µm
3	Medium damages	Ø ≤ 100 µm	Ø ≤ 100 µm	w ≤ 100 µm
4	Medium damages	Ø ≤ 200 µm	Ø ≤ 200 µm	w ≤ 200 µm
5	Severe damages	Ø ≤ 300 µm	Ø ≤ 300 µm	w ≤ 300 µm
6	Severe damages	Ø ≤ 500 µm	Ø ≤ 500 µm	w ≤ 500 µm
7	Destroyed	Ø > 500 µm	Ø > 500 µm	w > 500 µm
8	Complete destruction and/or detaching of the film			

The lowest value for each power is below 140 mΩ/sq, indicating that a higher voltage can compensate shorter pulse duration. A shorter pulse duration means, that a certain power of the lamp is applied for a shorter time. According to the manual of the photonic sintering tool, the electric energy of one pulse can be derived from Eq. 3.3 on page 69. It shows that the output power is constant over the pulse duration and at a fixed voltage, the energy output directly depends on the pulse duration. This formula also shows that the power to the lamp is 353 kW, 462 kW, 589 kW, 734 kW, and 896 kW for the voltages used here.

When comparing the sheet resistance R_S and the pulse energy E_{Pulse} of the first pulse, we found an overlap between the individual curves for the different power values. The only exception are the energy and power levels that completely destroy the patterns. The relation follows Eq. 3.5 with the parameters $a = 3.27\,\Omega/\mathrm{sq}$, $b = 8.66\,kJ^{-1}$, and $c = 0.115\,\Omega/\mathrm{sq}$. This relation is visualized in Figure 3.8a as a dashed red line in comparison with the sheet resistance curves of different lamp powers.

$$R_S = a \cdot \exp(-b \cdot E_{Pulse}) + c \qquad \text{Eq. 3.5}$$

Similarly, a relation between the energy and the destruction grade can be made. At low powers, no destruction occurs until a pulse energy of a bit more than 1000 J. At higher powers, this is shifted to a value lower than 500 J as shown in Figure 3.8b.

The resistivity and the grade of intactness of the sample are two important criteria for the sintering of printed electronics. However, they are contradicting. The sheet resistance can even be low on a quite destroyed sample. For large printed areas, it may be favourable to have a lower resistance with some minor damages whereas, for fine patterns, this can lead to malfunctioning.

Here we suggest a simple figure of merit for a comparative quality rating in a set of sintered samples that accounts for a low sheet resistance and a low destruction grade at the same time. The quality rating Q is calculated as the sheet resistance R_S normalized to the minimum sheet resistance multiplied with the destruction grade D according to Eq. 3.6. The lower the quality rating, the better compromise was found between the two criteria. This criterion assumes, that the intactness of the thinnest line (D=1) is equally important as halving the resistance. Ideally, the quality rating is equal to 1. For other applications, the weighting exponents a and b can be modified to better fit the desired properties.

$$Q = \left(\frac{R_S}{\min(R_S)}\right)^a \cdot D^b \qquad \text{Eq. 3.6}$$

Following this figure of merit, Figure 3.9 was created. It shows that there are two ideal energy regions that may be used for to obtain intact and highly-conductive structures. For low powers with a lamp voltage of 2.25 kV or below, it is the region around 1000 J pulse energy, that is equivalent to

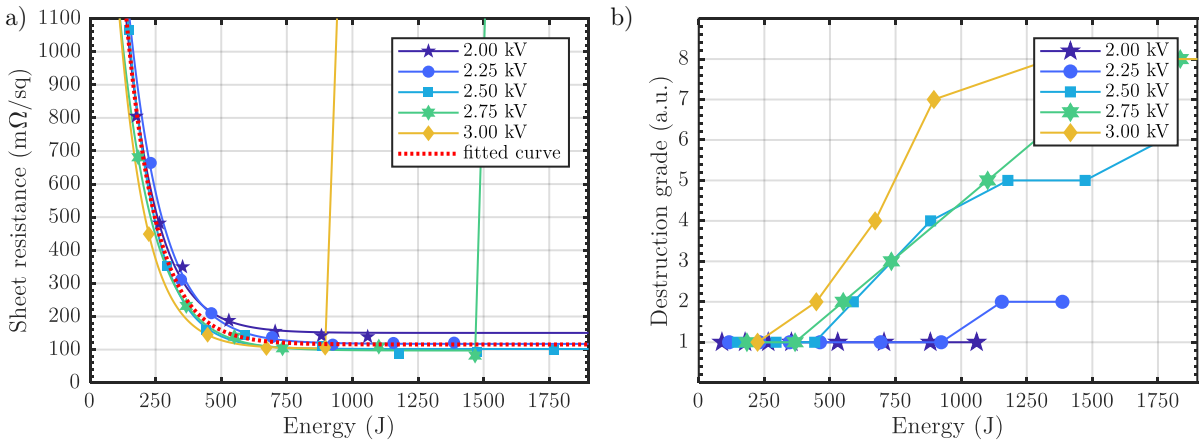

Figure 3.8. a) Sheet resistance and b) destruction grade of IPL-sintered Ag-NPs depending on the pulse energy and the lamp voltage. Adapted from [194].

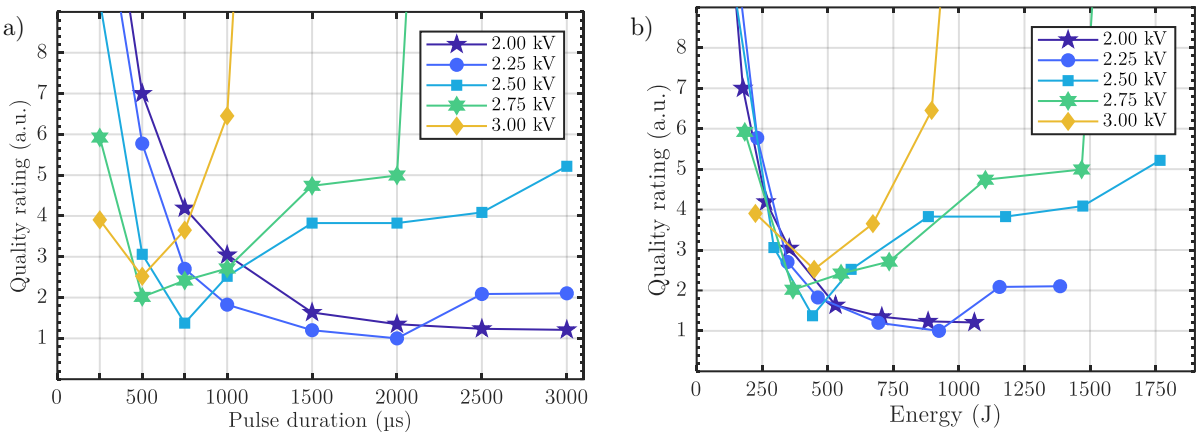

Figure 3.9. Quality rating of IPL-sintered Ag-NPs for different lamp powers and different a) pulse durations and b) pulse energies. Adapted from [194].

a pulse duration of 3000 µs and 2000 µs for 2 kV and 2.25 kV, respectively. For medium and high powers using a lamp voltage of 2.5 kV and above, a pulse energy around 400 J is ideal. This equates to a pulse duration of 750 µs for 2.5 kV and 500 µs for 2.75 kV. A higher lamp voltage does not improve these results.

Until now, we only showed results for the first flash. It was shown previously, that additional flashes can improve the conductivity even more [195]. We investigated this for samples that were already sintered at the ideal pulse durations for 2.75 kV and 2.5 kV, namely 750 µs and 500 µs, respectively. The pulse duration of the second pulse was then increased from these values up to 3000 µs. It was possible to reduce the sheet resistances to values down to 90 mΩ/sq, which is a reduction of 61 % or 43 % compared to the resistance value measured after only one pulse. Again, a clear decrease of sheet resistance is visible from the data in Figure 3.10a. The Ag-NP film that was already sintered with a short first pulse showed to be much more resistant to destruction during the second pulse. Figure 3.10b shows that even 3000 µs pulses did not destroy the film at 2.5 kV and no damage occurred for pulses up to 1000 µs at a voltage of 2.75 kV.

The sample sintered at 2.50 kV for 750 µs followed by a 3000 µs pulse showed a sheet resistance of 89.8 mΩ/sq without any damage. Thus, these are the recommended sintering parameters for this photo paper. We found that additional pulses do not decrease the sheet resistance anymore. These parameters are not directly transferable to other substrates. The size of the substrate and the percentage of the silver-covered area play a role as well. Thus, it is recommended to use a white sheet of paper or even a mirror on the table in the Sinteron to compensate the reflected light for smaller sample sizes.

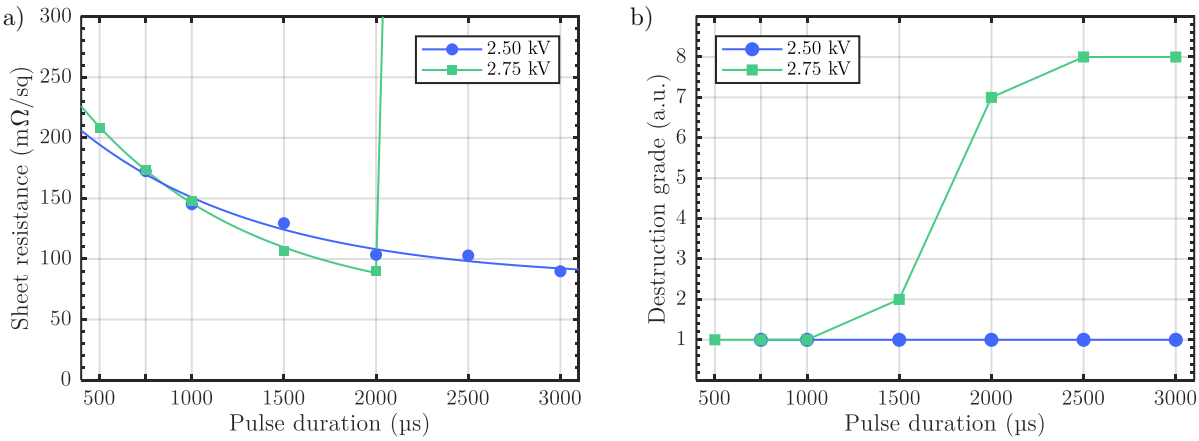

Figure 3.10. a) Sheet resistance and b) destruction grade of IPL-sintered Ag-NPs for a second pulse at the two voltages after a first pulse of 750 µs for 2.50 kV and 500 µs for 2.75 kV, respectively.

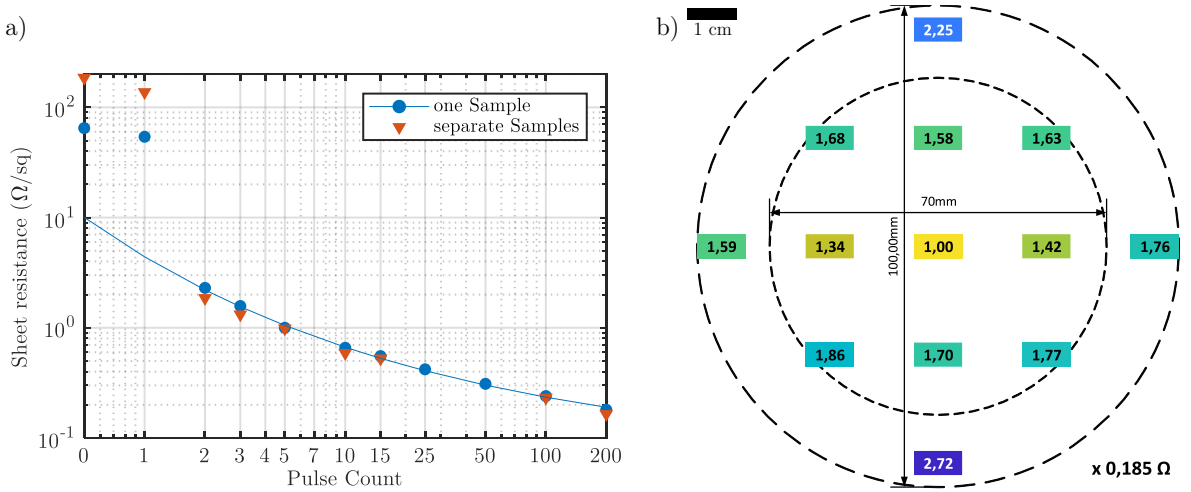

Figure 3.11. a) The sheet resistance of IPL-sintered Ag-NPs after a certain number of 500 µs pulses at 2.50 kV. Blue markers show the sheet resistance of one sample that was alternately measured and sintered. The blue line Red shows the measurement of 9 samples that were sintered with a 3 s pause between the pulses. b) Influence of the position on the sample holder on the sheet resistance due to inhomogeneous illumination.

A general rule to find the sintering parameter is picking a medium to high voltage (e.g. 2.50 kV) and decrease the pulse duration starting at a long pulse duration until no damages occur. Then a second pulse can be conducted with the same strategy. A more practical solution to sinter unknown substrates is also to increase in the number of pulses. The blue markers in Figure 3.11a show the sheet resistance of a sample that was alternately measured and then sintered with 500 µs pulses at 2.50 kV. The absolute values are not comparable as the sample was not dried in an oven before and no white background paper was used. The first pulse seems to evaporate the solvents but not sinter the sample. The second pulse drastically decreases the sheet resistance and all further pulses decreased it further down to 180 mΩ/sq. Drying and the ideal sintering parameters are crucial to obtaining low resistance values. This behaviour is in accordance with Klokkenburg et al. [195]

The time delay between the pulses seems to be irrelevant as long as they are long enough. The red markers in Figure 3.11a show 9 individual samples that were sintered at the same parameters but with a fixed period of 1 ms. The resistance values match closely to the ones of the single sample that was alternately sintered and measured with a longer pulse period. The minimum period of the Sinteron still seems to be long enough to cool down the entire film.

The illumination of the chamber is crucial. The manual of the Sinteron shows already, that it is not homogeneous across the process table. Figure 3.11b shows the sheet resistance values measured at different positions in the chamber and a large deviation was found. It is suggested to use samples with a width of less than 50 mm. For long samples, it may be helpful to reduce the sintering power and sinter at two different positions to average the inhomogeneous illumination.

Inkjet-Printed Au-NPs - For Au-NPs, a similar optimization scheme was conducted. The main difference was, that it is necessary to sinter the patterns as they are not conductive after drying only. Unfortunately, we did not have enough samples to conduct an as detailed analysis as for the Ag-NPs. The lowest sheet resistance that we achieved was 435 mΩ/sq. With a thickness of 193 µm, this is would result in a conductivity of about 29.1 % of the bulk conductivity. For some voltages, the same exponentially decaying relation between the sheet resistance and the pulse duration or the energy was found and is shown as fitted curves in Figure 3.12. For 2.00 kV and 2.75 kV, the sheet resistances were higher for a longer pulse duration. We assume that this rather originates from the thickness of the gold film and the pattern shown by the fitted curves applies to these two voltage values as well. Figure 3.12b shows that the relation between the sheet resistance to the electric power to the flash lamp is not as defined as for the Ag-NPs and the measured values shown as markers are distributed around the dashed fitted curve.

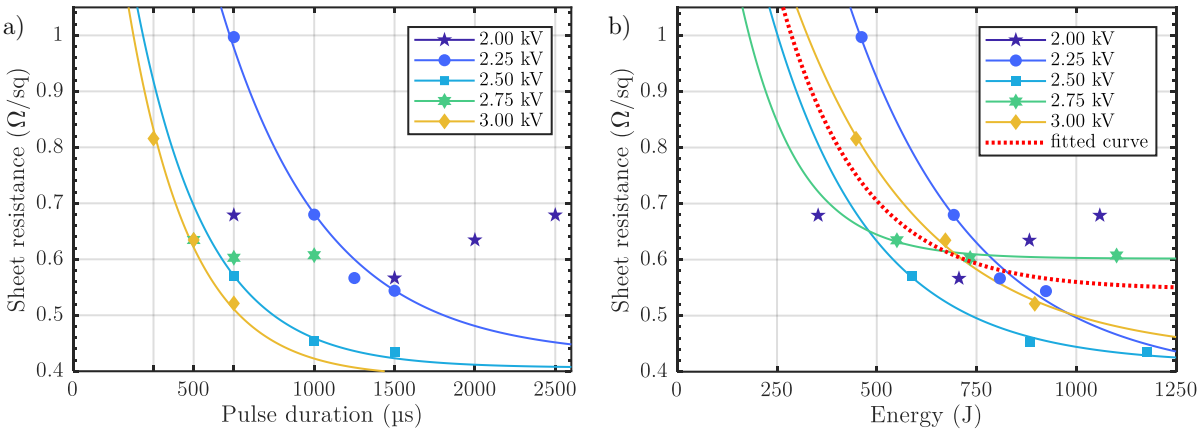

Figure 3.12. The sheet resistance of IPL-sintered Au-NPs and depending on a) the pulse duration and b) the electrical energy to the lamp.

The required pulse energies for AuNPs in comparison to AgNPs and is in accordance with the considerably higher melting point. The Au-NP films were destroyed by too high powers or too high pulse energies, too. Figure 3.13a shows the destruction grades for all measured samples. For voltages of 2.5 kV and above, damages can occur already at pulse durations below 1 ms. For lower voltages, the samples remain intact for a pulse duration up to 2.5 ms. None of our samples was destroyed completely because we tried to stay around the ideal sintering parameters and avoided high voltage and high pulse duration simultaneously. We expect a complete destruction at high powers and durations similar to the silver nanoparticle film The quality rating was calculated according to Eq. 3.6 with a = 2 and is shown in Figure 3.13b. This figure of merit shows that a lower voltage is more favourable with 2.00 kV leading to the best values. Hence, we recommend this voltage and a pulse duration of 2 ms. We expect that a second and more pulses following a non-destructive pulse can reduce the sheet resistance even more.

Screen-Printed Silver - The screen-printable micro-flakes paste ECI 1010 E&C and nano-flakes paste ECI 1010 E&C of Loctite (Henkel) were printed on a PET film and also investigated before and after photonic sintering. The resistance after drying for 60 min at 100 °C was 544 mΩ/sq for the micro-flakes paste and 31.9 mΩ/sq for the nano-flakes paste. The heights of the layers were 5.2 µm and 4.4 µm, respectively. This shows, that the resistance of the pastes is considerably higher than the manufacturer claims in the datasheets, which should be 7.3 mΩ/sq and 2.9 mΩ/sq, respectively, for these thicknesses. We think that this originates from an incomplete drying of the layer and that the binder matrix did not sufficiently develop. The PET film that we used was stable up to about 120 °C, so we could not increase the temperature to the recommended 150 °C. Therefore, we want to investigate, if photonic sintering is able to process the screen-printed films to achieve such a low resistivity also on heat-sensitive substrates.

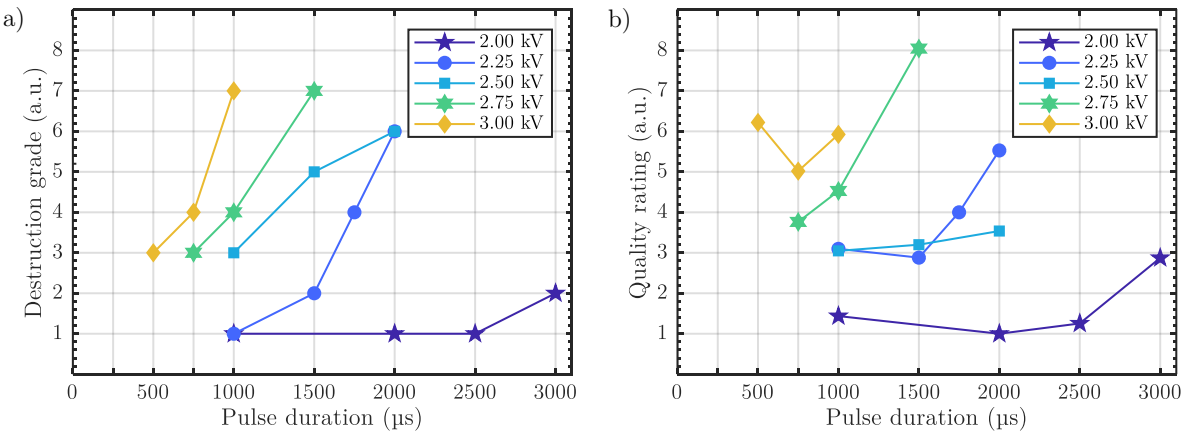

Figure 3.13. a) Destruction grade and b) quality rating of IPL-sintered Au-NPs depending on the pulse.

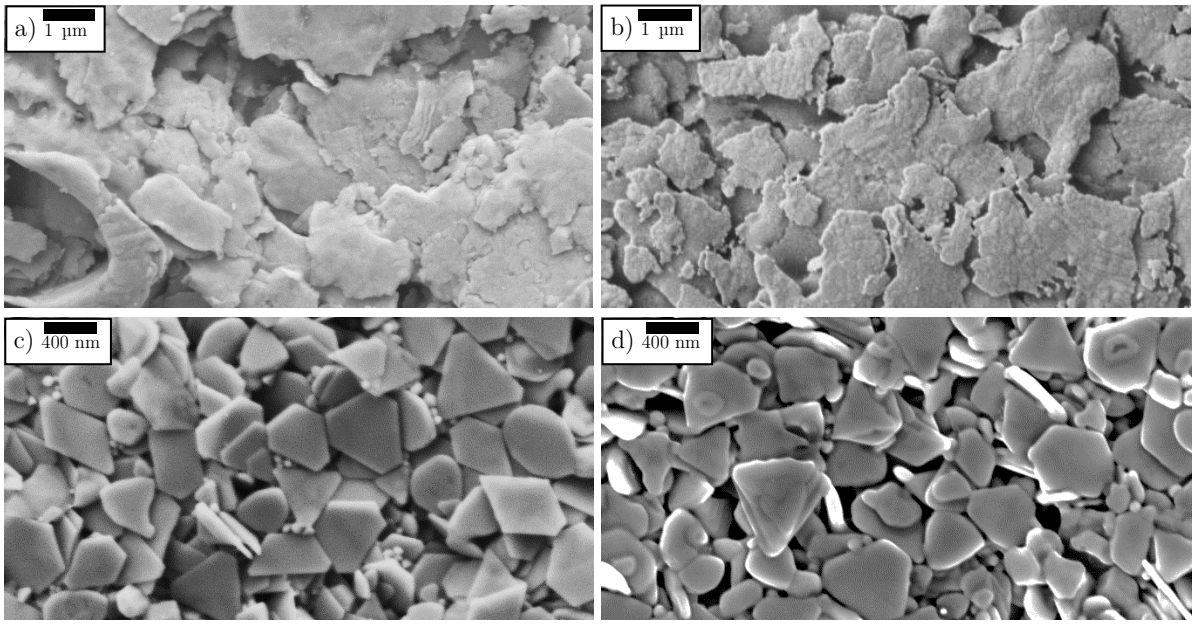

Figure 3.14. Screen-printed silver pastes before and after sintering. a) Micro-flakes paste after drying and b) after strong IPL sintering. c) Nano-flakes paste after drying and d) after strong IPL sintering.

To investigate the morphological changes within the inks, we recorded SEM images that are shown in Figure 3.14. The left images show the two non-sintered silver pastes ECI 1010 and ECI 1011 and the right images show them after strong sintering. For the micro-flakes paste, no major transition can be found. Still, we have the impression that the distribution got more homogeneous after sintering and the amount of perpendicular oriented particles on the surface decreases. This may occur because such particles are not well connected to the rest of the film and thus are heated much more because the heat conduction paths are limited. This leads to a modification in their shape. A contact to other particles is favourable because then the heat can be conducted away and the particle cools down at this position. In the nanoflakes paste, a real transformation is visible. The completely flat nanoflakes before sintering turn into more round and bend flakes after sintering. Furthermore, neck-creation can be observed. We only conducted one flash on both pastes and expect that a higher number would lead to a more pronounced change in morphology.

Figure 3.15a shows that the resistance of the micro-flakes paste can be drastically reduced towards the given value. A clear dependence on the energy was found and is shown in the inset. The lowest values that we measured are even lower than the value from the datasheet. However, our measurement setup is not suitable for such small resistances and the noise level is high. Furthermore, the

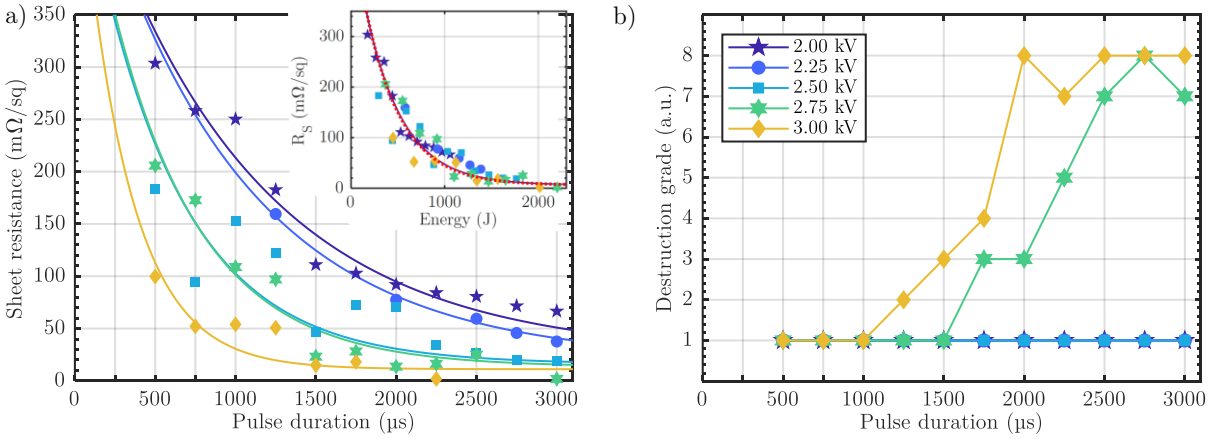

Figure 3.15. a) Sheet resistance and b) destruction grade of screen-printed silver micro-flakes after IPL-sintered depending on the pulse duration. The inset shows the dependency of the sheet resistance over the energy to the lamp. The legend in (b) applies to all graphs.

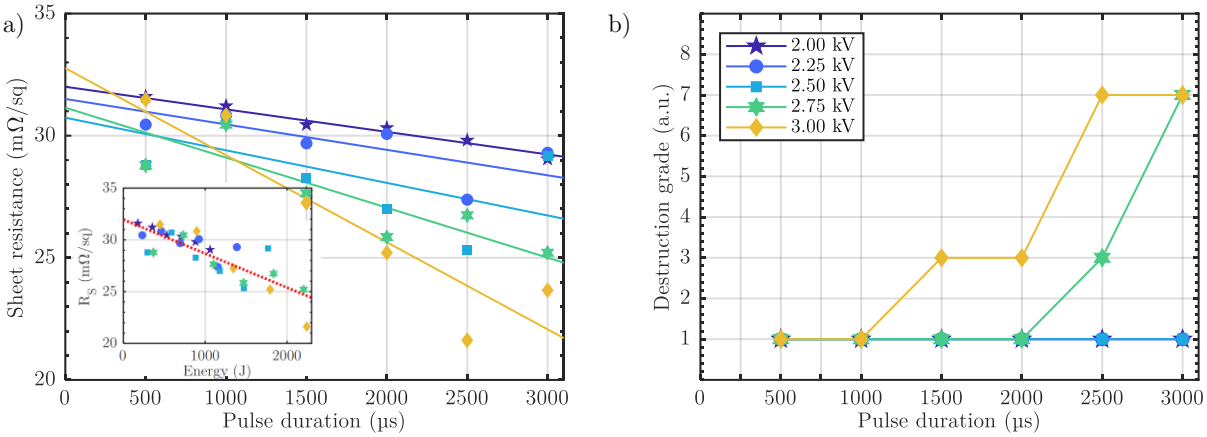

Figure 3.16. a) Sheet resistance and b) destruction grade of screen-printed silver nano-flakes after IPL-sintered depending on the pulse duration. The inset shows the dependency of the sheet resistance over the energy to the lamp. The legend in (b) applies to all graphs.

voltages of 2.75 kV and above as can be seen in Figure 3.15b. We recommend long sintering times (3 ms or even longer if the device allows) at medium power around 2.5 kV.

The screen-printable nanoflakes paste ECI 1011 did not reduce its resistance significantly. The lowest resistance without destroying the sample is about 25 mΩ/sq and more than eight times higher than predicted in the datasheet. Figure 3.16 shows the resistance and the destruction grades for different pulse durations at different voltages and in the inset the sheet resistance depending on the energy to the lamp.

In general, screen-printing pastes can bear a much higher energy before showing damages. This is related to the thicker film and its higher heat capacity. IPL sintering is a suitable method to decrease the resistance of screen-printed patterns on heat-sensitive substrates, especially for the micro-flakes paste. However, the resulting resistance after only one pulse is still much higher than the bulk resistance. The ideal sintering parameters are long pulses at medium powers. We were limited by the maximum pulse length of the IPL equipment and could not reach pulse durations above 3 ms. Multiple pulses may help to reduce the sheet resistance as we have shown for the NP inkjet inks.

3.1.4 Triggering of Chemical Reactions

Intense pulsed light (IPL) can be also used to rapidly trigger chemical reactions. This can be as simple as cleaning or sterilizing surfaces by burning all organic material. Furthermore, IPL is used to destroy the DNA of bacteria in water and for food preservation [196]. Medical use of IPL involves sterilization of pharmaceuticals and medical devices [196], as well as treatments for the removal of hair and tattoos [197] as well as the rejuvenation of photo-damaged skin [198]. In the field of printed electronics, IPL can trigger chemical reactions in the printed film. Novacentrix, a major producer of IPL systems, produces inkjet printing inks and screen printing pastes that contain fully oxidized CuO that can be converted to copper by IPL sintering. This avoids the typical problem with the high surface energy at printing copper which is the oxidation of the small particles. [199] The inks and pastes containing copper oxide are stable for a long time because the non-noble metal is already oxidized. It is not exactly clear how this reduction of copper exactly works, but in literature the work of Ryu et al. gives some insight. They describe that CuO-NPs coated with photo-reactive polymers can be reduced by intense light in an alcoholic environment. The reducing agents may be intermediate acid created by UV light or hydroxyl end-groups that are long-chain alcohol reductants. [200]

In this thesis, the sintering of inkjet-printed copper oxide NP layers is investigated. Figure 3.17a shows an SEM image of a completely dried CuO film. The film consists of CuO flakes of about 120 µm size as indicated in the datasheet of the ink. Due to the low conductivity of the film, some

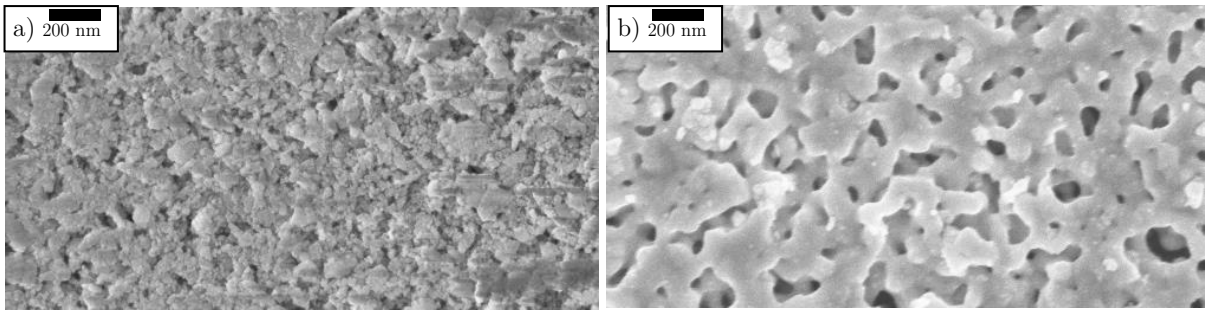

Figure 3.17. SEM image of a) an inkjet-printed CuO layer after drying and b) the IPL sintered film.

artefacts are visible in the image. Still, it shows a rather flat and homogeneous film that consists of flakes and probably other remaining ink components or their degradation products. A single pulse from the flash lamp changes the structure massively as shown in Figure 3.17b. A sponge-like, porous network of copper has been formed. In comparison to the sintered silver-based inks, no individual particles are visible. The necks around the pores are wide and only a small variation across the image is visible.

The influence of the first pulse on the sheet resistance of printed film on a porous substrate was studied. The samples were dried for 30 min at room temperature according to the findings of Paquet et al. [175] although we could not find any influence of a longer or shorter waiting time. It was found, that considerably higher sintering powers are necessary to turn the dark copper oxide layer into a copper-coloured and conductive film. This originates partially from the about 125 °C higher melting point of copper in comparison to silver and the necessary energy to drive the reduction of CuO to copper. Figure 3.18a shows, among others, the two continuous curves for 2.75 kV (blue) and 3.00 kV (green). For both voltages, a pulse duration of at least 1500 µs and 2000 µs, respectively, was necessary to achieve sheet resistances of about 400 mΩ/sq. This is higher in comparison to the silver layers, which partially originates from a lower film thickness of only 212 nm. In contrast to the results of sintering of noble-metals, a further increase of the pulse width did not show a considerably lower sheet resistance. The sheet resistance at higher pulse durations remains constant, which indicates that a certain energy is required to convert CuO to copper and all additional energy is wasted.

Figure 3.18a shows also the results of sintering with two consecutive pulses at a time delay of 1 s. These are marked in the legend by an “x 2” and are plotted with dashed lines. They show that with a second pulse, it is possible to employ a lower voltage, e.g. 2.50 kV, or a shorter pulse duration for the two higher tested voltages. However, for the same voltage and pulse duration, a second pulse was detrimental in most cases. Figure 3.18b shows the same results plotted over the energy showing that a minimum energy of about 1300 kJ for one pulse and about 800 J for two pulses is necessary to

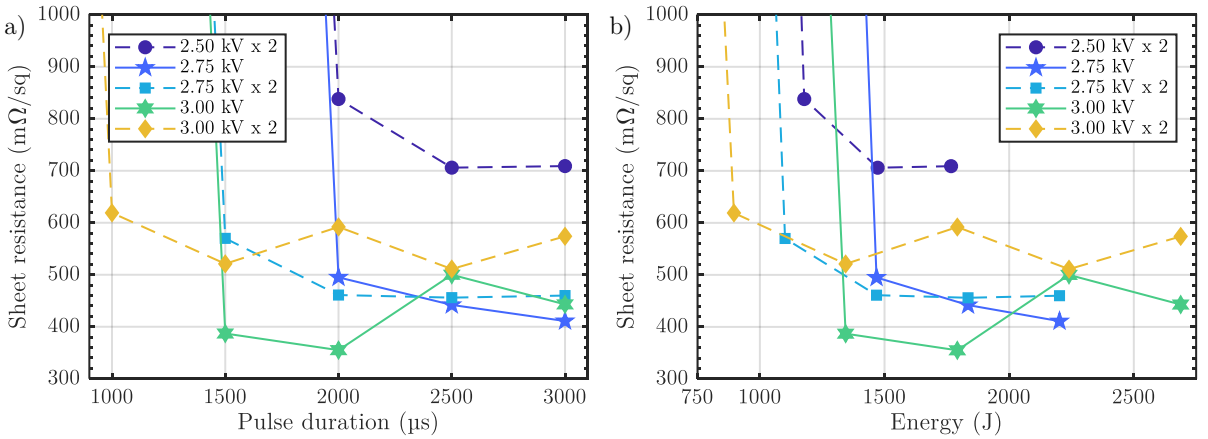

Figure 3.18. The sheet resistance of inkjet-printed CuO-NP films sintered at different conditions with regard to a) the pulse duration and b) the pulse energy. Some samples were sintered with one pulse and some with two pulses, which is indicated by “x 2” in the legend.

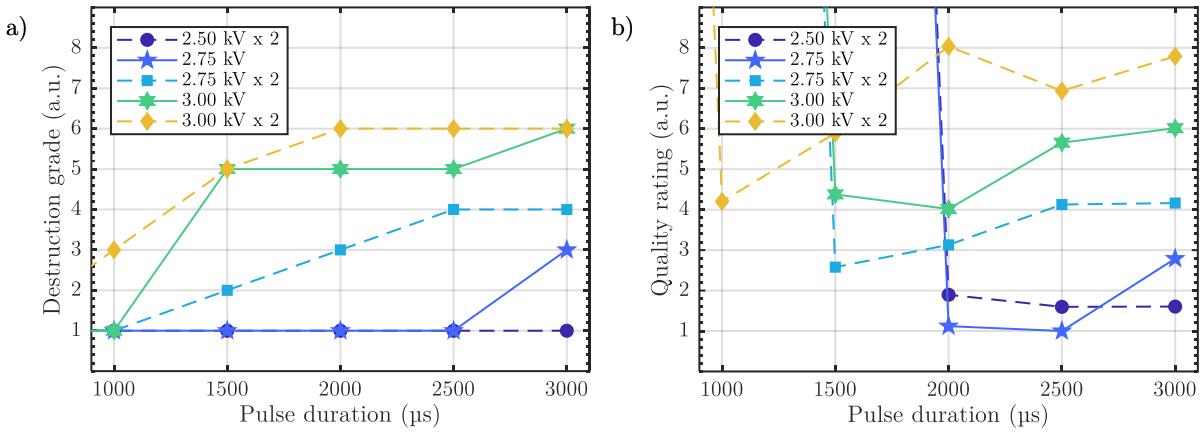

Figure 3.19. a) Destruction grade and b) Quality rating of the CuO films sintered at different conditions. Some samples were sintered with one pulse and some with two pulses, which is indicated by "x 2" in the legend.

trigger the conversion. Energies higher than this threshold do not decrease the sheet resistance any further.

Too high sintering energy and power damage the copper film. In comparison to AgNP and AuNP, the maximum energy of our photonic sintering tool is not sufficient to completely destroy or detach the metal film. The damage to the printed film occurs only at the edges of the copper pattern, which destroys fine lines. This is probably related to the excess of energy at the edges where the heat cannot flow to other regions of the pattern. The damaged parts are not detached but show a matte orange colour instead of the shiny copper colour. A second pulse or any further number of pulses continue the destruction of the edges.

Only sintering with one pulse at 2.75 kV and two pulses at 2.50 kV left the sample intact and conductive. Figure 3.19b shows the quality rating according to Eq. 3.6 and shows that the mentioned settings are a good compromise for low sheet resistance and low damage. We recommend one pulse with a duration between 2000 µs and 2500 µs at a voltage of 2.75 kV for an intact and highly-conductive copper layer. In general, the lowest pulse duration the drives the CuO reduction was found the most suitable. As the damages only occur on the edges of the patterns, it may be favourable for large patterns to obtain a lower sheet resistance and accept a damaged edge of a few hundred micrometres. Then, a sintering with one 1500 µs pulse at 3.00 kV is recommended.

3.1.5 Promotion of Adhesion

Printed patterns often exhibit a rather low adhesion to the substrate. Especially inks under development do contain no or little binder that fixes the particle or the film onto the substrate. Even if the ink contains a binder, the temperature during drying may not be sufficient to harden it. Intense pulsed light (IPL) sintering has been shown to improve the adhesion in both cases. Jiu et al. showed in two papers that silver nanowires on PET or PVC can be effectively sintered with IPL. At the same time, the polymer film is locally heated at the contact areas with the silver nanowires by a heat transfer from them. This leads to local embedding of AgNWs into the polymer film. Without photonic sintering and at low energy densities, the film could be peeled off easily with a firmly pressed adhesive 810 Scotch tape of 3M. In contrast to after IPL sintering at higher energy densities, the film was stable and did not change its resistance even after ten peeling tests. High powers, however, can lead to a degradation of the polymer substrates similar to overheating. On other polymers like PI and PC and on glass, the sintering effect can be observed, but the adhesion is not significantly increased because the created temperature is not sufficient to melt the surface area. [201], [202]

Our experiments showed that the adhesion of silver nanowires on PET and PP can be improved significantly. Before IPL-curing all films were destroyed in major parts after only one peeling. After

sintering with high powers (a voltage of 3.0 kV) and long pulses of 2 ms, the thin film of wires could withstand at least 10 peeling cycles without a significant increase in resistance. The detailed results can be found in the dissertation of Marco Bobinger [141].

3.1.6 Comparison

We could show, that we can sinter Ag-NPs to conductivities of about 42 % with respect to the bulk conductivity, Au-NPs to 29 %, and copper NPs to 23 %. These values were calculated using the thickness of the film. If only the calculated amount of metal (see Section 2.2.3) is taken into account, the conductivities are up to 81 ± 18 %, 46 ± 10 %, and 45 ± 9 % for silver, gold, and copper, respectively. The large uncertainty originates from the weighting of the small ink volume. For the screen-printed layers, we could not calculate the conductivity reliably, because the smallest measured sheet resistances have a large uncertainty and the samples are rough. By estimations, we are ranging in the high two-digit percentage, too. In comparison to other researchers, these values are the highest or rank among the highest [64], [152], [157], [160], [175], [177]. For screen-printed silver, there are only few references in literature that used other curing methods than thermal curing, but it is in use in the industry already. We reached the indicated conductivities in the datasheets with a lower drying temperature followed by IPL sintering. This shows that IPL curing is able to achieve highly-conductive patterns on temperature-sensitive substrates.

3.2 Transparent Conductive Patterns

During the work of this thesis, different transparent conductive patterns have been printed with inkjet-printing, screen-printing, and spray-deposition. To form a transparent layer, the films must be sufficiently thin and homogeneous. A few different approaches can be found in the literature and a complete review was done by Hecht et al. [203]. The traditional approach employs tin-doped indium oxide (ITO) coated films that forms cracks already at a strain of about 1 %, which is equivalent to a bending of a 100 µm thick polymer film at a bending radius of 10 cm. [204] Thin metal films of less than 20 nm thickness are transparent, flexible, and stretchable to some extent. [203], [205] Another approach is the formation of metal grids or other metallic structures that have a sufficiently high opening ratio. [143], [206] Transparent polymers like PEDOT:PSS [207], [208] and polyaniline (PAni) [209]–[211] with their slight blue and green tinge, respectively, as well as carbon-based materials like graphene [212]–[214] can be deposited in thin films. The thickness of the film is important and needs to be homogeneous to avoid visible edges. [203] Furthermore, randomly arranged networks of metal nanowires [22], [118], [119], [142], [215], [216] or carbon nanotubes [58], [143], [217], [218] are transparent and conductive when the percolation threshold is exceeded. At last, hybrid materials made of a combination of two or more of the mentioned materials can combine the advantages of them. A prominent example is the use of PEDOT:PSS as a conductive smoothing layer on top of a nanowire layer. [203]

3.2.1 Transmittance and Sheet Resistance

We spray deposited the three materials onto a glass slide to measure the optical and electrical properties on the created thin films. By visual inspection, all thin films produced in this work showed more or less the same transparency, with silver nanowires and carbon nanotubes forming a rather grey film and PEDOT:PSS a blue layer on transparent substrates. All materials had to be sprayed in multiple layers to achieve a conductive film. Therefore, the automatic spray robot was programmed to spray multiple times across a glass substrate. The transparency of 10 layers of each material was measured on glass and is shown in Figure 3.20a. The CNT layer shows the highest transparency in

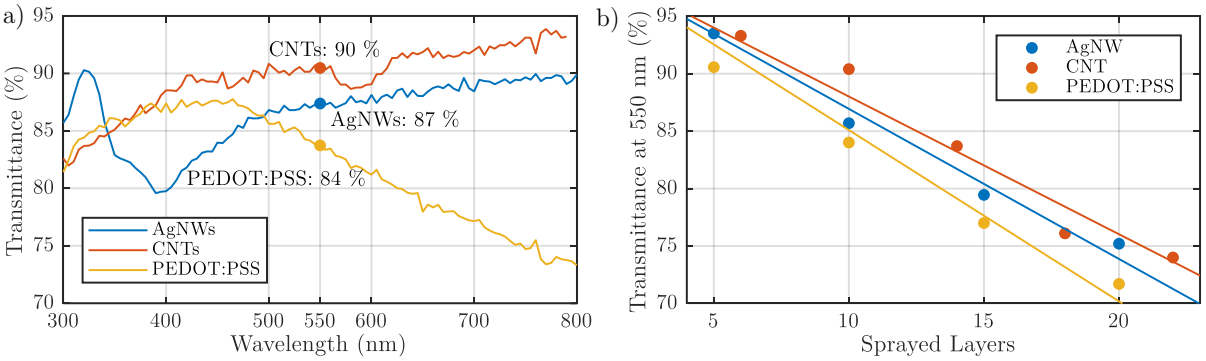

Figure 3.20. a) Transparency of 10 layers of silver nanowires (AgNWs), carbon nanotubes (CNTs), and PEDOT:PSS in the visible range. Adapted from [22]. b) Dependence of transparency on the number of layers.

the visible range with an almost constant transparency throughout the visible range. The transparency at the maximum sensitivity of the human eye in the green region at 550 nm was about 90 %. Silver nanowires reach a lower value of 87 % at 550 nm and a clear dip in the transmittance curve in the blue and near ultraviolet range. The bluish appearance of PEDOT:PSS results from a lower transmission of yellow and red light that also reduces its transmittance at 550 nm to only 84 %. These values are comparable to literature and show, that CNTs and AgNWs are a feasible solution to reach transparent electrodes also in the infrared region, where ITO and PEDOT:PSS are almost opaque. [141], [216], [219]

The average thickness of the layers measured with a surface profilometer is 98 nm, 267 nm, and 248 nm for AgNWs, CNTs, and PEDOT:PSS, respectively. AgNWs show a high surface roughness higher than the film thickness. However, the surface profilometer is not a suitable tool to measure the thickness of AgNWs and CNTs as the tip may not reach the openings between the wires. Still, it gives a rough idea about the thickness of the films.

Figure 3.20b shows that the transparency depends on the number of sprayed layers. The expected linear dependence could be shown for silver nanowires and PEDOT:PSS and was assumed for the single measurement point of the CNTs. The shape of the transmittance curves does not change significantly in relation to Figure 3.20a.

Next to the transparency of the layers, the conductivity is an important criterion. Figure 3.21a shows the sheet resistance of the three materials for a different number of layers. Silver nanowires (AgNW) show a rather high sheet resistance of 4.8 kΩ/sq for only five spraying cycles, which seems to be around the percolation threshold. For a higher number of spraying cycles, the sheet resistance decrease to 52 Ω/sq, 29 Ω/sq, and 14 Ω/sq for 10, 15, and 20 cycles, respectively, reaching the lowest sheet resistances of all three materials. The carbon nanotube (CNT) layers start at 52 kΩ/sq for 5 layers and only minor decrease to 34 kΩ/sq for 10 layers. PEDOT:PSS shows a low sheet resistance of 181 Ω/sq and decreases almost linearly down to 53 Ω/sq.

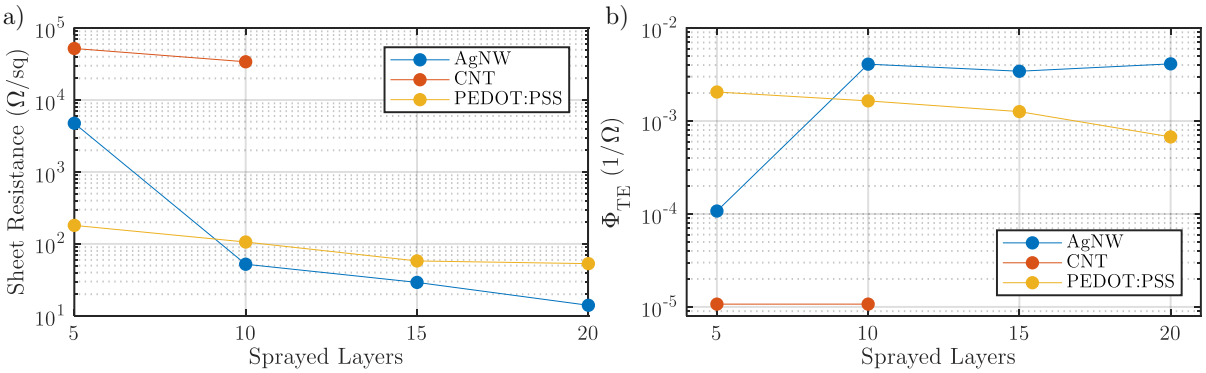

Figure 3.21. a) The sheet resistance of thin-films with a different number of layers of silver nanowires (AgNWs), carbon nanotubes (CNTs), and PEDOT:PSS. b) The figure of merit according to Eq. 3.7.

As both the transparency and the sheet resistance decreases with the number of spraying cycles, a trade-off has to be found to achieve highly conductive and transparent patterns. Haacke developed the figure of merit shown in Eq. 3.7, which is commonly used in literature to evaluate transparent conductive films. [206], [216], [220]

$$\Phi_{TE} = \frac{T^{10}}{R_S} \qquad \text{Eq. 3.7}$$

Figure 3.21b shows the calculated figure of merit for all three materials. Silver nanowires with more than 10 sprayed layers show the highest values of up to 4.1 $k\Omega^{-1}$. PEDOT:PSS lies at a layer count of 5 at a figure of merit of 2.1 $k\Omega^{-1}$, whereas CNTs are far lower with only 10.7 $M\Omega^{-1}$. This shows, that silver nanowires and PEDOT:PSS are suitable to produce conductive layers with a high transparency of around 85 % and a low sheet resistance of around 100 Ω/sq.

3.2.2 Applications

Transparent conductive patterns can be used for transparent electrodes of silicon and organic solar cells, organic and polymer light emitting diodes (OLED, PLED), touch panels, a variety of displays, and as transparent heaters for aeroplane and car windows, transparent speakers, electromagnetic shielding for microwaves an other electromagnetic radiation, and transparent thin film energy harvesting or storing devices. [203], [216] In Section 4.3.1 of this thesis, we show transparent temperature sensors based on thermocouples using a pair of the three presented materials. These may also be used for energy harvesting.

Here, we briefly show a large area transparent heater on a polyimide substrate shown in Figure 3.22 that as built as an extension to our screen printer to heat the printing table. It had the dimension of about 20 x 22 cm^2 and consist of spray-coated AgNW on top of screen-printed electrodes on the side. The screen-printed electrodes were used to form a low-resistive path on the sides to homogeneously distribute the current. We could show, that the heater worked well with local temperatures up to 200 °C but found that the distribution of the heat is depending much on the surface, the heater was lying on. Therefore, we refrain from showing the recorded IR images here. On a glass plate, high temperatures could be reached whereas, on the aluminium table of the screen printer, the temperatures were much lower. We don't exactly understand the reason behind as the polyimide should have a rather low heat conductance. However, the heat loss must be related to the heat conductance of the underlying materials. This was shown by the large differences in temperature if some air was in the background or if it was lying flat. On the screen printer table, we had vacuum that provided a flat positioning on the surface. Then, maximum temperatures of only 45 °C could be measured, which

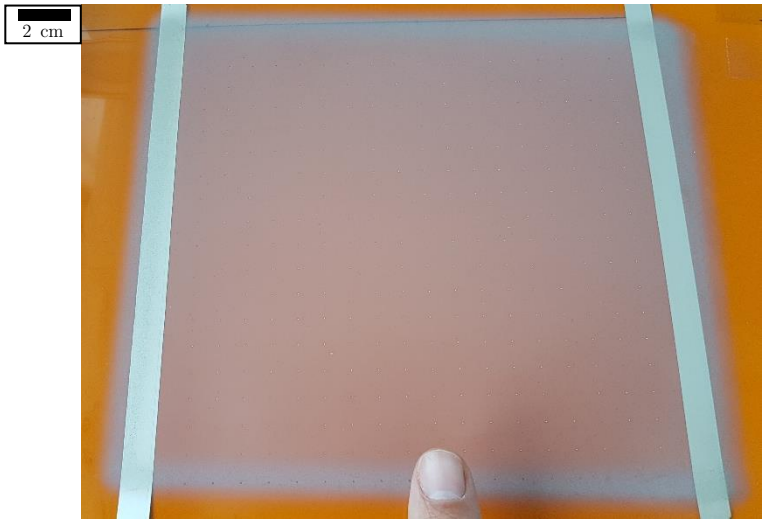

Figure 3.22. Large area transparent heater with screen-printed bar electrodes and spray-AgNWs.

were too low for drying of printed layers on top. Furthermore, the substrate table heated up to almost the same temperature. The encapsulation of the AgNWs with screen-printable dielectric decreased the maximum temperature even more.

To fix another substrate on top, the polyimide layer was first perforated with holes by laser cutting, which matched the position of the vacuum holes on the substrate table of the screen printer. We investigated also the stacking of multiple perforated polyimide films but could not increase the temperate significantly. Therefore, we recommend following another approach for heating the screen-printers substrate table. One method could be the formation of the substrate table from glass or acrylic glass. Then, this approach may feasible. Another method would be the construction of another kind of vacuum table implementing Peltier elements to be also able to quickly cool the top side of the table. This may help in multilayer printing of exactly the same pattern as each layer could be dried on the table without the need for registration and alignment.

3.3 Stretchable Conductive Patterns

The necessity to place sensors far away from the processing unit in smart clothes or artificial skins for robots may require conductive wirings on stretchable materials at low-cost. Comfortable clothes as well as the human skin and a potential robotic skin are or should be made from a stretchable material to adapt to the movement of the person. Different methods have been investigated and are presented in the following.

Some researchers worked with functional or metallic threads as well as thin cuts of a polymer film with a functional layer on top. These were then woven to or into clothes [221]–[225] or knitted and braided onto the textiles [226]–[228]. The other option is direct printing of functional materials onto the textile. Typically, all kinds of textiles have a different, but rough surface and are difficult to print on. Many groups went for a pre-coating of the substrate, to form a flat and connected surface that facilitates printing, especially for inkjet-printing [108], [114], [229]–[232]. The third option to achieve stretchable electronics on textiles is printing the circuitry onto an intrinsically stretchable substrate and then fix it to textiles [233]. [234]

In recent years, researchers followed two complementary ways to achieve conductive patterns on non-textile, stretchable materials. [235] The first group of researchers applies conventional conductive materials like gold, silver and copper in a sufficiently thin layer to be bendable onto a sheet of stretchable material like rubber. This approach can make use of the high conductivities of metals and semiconducting properties of thin silicon sheets at the same time within conventional semiconductor technology. [236]–[242] The second approach depends on new materials that are intrinsically stretchable or able to rearrange particles in a stretchable matrix to realize conventional flat patterns [243]. Such new materials were developed with metal particles [244]–[247] or wires [248], [249], conductive polymers [207], [248], graphene [214], [250] and carbon nanotubes [251]. In this approach, much cheaper processes and materials can be used that are already fulfilling the requirements as a bulk material. [234], [252] However, such materials currently possess only a rather low conductivity and have to be synthesized as they are not commercially available. The rest of this section of an engineering thesis focuses on commercially available substrates, inks, and pastes.

A literature review and an evaluation of different substrates for inkjet- and screen-printed stretchable wires are shown in Section 3.3.1. Section 3.3.2 shows our results when inkjet-printing silver nanoparticles on a silicon rubber film. The last section concludes with an idea to combine rigid and stretchable sections in applications.

3.3.1 Intrinsically Stretchable Substrates

In contrast to most textiles that are elastic due to the reorganization of the threads, elastomers are intrinsically stretchable without the need for weaving or knitting. Elastomers are macro-molecular materials that substantially deform under exposure to small mechanical loads and recover after the load is removed. Most elastomers are polymers that have a sufficiently long chain to possess a glass transition temperature below room temperature or that were cross-linked by vulcanization. [253] Polymer chains at a temperature above their respective glass transition temperature can rearrange the orientation of parts of their chain under an applied stress. Cross-lined elastomers show a higher elasticity because the links ensure that the elastomer returns to its original configuration. [254]

Most commonly used elastomers base on a carbon or a silicon-oxide backbone. Synthetic rubbers vulcanized from various petroleum-based monomers are typically not used for thin stretchable films. Siloxane polymers consist of an alternating silicone and oxide backbone that forms a chemically strong chain. The most known siloxane is polydimethylsiloxane (PDMS) that contains two methyl groups on each silicon atom in the chain. Extensive research has been done on the cross-linking agents and the ratio of it to the polymer, which influences elasticity. [255] Films of PDMS are easy to produce and are commercially available. Polyurethanes (PU) are also well-known and widely available as films. They possess a higher glass transition temperature and higher dielectric constants than PDMS. Other elastomers are polystyrenes, polyamides, and polyacrylates that can be processed in thin films and is sometimes used for adhesive tapes. [253]

3.3.2 Inkjet-Printing on PDMS

We tried the elastic properties of several polyurethanes and a silicone film. The recovery of the polyurethanes showed to be slow and with all, a remaining strain was left. The best-performing stretchable substrate of our small selection was the Elastosil Film 2030 of Wacker Chemie AG. It is available in thicknesses ranging from 20 µm to 400 µm and can be stretched up to 450 % according to the manufacturer. Our experiments showed, that more than 300 % is realistic for a 200 µm thick film. It has a hardness of 27 Shore, is temperature stable, and forms back to its original position within up to some hours.

Inkjet-printing of a silver layer onto the silicon rubber film requires pre-treatment of the film because of the high surface tension. Typical values for the contact angle of a water drop on a non-porous surface suitable for inkjet-printing were measured to be between 60° and 85°, whereas the silicon rubber showed a contact angle of about 110°. This last value is in accordance with literature for plain PDMS. [91] The contact angle of the ink on the substrates leads to contact angles of about 15° – 30° for well-performing inks and about 60° for the Elastosil film. The latter value is too high for inkjet-printing.

Oxygen plasma was conducted on the silicone rubbers for 30 s at a power of 30 % inside an aluminium cage that absorbs most of the microwave radiation. A wide range of parameters was found suitable for this process, however, we find that the longer exposure leads to a longer process window. Brent and Steinbock, for example, show that the contact angle rapidly increases again after PDMS is in contact with air. We tried to use the treated substrate as soon as possible but found no significant change within about 30 min. Afterwards, the printing quality decreases and the ink agglomerates in drops on the substrate.

Inkjet-printing with the Epson printer or our modified flatbed printer proved to print more homogeneous silver layers as the ink is printed much faster than with the Dimatix printer. The short printing time in comparison to the drying time of the ink allows horizontal and vertical, inkjet-printed lines to merge and form a homogeneous area coverage. The disadvantages are a lower resolution and some satellite drops next to the intended printing region. The minimum line width was

0.5 mm that was still conductive for more than a few centimetres. The major reason for this limitation was the difference in wettability of the substrate after plasma-treatment. On some locations, the substrate seems to be less hydrophobic and a visible change in colour occurred there. A second layer of inkjet-printed silver with the flatbed printer improved the visual impression and also the printing yield of thin conductive lines.

Figure 3.23 shows optical microscope images of double-printed inkjet-printed Ag-NPs on the Elastosil film after drying at 60° for 30 min. In the left image, a crack-free section of a 1 mm wide line can be seen that possesses homogeneous line edges except for the few satellite drops at the top. Other sections of the same wire show small cracks that still allow a current flow through the wire. These result probably from the relaxation during cooling down after the drying as the thermal expansion coefficient of rubbers and metals are differing by about a magnitude [256].

Several widths and shapes of conductive wires have been printed and some are shown in Figure 3.24. All have in common, that the contact pads that are separated by 60 mm are larger to decrease the resistance at the clamps of the strain setup (See Materials and Methods section M.4.1), which scratche the surface of the wire under strain. It also allows a better connection of the wires with epoxy. All inkjet-printed wires showed a resistance of below 1 Ω/sq for one layer of Ag-NPs and about 0.6 Ω/sq for double printed Ag-NPs. We found, that sintering does not enhance the conductivity significantly, but reduces the stretchability. Thus, all further samples were prepared with only an inkjet-printed Ag-NP layer that was dried at 60 °C after printing.

Investigations of the profile of an inkjet-printed line on the silicon rubber film revealed that the top of the silver layer is 3.85 µm higher than the non-imprinted parts of the film. This is a high value in comparison to imprinted PET or photo paper that only show a silver film height of 600 - 800 nm. In both cases, the same printing parameters were used and the ink volume should be the

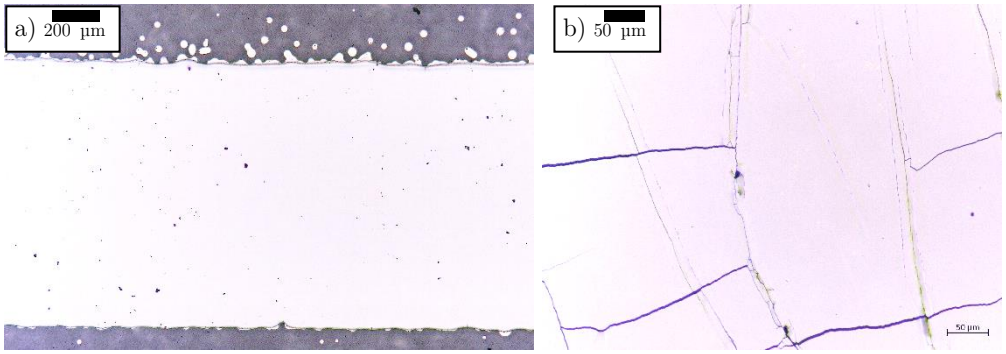

Figure 3.23. Optical microscope images of inkjet-printed Ag-NPs on silicon rubber film. a) Crack-free section of an about 1 mm wide line. b) Magnification of a cracked area.

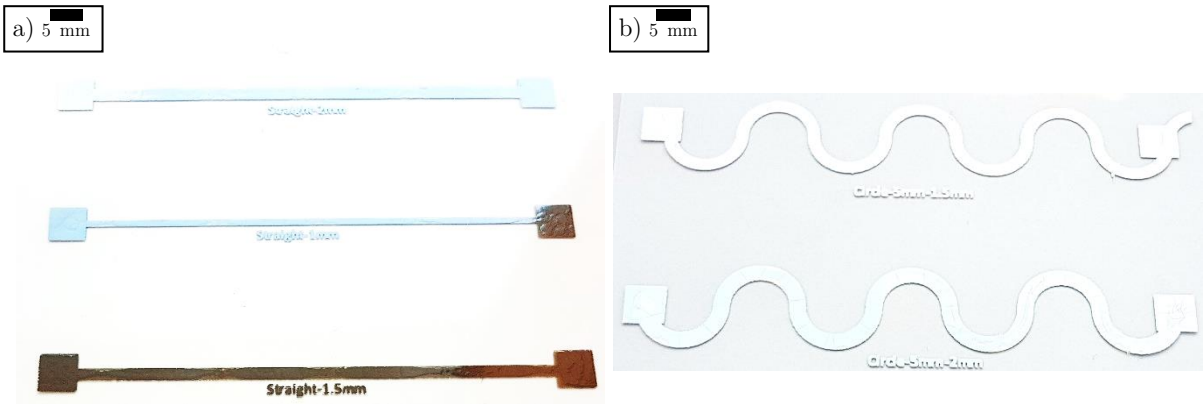

Figure 3.24. a) Straight and b) horseshoe-curved inkjet-printed silver wires on a silicon rubber film. The distance between the contact pads is approximately 60 mm, the width is indicated by the last number in the centre of the print, and the circle diameter in b) is 5 mm.

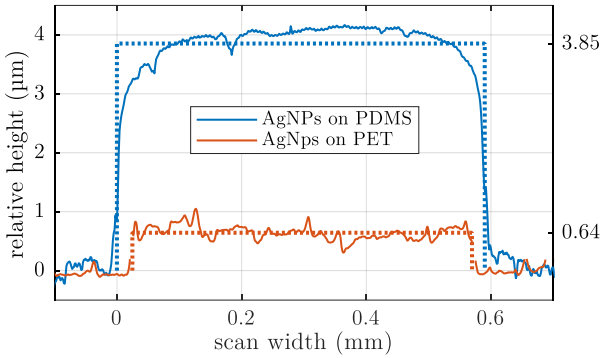

Figure 3.25. Profile of inkjet-printed Ag-NPs on a PET film and on the PDMS film. The width and the average heights are marked by dashed lines. The average values are also listed on the right axis.

same. Figure 3.25 shows two profiles of 500 µm wide lines on silicone rubber film and a PET film. The dashed lines indicate the average thickness and the width of both profiles. The average thickness values are also listed on the right axis.

The deviation is too big to be explained by a different drying behaviour. We think, that the silver layer thickness is approximately similar to PET, however, the silicon rubber substrate swells due to the solvent. In literature, the swelling of PDMS was well investigated, especially for microfluidic devices. [257]–[259] Lee et al. found that the swelling of PDMS is related to the Hansen total solubility parameter. [258] This parameter is 21.8 $(J/cm^3)^{0.5}$ for TGME, the solvent of the used silver ink. This value was calculated using the parameters from the handbook of Hansen, the inventor of these parameters. [260] The study of Lee et al. shows that solvents having a similar (± 5 %) parameter show a swelling between 3 % and 21 %. Assuming a value in the middle of this interval (12 %), a penetration of the solvent into the top 25 µm of the silicon rubber film can cause a swelling of 3 µm. Such a swelling should be visible by an increase of the film thickness already next to the silver. Unfortunately, the used profilometer is not able to record an image in parallel to the profile. Still, the falling edges on the left and right side of the profile and the increased width in comparison to imprinted PET indicate that swelling causes the high profile.

Figure 3.26 shows an exemplary stretching and recovery cycle of a 65 mm long silver wire with a width of 1.5 mm. The wire was stretched slowly at a rate of 0.84 %/min and the resistance was constantly monitored. The first stretching cycle shows a linear increase of the resistance from initially 0.65 Ω/sq to 0.85 Ω/sq at a strain of 1 %. Afterwards, the resistance increases exponentially and at about 4 %, the wire is not conductive anymore. The wire was then further stretched to 15 % and then slowly relaxed. The point at which the conductivity is restored is at about 6.5 %, which is almost double of the loss point. From 6 % down to the relaxation point, the resistance decreased

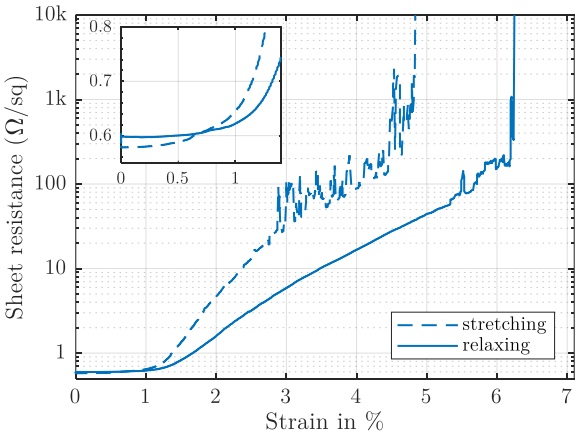

Figure 3.26. The calculated sheet resistance of an inkjet-printed Ag-NP film on a silicon rubber film under strain at a low stretching speed of 0.84 %/min.

exponentially to about 0.6 Ω/sq, which is even lower than the original value. We think that some NPs may have filled the initial cracks during the stretching cycle and form a better contact at some locations. After 10 s waiting in the idle position, the resistance decreases even down to 0.55 Ω/sq.

This self-healing property of the conductive wire can also be observed for different strains until the breaking of the substrate. Figure 3.27 shows the resistance value from 0.5 s after the relaxation of the wire from different strains. The relaxation speed was about 60 %/s. Small to medium strains of less than 80 % only lead to a small increase of the resistance of less than 0.2 Ω/sq. High strains of 100 % up to 300 % increase the sheet resistance by a factor of 1.5 to 2.5, which is still in the tolerance of most systems. After some time in the idle position, the resistance decreases inversely logarithmically towards the original value. It has to be mentioned, that the measurement of the high strain values was conducted before the substrate relaxed completely. Thus, the real resistance values may be even lower than the shown ones.

At a strain of about 300 - 350 %, most of the samples broke. The deviation to the datasheet (450 %) probably results from a mix of the following reasons: The films were not cut to an equal width over the entire length, so the local forces may be higher at some points. The cutting of the film with normal scissors introduces small cracks on the edges that increase the probability of further tearing. This is enhanced by the reduction of width during stretching that stretches the edges more than the central region. Furthermore, we found that the films are not perfectly homogeneous in surface tension and think, that the strain resistance varies a bit with the composition of the film.

In the following, we want to investigate, how often, the wire can be stretched. This wire had an initial sheet resistance of 0.73 Ω/sq. The wire was stretched by 20 % with a speed of 61 %/s and then completely relaxed with the same speed. After 10 s relaxation time, the resistance was measured. It increased to 0.75 Ω/sq after this first cycle. This stretching, relaxing and measuring was repeated. After 15 cycles, the resistance value was still similar to the initial resistance as shown in the inset of Figure 3.28. Then the resistance rapidly increased within a few cycles to about 1 Ω/sq, but after a few more cycles it decreased again. This behaviour was measured with a few different samples. We think, that it is related to the viscoelastic behaviour of the silicone rubber. Our measurements were too fast, so the film could not completely relax. This explains the linear increase in resistance to the rising number of cycles after that point. It took 550 cycles to obtain a doubling in the sheet resistance and more than 5000 cycles for the tenfold as can be seen in the left graph of Figure 3.28.

We think this behaviour is more than suitable for many applications that require over-stretching tolerant wires. As discussed before, the viscoelastic substrate slowly relaxes to its original position. It was clearly visible, that the substrate was stretched by a few percents in comparison to the beginning of the experiment. After 36 h, it formed back to almost the initial length. During this time, the

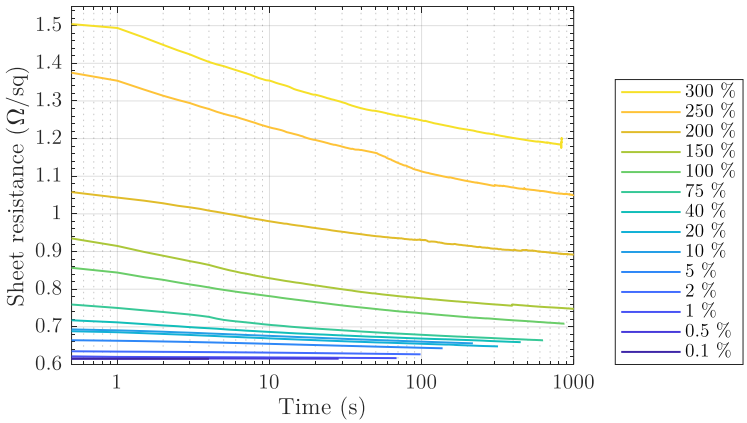

Figure 3.27. Recovery of the sheet resistance after relaxing from a different strain. After relaxing from all strains up to 300 %, the wire is conductive again after less than 1 s and then slowly recovers towards the initial resistance.

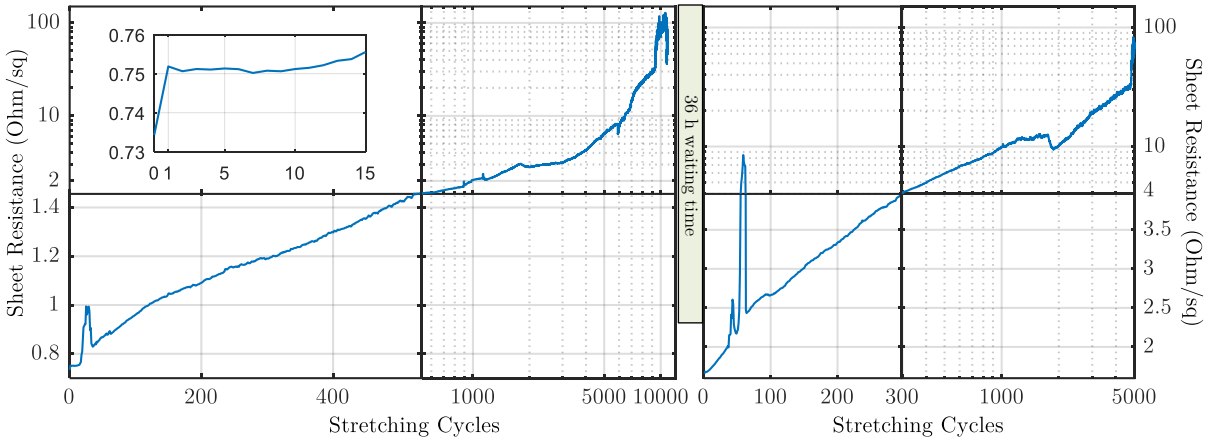

Figure 3.28. The sheet resistance of inkjet-printed Ag-NPs on silicon rubber film up to 11,000 stretching cycles followed by 36 hours waiting time and another 5,000 stretching cycles to a strain of 20 %. The inset shows the resistance values for the first 15 cycles.

sheet resistance decreased down to 1.66 Ω/sq, which is only slightly more than double the initial resistance. This indicates, that the mechanical stress does not harm the silver layer significantly.

We continued the described measurement after this waiting time of 36 h with the wire in its idle position. The right graph in Figure 3.28 shows a similar but faster increase of the sheet resistance of the already tested sample. After in total 16000 cycles, it was still conductive and recovered with a low sheet resistance after another 36 h of waiting time. We think that in comparison to many real-life applications, our measurement procedure is harsh. In reality, we expect much longer relaxation periods and smaller strains, which leads to a constantly low resistance.

3.3.3 Stretchable Material with Islands

The most fragile part of stretchable electronics are the contact pads to any rigid component. For a long-living demonstrator, the contact areas and the pads of all surface mount components should be enforced by some rigid material. One method is shown in Figure 3.29. Two pieces of coated PET film are embedded into a PDMS film by placing them carefully into the not yet cured PDMS. These rigid “islands” offer a porous surface suitable for high-resolution inkjet printing and allow the printing of circuitry, e.g. a small microcontroller-based sensor module. The stretchability of these islands is low so that the mechanical stress on electrical contacts is limited. Between the islands, there is highly elastic PDMS that can also be inkjet-imprinted with a lower resolution after plasma- treatment. The PDMS can serve as a stretchable connection wires between the islands. If the islands are sufficiently small, the entire film is macroscopically stretchable. This approach finds use in several publications already, e.g. for a stretchable LED matrix using normal surface mount LEDs [236], and distributed electronic circuitry in medical applications [243], [261]. Other ways to create rigid islands are pulsed laser ablation of graphite through a shadow mask [262], or a sophisticated patterning of PDMS [263].

Figure 3.29. Two non-stretchable pieces of coated PET surrounded by elastic PDMS on a Kapton carrier material. The non-stretchable parts could serve as high-resolution inkjet-printing of a complex circuitry that is connected elastically to each other after peeling off from the carrier material.

3.4 Summary

This chapter of the thesis presented the functional characterization of inkjet-printed, screen-printed, and spray-deposited layers. To achieve a high conductivity, many different curing methods for printed conductive patterns were presented with a focus on photonic curing by intense pulsed light (IPL) from flash lamps. The components of IPL curing tools, the involved physical processes, and a literature review about opportunities and difficulties was given. The photonic curing tool used during this thesis was described and an overview of the operation procedure was given.

Then, the sintering of inkjet-printed silver nanoparticles (Ag-NPs) and gold nanoparticles (Au-NPs), as well as screen-printed silver microparticles and Ag-NPs, was conducted and the findings presented. All experiments were conducted on temperature-sensitive substrates like photo paper or PET film. The resulting sheet resistance of sintered inkjet-printed Ag-NPs showed to be closely related to the energy provided to the lamp and almost independent of the pulse power. However, the amount of destruction that the sample experienced can be controlled by the power. Therefore, the ideal sintering parameters were a medium voltage of 2.5 kV and a pulse duration of 750 µs. This combination resulted in destruction-free and highly-conductive thin films after sintering a pre-dried film. A second pulse was able to increase the conductivity even more up to 46 % of the silver bulk conductivity without damaging the thin film. SEM images were presented to show the transformation from a nanoporous to a microporous layer with a strong creation of necks between the particles. The same experiments were conducted with inkjet-printed Au-NPs that showed a similar relation but a less defined dependence on certain parameters. This may be related to varying thickness in the not accurately printed layers and the low number of samples that could be printed with the expensive ink, which was also difficult to print. Still, a recommendation for the first pulse was given with a low voltage of 2.0 kV and a long pulse duration of 2 ms. It is expected, that a second pulse can decrease the resistance even further. Screen-printed silver micro-flakes that were already heated to 100 °C for 30 min to evaporate all solvents were presented next. Still, IPL sintering was able to increase the conductivity by two orders of magnitude to low regions that were difficult to measure precisely. Therefore, it was not possible to give an exact value for the conductivity. Screen-printed NPs showed a much higher conductivity after drying at 100 °C and the resistivity could only be decreased by about one third (33 %). For both screen-printed pastes, the energy of our curing tool was not sufficient to find the ideal parameters. The best results were achieved for a medium voltage of 2.5 kV and a pulse duration of the maximum of 3 ms. Additional pulses may still reduce the resistance of these layers.

IPL-curing can also be employed to deliver the activation energy for the reduction of metal-oxide inks. We showed this in the example of a commercial copper-oxide ink that consists of fully oxidized copper nanoflakes. After only one high-energetic light flash, a conductive copper layer was formed that shows a conductivity of 23 % in comparison to bulk copper, which is the highest we could find in literature for this inkjet ink. [175] We compared different sintering conditions and identified two as recommendations. A destruction-free sintering can be achieved with a voltage of 2.75 kV and a pulse duration of 2.0 to 2.5 ms. If no small patterns are sintered and small damages at the edges of the patterns are acceptable, sintering at 3.0 kV for 2 ms will result in a 20 % smaller resistance. Additional pulses do not decrease the resistance anymore and should be avoided. Furthermore, IPL curing was employed to improve the adhesion of silver nanowire layers on temperature-sensitive substrates like PET and PP.

In the second part of this chapter, we presented different conductive patterns. First, transparent conductive patterns made from silver nanowires (AgNW), carbon nanotubes (CNTs), and PEDOT:PSS were characterized according to their sheet resistance and transparency. AgNW showed the lowest sheet resistance when comparing electrodes with the same transparency. For an 85 %

transmitting (at 550 nm) electrode a sheet resistance of about 50 Ω/sq was achieved and for a 77 % transmitting film a sheet resistance of about 14 Ω/sq. The sheet resistance of the CNTs lies about two to three orders of magnitude higher at comparable transmittance. PEDOT:PSS showed an approximately threefold of the sheet resistance when compared to AgNW at the same transmittance (about 50 Ω/sq at 77 % transmittance). These experiments were mainly focused on the production of spray-deposited thin films for thermocouples that will be investigated in the next chapter. We showed a large area (440 cm^2) heater production by a combination of laser-cut perforation, spray-deposited AgNW thin films, and screen-printed electrodes and encapsulation.

Stretchable conductive patterns were also presented in this chapter by means of inkjet printing on top of silicone rubber film. This is a different approach to most other research groups that focus on polyurethane as the stretchable substrate. Silicone rubbers show a much higher elasticity and do return to the initial shape after strong strains. The employed silicone rubber film has superior elasticity and the remaining strain after a stretching to 300 % was only a few percents after a few seconds that vanished after a couple of hours completely. The main difficulty is the low surface energy that makes it difficult to imprint the surface. We tried MPTMS coating without success as the resulting wettability was inhomogeneous. Light oxygen plasma for 30 s at a power of about 100 W and inside a Faraday cage showed a much better performance with respect to homogeneity and contact angle. After oxygen plasma treatment, the silicone rubber films were printable for about 30 min, which was sufficient to inkjet-print Ag-NPs. We showed that the sheet resistance can be as low as 1 Ω/sq without sintering and that the patterns can be stretched up to about 7 % without losing conductivity. Higher strains interrupted the connection but even after stretching the film to 300 % and then releasing it, the conductivity recovered within less than a second. After a sufficient waiting time, the resistance was almost similar to the original resistance. These self-recovering conductive wires were discussed in detail and their application as strain sensors will be the topic of the first section of the next chapter.

Chapter 4

Printed Sensors

Printed electronics possess the advantage to reduce the number of production steps because several components of a device can be fabricated with similar technologies. In particular, the assembly of non-printed components onto printed conductive patterns is still one of the main challenges. Printing techniques are usually much faster and possess a higher accuracy than pick-and-place machines used for the assembly. One solution is to reduce the number of assembled components and try to print these instead. Passive components like resistors, inductors, and capacitors can be printed already with at least a low quality and reproducibility. In most cases, this is sufficient as the following examples show: Pull-up or pull-down resistors in many circuits only have the task to pull a wire to a specified voltage level. Other resistors are used for simple analogue low-pass filtering. Only the order of magnitude of the resistors is important and the tolerance is large. The same applies to capacitors that are implemented to reduce high-frequent jitter and inductors that smoothen abrupt

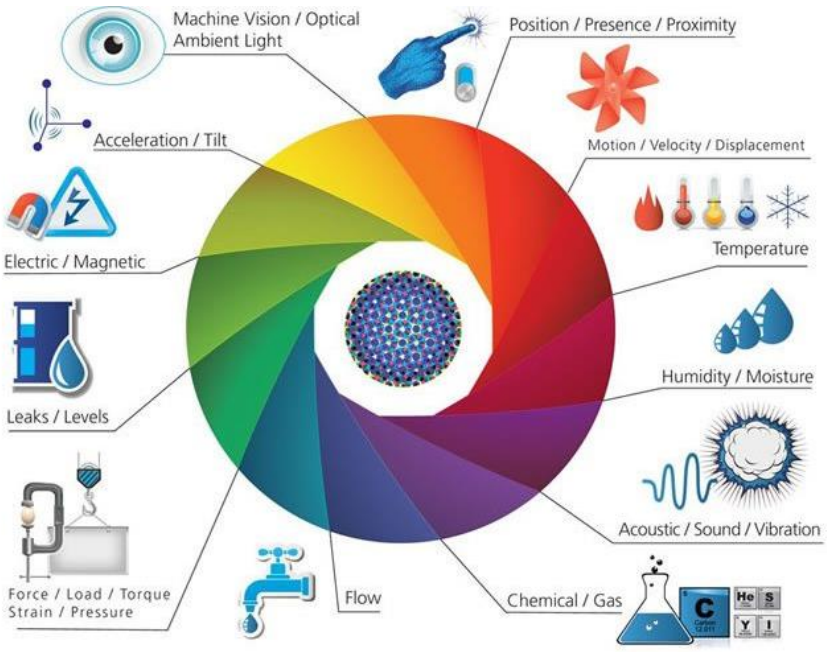

Figure 4.1. Overview of sensor categories in the Internet of Things. Source: IoT infographic Postscapes and Harbor Research

changes in currents. An overview of printed passive and active devices is given in the work of Tobjörk and Österbacka [2] A necessary component of many light-weight and wearable devices is a sensor or even multiple of them. Especially for wearables, these sensors need to be at certain positions, for example, skin electrodes. This is often not achievable with conventional electronics and printed electronics may show a feasible way. Figure 4.1 shows an overview of different sensor categories required in the Internet of Things.

This chapter focuses on different kinds of sensors that were produced during the work on this thesis. Inkjet printing, screen printing, stencil printing, and spray deposition were combined with thermal curing, intense, pulsed light curing, and oxygen plasma treatment to produce a wide range of sensors. Mechanical, environmental, chemical, and medical sensors are presented in the following sections. The chapter starts with inkjet-printed strain sensors in Section 4.1. Then, it continues with resistive and capacitive force and pressure sensors in Section 4.2. Temperature and humidity sensors are discussed in Section 4.3. Section 4.4 presents briefly some progress to achieve chemical and biochemical sensors. Representatively for the many applications in healthcare, skin electrodes are presented in Section 4.5 for electrocardiography and electrooculography. Section 4.6 summarizes the main intermediate steps and concludes this chapter.

For some of the sensors, specific characterization tools have been built during the work on this thesis. Detailed information about these can be found in the Materials and Methods Section M.4.

4.1 Strain Sensors

Printed conductive structures on stretchable substrates can serve as strain sensors. If the ink or paste is suitable for the stretchable substrate, a simple resistance measurement and calibration can be conducted on a printed line pattern. Here, we discuss the strain-sensing capabilities of silver nanoparticles (Ag-NP) films that were inkjet-printed on a stretchable substrate in Section 4.1.1. Their accuracy is limited to certain conditions. Promising applications can be bipolar threshold sensors as shown in Section 4.1.2. For the characterization of the sensors, we specifically built the Bending and Stretching Setup that contains a stepper motor that moves a carriage with a clamp away from another clamp. The measurement is automated in Labview and described in detail in the Materials and Methods Section M.4.1.

4.1.1 Strain-Sensing Capability of Inkjet-Printed Conductors

We showed in Section 3.3.2 that inkjet-printed Ag-NP films can be stretched up to a few percents while remaining conductive. Furthermore, it was shown that the stretchable conductive wires can be stretched thousands of times without changing their resistance in the idle position significantly if a long enough recovery phase is provided. Figure 4.2 shows, that this is true after the first stretching cycle, which is probably necessary to form the micro-cracks. The second and third cycles provided very similar responses and the sensor behaves in a reproducible manner. The initial sheet resistance was about 0.55 Ω/sq and it increased only minor for strains below 1.5 % and then exponentially. The maximum strain at which the wire was still conductive was about 5 %. At about 6.5 % remaining strain, the wire regained conductivity again and recovered exponentially on a smooth curve. The remaining sheet resistance was about 0.6 Ω/sq, which is only slightly higher than the starting value.

Figure 4.3 shows the sheet resistance of the printed wires for different stretching speeds. The measured curves for low speeds below 0.1 %/s exhibit almost no difference as shown in Figure 4.3a. The resistance always returns to the initial value around 0.6 Ω/sq after a few seconds in the idle position. Higher stretching speeds influence the resistance during stretching whereas the relaxation

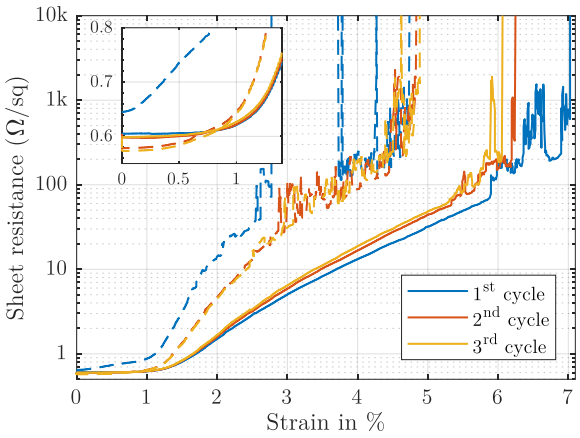

Figure 4.2. The calculated sheet resistance of an inkjet-printed Ag-NP film on a silicon rubber film under strain during the first three stretching cycles at a low speed of 0.022 %/s. The measured values during stretching are shown with a dashed line and the relaxing with a solid line. The inset magnifies the first 1.5 % of strain.

curve remains similar, as shown in Figure 4.3b. During stretching, the resistance increases faster at high speeds than at low speeds.

In general, the amount of strain, the holding time, and the speed of stretching influence the resistance curve slightly. It is too much to be used as a precise strain sensor. Therefore, a linear resistance increase with strain would be desirable and a change of resistance below three orders of magnitude. Still, the low resistance allows the use of the patterns as a stretchable conductor that has a high conductivity in the idle position and can be stretched up to a few percents in operation. This can be used as a bipolar threshold sensor. The most important characteristic is the tolerance to overstretching. After temporary short strains of up to 300 %, the conductivity is regained within less than 1 s to about 50 % of the original value. Still, we were able to implement the conductors in wearable as the next subsection shows.

4.1.2 Inkjet-Printed Conductors as Threshold Strain Sensors

Stretchable conductors are essential for the application of electronics in wearables. As discussed in Section 3.2, there are two basic approaches to achieve stretchable wiring. The first approach uses thin threads of metal that are woven, knitted or braided into the textiles. The second uses a stretchable and conductive material on top of the textiles. This second approach can be done by means of printed electronics and will be followed here. The stretchable material is required to withstand strains up to the maximum strain of the underlying textiles, which are typically around 100 %. [248], [264]

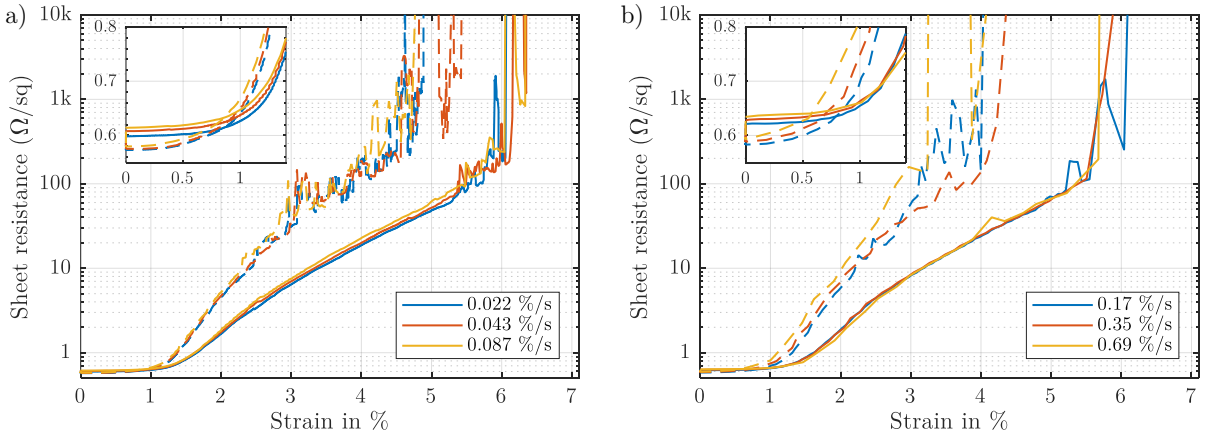

Figure 4.3. Sheet resistance of inkjet-printed Ag-NPs on silicon rubber film over a strain from 0 to 15 % with a) low and b) high stretching speeds. The measured values during stretching are shown with a dashed line and the relaxing with a solid line. The insets magnify the first 1.5 % of strain.

This maximum strain is typically only used for putting on and off the clothes. Whereas shirts and wide trousers are only little stretchable, socks, sportswear, tights, and compression wear are highly stretchable. Many applications that require electronics integrated into clothes, use the second group of textiles. Applications like pulse measurement, sweat analysis, electrocardiography, and pressure measurements require clothes that are in direct contact with the skin. However, in most applications, it is not required, that the functional material shows its intended function during putting on and off. It is only necessary, that the functional material, e.g. conductive wire, maintains its properties during the involved mechanical stress.

Inkjet-printed Ag-NPs on silicon rubber film are a simple and highly customizable way to achieve this. As shown, they survive strain up to 300 % and recover conductivity quickly within about 1 s. Figure 4.4a shows one of our stretchable wires attached to regular women tights. A surface-mount light emitting diode (LED) and two connection wires were attached to the film by conductive epoxy. The film is conductive in the current relaxed state and the application of only 1.8 V made the LED light up. As the wire has a resistance of several tens of Ohms, it can act as a current-limiting pre-resistor. Figure 4.4b shows a magnification of the lighting LED in the idle position. When the author applied some strain to the wire, the LED switches off (Figure 4.4c). In this case, only about one millimetre is enough to interrupt the conductive path. After releasing the strain, it switches on again with the same brightness (Figure 4.4d). This could be repeated several times without damaging the wire. The weakest point of the demonstrator was the conductive glue that showed a low adhesion to the silicone rubber. We recommend to apply the epoxy directly after the printing when the plasma activation is still present or use a more elastic glue.

We could use the strain sensor successfully on a wearable to detect strain on the silicone rubber attached to the textile. This could be used to detect indirectly also the pressure of the tight, which is important for compression wear. The on-off behaviour of the LED can serve as a suitable indicator for untrained persons to put on medical compression socks or tights.

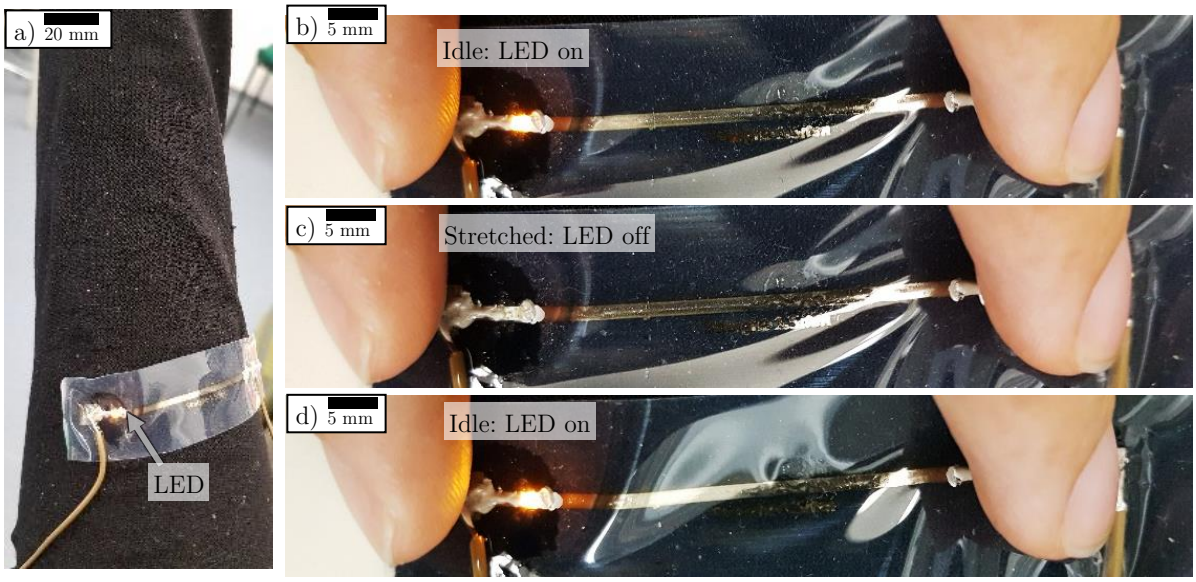

Figure 4.4. a) The stretchable wire attached to a tight. A surface mount light emitting diode (LED) was assembled to show optically whether the wire is conductive or not. b) Initially, the LED lights as the wire is conductive in the idle position. c) The LED fades out as the strain increases and d) it turns on as the strain is released.

4.2 Force and Pressure Sensors

Another type of mechanical sensors includes force and pressure sensors, which are presented together in this section because of the close relationship between the two quantities. Our focus is on sensors utilized in human-machine interaction. The force range starts at the perception level of humans of around 0.4 kPa [265] and ranges up to a few MPa on the heel of the human. The human discrimination level between two forces (Weber fraction) lies around 3 % to 30 % depending on the involved body part, the orientation of the force, and whether other human senses are involved. [266]–[268] This means that force or pressure sensors for human-machine interactions should cover a wide range of forces and have a signal that is proportional to the logarithm of the force. The measured signal M for a pressure P can be expressed by Eq. 4.1 having the sensitivity S and an offset O.

$$M = S \cdot \log\left(\frac{P}{P_0}\right) + O \qquad \text{Eq. 4.1}$$

A reference pressure P_0 of 1 kPa will be used, which lies around the perception level of humans. Ideally, the sensitivity S should be constant in the desired force region and the ratio of the signal to the offset S/O high.

The measurements in this section were executed on the Force and Pressure Setup described in the Materials and Methods Section M.4.1 that was built during the work of this thesis. It consists of a stable stage on which a linear actuator is mounted. This actuator has an internal force sensor and a position sensor and can be controlled via a Labview program. For simultaneous measurements of a sensor, the force, the position, and the electrical measurements from a multimeter, an LCR meter, a source meter, or digital inputs via a COM-Port or an I2C bus can be recorded.

In literature, three types of force and pressure sensors can be found that will be explained in the following three subsections: Resistive pressure sensors base on a change in the contact area between the electrodes and a resistive material and are presented in Section 4.2.1. Piezo-resistive pressure sensors base on composite materials that change its resistivity or its dimensions and are presented in Section 4.2.2. Typically, a current-source is required and a voltage is measured. Section 4.2.3 presents capacitive pressure sensors based on the change of the distance, area, or permittivity between two electrodes. Our capacitive sensing technique allows the measurement of shear forces. Section 4.2.4 presents a possible design and its characterization. Piezo-electric pressure or force sensors use a piezo-electric material and evaluate the voltage without the need for a current source (Section 4.2.5). A comprehensive overview of all types of pressure sensors that use other measurement principles can be found in the review of Dahiya et al. [269] and the books of Cutkosky et al. [270] and Dahiya et al. [271].

4.2.1 Resistive Pressure Sensors

The company Henkel (Germany) uses a simple approach without the need for a material that changes its properties. Their multilayer sensor that changes the values of the three dimensions of the contact area between two conductive layers for different pressures. Figure 4.5a shows a photo of the force-sensing resistor circuit. It consists of two imprinted polyester films that are sealed together with the printed side inside separated by a spacer material. On the top film in the figure, a finger structure and the contact wires are printed with silver paste and a turquoise isolating material surrounds the finger structure. On the other film, a carbon paste is printed on a filled circle of about 1 cm in diameter without any contacts. The two films are then laminated together with a sealing material that is applied everywhere except the sensor locations. In the idle state, there is a small gap between the finger structure and the carbon pad. This gap has a height of the sum of the heights of the isolating and the sealing material minus the heights of the carbon and the silver paste. If the two layers are in contact, current can flow between the two sides of the finger structure. At low pressures,

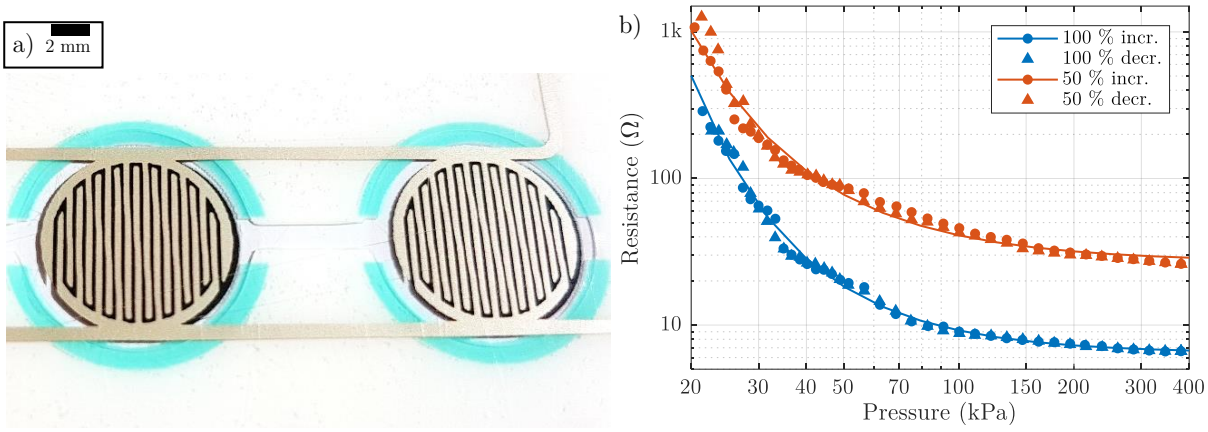

Figure 4.5. a) Photo of a force-sensing resistor circuit provided by Henkel consisting of two imprinted polyester films sealed together having a space between them. b) The resistance of force-sensing resistors with pure (100 %) and 50 % blended carbon paste during pressing with a specified pressure on a circular area with a diameter of 4 mm in the centre of the resistor.

only a small area of the fingers is in contact with the carbon layer. At increasing pressures, more and more of the fingers' surface touch the carbon layer and the contact resistance decreases. This leads to a decrease of the resistance between the two fingers. The value of the resistor can be adjusted by adding non-conductive blend to the carbon paste. We evaluated the behaviour of a sensor without blend and one with 50 % blend.

We characterized the sensor with an applied force from 10 mN up to 7.5 N on a rod with a diameter of 5 mm. This results in a pressure range from 0.5 kPa to 382 kPa. We found that the sensor has a threshold limit of around 20 kPa and cannot detect lower pressures. At 25 kPa, a resistance of about 150 Ω can be measured. At higher pressures, this resistance decreases rapidly to 9 Ω for 100 kPa and then slowly to 6 Ω for 400 kPa. For decreasing pressures, almost the same behaviour was measured and a hysteresis below the measurement accuracy was found. Figure 4.5b shows the measured resistance values over the pressure range for increasing and decreasing forces on the sensor without blend (100 %) and the blended sensor (50 %). For both sensors, a fit curve was calculated for the measured resistance R in relation to the applied pressure according to Eq. 4.2 with the reference pressure P_0 = 1 kPa and the three parameters a, b, and c. These are approximately a = 6.4 Ω, b = 200, and c = 1.55, and for the sensor without blend and a = 27 Ω, b = 89, and c = 1.35 for the sensor with 50 % blend.

$$R = a \cdot 10^{b \cdot (\frac{P}{P_0})^{-c}} \qquad \text{Eq. 4.2}$$

These sensors show a rapid decrease in resistance for a small force range, which is in accordance with the results of other researchers. [30] Additionally, the resistance change for a change of one decibel (~ 26 %) of pressure change is also exponentially decreasing with increasing pressures. Figure 4.6a shows the sensitivity, which is above 100 Ω/dB for forces close to the threshold and rapidly drops to 10 Ω/dB, 1 Ω/dB, and 0.1 Ω/dB at around 45 kPa, 110 kPa, and 400 kPa, respectively. For measurement purposes, it is advantageous to see the slope of the curve in relation to the absolute value. Figure 4.6b shows the relative sensitivity depending on the pressure on the two sensors.

Typical resistance measurements are either conducted by a voltage measurement during applying a constant current to the resistor or, much simpler at a voltage divider with a known reference resistor. Measuring the small resistance changes at the high end of the pressure spectrum is challenging with low-cost microcontrollers. For this sensor, the first approach is only feasible for small pressures below 50 kPa as the current values must be high to reach a significant voltage level. By blending the carbon paste, this values can be shifted towards higher pressures, but the curve remains the same. The second approach uses a non-linear sensitivity to the resistance values and a smart choice of the reference resistor and can increase the force range up to 200 kPa (R_{ref} = 10 Ω). A slight

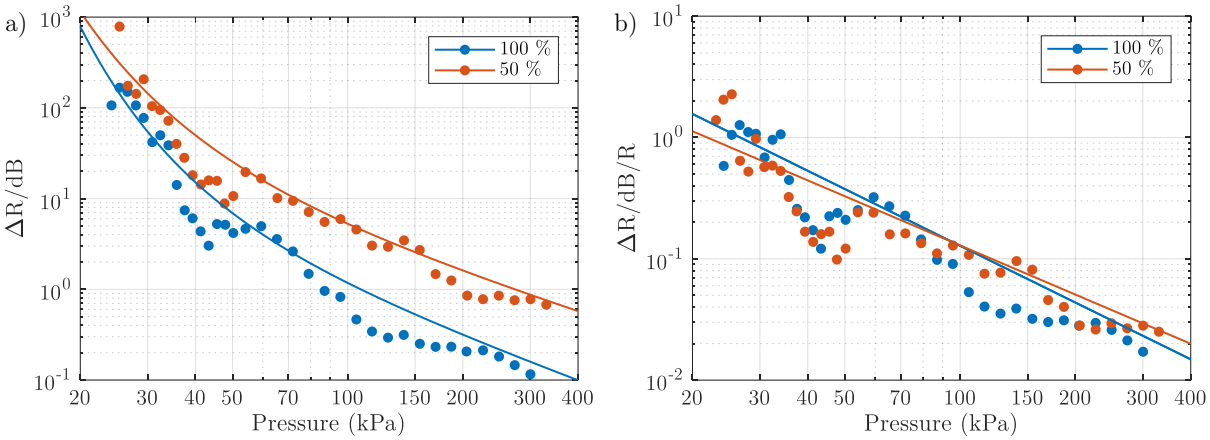

Figure 4.6. a) Sensitivity per decibel of pressure change of the two sensors and b) sensitivity relative to the resistance value. The markers show calculated values from the measurement and the line shows the derivation from the fit curve in Figure 4.5.

increase in the sensing range may be achieved by blending the sensor material and using an analogue differencing amplification.

In conclusion, the approach of a resistive force sensor at a gap to the sensing electrodes is only feasible for a small range of force, e.g. 25 kPa to 200 kPa. Most possible improvements in the design, e.g. varying the distance of the IDES, may increase the measurement range, but not significantly.

In literature, other groups employed similar sensor designs. Ahmad et al. used similar carbon blend mixtures to screen-print a pressure sensor with similar behaviour than the presented. [30] Castellanos-Ramos et al. placed a rough film of a conductive polymer sandwiched between two electrodes that change the contact area to the rough polymer under pressure. [272]

4.2.2 Piezo-Resistive Pressure Sensors

In literature and already in some products, other approaches for resistive pressure sensors can be found that employ pressure-sensitive resistive materials. Most of them fill a rubber with conductive materials to an extent that lies above the percolation threshold. A pressure on the material forms more connection between the fillers and decreases the resistivity. The most used filler materials are carbon black [273]–[275], metal [274], [276], and semi-conductive particles [274] in the nanometre or low micrometre range and CNTs [275], [277]–[279] and metal nanowires, or a mixture of the mentioned materials [275]. The company Interlink Electronics The company Interlink Electronics (US) produces force sensing resistors (FSR) that decrease the resistance exponentially over an exponential increase in pressure. [280] Tekscan Inc. (US) claims to produce a resistive, pressure-sensing material that changes its conductivity linearly with pressure. [281], [282] Chang et al. used an unknown resistive material and achieved an inversely exponential decrease in resistance to increasing pressure. [283]

4.2.3 Capacitive Pressure Sensors

Another type of electrical pressure sensors employs the change of the capacitance of an arrangement of electrodes. A typical arrangement is the parallel plate configuration shown in Figure 4.7a. A dielectric (blue) is sandwiched between two electrodes (dark grey) with an area A that are printed onto a substrate (light grey). The dielectric of the thickness d_0 should have a high relative permittivity ε_r and be compressible. On pressure application, the dielectric is compressed and the two electrodes are closer together, meaning that the distance d(P) between them is smaller than the initial distance d_0 as shown in Figure 4.7b. The capacitance in relation to the pressure can be calculated with the well-known formula for a parallel plate capacitor shown in Eq. 4.3, if the thickness of the compressed dielectric is known.

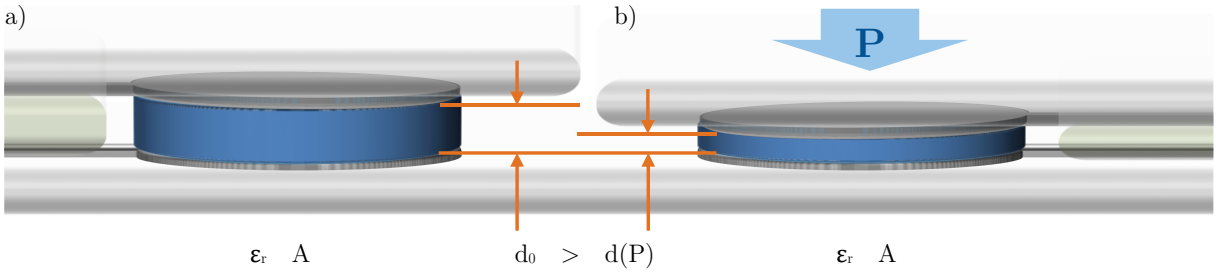

Figure 4.7. Schematic of the capacitive force sensors with dielectric (blue) sandwiched between electrodes (dark grey) that are printed onto polymer film (light grey). a) Initially, the capacitance value depends on the electrode area A, the relative permittivity ε_0 and the distance d_0 between the electrodes. b) On pressure application, the distance d(P) is reduced whereas the area and the relative permittivity remain constant.

$$C(P) = \varepsilon_0 \varepsilon_r \cdot \frac{A}{d(P)} \qquad \text{Eq. 4.3}$$

The compression ratio Δd of the dielectric layer is closely related to the Young's or elastic modulus E according to Hooke's law (Eq. 4.4). [284] The elastic modulus is a mechanical property that describes the stiffness of an elastic material and lies around 2 MPa for PDMS. [285] Hooke's law assumes a linear elastic material, which is not always valid for many elastic polymers.

$$\Delta d = \frac{\Delta P}{E} \cdot d_0 \qquad \text{Eq. 4.4}$$

Most elastic materials suitable for printing as a dielectric are rubbers, like the much-used polydimethylsiloxane (PDMS), and are not linearly compressible. This means that a compression in one direction leads to an expansion in the two directions. The ratio between the transverse strain and the axial strain is called the Poisson ratio ν and influences Hooke's law according to Eq. 4.5. Many elastomers like PDMS have a Poisson ratio closely below 0.5, meaning that they are incompressible and require a lateral expansion on compression. [25] This expansion is limited in thin films as at least one surface of the film is bounded onto another material. Thus, Eq. 4.5 leads to a small change in distance Δd.

$$\Delta d = \frac{P}{E} \cdot (1 - 2\nu) \cdot d_0 \qquad \text{Eq. 4.5}$$

Polymers with a Poisson ratio close to 0.5 are better described by hyperelastic models like the Neo-Hookean law for low strains (< 50 %), the Mooney-Rivlin law for medium strains (50 % – 80 %) and the Ogden law for large strains. [255], [286] However, these laws only prove, that a certain compression is possible, but do not solve the problem with a small displacement of the top electrode.

One option to provide a volume to the PDMS to expand on pressure is described by Mannsfeld et al. [287] They micro-structured one surface of the elastomer with tetrahedral "pyramids" and found that the sensitivity is thirty times higher than for a plain film and the recovery time is significantly shorter. The higher sensitivity can be explained by a lower elastic resistance due to a lower amount of elastomer as well as the release of air between the structures that increases the relative permittivity with increasing pressure. [287], [288]

Here, we want to present a screen-printed pressure sensor using a similar approach. In Section 2.3.4, we showed that the aspect ratios of hill-structures on screen-printed elastomers can be 23.5 % and that they can be modelled as paraboloids with a volume of $V = \frac{\pi}{2} \cdot r^2 \cdot d$. When using these hill-structures as a dielectric, a printed pressure sensor like schematically shown in Figure 4.8 can be created. It consists of two layers of imprinted polymer films that carry the two electrodes. The electrodes are aligned as a parallel plate capacitor. One of the electrodes is imprinted with a thin isolating material to avoid shorting of the plates. This can be any isolator,

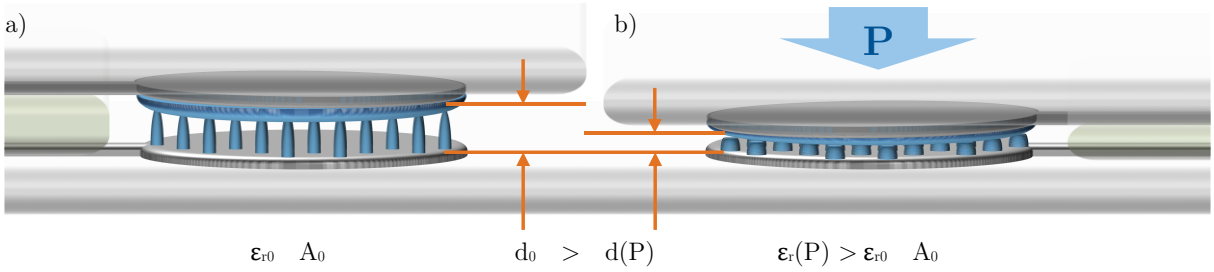

Figure 4.8. Schematic of the capacitive pressure sensors with a structured dielectric (blue) sandwiched between two electrodes (dark grey) that are printed onto polymer film (light grey). a) Initially, the capacitance value depends on the electrode area A, the relative permittivity ε_{r0} and the distance d_0 between the electrodes. b) On pressure application, the distance d(P) reduces and $\varepsilon_r(P)$ increases with the pressure P.

for example, a thin layer of PDMS. On the other electrode, the structured PDMS is screen-printed with hills of as equal size and height as possible.

Figure 4.9a shows three exemplary hills approximately in the form like they are screen-printed. The designed diameter of the pillars is indicated by the circle at their bottom and the height d is marked by the orange arrow. The volume of the straight, equilateral prism formed between the central axes of the three hills as shown in the figure is half of the effective volume per pillar in the sensor. Eq. 4.6 gives the formula for the effective volume per pillar with the centre-to-centre distance a between the pillars. On pressure application perpendicular to the plane of the electrodes, these hills have space to expand laterally and can preserve their volume. This approach reduces the volumetric compression and a closer accordance to Hooke's law may be reached. Several researchers evaluated that PDMS with an aspect ratio between height and diameter of around 0.5 to 1 deform linearly with applied pressure. [273], [289]–[291]

$$V_{eff} = \frac{\sqrt{3}}{2} \cdot a^2 \cdot d_0 \qquad \text{Eq. 4.6}$$

With the assumption that the volume of the PDMS layer in this sensor is not compressed at all (Poisson ratio equal to 0.5) and that air can move in and out of the sensor, the percentage of PDMS between the electrodes increases with increasing pressure. The factor f_V is the volume fraction of PDMS hill in the effective volume per pillar (to Eq. 4.7). We approximated it by using a paraboloid with the radius r_0 and the height $d_0(r_0) = 0.542\ r_0 - 18.6\ \mu m$ (see Eq. 2.4 on page 55).

$$f_V = \frac{V_{hill}}{V_{eff}} = \frac{\pi \cdot r_0^2}{\sqrt{3} \cdot a^2} \cdot \frac{d_0(r_0)}{d} \qquad \text{Eq. 4.7}$$

This means that the effective relative permittivity increases depending on the distance between the electrodes. In literature, many different approaches are presented to calculate the effective permittivity of mixtures. An overview can be found in the work of Kärkkäinen [292]. The hill structure can be approximated by cylinders having the same volume. Then, the comparably simple Maxwell-Garnett mixing rule (Eq. 4.8) can be employed to calculate the effective relative permittivity ε_{eff}

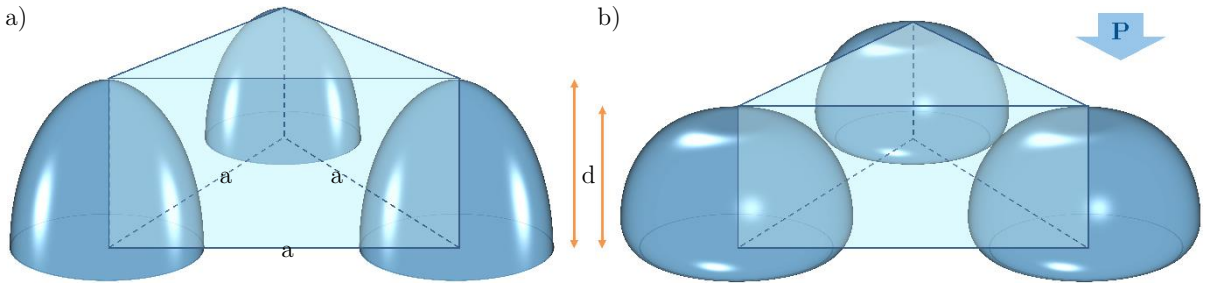

Figure 4.9. Three PDMS hills and the volume formed by the prism between the centres of the pillars (edge length a) and their height d. The pillars without pressure (a) are deformed on pressure application (b) reducing their height d and preserving most of their volume by expanding laterally.

depending on the relative permittivity of PDMS ε_{PDMS} and of air ε_{Air}. [292] Having $\varepsilon_{Air} = 1$ and $\Delta\varepsilon = \varepsilon_{PDMS} - \varepsilon_{Air}$, this formula can be simplified.

$$\varepsilon_{eff} = \varepsilon_{Air} + 2f_V\varepsilon_{Air}\frac{\varepsilon_{PDMS} - \varepsilon_{Air}}{\varepsilon_{PDMS} + \varepsilon_{Air} - f_V(\varepsilon_{PDMS} - \varepsilon_{Air})} = \frac{2 + \Delta\varepsilon(1 + f_V)}{2 + \Delta\varepsilon(1 - f_V)} \qquad \text{Eq. 4.8}$$

Figure 4.10a shows a **Numerical evaluation** of the effective relative permittivity for different radii of the hill from 100 µm to 500 µm at a distance of 1 mm. Due to the assumption of volume conservation, the minimum distance between the electrodes is reached when $f_V = 1$. Theoretically, this means that the pressure is strong enough to press out all air. This describes the maximum possible deflection of the electrodes max(Δd) and leads to a relative permittivity of 2.7. The percentage of the maximum possible deflection from the initial distance can be read from Figure 4.10a at the points where the curves reach the permittivity of 2.7. For a larger radius, this happens earlier and the initial permittivity is higher because there is more silicone present. For small radii below 200 µm, a large deformation above 60 % is necessary to change the relative permittivity significantly. For larger radii, the permittivity changes already at a low displacement of a few percents.

The effect of both, the displacement and the change in relative permittivity on the capacitance was investigated and the calculated capacitance is shown in Figure 4.10b. The figure and all calculations assume that the volume of the silicon rubber is not compressible. Thus, the deflection of the electrodes Δd can only reach the maximum value max(Δd). The figure shows the deflection of the top electrode on the x-axis and the resulting theoretical capacitance on the y-axis. For low displacements mainly the height of the hills is the dominant effect that leads to a higher capacitance for smaller hills. At larger displacements, the rising permittivity can overcome the displacement, e.g. the capacitance at 50 % displacement is higher for a 500 µm hill than for a 300 µm hill. The dashed lines indicate the theoretical capacitance without considering an increase in the relative permittivity. It can be seen that for low deflections or low radii, the main factor influencing the capacitance value is the distance between the electrodes. Only for large and high hills, the increase in relative permittivity plays a role. For example, the dashed line only increases minor for the 500 µm radius (yellow), whereas the solid line increases much faster.

The simulations were verified by **Experiments** with the Force and Pressure Setup described in the Materials and Methods Section M.4.1 that was constructed during the work on this thesis. To evaluate the behaviour during the interaction with a human, an exponentially increasing force profile was developed. A minimum force of 10 mN was necessary to make the force application bar rest on top of the sensor and presses the top electrode slightly to ensure that it is flat. Every five seconds, the force was increased by 20 % starting from 10 mN up to 15 N, the maximum allowable force. The resulting pressure starts at around 500 Pa and increases by 20 % every five seconds up to about

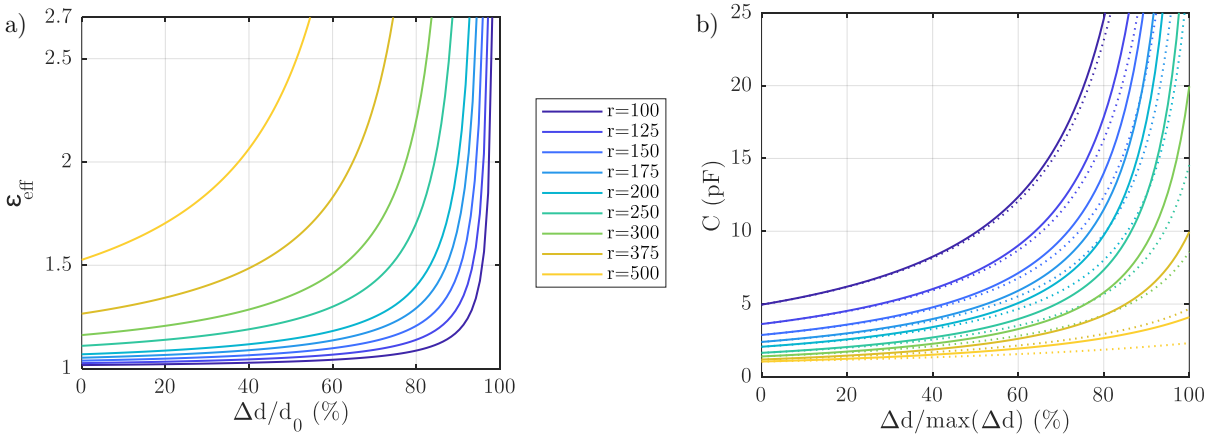

Figure 4.10. a) Effective relative permittivity ε_{eff} for a displacement of the electrodes Δd from an initial distance d_0 and b) theoretic capacitance value for Δd in respect to the maximum possible deflection and for different radii r of the hills at a distance of a = 1 mm. The legend applies to both graphs.

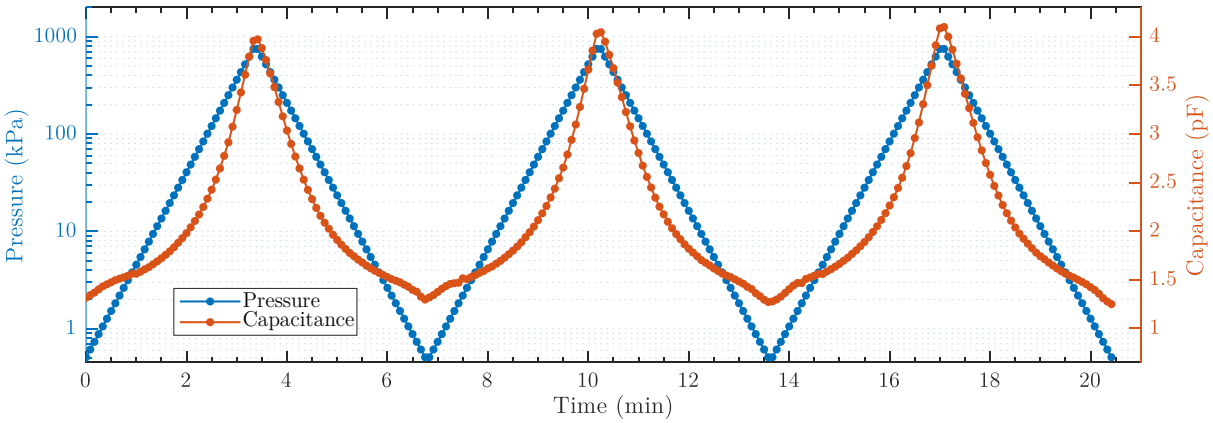

Figure 4.11. The applied pressure "ramp" profile (blue) and the capacitive pressure sensor's response (red) for three consecutive cycles.

750 kPa. After reaching the maximum, the force was decreased with the same steps down to 10 mN. Such a cycle was repeated three times to be able to detect drifts in the sensor response. Figure 4.11 shows the pressure profile as blue markers, which will be called the "ramp" profile in the following.

At each step, the current pressure was held for five seconds and the capacitance was measured before increasing it to the next step. The red markers show the resulting capacitance value for a pillar structure with a centre-to-centre distance of 1000 µm and a radius of 500 µm. The initial capacitance value at 0.5 kPa was about 1.31 pF and it increased up to 3.97 pF during the first cycle and then decreased to 1.32 pF again. This was stable for the next two cycles with maxima at 4.04 pF and 4.10 pF and, finally, another minima at 1.27 pF. It can be seen, that the minimum values are stable for ± 50 fF and the maximum values for ± 103 fF. The latter has a slight drift to higher values. With this, we can determine our sensor response to 315 % of the baseline value, which is much higher than other reported values [287], [293], [294].

The capacitance curve is steep for low and high forces with an intermediate lower gradient. This results in a lower sensitivity in this region with respect to a relative increase in pressure. The sensitivity at high pressures is still high and no saturation was found until the limit of our setup. This indicates, that the sensor may be applied for much higher pressures, too. Furthermore, the capacitance curve on the decreasing side is shifted slightly towards the right in comparison to the pressure curve at medium to high pressures. This shows that the sensor has a slight hysteresis. Still, the capacitance value follows the force curve within a few seconds and the measurement is repeatable for multiple cycles. It has to be mentioned, that the entire characterization ran for about one hour. This shows that the baseline of the sensor is stable at least if both force-exerting objects are grounded.

In between each of the cycles, a different force profile was exerted on the sensor. It uses the same amplitudes, but between each step, the force is set down to 10 mN for 5 s. This "pulse" profile is visualized in Figure 4.12 with blue markers and blue lines that show the rectangular pressure pulses. The pulse profile was repeated three times in total for each sensor. The measurement of the capacitance was conducted always after 5 s of force stabilization time and is indicated by the location of the blue markers. The red markers show the measured capacitance values for the high and the low pressures on two separate curves. The almost constant lower curve proves that the tested sensor is stable for pressures across three orders of magnitude. All measured capacitance values after a relaxation time of 4 – 5 s lie between 1.23 pF and 1.30 pF for the presented cycle and between 1.22 and 1.34 pF for all three cycles. This low variation of less than 5 % from the mean value shows the high baseline stability of our pressure sensors. The capacitance values measured at the end of the pressure peaks are related to the pressure almost similarly to the ramp profile. The major difference is, that the curve has a higher degree of symmetry, which results in a decreased hysteresis.

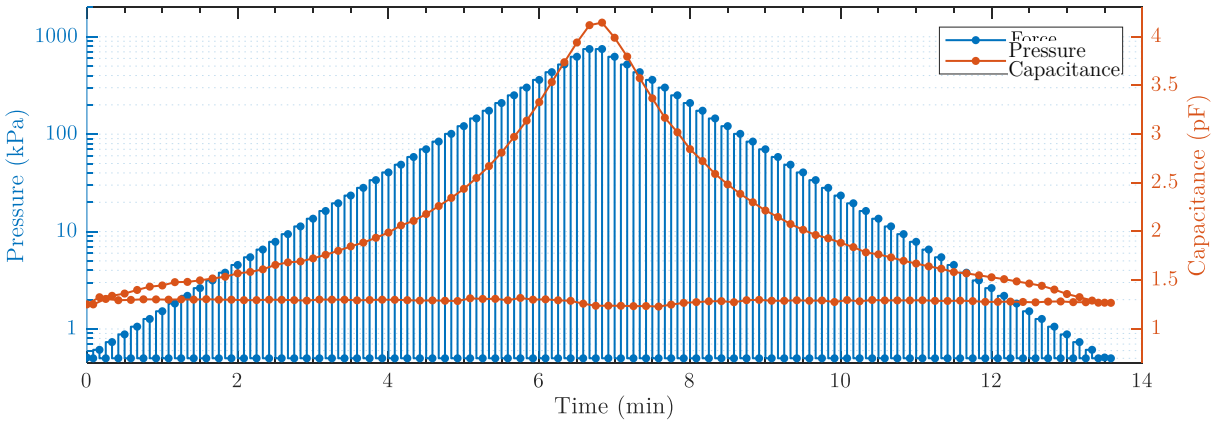

Figure 4.12. The applied pressure "pulse" profile (blue) and the capacitive pressure sensor's response (red) for one out of three cycles.

Figure 4.13 shows the hysteresis curves for both force profiles by displaying the measured capacitance over the applied pressure. The three cycles are shown in different colour and the response to increasing pressure is marked by round markers connected by a solid line and to decreasing pressure by triangular markers connected by a dashed line. All measured values are almost at the same location and hidden by the markers of the next cycle. The mentioned assumption, that the sensor has only a small drift can be confirmed for both profiles. The highest drift can be found for the high pressures. The main difference between both graphs is the size of the hysteresis, which is small (below 50 fF) for pulsed pressures and can be up to 300 fF for ramp pressures. These values are equivalent to about 15 % and 50 % of the pressure value. The hysteresis width gives the point of the lowest accuracy in the measurement range. Thus, we can claim, that our pressure sensors are able to measure pressures within three orders of magnitude between 0.5 kPa and 750 kPa with an accuracy of at least 50 % for varying pressures and 15 % for pulsed pressures.

This accuracy can be extended to increasing pressures as shown in Figure 4.14a, which shows the last cycle of both the ramp and the pulse pressure profile. The response to increasing pressure during the ramp profile is congruent to the response to pulsed pressures. This figure shows, that the measured capacitance value is linear with the square root of the applied pressure. This was visualized in the figure by exchanging the logarithmically scaled axis by a square-root scaled axis. This extends to pressures above 2 kPa and will be used for further graphs regarding our pressure sensors.

The response time is the longest for high pressures. Figure 4.14b shows the time response of the sensor to high pressures. The force setup is able to apply the set force within tens of milliseconds and it can be seen, that the sensor follows this instantly. The limit of the querying of force and capacitance is 200 ms and at the first measurement after setting the force, the change in the capacitance value

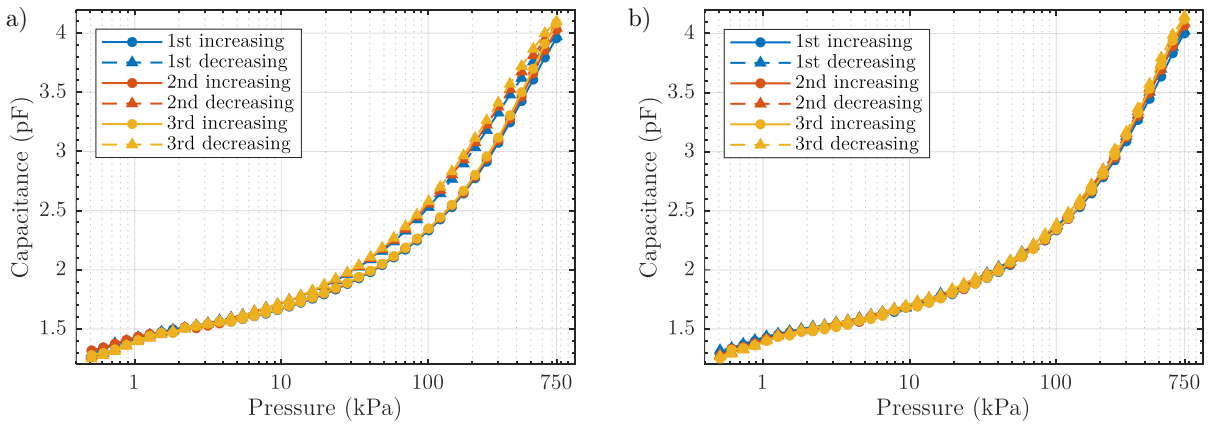

Figure 4.13. Hysteresis curves of the response of the capacitive force sensor for three cycles of pressure application with two different pressure profiles: a) The ramp profile and b) the pulse profile.

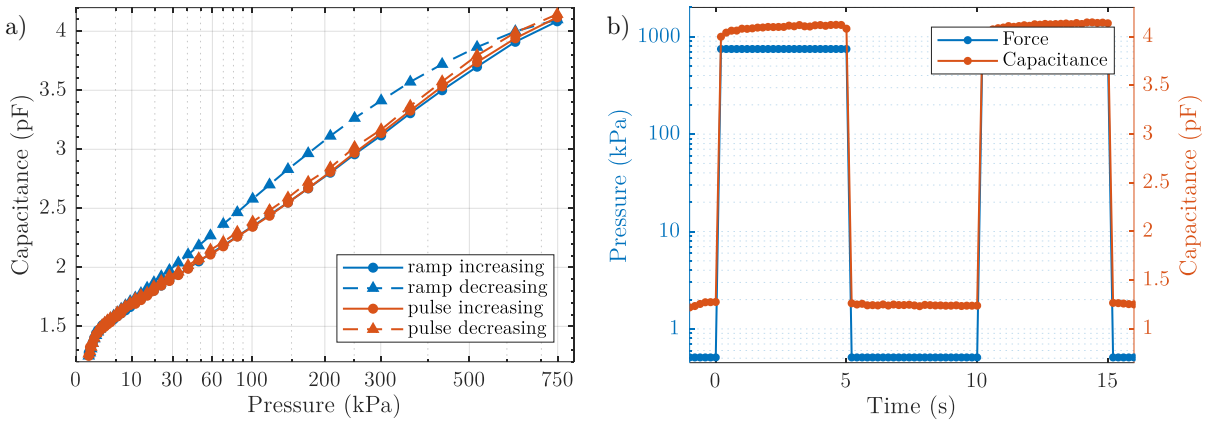

Figure 4.14. a) The response of a sensor with hills of a diameter of 375 µm during the last cycle of the ramp and the pulse pressure profile over an axis scaled with the square root of the pressure. b) Time response of the printed pressure sensor on two pulsed pressure of 750 kPa for 5 s and then return to 0.5 kPa holding pressure.

already reached 96 % of the final value. After reducing the force, the capacitance value decreases instantly and after 200 ms is just 0.9 % higher than the final value after 5 s. This shows that our sensor has a low response time in the high microseconds range and is faster than other reported sensors [287], [293], [294]. For low pressures, the response time is even faster.

In the following, we will investigate the **Influence of the radius of hills**. When measuring force sensors with a small radius, we found, that these were shorted at a certain point. We found, that the lowest hill radius was 175 µm to build a sensor that can measure pressures up to 750 kPa. Figure 4.15a shows the response of this sensor to the third cycle of both, the ramp and the pulse pressure profile. We found that both the responses in the idle position (0.5 kPa) and in the maximum pressure of 750 kPa were much higher than for the larger hill radius. These were 3.0 pF and 12.3 pF, which corresponds to a sensor response to high pressures of 410 %. However, the hysteresis for decreasing pressures is much larger (3.0 pF), which is about the value of the base capacitance. The time response of the sensor with smaller hills is shown in Figure 4.15b and it can be seen, that the sensor is still fast, but slower than the one with the larger hills. The sensor's response reached 89 % of the final value after 200 ms and 96 % after 600 ms. This is still sufficient for most applications. However, the hysteresis may not allow precise measurements.

In the following, we want to discuss in detail the results of the characterization of many sensors with varying hill radii. We designed a screen as shown in Figure 2.36 on page 53 with radii starting from 25 µm up to 375 µm. As the small hills were not printed, we only characterized seven sensors with the following radii: 125 µm, 150 µm, 175 µm, 200 µm, 300 µm, and 375 µm. Figure 4.16 shows the capacitance values of the seven sensors with the radii indicated in the legend under pressure. A

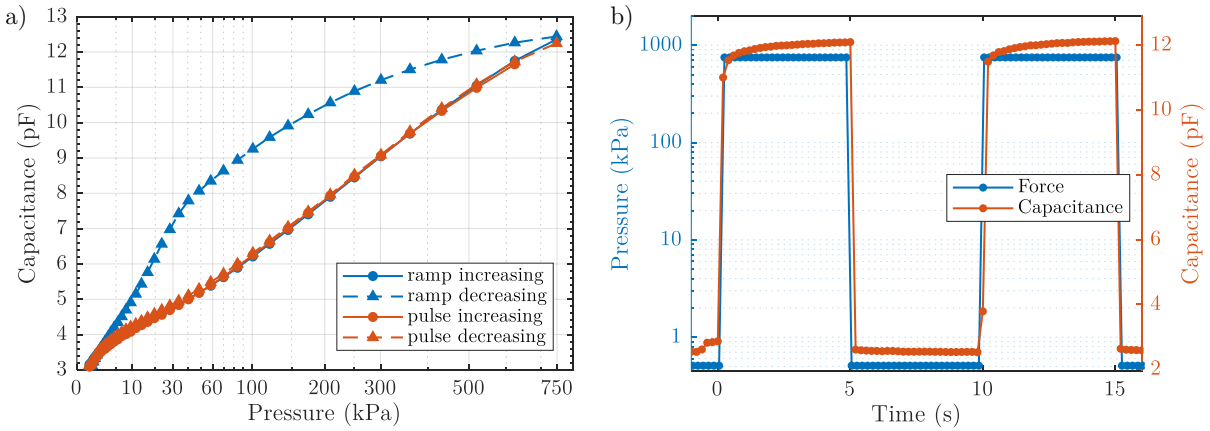

Figure 4.15. a) The response of a sensor with hills of a diameter of 175 µm during the last cycle of the ramp and the pulse pressure profile. b) The time-response of the same sensor.

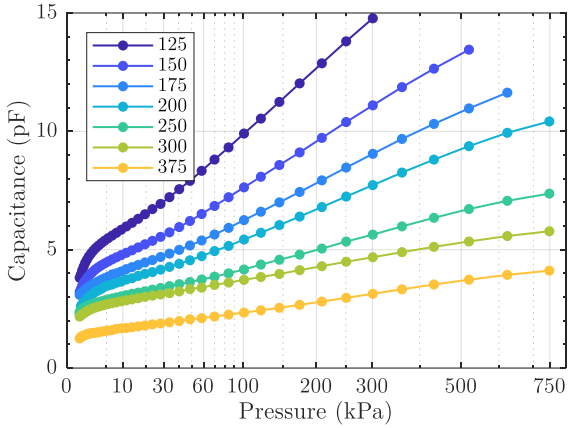

Figure 4.16. Capacitance values during increasing pressure for the seven sensors that possess hills with varying radii as indicated in the legend.

clear decrease of the curves for higher radii can be found, which is in accordance with theory as the larger hills are also higher and the distance between the electrodes is larger. The steepness of the curves increases as well.

To compare the different sensor responses, we chose four characteristic points on the curves. Figure 4.17a shows the following measured points as round markers. The maximum capacitance value (meas. max) is shown by round blue markers. A clear increase can be found towards lower radii, which makes sense because the amount of silicone rubber is less and the sensor is more compressible. It has to be noted, that the sensors with the smallest two hill radii (125 µm and 150 µm) were shorted at a certain force and the figure shows the maximum capacitance at the maximum pressure before shorting by empty round markers. These were about 300 kPa and 500 kPa for increasing pressures and about 100 kPa and 350 kPa, respectively, for the decreasing pressure profile.

The round red markers show the average capacitance (meas. min) when the sensor is in the idle position at 0.5 kPa. These are slightly increasing towards smaller radii, which is in accordance to the theory as the height of these hills are smaller as shown in Section 2.3.4. The maximum hysteresis is shown by round green markers and was measured during the third cycle of the ramp profile between the increasing and the decreasing curve. Sensors with a high hill radius show a negligible hysteresis, whereas, towards lower diameters, the hysteresis increases. The hysteresis only appears for decreasing

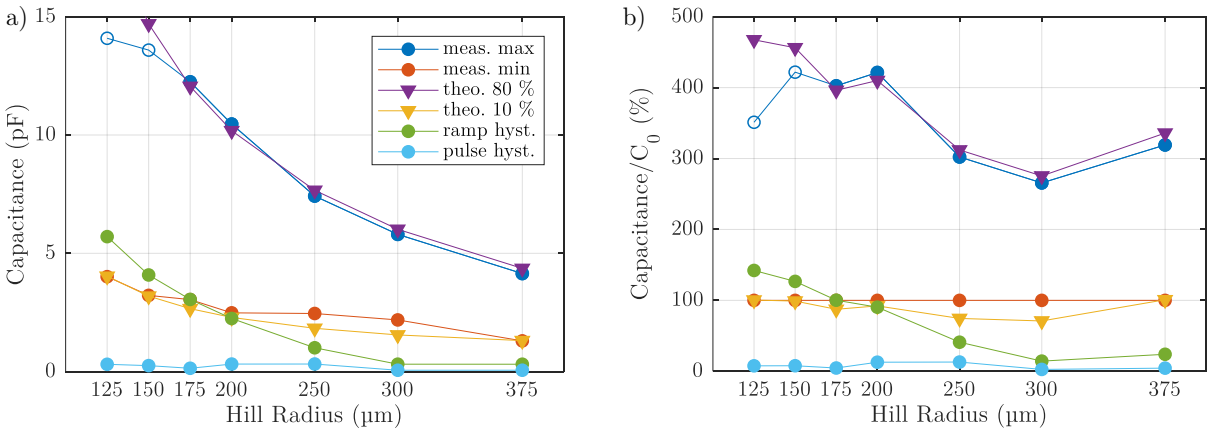

Figure 4.17. Selected sensors' measured (round markers) and theoretic (triangular) response values for sensors with varying hill radius. Blue markers show the measured capacitance at the maximum pressure (750 kPa, filled) or at the highest pressure before shorting (empty), red ones at the idle position (0.5 kPa). Purple markers show the theoretic capacitance at 80 % of the maximum possible deflection of the top electrode and yellow ones at 10 %. Green markers show the maximum measured hysteresis in the ramp profile and cyan markers the maximum hysteresis in the pulse profile. a) Absolute capacitance values of the selected points and b) capacitance values in respect to the capacitance C_0 in the idle position.

pressures and disappears within seconds or less after the pressure is decreased completely. Cyan markers in Figure 4.17a show the low hysteresis of below 320 fF for the pulse profile.

To compare the measured values to the theoretical model presented at the beginning of this subsection, we chose two arbitrary points on each of the curves from the theoretical model shown in Figure 4.10b on page 104. This figure shows the deflection of the top electrode in relation to the theoretic maximum of its deflection under the assumption that the volume of the silver rubber remains constant and fills equally the entire volume between the two electrodes. We chose a deflection of 10 % as the idle position with 0.5 kPa because the theoretic capacitance values were similar to the measured ones. These are shown by yellow triangular markers (theo. 10 %) in the figure and match the measured values in four points accurately. The capacitance values during the maximum pressure of 750 kPa were similar to the theoretic values at 80 % deflection. The values are shown by purple triangular markers in Figure 4.17 and are following the shape of the capacitance values at the maximum pressure accurately. The closest values for all measured values lie between 78 % and 83 % of the maximum deflection.

Figure 4.17b shows the same values with respect to the capacitance in the idle position C_0, which is shown by the red line with the red round markers. It can be seen that the sensor's response can be tuned between 270 % and 420 % depending on the radius and height of the hills. A trend towards higher sensitivities can be found for lower radii, especially if one considers that the baseline of the sensor can be easily affected by the positioning on the measurement stage. Assuming that the yellow line displays the minimum more accurately, this trend is clear. The second trend apparent in the figure is the increasing hysteresis for smaller pillars. For large radii, the hysteresis can be as small as 14 % of the sensor's baseline whereas for small radii it can be up to 140 %, which is much higher than the baseline of the sensor. It has to be mentioned, that the hysteresis only occurs for reducing forces and disappears if the pressure is reduced completely for a second or even less. This is visualized by cyan markers that remain below 13 % for all measured sensors.

Sensitivity - Figure 4.18a shows the evaluation of the sensitivity of our sensors for varying hill radius at different pressure points. In this plot, the sensitivity was defined as the linear derivation at a certain pressure. The sensitivity of all our sensors is the highest for low pressures. The maximum sensitivity of 81 %/kPa is reached for the smallest radius of 125 µm at the lower end of our pressure profiles (500 Pa), which is the highest published value to our knowledge. The larger the hills, the smaller the sensitivity reduces down to about 15 % for the largest hill with a radius of 375 µm. For higher pressures, the linear sensitivity S_{lin} decreases to values as low as 0.3 % for high pressure on the sensor with the largest hill radius.

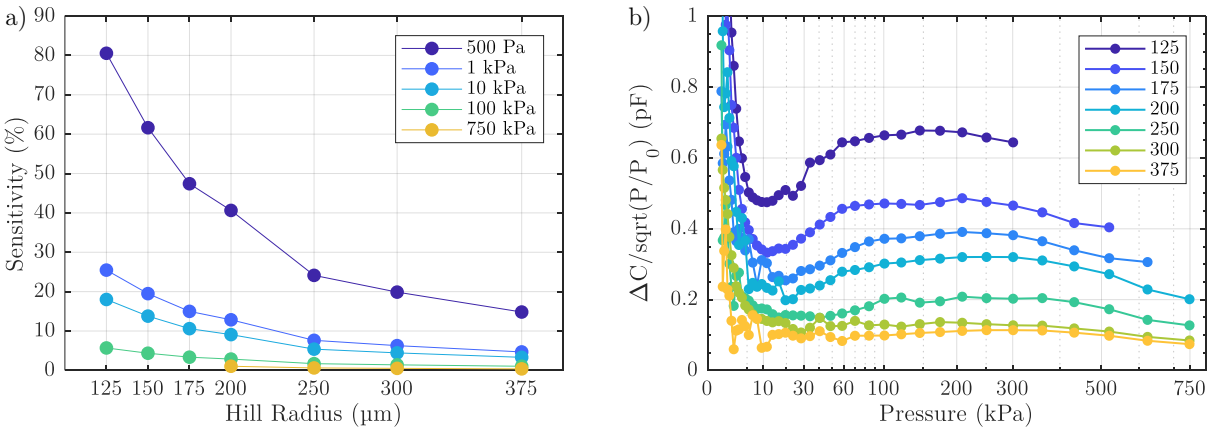

Figure 4.18. a) The linear sensitivity of our capacitive pressure sensors with varying hill radius at different pressure levels. b) Capacitance change per square root of the normalized pressure (to 1 kPa) on the different sensors (radius indicated in the legend) over the pressure range.

As we found out previously that our sensors almost linear with the square root of the pressure, we investigate this in detail in Figure 4.18b. It shows the change of the capacitance value divided by the difference of the square roots of the two adjacent pressure values (± 20 %) normalized to 1 kPa (see Eq. 4.10). The figure shows that all sensors have a high sensitivity of more than 0.5 pF/dS for low pressures. At pressures above 10 kPa, sensors with hills having a high radius show an almost constant sensitivity over two orders of magnitude.

$$S_{sqrt} = \frac{C_{+20\%} - C_{-20\%}}{\sqrt{P_{+20\%}} - \sqrt{P_{-20\%+}}} \qquad \text{Eq. 4.9}$$

If the pressures are not too small, the relations between the measured capacitance C(P) and the pressure (P) in Eq. 4.10 give a good approximation. The maximum error is less than 30 % for this simple formula.

$$C(P) = S_{sqrt} \cdot \sqrt{\frac{P}{P_0}} + C_0 \qquad P = \left(\frac{\Delta C}{S_{sqrt}}\right)^2 \cdot P_0 \qquad \text{Eq. 4.10}$$

The logarithmic sensitivity that is an important criterion for human-machine-interaction is evaluated and discussed in the following. Figure 4.19a shows the relative change of the capacitance value per decibel of pressure change. Again, it can be seen that sensors with smaller hills are more sensing than sensors with larger hills. All sensors show a minimum sensitivity of about 10 fF/dB to 50 fF/dB at pressures around 7 kPa. The maximum sensitivity of all sensors is one order of magnitude higher and between 1.1 pF/dB and 5.3 pF/dB at pressures around 500 kPa.

For the measurement of the change of capacitance, it is important how high the sensitivity is in respect to the amplitude of the signal. This relative sensitivity is shown in Figure 4.19b. It can be seen that the sensitivity of all sensors is approximately in the same region between 7 % and 35 % with a tendency to achieve higher relative sensitivities with smaller hills. All sensors are also more sensing at higher pressures. It has to be noted that the absolute sensitivity can be increased by increasing the electrode area, whereas the relative sensitivity is independent of the area and shows the normalized behaviour.

In this section, we could present capacitive pressure sensors with a high response of up to 420 % for a pressure of 750 kPa in comparison to 0.5 kPa and a maximum error of less than 13 % down to only a few percents. The sensor responses are linear to the root of the pressure values. The sensors consist only of a structured dielectric on a silver electrode that is then flipped and attached to another electrode. All components can be produced by screen printing followed by a lamination process. The structuring of the dielectrics as small hills makes the sensor easily scalable as the sensor response should not change. A larger area would linearly increase the capacitance at all pressure points. In comparison to other sensors reported in the literature, our sensor shows a much higher sensitivity,

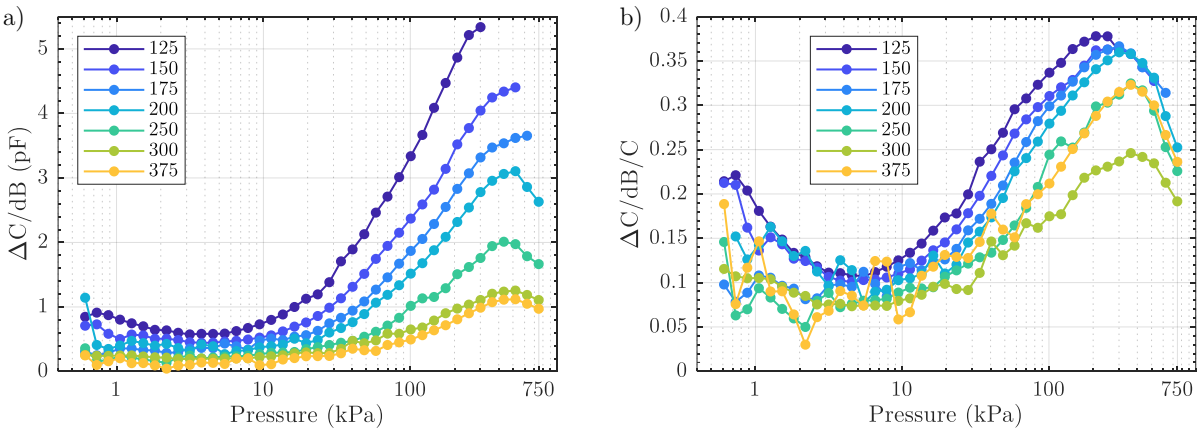

Figure 4.19. a) Absolute and b) relative logarithmic sensitivity of our seven capacitive force sensors.

less error, and is small and scalable. In 2014, Mannsfeld et al. published in Nature Materials a sensor with a structured dielectric that is sensitive (55 %/kPa) to small pressures below 2 kPa and 15 %/kPa for pressures at around 5 kPa [287]. Lipomi et al. published in Nature Nanotechnology capacitive pressure sensors with a linear sensitivity of only about 25 %/MPa up to 1 MPa [279]. One of our sensor configuration (r = 125 µm) has a sensitivity of 80 %/kPa for small pressures and 25 %/kPa at around 5 kPa. Unfortunately, Mannsfeld et al. do not show the hysteresis of their sensor and we have to assume that their sensors show a large hysteresis. Our most sensible sensors show a large hysteresis, too. Yet, we also showed how to overcome it by using larger hills. Maddipatla et al. showed a capacitive pressure sensor with an unstructured 1.15 mm thick dielectric and an electrode area of about 180 mm^2. They achieved a change of capacitance of only 0.6 pF from 0 kPa to about 340 kPa with a relative change of only 8.3 %. [293] Our sensors achieve a capacitance change between 2.0 pF and 10.8 pF for the same range with a change of 156 % to 270 %. Cagatay et al. achieved a relative change of 20 % between 0 and about 50 kPa with a capacitive sensor with a structured dielectric [294].

4.2.4 Capacitive Shear Force Sensors

Next, to the described normal pressure and force sensors, we also investigated shear force sensors. This section bases on our conference contribution [295] but is extended to highlight certain aspects. In literature, several different capacitive sensors are described and demonstrated. We conducted an evaluation of some approaches that are compatible with printing techniques. For example, Chase et al. [296] presented a shear and normal force sensor with five square electrodes. A single square electrode is located on the top side of the sensor. Four electrodes divide the bottom side of the sensor into four quadrants and form four capacitances between each of them and the top electrode. An elastic dielectric is compressed on normal force increasing all four capacitances due to the reduced distance between the electrodes. On shear force, the top electrode moves across the bottom electrodes and increases the area of some of the capacitors while decreasing the others. The amplitude of the shear force and the direction are then determined by calculating the ratios of the four single capacitance values. The relative change in the capacitance values in this configuration are small, especially for shear deformations. In 2013, Dobrzynska and Gijs [297] presented an approach that uses finger-structured patterns as the top and the bottom electrode. They built up the entire capacitive structure as a stack with evaporation and coating steps. We wanted to transfer the knowledge of the printed normal pressure sensors with the structured dielectrics to this design.

Similar to the previous section, we printed the electrode structures onto two separate sheets of PET and then flip the top print and press it with the print side down onto the bottom print. Figure 4.20 shows the design of our shear force sensor that consists of four parallel plate capacitors C1 .. C4. Each of them is formed between a finger structure at the bottom that has the size of one of the four squares plus a wiring. The bottom prints are shown in yellow and the top print is shown in dark blue. The overlapping area of the top and the bottom print is shown in green and the dielectric spacer (PDMS) is shown in beige. The contact pads on the right side are connected to each of the electrodes. They are all on one side and as far away from the sensing area as necessary to be able to contact them outside of our shear force setup (see Materials and Methods section M.4.3). The central one is connected to another contact pad that exists on both print patterns and links the top and bottom print next to the dielectric layer. We decided to number the capacitance values with the location of the contact pads from top to bottom. Thus, the counting starts with C1 in the top right corner and continues counter-clockwise.

Figure 4.20 shows a magnification of a part of all electrodes on the right side and allows a closer look at the design of the electrodes. Again, the bottom electrodes are shown in yellow, the top electrodes in dark blue and the overlapping areas in green. The top right and bottom left electrodes

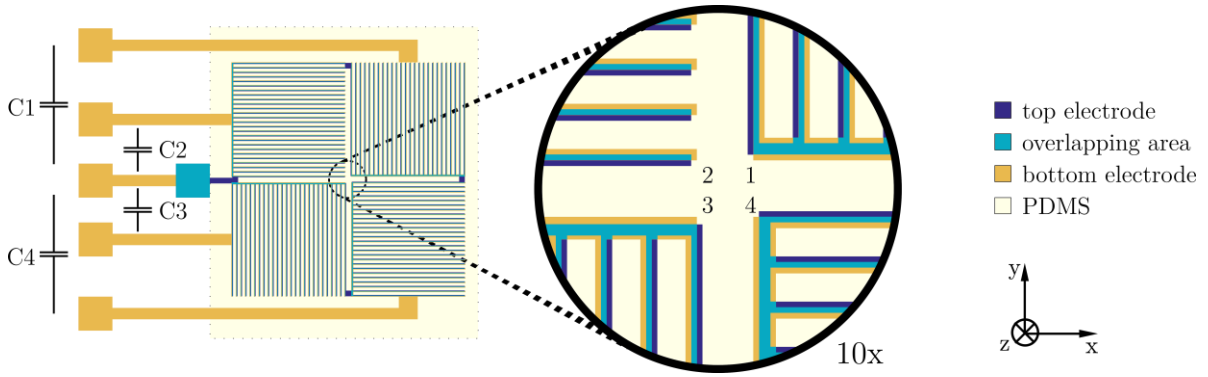

Figure 4.20. Design of our normal and shear force sensor with the four sectors that form the four capacitances C1 .. C4 between the separated bottom electrodes and the single top electrodes (central contact pad). The magnification shows that the electrodes are designed that the respective capacitance is only sensitive to forces in either the x- or in the y-direction. Adapted from the author's publication [295].

change the overlapping area of the fingers if a force in the positive or negative x-direction is applied. For positive forces in the x-direction, the overlapping area increases for C1 and decreases for C3 and vice versa for negative forces. The maximum allowable shift in the x-direction is half of the electrode width. For shear forces in the positive or negative y-direction, the overlapping area does not change until the same limits because the bottom electrodes are larger than the top ones. The top left (C2) and bottom right (C4) electrodes increase and decrease their overlapping area for a positive force in the y-direction. The tip of the fingers as can be seen in the magnification of C2 is extended for the bottom layer to allow a movement in x-direction without altering the overlap area.

Model - The sensor was modelled using a simple approach with a parallel-plate capacitor formed by the top and bottom electrodes. An exactly 50 % overlap area for the fingers, a 100 % overlap of the connection wires between the electrodes, and no influence of the wiring and the pads were assumed. The areas of all four squares were designed identically with the area $A = A_1 = A_2 = A_3 = A_4$. We assumed that the dielectric is equally thick across the entire sensor with a thickness of d. Therefore, the basic parallel plate capacitor formula (Eq. 4.11) can be employed for the initial capacitance C_0.

$$C_0 = \varepsilon_0 \varepsilon_r \frac{A}{d} \qquad \text{Eq. 4.11}$$

A force in z-direction reduces the distance by Δd_z, which increases the capacitance of all four capacitors. A force in x-direction increases the area of the capacitor C_1 by ΔA_x and decreases the area of C_3 to the same extent while not influencing C_2 and C_4. The resulting capacitance values are shown in the first equation in Eq. 4.12. Similarly, a force in y-direction increases the overlap area of capacitor C_2 by ΔA_y and decreases the area of C_4 to the same extent and not alter C_1 and C_3 as shown in the second equation.

$$C_{1/3} = \varepsilon_0 \varepsilon_r \frac{A \pm \Delta A_x}{d - \Delta d_z} \qquad C_{2/4} = \varepsilon_0 \varepsilon_r \frac{A \pm \Delta A_y}{d - \Delta d_z} \qquad \text{Eq. 4.12}$$

The average value of all four capacitances cancels out all area changes caused by x- and y-forces because we assumed that an area increase of one capacitor is equally compensated by an area decrease of another. The average value only depends on the distance between the parallel plates according to the normal force. This force in the z-direction can be determined by the change of the calculated average capacitance C_z divided by the initial capacitance C_0 as shown in Eq. 4.13. An approximation for small deflection of the top electrodes is given that shows that for small forces, the behaviour is almost linear.

$$C_z = \frac{1}{4}\sum_{n=1}^{4}\frac{C_n}{C_0} = \frac{d}{d - \Delta d_z} \approx 1 + \frac{\Delta d_z}{d} \qquad \text{Eq. 4.13}$$

The increase or decrease of C_1 and C_3 for a shear force in the positive direction can be expressed in relation to C_z as shown in Eq. 4.14. Similarly, the expression for C_2 and C_4 is shown.

$$C_{1/3} = \left(1 \pm \frac{\Delta A_x}{A}\right) \cdot C_z \cdot C_0 \qquad C_{2/4} = \left(1 \pm \frac{\Delta A_y}{A}\right) \cdot C_z \cdot C_0 \qquad \text{Eq. 4.14}$$

A subtraction of each pair of capacitances leads to an expression that reduces the z-dependence and can serve as indicators for the applied shear forces in x- and in the y-direction as shown in Eq. 4.15. Each value remains constant for a force in the perpendicular direction because it is only depending on the changes in the area. If the subtraction of the pairs is divided by C_z, also the z-direction dependence can be eliminated. It has to be noted, that the typical changes of the capacitances are low. A small noise caused by the measurement of the capacitances can introduce a large error when calculating this division.

$$C_x = \frac{C_1 - C_3}{2 \cdot C_z \cdot C_0} = \frac{\Delta A_x}{A} \qquad C_y = \frac{C_2 - C_4}{2 \cdot C_z \cdot C_0} = \frac{\Delta A_y}{A} \qquad \text{Eq. 4.15}$$

A numerical simulation was conducted to estimate the amount the capacitances change and the influence of the distance reduction to the difference of the capacitance pairs. One capacitor consists of 31 fingers with a width of about 60 µm and a length of 5.95 mm. the connecting bridge has an area of 1.22 µm². For the calculations, we took a 40 µm thick dielectric in the idle position and the relative dielectric permittivity of PDMS was taken as 2.5 [298]. The relative change of the capacitances due to a displacement of the top electrode by a certain distance on the impact of a normal force in the z-direction is depicted as a blue line in Figure 4.21a. The linear approximation according to Eq. 4.13 is drawn in red. It can be seen, that the change for the capacitance is about linear for a small displacement until about 4 µm, which is 10 % of the total dielectric's thickness. At a higher displacement, the capacitance changes at a higher rate according to Eq. 4.12. As PDMS is hardly compressible, we assume that it is a reasonable assumption that the displacement is small enough to still follow a linear curve. Figure 4.21b shows the normalized capacitance for a shear force in the +x-direction. As shown in Eq. 4.14 these are linearly dependent on the force-induced area change, which in turn is linear to the displacement. The slope of C_1 is positive with the same gradient than C_3 is decreasing. A subtraction of C_3 from C_1 results in a linear relation, too. Force in x-direction do not change the capacitances C_2 and C_4. Similar results can be achieved for forces in the y direction and C_2 and C_4 are changing while the other two remain constant.

In the work of Dobrzynska and Gijs [297], it is assumed that all changes are linear and independent of other forces. When calculating the changes of the capacitances, one notices, that this is not true and already small displacements of the top electrode in z-direction have a large impact on all capacitances and simultaneously occurring shear forces are overestimated. Figure 4.22a shows the capacitance values during a shear displacement for five different normal loads that lead to a displacement

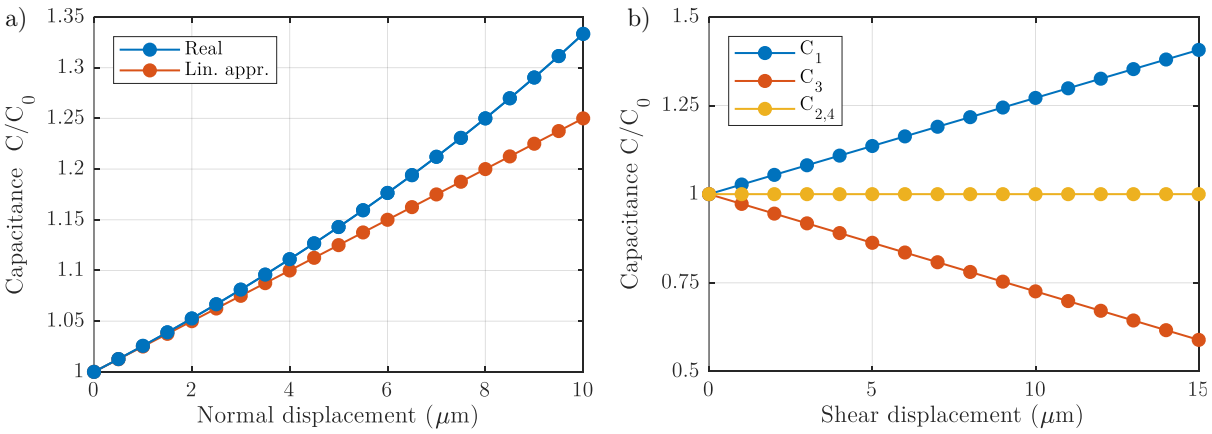

Figure 4.21. A theoretical model of the sensor's response to a displacement due to a) normal force in the z-direction and b) shear force in the x-direction.

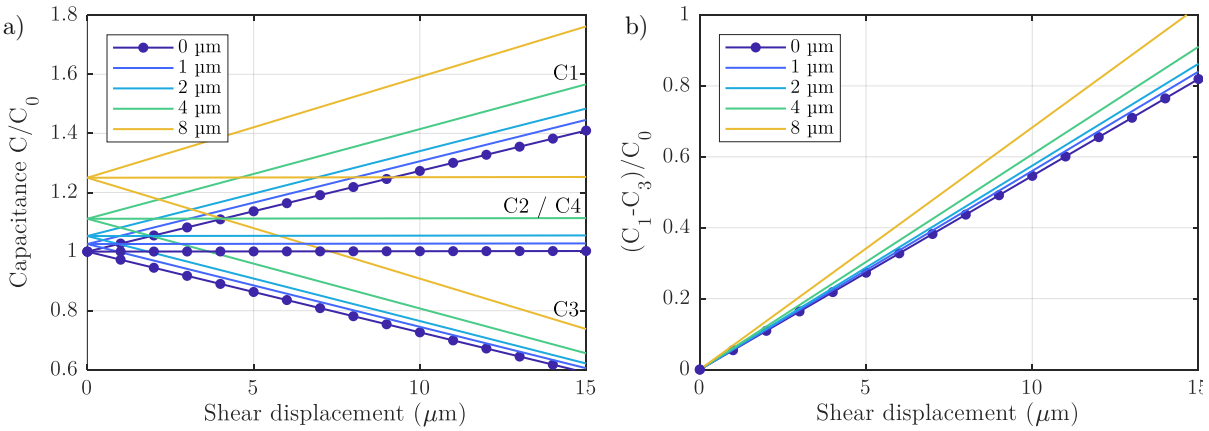

Figure 4.22. Calculated capacitance values for the four individual capacitors for a varying shear load in the y-direction at five different constant displacements (0 ... 8 µm) due to a normal force. a) Capacitance in relation to the initial capacitance C_0 and b) the subtraction of the two x-sensitive capacitances relative to C_0.

of 0, 1 µm, 2 µm, 4 µm, and 8 µm indicated by the different colours in the graph. The labels on the right side indicate which group of lines describes which capacitance. C_1 is increasing, C_3 is decreasing, and C_2 and C_4 are identical for any x- and/or z-force. In blue, the capacitance curve is identical to the values shown in Figure 4.21b. A higher normal displacement not only shifts all curves to a higher level but also increases the slope. This is highlighted in Figure 4.22b, which shows the subtraction of C_3 from C_1. For small displacements in the z-direction, the shear force can be well estimated by only looking at the subtraction of the two x- sensitive capacitances. For either a high normal force or a high shear force, a deviation of several tens of percent occurs. This is the reason, why we suggest the division by the average capacitance to eliminate the effect.

Production - We decided to employ inkjet printing as the manufacturing technique for the sensor electrodes because the layer thickness is approximately one order of magnitude smaller than for screen printing. Figure 4.23 shows the inkjet-printed finger structures for two different finger geometries. On the left, fingers with a width of two drops to ensure the electrical connection even though one drop may not be correctly printed. A gap of three dots was necessary to achieve a suitable distance between the fingers. A drop-spacing of 20 µm was chosen to be ideal for the repro film (T6). Due to the drop gain of the inkjet-printed drops, the final finger widths is about 60 µm and a gap of 40 µm. Still, the inkjet-printing of the pattern was not reproducible and we obtained broken fingers on a regular basis. Furthermore, the alignment of the top and bottom electrodes turned out to be more difficult than initially assumed. These were the reasons why we decided to continue the work with larger fingers as shown in Figure 4.23b. The finger width is 210 µm and the not perfectly printed areas on the fingers are of minor importance. To still reach relatively high capacitance values, we increased the length of the 22 fingers to 8.8 mm. The average thickness of the thin-film forming the electrodes was 412 nm. It is about 1 % of the thickness of the 40 µm thick dielectric that was applied by stencil printing on top of the fingers and can be neglected.

The top electrode was then aligned on top of the bottom electrode and pressed with the help of a glass slide onto the still wet stencil-printed PDMS without squeezing it out of the defined area. For a first investigation, we built a sensor that only uses one-quarter of the final sensor. Figure 4.23c shows the assembled quarter of the sensor with the dielectric printed across the entire area, except the left side of the photo where a white shadow is perceivable. Especially, the upper electrode, which is the bottom electrode is shown milky because the employed PET film is milky. On contact with PET, it turns transparent and both electrodes can be clearly seen.

The fabricated sensor was contacted at the wires by cutting off the opposing PET film and attaching small wires to the printed wires with a conductive epoxy. Then, it was fixed in the normal force measurement setup by covering it with a 2.5 x 2.5 mm^2 glass slide to equally distribute the applied

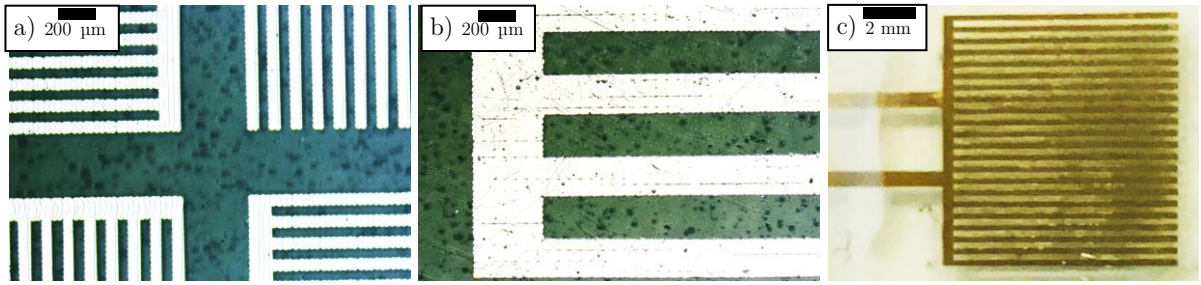

Figure 4.23. Inkjet-printed electrodes with different finger widths of a) 60 µm and b) 210 µm. The silver can be seen bright, while the substrate is dark. c) A readily assembled quarter of the sensor with inkjet-printed silver in dark colour.

force. A force profile as shown as a blue line in Figure 4.24a was applied to the top cap of the setup. It consists of an exponentially increasing force ramp that increases the force in steps of 10 % from 10 mN to 8 N and holds the force for 5 s at each step. Then, the force is decreased with the same steps down to 10 mN. This cycle was repeated three times to investigate the long-term stability. Before increasing the force to the next step, the current capacitance was measured four times, the average value was recorded, and is shown in the figure as a red curve. In general, the capacitance changes are small and lie in the region of several tens of Femtofarads. The maximum capacitance change was about 40 fF higher than the measured capacitance at the lowest force. The shape of the curves of the recorded capacitance values matches accurately to the shape of the force curves. The sensor was able to accurately follow the first three cycles of the force application. A slight drift of the sensor signal to higher values can be found. This is caused by the viscoelastic behaviour of PDMS. High forces on PDMS strongly deform the material and it takes several minutes to recover to the original value. Our force profile did not allow this time frame. Thus, a remaining displacement of the top electrode is summing up during the measurement. This also explains the slight time delay of the measured capacitance to the applied force curve. Especially for the unloading, the capacitance follows tens of seconds after the force signal. Please note that due to the low capacitance changes, the sensor is sensitive to noise. A high noise region between minute 8 and 9 was removed in the graph.

Figure 4.24b shows the measured capacitance values in relation to the applied force. Each marker represents one measured point whereas the lines are only eye-guides. Each cycle of the force profile is shown with a different colour. This visualizes the continuous drift towards higher capacitance values. Each increasing part of the three cycles of the force profile is labelled with R and shown as a solid line with round markers. Each decreasing part is labelled with D and shown as dashed lines with triangular markers. If we assume, that the static force curve lies between the increasing and the decreasing values, an almost linear relation between force and capacitance could be determined with

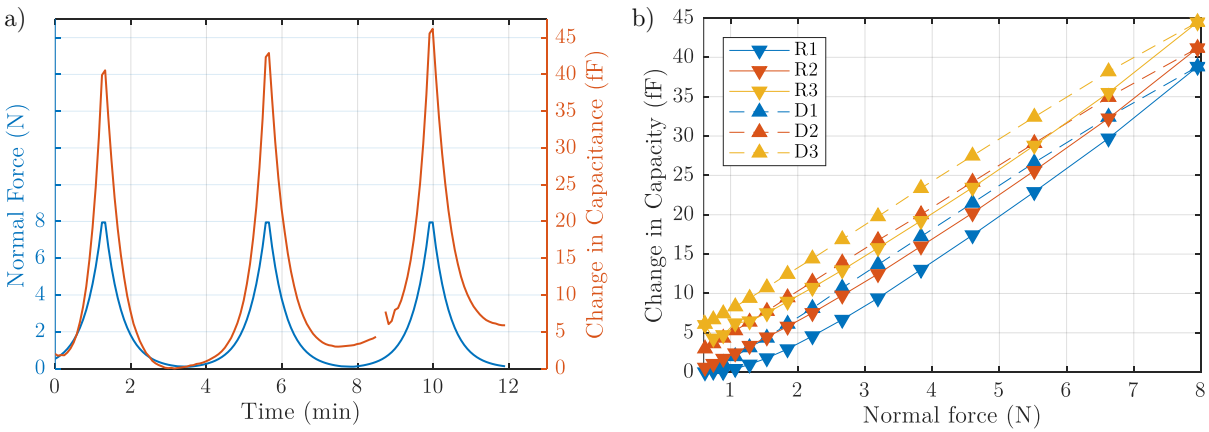

Figure 4.24. a) The applied force profile (blue) and the sensor response (red) for normal force. b) The linear sensor response to the three increasing (R, solid) and decreasing (D, dashed) cycles of the normal force. A drift towards higher signals was found that can be explained by the viscoelastic behaviour and is reset eventually.

a sensitivity of 5.2 fF/N, which is quite small. The reason lies in the large area of the glass slide that we used to distribute the normal force equally across the sensor's area. The 2.5 x 2.5 mm^2 glass slide only allowed a maximum pressure of about 12.8 kPa. The sensitivity in terms of pressure is 3.25 fF/kPa. As we only characterized one quarter of the sensor, the sensitivity of the full sensor would be four times higher, meaning 20.8 fF/N or 13 fF/kPa. These values are slightly higher than in the work of Dobrzynska and Gijs [297], which achieved about 11 fF/kPa. The measured curve indicates, that higher pressures would still produce higher changes in capacitance, but we were limited by our setup. Especially towards the higher force region, our sensor is linear in comparison to other sensors presented in the literature [297] and we expect that the linear region extends to a much higher force. Eventually however, the sensor's capacitance values will saturate. The sensor's response is small and allows an accurate force measurement with a temporal resolution in the order of seconds. The overall size in capacitance can be increased by increasing the area or lowering the thickness of the dielectric. A structuring of the dielectric could increase the sensitivity to normal force as we showed in the previous section for purely normal force sensors.

For the **Characterization** of the sensor for shear forces, the assembled sensor was fixed in the shear force measurement setup as described in Section M.4.3 in the Materials and Methods by using doubled sided adhesive tape between the PET films and the static and the dynamic part of the setup. Figure 4.25 shows the same force profile but now applied in parallel to the sensor's plane in the perpendicular direction to the finger orientation. The dashed red curve shows the recorded capacitance signal with a maximum peak height around 100 fF for a force of 8 N in the –x-direction. As the first cycle was different to the two following ones, we decided to use the capacitance after the first cycle as a reference and show the change in capacitance from this point. For the second and the third cycle, an accurate reproduction of the force curve by the capacitance curve was found after removing highly noisy parts of the recorded curve. The capacitance curve has a small delay of tens of seconds after the force curve because of the viscoelastic deformation of PDMS. A slight increase in the sensitivity was recorded for the last cycle.

As a third measurement, the measurement table of the shear force setup was turned by 180°. This is possible with our setup without removing the sensor. Then, the same force profile is applied in +x-direction and the recorded capacitance is shown as a red solid line in Figure 4.25. Almost the same curve shape could be recorded with a change in the opposite direction. This time, the first cycle does not differ much from the other cycles. We assume, that during the first cycle, some strain within the different layers was released and starting then, the sensor is in a reliable state. The shape of the curve and the amplitude are similar to the force application in the other direction. This shows, that our sensor is truly bidirectional and gives the same amplitude of change in both directions.

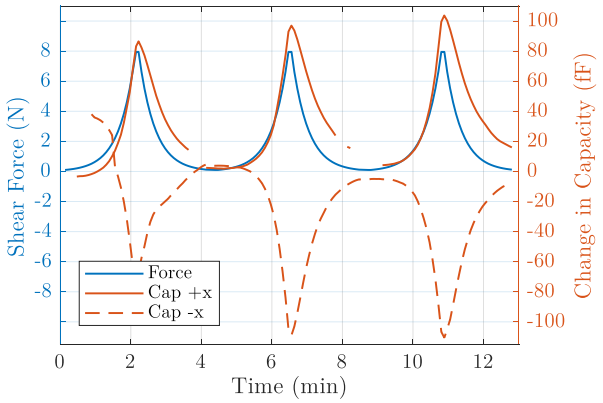

Figure 4.25. The applied force profile (blue) and the sensor response (red) for shear forces in the x-direction (solid) and –x-direction (dashed).

Figure 4.26 shows all measured values for forces in both –x and +x-direction. The markers visualize every measured force value, which was kept for about 5 s and the average force and capacitance values of the last four sampling points are marked. The blue markers show the first force cycle, red the second and yellow the third. Each rising (R) edge is shown by round markers connected by a solid line and each decreasing (D) edge by triangular markers interconnected by a dashed line. The first measurement cycle is shown in blue in Figure 4.26a and deviates much from all other cycles. This is the reason, why we decided to neglect it. Anyway, it has to be shown to highlight the importance that the sensor may not work immediately as intended, but may require one or more priming cycles. The following two cycles are similar, with a slight drift towards lower capacitance values. This was observed for both, positive and negative shear forces as well as for normal forces and is probably caused by viscoelastic deformations of the dielectric spacer, PDMS. Our measurement times of only 5 s per point is rather short and does not allow the PDMS to completely adapt to the exerted force. This may also be the reason for the large hysteresis with a width of up to 1.5 N. We expect that a longer measurement time would increase the absolute capacitance values of the rising edges and decrease the ones of the decreasing edges, and thus, decrease the hysteresis. The capacitance values in respect to the force would follow a linear relation with a sensitivity between 12.3 fF/N for the +x-direction and 13.8 fF/N for the –x-direction. When the full sensor would be built, this would double to about 26 fF/N because two capacitors will contribute to the measurements. Both shear force sensitivities are similar and are about twice of the sensitivity values of the sensor in the work of Dobryzynska and Gijs [297], which was built similarly but without printing techniques.

The capacitance values of our sensor are considerably lower than the theoretical values. From the profilometer measurement, we know that the thickness of the dielectric PDMS layer is about 40 µm and the area of the electrodes is about 44.4 mm². The theoretical capacitance for an overlap of 50 % is 12.3 pF. Despite careful calibration of the measurement tools, our measured capacitance of 6.82 pF was only about half of the theoretical value. This would correspond to a distance of 96.8 µm, which is too high, even when assuming an imperfect planarity. When checking the real overlap of our sensor under the microscope, we found that the overlap in the idle state was about two thirds (67 %) as shown in Figure 4.27a. This slightly higher than desired value would lead to an even higher theoretic capacitance value of 16.5 pF. The significant deviation of the real value may originate from some trapped air between the top electrode and the stencil-printed dielectric layer. In the optical microscope image in Figure 4.27b some areas of air are marked with a red colour to increase their visibility. Such air bubbles would increase the average distance, but not explain a factor of 2.5. Additional to the distance increase, the lower relative permittivity of air compared to PDMS decreases the overall capacitance. Eq. 4.8 on page 104 is one of some equations to estimate the effective

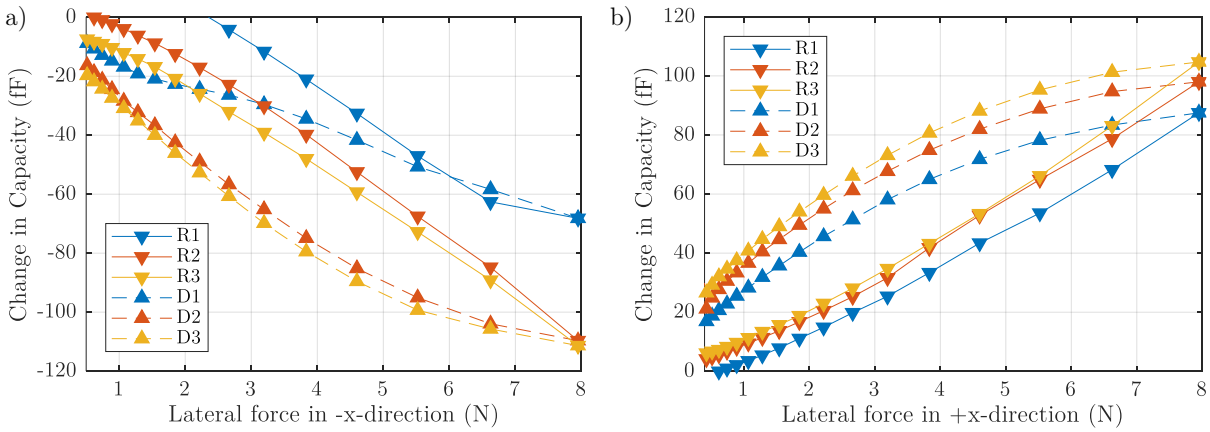

Figure 4.26. The sensor response to three increasing (R, solid) and decreasing (D, dashed) cycles of shear force in a) –x-direction and b) +x-direction. The –x-direction was measured first and a clear deviation of the first cycle to all other cycles was found. A large hysteresis was determined and a small drift of the signal because of the viscoelasticity of PDMS.

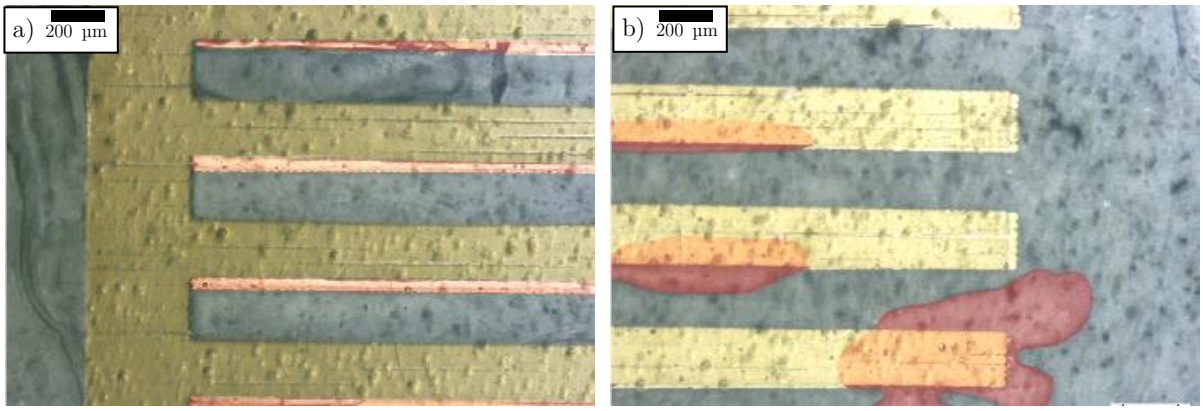

Figure 4.27. Optical microscope images that show the inkjet-printed silver in bright and the substrate in dark. a) The overlapping area of the electrodes are coloured in red and b) trapped air coloured in red.

relative permittivity and shows for example, that the relative permittivity is decreased to 2.1 for 20 % of air. The lower effective permittivity and a higher distance explain the low measured capacitance to some extent. The values of this paragraph are listed in Table 4.1, which shows all assumptions in normal font and all calculated values in bold.

The table also shows the theoretical displacement Δd of the top electrode to achieve the measured changes in capacitance (45 fF) on the impact of the maximum measured normal force of 8 N. The displacement heavily depends on the assumed distance between the electrodes and gives only a rough estimation. The overall range of hundreds of nanometres is reasonable since PDMS has a Poisson's ratio of almost 0.5 that makes it only little compressible if the lateral expansion is limited. The theoretical displacement Δx in the x-direction for a capacitance increase of 105 fF for a shear force of 8 N is also listed and was found to be in the low micrometre range. This is also in a reasonable range as the forces were rather low and the PDMS layer is only 40 µm thick. The 210 µm wide electrodes only slightly change the overlap by about 1 %, which is rather low.

In conclusion, we could successfully build a shear force sensor with only using printing techniques. The electrodes were inkjet-printed on a flexible polymer film and the dielectric spacer was stencil-printed on top of one electrode before aligning and pressing the other electrode on top. In the force range of 0.1 to 8 N, we could find a linear relationship between the capacitance values and the exerted normal and shear forces. For normal forces, a sensitivity of 5.2 fF/N was determined and for shear forces, it was 13.1 fF/N. These values were measured only for one quarter of the sensor of an area of about 80 mm². When employing four of the sensors in a different orientation, the shear force sensitivity can be doubled to 26.2 fF/N and the normal force sensitivity quadrupled to 20.8 fF/N. These are comparable to other sensors in literature and has the main advantage that only printing techniques are employed. Only additive deposition techniques were used and the only difficult step is the alignment of both electrodes. The reduction of the finger width to the planned 60 µm or eventually 40 µm would either allow more fingers or a smaller sensor. The first would have an

Table 4.1. Comparison of the theoretical and measured capacitance values, the thickness of the dielectric spacer d_0 in the idle state, the theoretical displacement in z-direction Δd and in x-direction Δx. Bold values are calculated from the other columns in the same row.

	C_0 (pF)	Overlap	Air	ε	d_0 (µm)	Δd (nm)	Δx (µm)
Ideal 50 %	**12.3**	50 %	0 %	2.5	40.0	**146**	**1.12**
Ideal 50 %	**16.5**	67 %	0 %	2.5	40.0	**109**	**1.34**
Measured	6.82	67 %	0 %	2.5	**96.8**	**635**	**2.77**
Measured, 25 % air	6.82	67 %	25 %	**1.8**	**69.7**	**457**	**2.78**

approximate increase of the sensitivity closer to the Picofarad region. The second would decrease the area and increase the sensitivity with respect to forces as the local pressures are higher. Another improvement could be the use of structured dielectrics as shown in the previous section to reduce the stiffness of the dielectric.

All of the materials and methods used here are low-cost and cause a very small amount of chemical waste, especially when compared to conventional semiconductor processes. This allows the production of sensors on large and flexible substrates as they are needed for artificial skins. Such skins may be employed in advanced humanoids and in healthcare for patients without sensing capabilities on parts of their body.

4.2.5 Piezo-Electric Pressure and Vibration Sensors

The piezo-effect describes the creation of an electric potential on mechanical deformation of materials consisting of dipoles. This can be used to build pressure sensors. Khan et al. presented a screen-printed flexible pressure sensors array with the piezo-electric Polyvinylidene Fluoride-Trifluoroethylene (P(VDF-TrFE) sandwiched between two metal electrodes and achieved a more or less linear relationship between pressure and voltage for quick force changes. [138] Seminara et al. used polyvinylidene fluoride (PVDF) between inkjet-printed electrodes but does not elaborate on the practical usability of the small charges that were measured. [28] Zirkl et al. have been granted a patent that describes piezo-electric pressure sensors employing screen-printed electrodes on two sides of a piezo-electric PVDF film. [299] Furthermore, the company Tekscan Inc (US) claims to produce a piezo-electric pressure-sensing material. [282]

Piezo-electric materials can not only be used for sensing static pressure, but also for pressure waves. In the following, we want to present a pressure wave sensor that consists of the stack of materials as shown in Figure 4.28. It may be used to measure vibrations as well as sound like a printed electrode structure is glued with the print-side down. The sensors must be fixed to a rigid or at least heavy surface that is not affected by the incoming pressure wave. The measurement principle is the compression of a piezo-electric polyvinylidene-fluoride (PVDF) film that was previously poled. Silver electrodes on both sides of the film collect the charges and wire the electrodes to an oscilloscope that records the temporal changes. As the pressures of sound waves are low (usually smaller than 1 Pa), the signal at the PVDF film would be small. We try to amplify the pressure by using a mechanical approach and modify the effective area. The pressure on the bottom of the thin PET film is transferred to a much smaller area and, thus, amplified. This is achieved by screen-printed pillars that are printed multiple times to reach a certain height. We want to avoid printing directly on PVDF as it is temperature sensitive and already curing temperatures of 60 °C lead to shrinking and wrinkling.

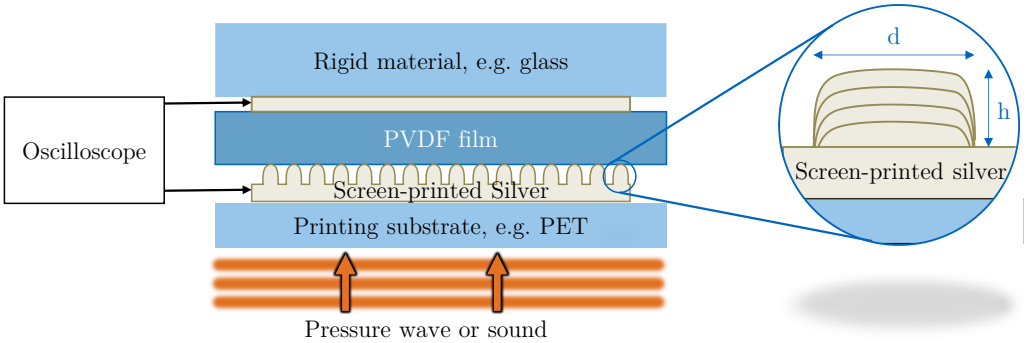

Figure 4.28. Construction principle of the piezoelectric vibration sensor for an incoming vibration (orange). An oscilloscope records the potentials created on the screen-printed electrodes on both sides of the piezo-electric PVDF film. The structured electrode amplifies the pressure on the PVDF film.

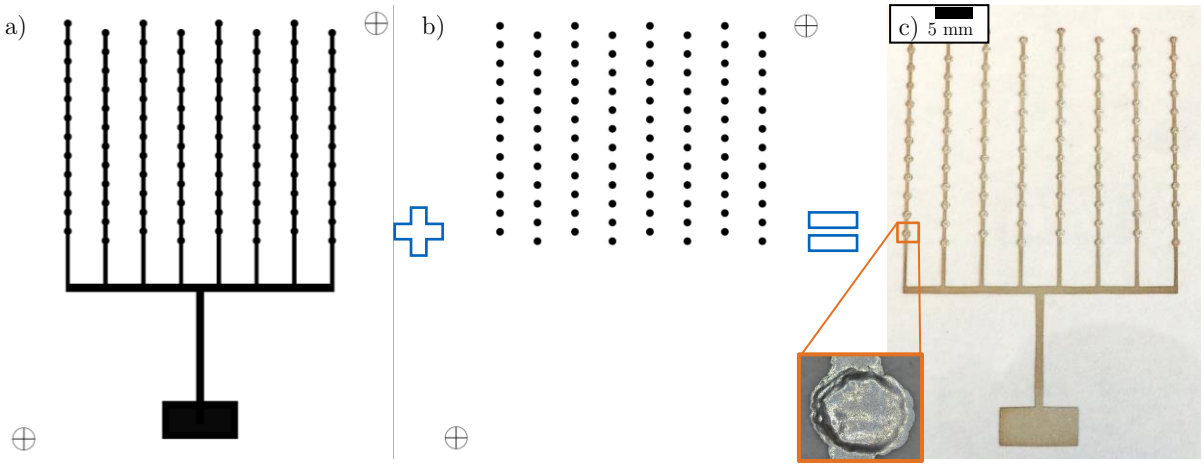

Figure 4.29. Construction principle and a photo of the screen-printed electrodes for the vibration sensor consisting of two different patterns: a) The bottom pattern includes the wiring arms of 0.5 mm in width and up to 35 mm in length. At equidistant locations, round circles of 1 mm in diameter were printed b) These dots are printed multiple times on top of each other to increase the height until more than 50 µm. c) Photo of the printed electrode with 96 dots on an area of 36 x 30 mm² and a microscope image of one of the dots.

In previous experiments, we found that the capacitive charging of electrodes on both sides of the piezoelectric film can have detrimental effects on the amplitude of the signal. Therefore, we want to remove the wires as far as possible from the PVDF film and developed the scheme shown in Figure 4.29. At first, all wiring is printed with the Ag 1011 paste onto a PET film. This paste showed a much smoother surface as shown in Section 2.3.5. The arms are up to 35 mm long and 0.5 mm wide. The arms connect the 96 dots that will transfer the force from the PET to the PVDF film. These dots are 1 mm in diameter and are printed several times on top of each other. Figure 4.29c shows a finished electrode structure on a PET film and a magnification of one of the dots.

The vibration sensor was assembled as shown in Figure 4.30a. It was characterized by the team of Prof. Larcher from the University of Modena and Reggio-Emilia. A screen-printed layer on a fixed underground forms one of the electrodes. On top, the poled PVDF film is fixed and then the screen-printed electrode structure is glued with the print-side down. Preliminary measurements show a low sensitivity around – 80 dB V/Pa in the range below 13.5 kHz and a much more reduced sensitivity at higher levels as shown in Figure 4.30b. This shows that the sensors still need a lot of optimization. The next steps are the glueing of PVDF directly on top of the pillars. We tried to fix the film onto the printed layer when the last layer of the pillars was still wet, but the screen printing paste did not dry due to too little ventilation. We want to try to achieve this with screen-printable epoxy as well as with UV-curable silver. Instead of PET, other substrates have to be evaluated that is mechanically more stable and lightweight at the same time to not damp the pressure waves.

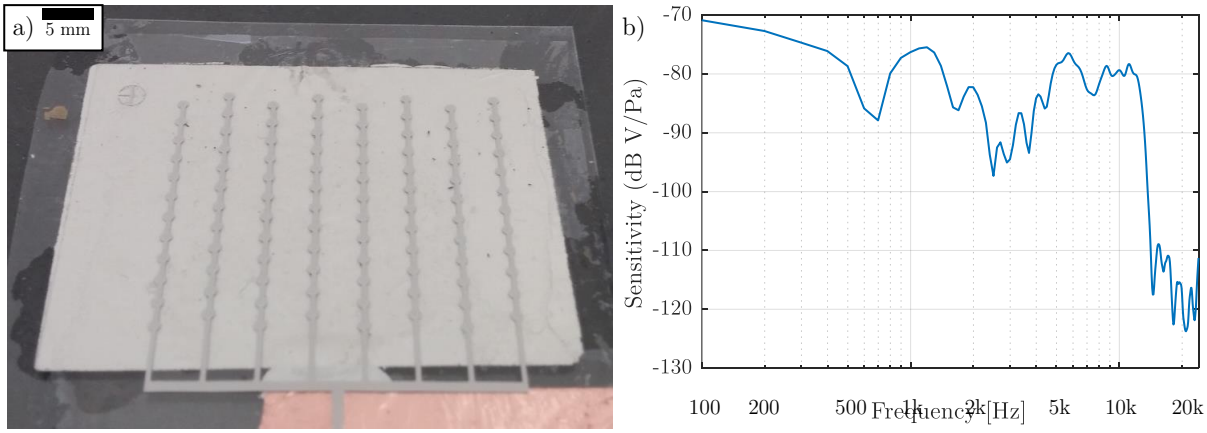

Figure 4.30. a) Photo of the vibration sensor with a silver foil fixed to a rigid background, a PVDF film on top, and at last the structured electrode face down and glued to the other layers. b) The sensitivity of the vibration sensor between 100 Hz and 24 kHz.

4.3 Environmental Sensors

Temperature and humidity are environmental parameters that can be measured with different approaches. In this section, we will investigate some of them from the view of their possibility to be printed. One option to print temperature sensors are thermocouples, which are presented in Subsection 4.3.1. Many groups already showed thermocouples, so we focused on the printability and the transparency of the thermocouple, a property that can be achieved by means of printed electronics. They are attractive for devices that are facing a temperature gradient within them and are compatible with ultra-low power devices and may even be employed for energy harvesting. Resistive materials that change their resistivity with temperature are evaluated for the use of a wireless temperature sensor in Subsection 4.3.2. These are independent of a temperature gradient, but need calibration and are usually only suitable for a rather small temperature range. Subsection 4.3.3 describes humidity sensors that measure the change of capacitance in the substrate for varying relative humidity. Ideally, all temperature sensors are independent of humidity and vice versa. The last subsection 4.3.4 shows the application of printed electrodes on solar cells.

4.3.1 Thermocouples

Thermocouples (TC) are thermoelectric devices that are based on the conversion of thermal energy into electrical energy by a phenomenon called "Seebeck effect". This effect generates an electric field along a temperature gradient in a conductive or semi-conductive material. [300] Among various temperature sensors, thermocouples have some distinct advantages. When only employing conductive materials on both legs, the signal is linear over a large range of temperature and has no offset. Biasing of the sensor is not necessary and does not consume energy from the measurement circuit. [131] The measurement is a simple voltage measurement and easy to integrate into microcontrollers. The major drawback is the necessity for a temperature gradient within the system that may not be achieved in every case. Additionally, the response time is rather slow. [301]

One solution to the slow response time can be thin-film thermocouples that have a large surface-to-volume ratio. However, too thin films in the range of the free mean path of the charge carriers decrease the sensitivity. This trade-off can be solved by using nanowires that have diameters in the nanometre range and are a few micrometres long. [301] Such nanowires can be made of carbon or metals like silver or copper and can be spray-deposited [59], [142], [215], [302], inkjet-printed [118], [119], [303], and screen-printed [304]–[306].

Some of these nanomaterials like silver nanowires (AgNW), carbon nanotubes (CNTs) and the conductive polymer composition PEDOT:PSS are additionally semi-transparent and conductive. Our focus in this section is the evaluation of the printability and the performance of semi-transparent thermocouples using a pair of the mentioned materials. Transparency and sheet resistance of the three materials have been discussed in Section 3.2.

The design of the thermocouples used during this thesis is shown in Figure 4.31. The temperature gradient is formed between the hot and the cold side marked in the figure. The four thermocouples consist of two legs of different materials with a width of 2.5 mm and a length of 27.5 mm and are shown in light and dark blue. The overlapping sections of the two materials are shown in an intermediate colour and are 7.5 x 7.5 mm^2 large. In our measurement setup, the distance between the heater and cooler are 20 mm. So the lengths of the legs are sufficient to place the ends reliably onto the heater and the cooler.

Figure 4.31b shows a photo of a manufactured series of four thermocouples made with silver nanowires (AgNW) sprayed first and then PEDOT:PSS sprayed on top. The silver forms a milky-white or silver layer and the blue/grey PEDOT:PSS layer overlaps at the contact regions. The hot area

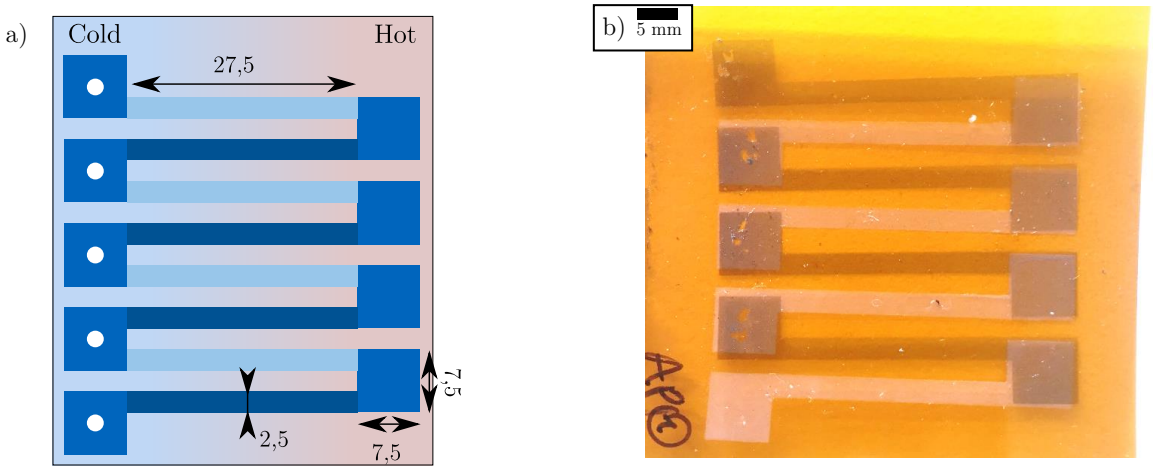

Figure 4.31. a) Schematic of the thermocouples including measures and indicators for the hot and cold side. Light and dark blue shows the two different materials that span over the temperature gradient and intermediate blue the overlapping area of both materials. b) Photo of a manufactured thermocouple with PEDOT:PSS (blue/grey) sprayed on top of silver nanowires (white/silver).

is on the right side and the cold area is on the left side similar to the schematic. Scratches from the spring pins are visible after the measurement, which shows that the layers are sensitive to abrasion.

To characterize such flexible and semi-transparent thermocouples, a custom-built measurement setup consisting of a flat, ceramic heater and a Peltier cooler embedded into a low-heat conductive isolating foam glass and all the measurement wiring was designed and built as described in the Materials and Methods section M.4.4.

We found a linear behaviour of the open circuit voltage, also called Seebeck voltage, over the temperature difference between the hot and cold side for all measured thermocouples that consist of different materials. Figure 4.32 shows the measured values over only one leg as filled markers and a linear fit curve with the slope indicated in brackets in the legend. The value of the slope is called the Seebeck coefficient. The combination of silver nanowires and carbon nanotubes showed the highest open circuit voltages. There is a significant difference of the open circuit voltage between the two legs having AgNW sprayed first and CNTs sprayed on top (54.6 µV/K) and the reverse spraying order (39.0 µV/K). We assume that this is related to the interconnection of the silver nanowires and the CNTs on the contact areas. As shown in Section 2.4.2, the AgNWs are stiff, whereas the CNTs are more bendable and can entangle around the AgNWs to form a better physical and electrical

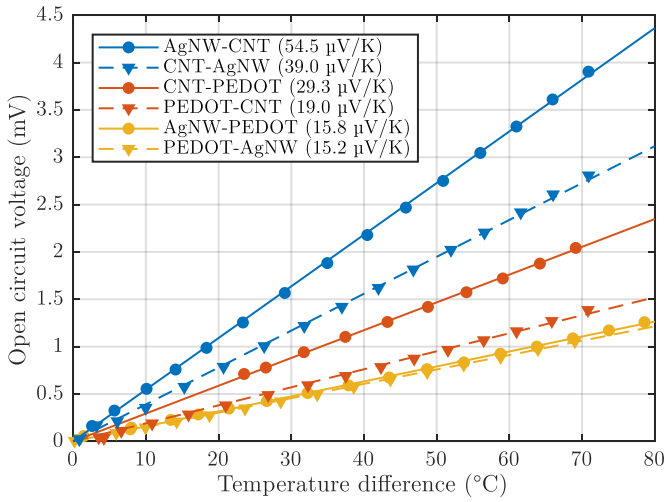

Figure 4.32. The linearity of the open circuit voltage over the temperature difference for thermocouple pairs made with two materials out of silver nanowires (AgNW), the conductive polymer PEDOT:PSS (PEDOT), and carbon nanotubes (CNT). The order of mentioning in the legend indicates the spraying order with the second material sprayed after the first one. Adapted from [22].

contact if sprayed as a second layer. The combination of CNTs and PEDOT:PSS shows a similar behaviour but a lower open circuit voltage of 29.2 µV/K having CNTs at the bottom and 19.6 µV/K having CNTs at the top. Here again, a better electrical contact may improve the first combination. AgNWs and PEDOT:PSS thermocouples are independent of the spraying order and show an open circuit voltage of only around 15.5 µV/K. The spraying of AgNW on top of PEDOT:PSS may dissolve the existing layer and still lead to a good electrical contact between the two layers.

Table 4.2 shows the measured voltages S_i at the other three legs of the thermocouple and indicates the spraying order in the header row. The measured open circuit voltages were in all but one case at least 70 % of the maximum value shown in Figure 4.32. The sum of the values is the measured voltage of the series of the four TCs and is as high as 201 µV/K, a value that can be resolved by low-cost analogue-to-digital converters integrated into microcontrollers. The distribution of the highest values in each column does not follow a specific pattern and shows that the spray-coating and the measurement setup are a reliable production and measurement technique.

Additionally, the functionality of the thermocouples as energy harvesters was investigated. Table 4.2 also shows the measured resistance values of the series of four thermocouples. All combinations having CNTs as one of the leg materials show a high resistance in comparison to the AgNW-PEDOT and reverse combination. Figure 4.33 shows the maximum power points calculated as the square of the half of the Seebeck coefficient divided by the resistance according to Eq. 4.16. To obtain the output power at a certain temperature, the given values have to be multiplied by the square of the temperature difference.

$$P_{Series} = \frac{(S_{Series}/2)^2}{R_{Series}} \qquad \text{Eq. 4.16}$$

It could be shown, that the power output of the AgNW-CNT composite thermocouples with their high Seebeck coefficient is around 110 fW/K². This low value originates from the high resistance mainly caused by the carbon nanotube leg. The reverse composition has a lower open circuit voltage of 62 fW/K². The power output is even lower for the composition CNT and PEDOT:PSS (16 fW/K²) and the reverse composition (3.4 fW/K²). The AgNW-PEDOT thermocouples with a rather low Seebeck coefficient show the highest power outputs of 161 fW/K² and 219 fW/K² for the reverse spraying order. The lower resistance of the layer increases the power output.

Table 4.2. Seebeck coefficient S_i of the four individual legs of the TCs for the three material combinations and the two spraying orders. The bold value marks the highest coefficient per material combination. The material mentioned first was sprayed first. The sum of all S_i, the resistance and the resulting power over the four thermocouples is indicated as well. Partially already published in [22].

Materials	**AgNW CNT**	**CNT AgNW**	**CNT PEDOT**	**PEDOT CNT**	**AgNW PEDOT**	**PEDOT AgNW**
S_1 (µV]	51.1	38.3	22.7	**19.0**	14.9	13.9
S_2 (µV]	53.9	36.5	27.8	6.2	14.6	14.3
S_3 (µV]	**54.5**	**39.0**	27.6	16.3	**15.8**	**15.2**
S_4 (µV]	42.2	36.1	**29.3**	13.6	13.6	13.8
S_{Series} (µV]	201.7	149.9	107.4	55.1	58.9	57.2
R_{Series} (kΩ)	92.2	90.2	179	222	5.38	3.73
P_{Series} (fW/K²)	110	62.3	16.1	3.42	161	219

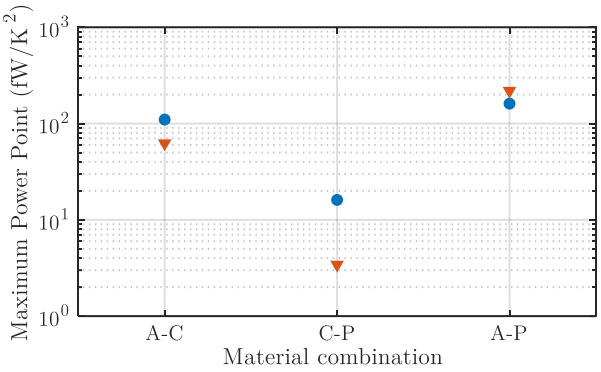

Figure 4.33. Maximum power points of four thermocouples produced with the three different material combinations. A, C, and P are the first letter of the respective material from Table 4.2. Round, blue markers indicate the spraying order as mentioned and triangular, red markers stand for the reverse spraying order.

The use of 90 % semiconducting CNTs did not pay off. We think that this is related to the still 10 % metallic CNTs in the layer. These may form small metallic path sections with a lower Seebeck coefficient that short the expectably higher voltage generated in the semiconducting CNTs. In general, the resistance of the CNT layers was high in comparison to previous works with spray coated layers [58]–[60]. Therefore, we suggest using a higher quality and a higher purity of semiconducting CNTs in the future.

As a conclusion, semi-transparent thermocouples could be produced by means of spray-deposition on a flexible polymer film, which shows an acceptable Seebeck coefficient that is comparable to other thermocouples used for temperature sensing. The coefficients of up to 54 µV/K² allow temperature gradient sensing in a low-power environment with analogue-to-digital-converters in low-cost microcontrollers used for small circuitries in printed electronics. For these applications, especially the thermocouples employing carbon nanotubes (CNT) as one of the leg materials were found useful. The better partner material was silver nanowires in comparison to PEDOT:PSS. For energy harvesting, the thermocouples without CNTs showed a higher output power because of the considerably lower resistance. To increase the efficiency of the CNT-containing thermocouples, the resistance of the must be reduced. However, a lower resistance of the legs can be only achieved together with a lower transparency. More research is needed on the intersection of the two materials and maybe a third material is necessary to improve this region.

4.3.2 Chip-less Wireless Temperature Sensing

We want to show a wireless temperature sensor that combines both, a chip-less RF communication and is fully printed by screen-printing. Passive wireless sensor nodes consist of two main components: An antenna for the communication, which can implement various protocols and the sensor that modifies the antenna parameters sufficiently so that the host system can reliably measure the change. Figure 4.34 shows a photograph of the printed sensor tag. The inductor was printed with silver paste. On the indicated dark area, the PTC paste was printed.

The wireless temperature sensor tag consists of a silver-printed high-frequency coil antenna connected to a co-planar printed capacitor that uses the PET film as a dielectric. On a small section of the interconnecting wire, the silver was substituted by the PTC paste. The section is sufficiently small to avoid increasing the overall resistance of the wire at low temperatures. At higher temperatures, the resistance of this section increases and dominates the resonant circuit.

The resonance frequency of a resonant circuit with a resistor in series to the inductor can be modelled according to Eq. 4.17.

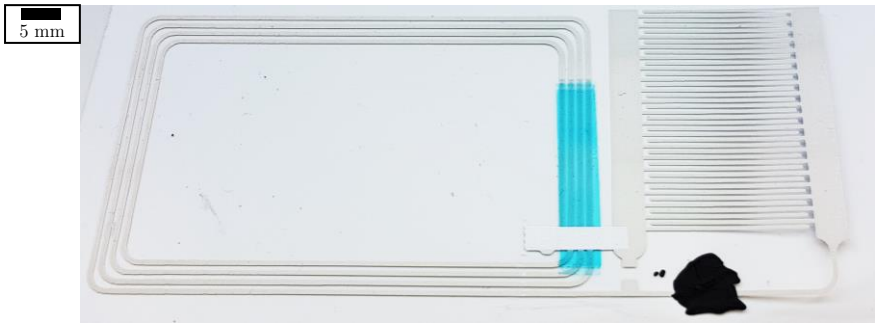

Figure 4.34. Wireless temperature sensing tag with inductive antenna and printed flat capacitor. A part of the wire was replaced by the temperature-sensing paste.

$$f_{Res} = 2\pi \cdot \sqrt{\frac{1}{LC} - \left(\frac{R}{L}\right)^2} \qquad \text{Eq. 4.17}$$

An increase in the series-resistance to the inductor will reduce the resonance frequency. This frequency shift was measured by a Keysight E4990A impedance analyser directly on the tag with a subminiature version A (SMA) connector and provides information about the current temperature. The temperature was measured inside VCL 4006 climate chamber of Vötsch (Germany) at a constant relative humidity of 60 % if not indicated otherwise.

Figure 4.35a shows absolute value (a) and phase (b) over the frequency range from 8 MHz to 17 MHz for a selection of temperatures between 15 °C and 70 °C. A clear decrease of the impedance at temperatures of 60 °C and above in comparison to temperatures below that value could be measured. This point is in accordance to the datasheet of the manufacturer that claims a large resistance increase at around 60 °C. At temperatures below 60 °C, the impedance curve shifts constantly to the lower frequency range. Similarly, the phase of the impedance shifts towards lower frequencies for increasing temperatures with an abrupt jump at about 60 °C. The zero crossing of the phase is marked by filled circles in the phase plot. It was linearly interpolated from the two adjacent measured points. The same frequency and absolute impedance values are marked in the respective plots to visualize the frequency shift.

For varying humidity, the impedance remains almost constant over the entire range from 20 % to 86 % relative humidity. This applies to both the absolute value and the phase within the measured range from 8 MHz to 17 MHz. Figure 4.35b shows the original measurement curves. Again the impedance and frequency at the zero crossing of the phase are marked but almost perfectly overlap.

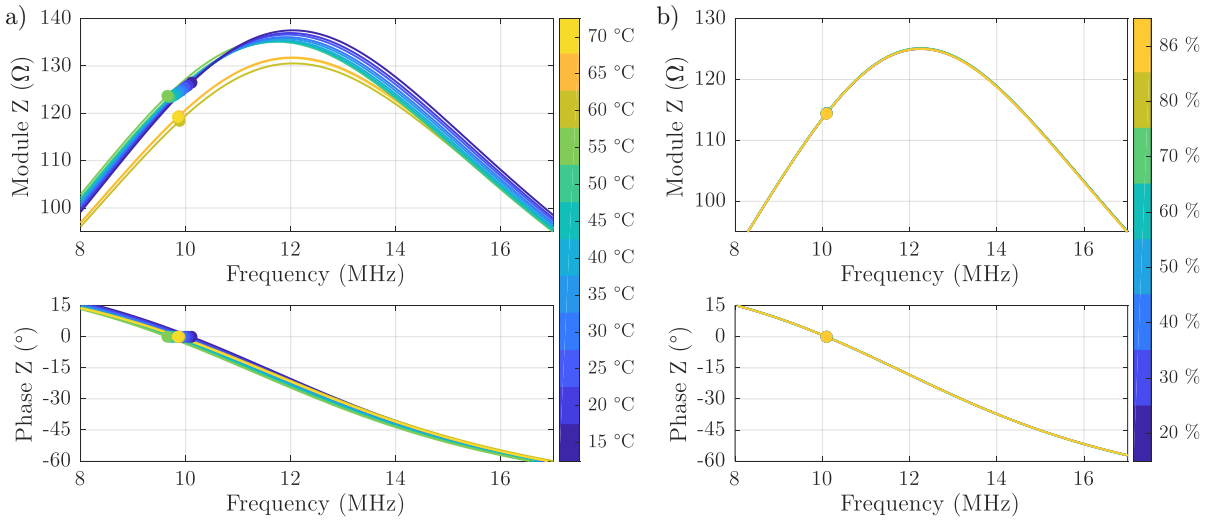

Figure 4.35. Module and phase of the wireless temperature sensor with a) varying temperature and b) varying humidity (no changes).

This shows, that our tag is sensitive to temperature changes but not to humidity changes. Figure 4.36a summarizes the frequencies at the zero crossing of the phase measured directly on the tag for both varying temperature and relative humidity are summarized. The resonance frequency decreases linearly by 11.4 kHz/°C in the range from 15 °C to 55 °C. At higher temperatures, the increased resistance leads to an abrupt change in the resonance frequency. The observed independence of the resonance frequency to the humidity is shown in the figure, too. The jump of the resonance frequency at the point where the PTC paste's resistance rapidly increases may be explained by assuming that the resistance at higher temperatures is so high that it can be modelled as another small capacitance in series to the main capacitor. This reduces the total capacitance and increases the frequency according to Eq. 4.17.

In a second step, a copper coil antenna was used to couple to the wireless temperature sensor tag. At a distance of 5 mm and 10 mm, the impedance spectrum was recorded. The resonance frequencies in this measurement are significantly different because now, the measurement was conducted on the reader antenna. At a distance of 5mm, a similar behaviour of the frequency at the zero crossing of the phase can be found for temperatures below the resistance jump. A linear decrease of the frequency with the temperature of 3.3 kHz/°C was found for the range below 55°C. Above this value, the frequency increases again with a similar slope. At a reading distance of 10 mm, however, we found that this increase does not occur anymore and the resonance frequency decreases linearly with increasing temperature for the entire range. The slope is 1.8 kHz/°C and considerably lower than for 5 mm distance. Figure 4.36b shows all interpolated frequencies at the zero-crossing of the phase for the temperature and humidity range at the two different distances to the reader. For a varied humidity, the resonance frequency of the antenna at a distance of 5 mm remains mostly constant. This is in accordance with the initial assumption and shows that not even a higher water content of the substrate influences the coupling behaviour. The lower slope of the decrease of the resonance frequency at a distance of 10 mm in comparison to 5 mm can be explained by a lower coupling of the two antennas at a larger distance. At a larger distance or without the presence of the tag, no change in the resonance frequency of the reader antenna is expected and can be confirmed by measurements.

As a conclusion, we can say, that this kind of wireless sensor is showing some change due to a variation of the temperature, while not showing any response to the humidity. However, the measured data does not correspond perfectly to theory and more research and experiments are needed to validate the behaviour.

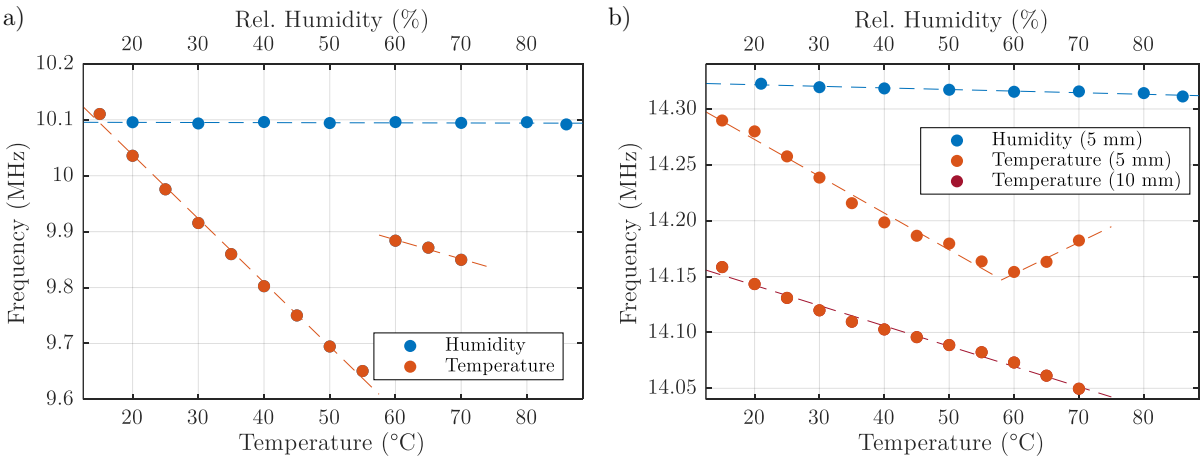

Figure 4.36. Determined reference frequencies a) directly on the tag and b) of the reader antenna at the indicated distances at varying humidity (blue markers) and varying temperature (red markers) with linear line fits for humidity and all temperature sections.

4.3.3 Chip-less Humidity Sensors

Moisture is present in various concentrations in most surroundings and greatly influences living organisms as well as a wide range of materials. Humidity measurement is vital to many production processes, in healthcare, and domestic applications. Relative humidity is a measure of the partial pressure of water vapour present in a gas with respect to the saturation vapour pressure of the gas at the current temperature. [307] Many types of humidity sensors have been presented and an overview can be found in chapter 18 of the book of Korotcenkov [307]. Humidity sensor configurations that can be printed are usually built with a humidity-sensing layer on top of interdigitated electrodes (IDEs). For a fast sensor response, it is desirable to use a large surface in contact with the measurement gas and a low thickness. The sensing materials available can be discriminated into resistive and capacitive materials. Resistive humidity sensors depend on a change in the resistance or impedance of the sensing material upon absorption or adsorption of water from the gaseous phase. This can occur by an increase in the resistivity or a change of the form factor, e.g. swelling on the absorption of water, or a mixture of both. Capacitive humidity sensors depend on the change of the capacitance between the electrodes. A change in the electrical permittivity of the sensing material is caused by adsorption of water into a porous matrix. Low-dielectric materials like polymer films ($\varepsilon_r \approx 2.5$) show a huge increase of their relative permittivity by water molecules ($\varepsilon_r \approx 80$) at the surface or in their matrix. Next to the adsorption, also capillary condensation occurs on narrow porous. [307]

Resistivity changes in a humidity-sensing layer are often caused by a conductivity increase of a polymer electrolyte that produces conductive ions upon adsorption of water molecules. This can be observed in the sensors produced by Su and Wang. [308] Another type of sensors bases on reduced graphene-oxide that changes its conductivity at adsorption of water molecules but also many other molecules [309]. Morais et al. produced low-cost humidity sensors based on inkjet-printed PANI and PEDOT:PSS as a humidity sensor [310]. Andersson et al. showed that plain inkjet-printed Ag-NPs can irreversibly alter in conductivity by a high humidity. [311]

Changes in the electrical permittivity were measured in thin layers but also in the substrate itself. Thin layers of graphene oxide and black phosphorus were inkjet-printed and investigated by He et al. [312] and successfully implemented as humidity sensors. Another option repeatedly shown in literature is the use of changes of the permittivity in the substrate itself. Paper [313] and polyimide (Kapton) [314], [315] has been shown to have a significant change in the adsorption of water.

The author's colleagues, Almudena Rivadeneyra and José Fernández-Salmerón were previously working on humidity sensors [48], [314]–[317]. During the work on this thesis, a wireless humidity sensor was produced that is based on a change of the capacitance due to humidity

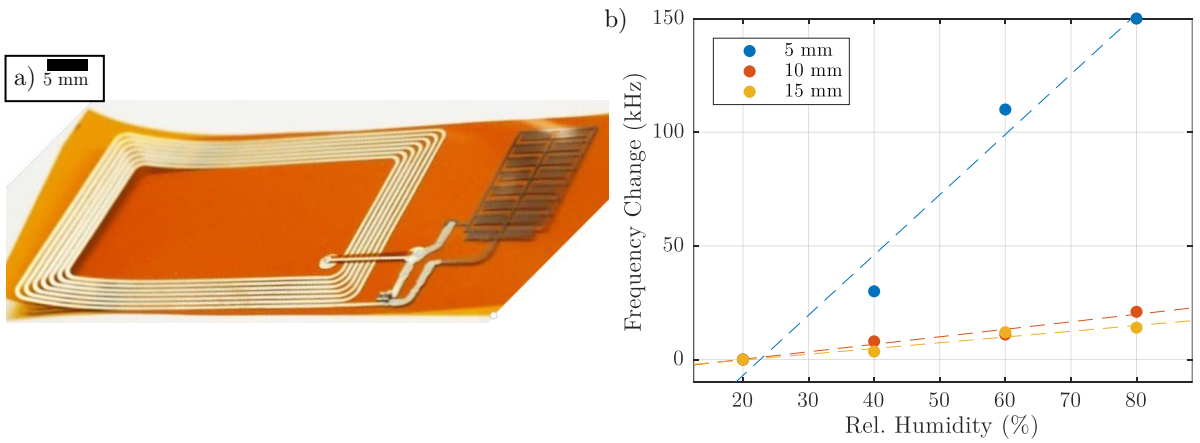

Figure 4.37 a) Wireless humidity tag consisting of a screen-printed coil antenna and an inkjet-printed capacitor. b) Change of the resonance frequency depending on the humidity level at different distances. Partially published in [318].

absorption into the polyimide substrate. [318] Figure 4.37a shows a photo of the tag comprising a screen-printed antenna on the left, and inkjet-printed Ag-NPs on the right. The small structures form interdigitated electrodes forming a capacitor. The tag was placed at a certain distance to a copper antenna that resonates at about 14.5 MHz. When a tag was in the vicinity, it decreases by about 0.5 MHz indicating a coupling. It has been shown before, that this configuration is suitable for humidity sensing and that the cause for the change lies in the change of the capacitance. Similar to the temperature tag shown above, the distance is crucial. Figure 4.37b shows measurement results that were conducted inside a climatic chamber with different humidity levels and different distances between the tag and the reader antenna. While at a distance of 5 mm, the change is rather large with about 2.5 kHz/%(rel. hum.), it is significantly smaller if the tag is positioned at a larger distance. This indicates a reduction of the inductive coupling due to the larger distance. The sensitivity decreases significantly but a small change is visible for varying humidity.

In conclusion, we were able to show that this configuration is able to sense different humidity levels wirelessly if the distance is kept constant. Still, this offers certain possibilities. For example, the coupling could happen through a plastic or glass wall and no wiring to the other side is necessary.

4.3.4 Solar Cells and Photodiodes

We investigated also the applicability of printed electrodes on organic solar cells. This is a challenging topic, because solvents may destroy the sensitive layer stack or pressure can punch holes into the only a few tens or hundreds of nanometres thick layers. A detailed description of the working principle of such organic solarcells and other options for the back contact can be found in the thesis of Marius Loch [319]. We found that our inkjet-inks are not suitable, as water is detrimental to the stack and also the solvent TGME attacks the stack. Therefore, screen-printing was investigated.

Figure 4.38 shows the screen-printed layers directly after printing on top of three organic solar cells employing different polymers. We show only intermediate results here, the full characterization and optimization are still in progress. We found that the silver microflakes pastes are causing shorts, which are probably related to the inhomogeneous and large size of the flakes that penetrate into the layers. The nanoflakes paste ECI 1011 lead to satisfactory results. Figure 4.38b shows one exemplary U-I curve measured in our sun simulator setup that shows the typical shape of a shifted diode curve. The current densities are rather low. Still, they work and have a maximum power of 4.4 mW/cm².

4.4 Chemical and Biochemical Sensors

Nanomaterials have gained increasing interest in chemical and biochemical sensing because of their large surface to volume ratio that potentially renders them sensitive to changes in their environment. Small, integrated sensors have been proposed with a large variety of different materials, among them carbon nanotubes (CNTs) on which there has been a continuous research at our institute. [58]–[60],

Figure 4.38. a) Screen-printed back electrodes of organic solar cells with three different organic polymers. b) The current density of one of the solar cells over the voltage shows the characteristic shifted diode curve.

[62], [320], [321] Although most of our sensors have a sensing material that is solution-processable and can be applied using printing or coating techniques, the electrode materials were still evaporated and structured by lithography or shadow masks. This section focuses on the printing of electrodes for these chemical and biochemical sensors. Most of them are operated as thin film transistors and require a gate electrode. For the biochemical sensors, this is immersed in an electrolyte and silver silver-chloride (Ag-AgCl) electrodes are the best suited to transfer a potential to an electrolyte. So far, a simple silver wire that was chlorinated galvanostatically is in use. Subsection 4.4.1 presents our work done on inkjet-printable reference electrodes. The rest of this section addresses specifically the other two electrodes for sensing transistors, in particular for biosensors (subsection 4.4.2) and gas sensors (4.4.3).

4.4.1 Inkjet-Printed Ag-AgCl Reference Electrode

This section shows inkjet-printed and screen-printed silver-chloride reference electrodes, the simplest reference electrode for chemical measurements in aqueous environments. Minot et al. highlighted the need for silver-chloride reference electrodes in CNT-based sensors to achieve a more reliable and predictable measurement [322]. Shinwari et al. describe many theoretical and practical considerations of reference electrodes and others for chemical sensors [323]. Many current applications in microsystems employ a silver wire that was chlorinated galvanostatically at its surface. Printed films have certain advantages compared to this, as the electrode can be printed directly together with the other electrodes on the same surface, the electrode area can be designed according to the needs of the sensing system. A possibly large area and high surface roughness can withstand high currents. On the other side, the usually thin films may require compromises in the live-time and a varying current-carrying capacity over its lifetime because of surface area changes. For both, inkjet-printing and screen-printing blends of silver and silver-chloride can be bought and printed as delivered.

We tried the galvanostatic approach with inkjet-printed silver layers. Sodium chloride (NaCl) was dissolved in water and a voltage of about 0.5 V is applied between a strip of PET substrate with an inkjet-printed Ag-NP layer on top and a silver wire, both dipped into the solution. After a short time, an about 2 mm dark green line appeared on the pattern just below the surface of the salt water and the current decreased. It was found, that the resistance of the inkjet-printed silver layer is too high to make this approach feasible. It was more electrochemically more favourable to completely chlorinate the film just below the surface. Due to the low electrical conductivity of silver-chloride, the electrical connection to the remaining silver layer below the surface was lost and the reaction stopped. We expect, that for screen-printed silver, this behaviour is less pronounced as the layers are much thicker. Probably, the reaction will stop or slow down, if a certain thickness was converted to silver chloride and continue at a location further below the surface of the salt water.

An more homogeneous chlorination can be achieved by dipping the printed silver layer into sodium hypochlorite (NaClO), a common household bleach [324]. We used a NaClO solution that contains 6 – 14 % active chloride as indicated in the datasheet and found that the reaction is fast. In order to be able to neglect the time required to take the printed film out of the solution and wash it with DI water, we decided to dilute the solution with DI water. A dilution with a volume factor of 12 was found suitable leading to a concentration of active chloride between 0.5 % and 1.1 %. Eight different samples of porous-coated PET film were inkjet-printed on an area of 4 x 40 mm² with one and two layers. They were dipped into the solution for different times between 3 s and 300 s. Figure 4.39a shows four of the electrodes after dipping them into the solution for different times. These times were 3 s for the stripe at the bottom, 10 s for the neighbouring, 60 s, and 300 s for the stripe on the top. On the right side of each stripe, the original silver can be seen. On the left side, the characteristic green colour of silver chloride appears gradually with the tipping time. The stripe on the top, which was in the solution for the longest time, shows also a brownish colouring, but still works as intended.

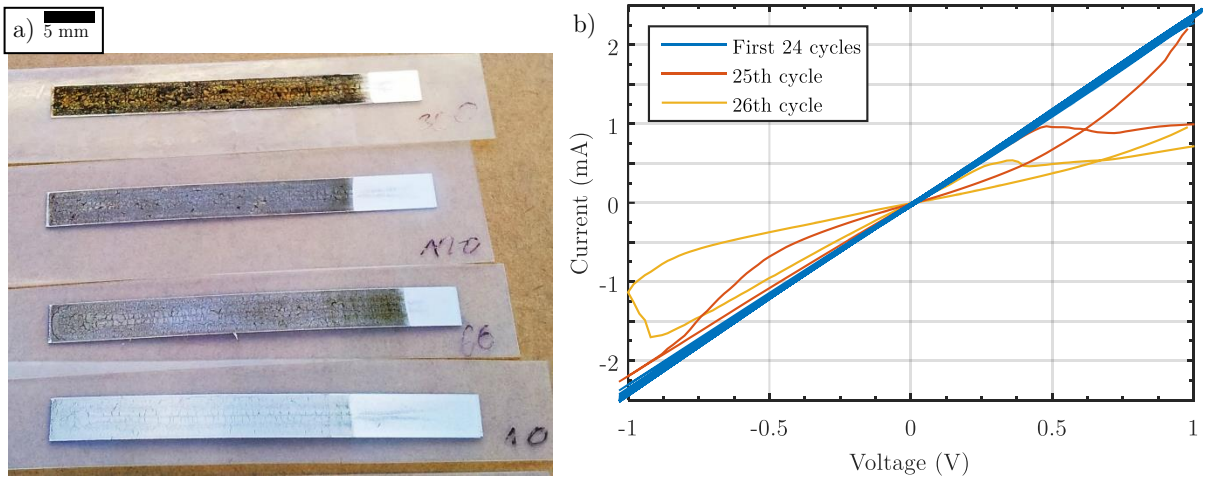

Figure 4.39. a) Inkjet-printed AgCl electrodes. The left side was dipped into NaClO solution for 10/60/120/300 s (bottom to top). On the right side, the original non-chlorinated silver can be seen. b) Voltage linearity of the chlorinated AgCl electrode (60 s, double printed) during the first 24 voltage sweeps (blue) between +1 V and –1 V for 40 s per cycle. During the 25th cycle (red) the destruction starts and is even more pronounced in the 26th cycle (red) when the silver layer detaches from the substrate.

The wet-chemically chlorinated printed stripes were characterized as reference electrodes in a 3 Mol/L sodium chloride solution. Cyclic voltage sweeps from +1 to –1 V were applied in steps of 20 mV for approximately 200 ms per step, which leads to a total cycle time of 40 s. The potential difference was applied to the printed structure and a commercial silver-chloride electrode and the current through the printed structure was recorded. Figure 4.39b shows the recorded current-to-voltage relation. Similar to commercial silver-chloride electrodes, the curve is linear for the first measurement cycles. Until the 24th cycle, approximately 16 minutes after starting, the curve only minor deviates from the first cycle. All 24 cycles are shown in blue in the figure. During the 25th cycle (red), a large deviation from the straight line was determined. Simultaneously, the inkjet-printed layer starts to detach from the substrate. During the following cycle, the delaminated film broke and fell to the ground of the beaker. Now, the measured current deviated much from the previous measurements. We found that a double-printed silver layer with 60 s in the solution survived for the highest number of cycles. The next stable protocol was the double-printed silver electrode that was dipped for 120 s into NaClO solution and was stable for 22 cycles, which is shown in Appendix A in Figure A.1a on page XXXI. A single printed electrode dipped for only 20 s (Figure A.1b) showed a linear behaviour for 5 cycles and then a similar behaviour than a non-chlorinated silver electrode (Figure A.1c). The last shows also a similar behaviour than a plain silver wire dipped into the solution (Figure A.1d).

The wet-chemical chlorination of silver layers is an easy and reproducible method to form silver-chlorite on the surface of the electrodes. When the wiring to the electrodes was previously coated with an encapsulation layer that withstands NaClO, the electrode areas can be selectively chlorinated requiring only one printing pass. The electrodes are stable and can withstand a much longer time in a real measurement environment compared to our harsh characterization. The pseudo reference electrodes may be employed in miniaturized planar sensors. The low material and production costs allow disposable sensors in mass-production. [324] An example of such a sensor platform was shown by Määttänen et al. [325]. They inkjet-printed two gold and a silver electrode that was then chlorinated in a more complex way. Schnitker et al. demonstrated a multi-electrode array with multiple silver chloride micro-reference electrodes [326].

4.4.2 Bio-Sensors

Since about a decade, biosensors based on a thin film of carbon nanotubes (CNTs) have gained interest because of their high sensitivity. With ion-selective membranes or functionalization, the selectivity of the sensors can be improved. [320], [321], [327] Figure 4.40 shows a schematic of a typical configuration of such electrolyte-gated field effect transistors (FETs). Usually, gold electrodes are evaporated and structured by photolithography onto a flexible or rigid substrate, e.g. Kapton or PET. These form the source and the drain of the FETs. On top, CNTs are applied by spray coating or other techniques. A functionalization or an ion-selective membrane makes the sensor selective. Then, the solution that shall be investigated is added on top of the sensor, often inside a defined form. In the schematic, it is universally called electrolyte, as such a sensor needs at least a certain conductivity in the solution. The gate electrode is also directly immersed in the electrolyte, often as a chlorinated silver wire. The electrolyte transmits the gate potential to the CNTs and influence the number of charged bindings on the CNTs, the functionalization, or the ion-selective membrane, respectively. This changes the mobility of CNTs significantly and they can be regarded as semiconductors. This setup of a transistor is often referred to as electrolyte-gated and the reference electrode has a large impact on the actual potential at the CNTs. [320], [322] In the previous section, we showed inkjet-printing of silver-chloride patterns. Next to already commercially available silver-silverchloride blends for screen-printing, this part of the sensor can be easily printed already today. In this section, we present a few results from trials to print the other electrodes, the drain and source.

The drain and source electrodes are often realized as interdigitated electrodes (IDE) as visualized in Figure 4.40b. The definitions marked in the figure relate rather to the functionality of the transistor than the intuitive dimensions. The finger width of the IDEs is not important. The crucial dimension is the gap width, which will be the transistor's channel length. As the CNTs have a large resistance at their intersections, it is important that the channel width is rather small, usually below 100 µm. However, for a mixture of semiconducting and metallic CNTs, it should not be too small for a metallic path to form between both electrodes. Therefore, the most common approach is to use some value between 50 µm and 100 µm [321], [327]. The channel length is formed in parallel to the electrode's fingers as indicated by the orange meandering line. A limitation from a printing point of view is that the electrodes cannot be printed with silver as this will form silver-chloride and change the electrodes properties. PEDOT:PSS is also unsuitable as it dissolves in water. The remaining candidates from our list of materials are gold and carbon.

We designed gold electrodes with a finger width of 50 µm and a gap of 100 µm and found that after inkjet-printed, the finger width and gap are almost similar at about 75 µm on average. Unfortunately, the printing process with the Dimatix printer was not reliable, so only a few candidates for a final sensor were available. During further processing, the aggressive bioreagents delaminated the gold electrodes from the substrates, both from PET and PI. Therefore, we refrain from showing images and will rather concentrate on improving the adhesion in the future. This may be achieved in several ways. A thorough investigation of different substrates should be conducted to evaluate

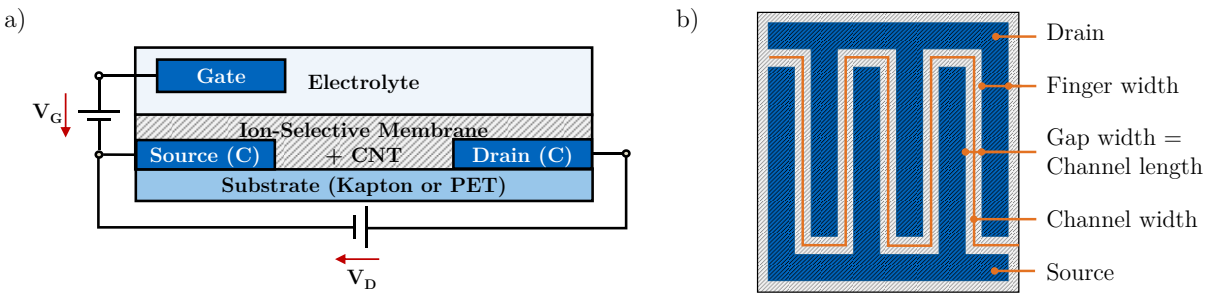

Figure 4.40. a) Cross-section (not true scale) and b) top-view of an electrolyte-gated CNT-based field effect transistor for ion-sensing in solutions.

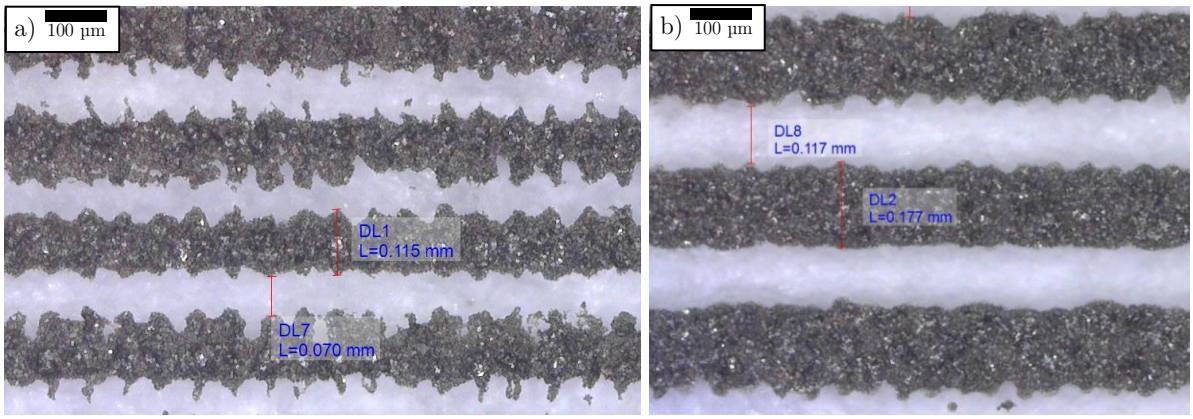

Figure 4.41 Screen-printed IDES using carbon (dark) on a screen with a mesh count of 165 on PET (white). a) Designed finger width of 75 µm and a gap of 113 µm results in almost the opposite dimensions (115 µm to 70 µm). b) The designed finger width and gap of both 150 µm result in a finger width of about 180 µm and a gap of about 120 µm.

systematically the adhesion in a reagent bath. Furthermore, the sintering parameters may be adjusted to increase the mechanical stability of the gold film and reduce the pores through which a reagent can reach the substrate. The evaluation may be conducted, for example, in an ultrasonic bath using acetone or any other reagent. In literature, laser sintered [148] or IR curing [325], [328] was successfully conducted on Au-NPs, so we think, we can achieve it with IPL curing, too. Another option would be changing the current processes for the fabrication of the biosensors at our institute, but this will not result in comparable results.

We also designed and printed carbon electrodes with varying electrode width and gap on PET and PI and already presented them in Figure 2.34 on page 51. Figure 4.41 shows two exemplary IDEs that are among the best ones achieved. The left microscope image shows a structure with a designed finger width and a gap of 75 µm and 113 µm that are printed to 115 µm and 70 µm, respectively. This shows the spreading of the paste by about 20 µm on each side of the finger. The ragged edge is characteristic for patterns with a small amount of paste that cannot flow together to create a homogeneous line. A designed finger width of 150 µm is better suited to achieve a homogeneous channel length and less outflow (10 µm). The resulting channel length is 117 µm and slightly above the targeted below 100 µm.

These results show that it is possible to print IDEs with channel lengths below 100 µm but some optimization of the process is still required. A higher emulsion thickness may improve the edges and remove the raggedness. A designated fine-line paste with smaller particles would be desirable as well. Still, the goal was achieved and the implementation as biosensors could begin. However, we faced delamination of these electrodes in an ultrasonic bath with acetone, too. Here we do not see any way to improve the electrodes except by using a paste that contains another binder. Still, there are many other biochemical applications that do not require such a harsh treatment during functionalization. Other applications of inkjet-printing and printing techniques for biosensors, in general, were summarized in the review of Komuro [329].

4.4.3 Gas Sensors

Carbon nanotube (CNT) based field effect transistors can also be used for gas sensing down to low concentrations [60], [63], [144]. At our institute, the production is similar to the above-described biosensors on an oxidized silicon wafer. The surface of the wafer is structured by photolithography and gold electrodes are evaporated. On top of the electrodes, a CNT layer is spray deposited. The silicon wafer is used as the gate and the oxide layer of the wafer acts as the gate dielectric. We found that this configuration is not achievable with printing techniques as the height of the electrodes is usually between 0.5 µm and 5 µm depending on the used printing technique [330]. Therefore, we suggest a

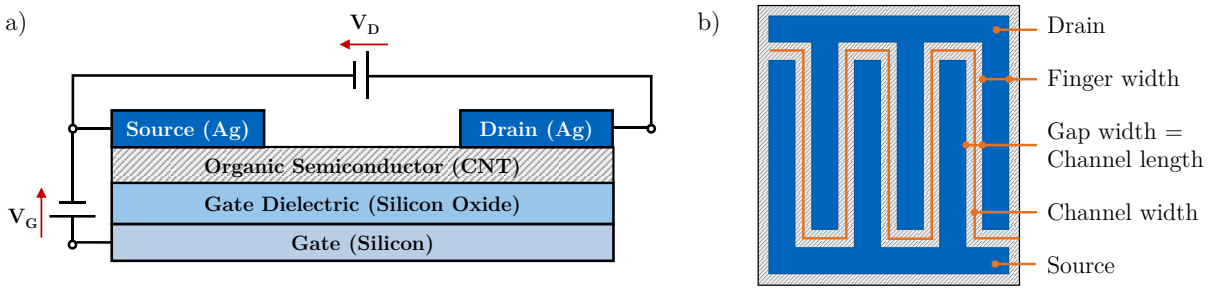

Figure 4.42. a) Cross-section (not true scale) and b) top-view of a CNT-based field effect transistor for gas sensing with electrodes on top of the semiconductor.

different layer stack as shown in Figure 4.42a. The source and drain electrodes are printed last on top of the CNT layer.

In different papers from our institute [62], [330], [331], inkjet-printing of the electrodes was investigated already for both resistive gas sensors and gas-sensing transistors. Here, We show in the following that screen printing is also an alternative to produce the required interdigitated electrodes. Figure 4.43a shows the ready gas sensor with CNTs spray-coated onto the silicon wafer and the screen-printed silver electrodes on top. Figure 4.43b shows a photo of the IDEs with a designed finger width of 100 µm and a gap of 100 µm, which should result in a channel width to channel length ratio of about 1300. The CNT layer is almost transparent and can hardly be seen, whereas the silver layer is bright on top of the blueish wafer. The microscope image in Figure 4.43c shows that the channel length is between 80 µm and 100 µm resulting in a channel width to channel length ratio of about 1470, which is higher than we expected. Figure 4.43d shows an SEM image of the intersection of a screen-printed electrode and the underlying CNT layer. We can still see, that the CNT layer is homogeneous. At the intersection with the silver particle, the CNTs are more pronounced in the image. This results from the higher charge transport during SEM imaging and proves the good contact between silver and the CNTs.

A short characterization of the sensors with ammonia (NH_3) showed that the sensors are working as gas sensors as can be seen in Figure 4.44. The measurement curve shifts to lower gate voltages and the threshold voltage is decreased for gas concentrations above 50 ppm. The low-current spikes are resulting from the employed Keithley source meter that seems to have troubles measuring Nanoamperes at the required speed. In the inset, the linear transfer curve can be seen in the negative gate voltage region. In comparison to gold electrodes, the silver electrodes showed a higher change in all four investigated transistor characteristics, the on-off ratio, the subthreshold slope, the field effect mobility, and the threshold voltage.

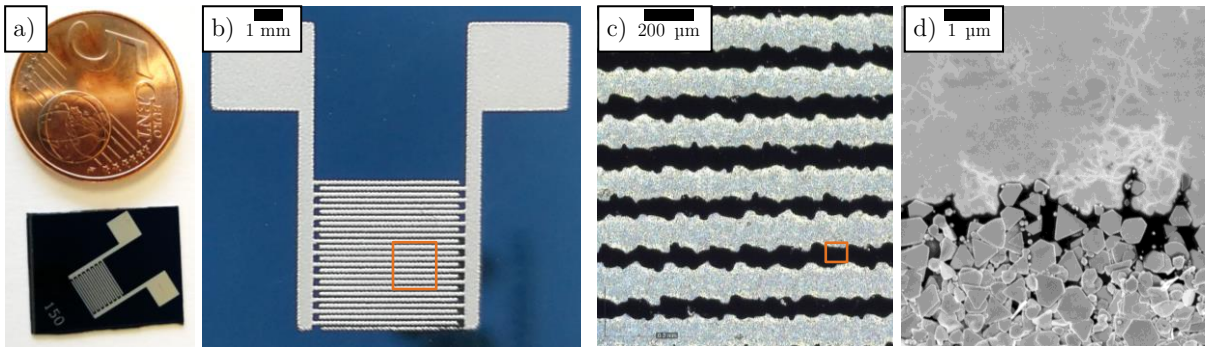

Figure 4.43. a) Comparison of the gas sensor to a 5 Eurocent coin. b) IDEs with a designed finger width of 100 µm and a gap of 100 µm made from screen-printed silver nanoflakes on a silicon wafer. b) Microscope image of the fingers showing the silver in bright colour and the substrate in black. c) SEM image of the intersection between screen-printed silver (flakes at the bottom) and silicon oxide (grey) coated with a few CNTs (white). The orange triangles indicate an exemplary position where the next image on the right could have been taken.

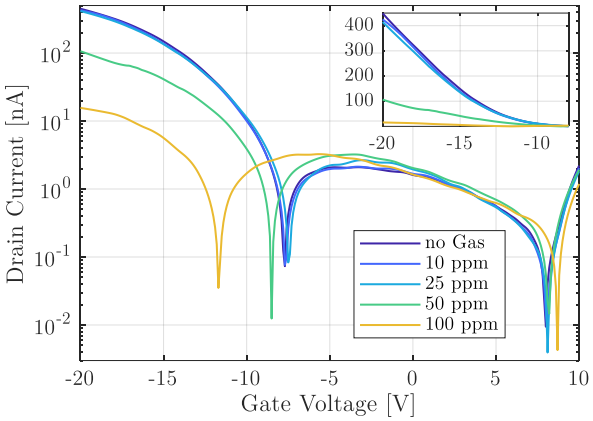

Figure 4.44. Gas sensor's VI curve with screen-printed electrodes during different NH_3 concentrations.

4.5 Skin Electrodes

Printed electronics can also offer many new kinds of products for healthcare. Next to biochemical sensors, also electrical parameters like body potentials can be measured and serve as indicators for serious illnesses. This section investigates several pastes for the use as skin electrodes and presents some prototypes. At first, electrocardiography with four different kinds of electrodes is investigated and then electrooculography with silver-chloride electrodes and wires is discussed and a ready-to-use prototype is shown.

4.5.1 Electrocardiography

Electrocardiography (ECG) covers different methods of recording the potential differences caused by the electrical activity of the heart. The potential changes arise from the depolarization and re-polarization of the heart muscles during each heartbeat. Often, electrodes are placed on the skin and detect the potential changes in Microvolts or low Millivolts over a period of time.

For our ECG measurements, we decided to use a simple printed layout with one printed conductive and one isolating layer embedded into a commercial skin tape. Figure 4.45 shows the multilayer approach that was employed in this work. At first, the electrodes and connection wires were screen-printed with silver silver-chloride or carbon paste onto a PET film. An isolator was screen-printed on top covering all connection wires but leaving free the electrodes. Then, the film was cut along the wires, which can be easily conducted with a laser cutting machine. The cut was attached to a stretchable adhesive skin patch with a transparent polyurethane film and a polyacrylate adhesive. The KlarMed KL17105 (Klein Ausrüstungstechnik GmbH, Germany) skin patch is skin-friendly and permeable to air and water vapour. The stretchability of the adhesive and the cutting of the electrodes are

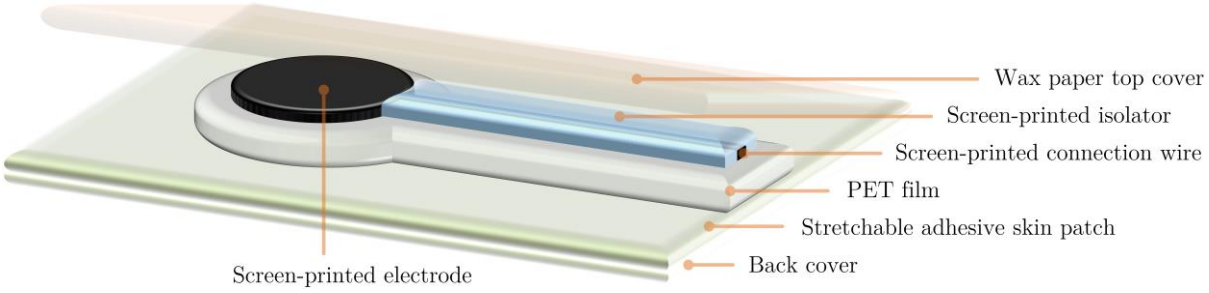

Figure 4.45. Schematic of the layers of the screen-printed skin electrode. Onto the adhesive skin patch, the cut PET film carrying the screen-printed electrode and wires as well as a screen-printed isolator for the wires are placed and covered by the wax paper as a top cover.

necessary to lie flat on double-curved surfaces like the human head. The entire print was then covered with wax paper. Then, the back cover and wax paper were cut leaving approximately 1 cm of both next to the previously cut PET film. This is enough to stick the pattern safely on the skin and is convenient to carry for a longer time.

A hand-made prototype including even two electrodes (circles on the left) different materials is shown in Figure 4.46a. The black electrode was printed with carbon paste and the grey electrode with silver chloride paste. The ends of the wires on the right side of the photo were attached to conventional knob connectors so that a commercial ECG system could be used. This was an MP150 of Biopac Systems Inc. (US) with an ECG100C extension. On the bottom side, a wax paper is added to the electrode that has to be removed before application. On each hand of the patient, one patch was attached and then the green-transparent top cover was removed. On the photo in Figure 4.46b, the patch can be seen on the hand of the author. The transparent stretchable skin plaster can only be seen at the right edge where the wires leave the skin surface. A conventional gel-electrode at the right foot of the patient was used as the reference electrode to exclude effects of the reference electrode. The double patch shown in Figure 4.46 was used to compare two signals without the need to remove the skin patch. The measurement was always conducted with two electrodes printed with the same material.

The measurement of the following results was conducted in the normal mode with a gain of 5000, a low pass filter of 35 Hz, and a high pass filter of 0.05 Hz. The connection of the patient followed the Einthoven I or Einthoven's triangle connection. A typical recorded ECG signal of one heartbeat of the author is shown in Figure 4.47. The R, S, and T peaks are clearly visible whereas the P and Q peaks are not that clear. They were selected with a simple algorithm as shown in Table 4.3. It was found, that the heartbeat had a frequency of around 0.8 Hz. At first, the local maxima of the entire recorded ECG signal were searched under the condition that they need to be at least 0.75 s apart from each other. These were marked as R-peaks and were recognizable in each of the recorded measurements. Starting from the time t_R of the R-peak, the minima during 0.1 s before and 0.2 s after t_R were marked as Q- and S-peaks with the times t_Q and t_R, respectively. The maxima within 0.15 s before t_P and within 0.5 after t_S were marked as P and T peaks at the times t_P and t_T, respectively. The found peaks are shown by round markers in Figure 4.47.

The algorithm was then used to process the entire recorded ECG signal of about three minutes as it is shown in Figure 4.48. 144 R-peaks were detected, which leads to an average heart rate of 0.8 Hz or 48 beats per minute. This is low but is reasonable for a fit and sitting person. Some low-frequent noise can be seen that lets the baseline drift, for example around 45 s and 110 s after the start of the

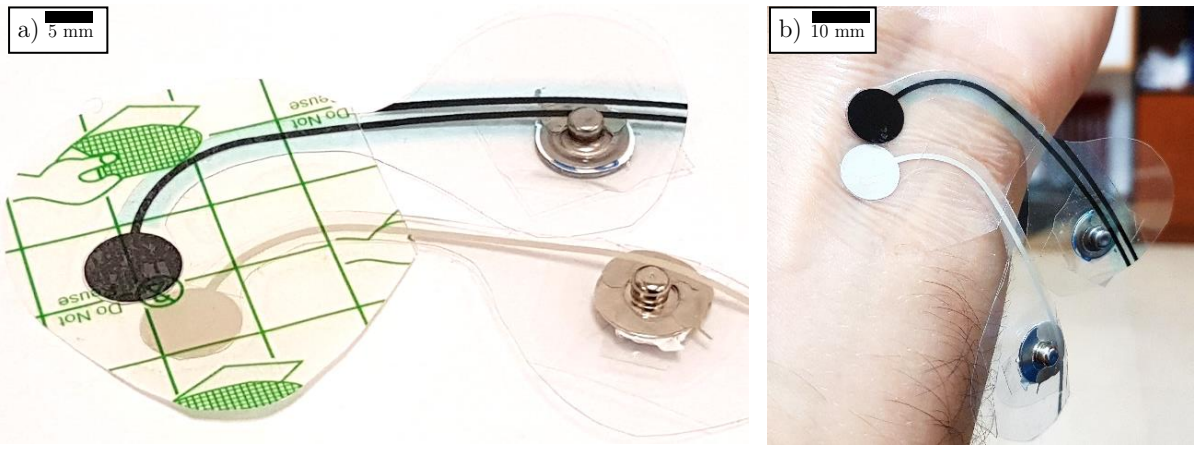

Figure 4.46. Screen-printed dry electrodes with connecting wires and knob connectors for electrocardiography and other applications. The black electrode is carbon-based, the silver one is silver-chloride-based, and the blue layer is the isolation from the skin. a) Electrodes with adhesive, stretchable skin patch and top and bottom cover. b) Electrodes attached to the arm of the author with adhesive patch only.

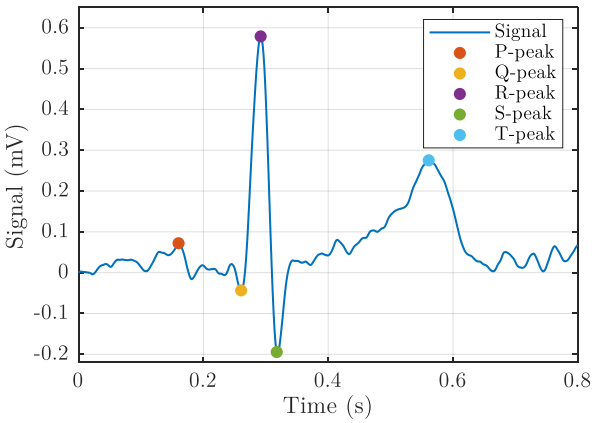

Figure 4.47. An exemplary ECG pulse measured with the silver-chloride electrodes including marked peaks.

Table 4.3. Steps of the algorithm used to detect the different peaks in the ECG recording.

Peak	Description	Time
R	Find local maxima with a distance of at least 0.75 s	t_R
Q	Find local minima within 0.1 s before t_R	t_Q
S	Find local minima within 0.2 s after t_R	t_S
P	Find local maxima within 0.15 s before t_Q	t_Q
T	Find local maxima within 0.5 s after t_S	t_T

measurement. Still, the algorithm could detect the three largest peaks of the signal reliably. With the help of Encarnación Castillo of the Universidad de Granada in Spain, a wavelet transform was used to remove low-frequent components to decrease the wandering of the signal. The resulting data is shown in Figure 4.49. A clear decrease of the low-frequent noise can be perceived. The average signal amplitude of all peaks is more homogeneous and the baseline is almost straight. The average peak height of the R, S, and T peaks are 0.55 mV, -0.23 mV, and 0.24 mV, respectively. This proves that the silver-chloride electrodes are well suited for ECG recording in the Einthoven triangle to detect the heart rate and at least two other hills. It is assumed, that the electrodes are also suitable for measuring on the chest. Unfortunately, only a one-channel ECG was available, so no more detailed evaluations could be conducted.

In the following, we want to investigate the influence of the electrode and wire material in more detail. Therefore, it was necessary to record ECG signals with different materials. We chose the previously mentioned screen-printed silver-chloride electrodes, screen-printed carbon electrodes, as

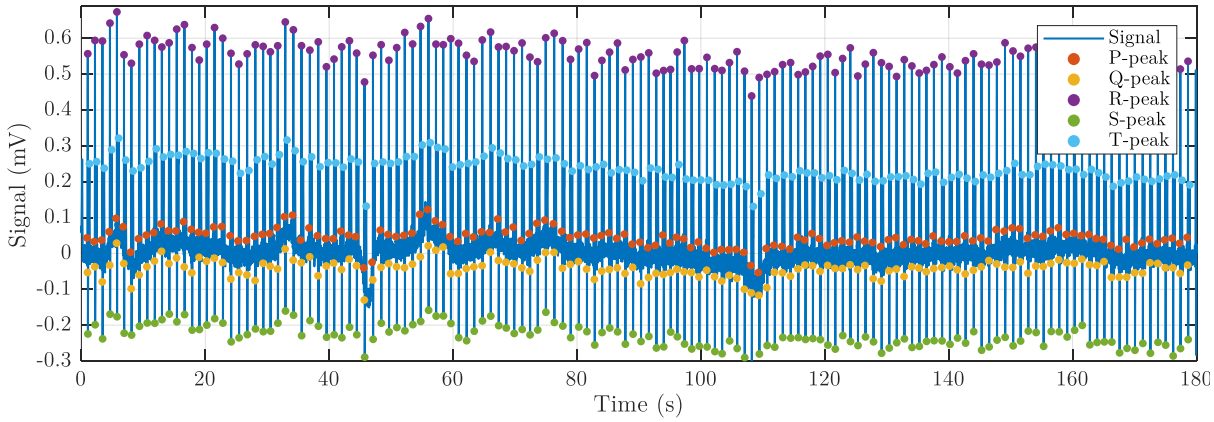

Figure 4.48. Three minutes of the original signal of an ECG recorded by screen-printed silver electrodes on both arms.

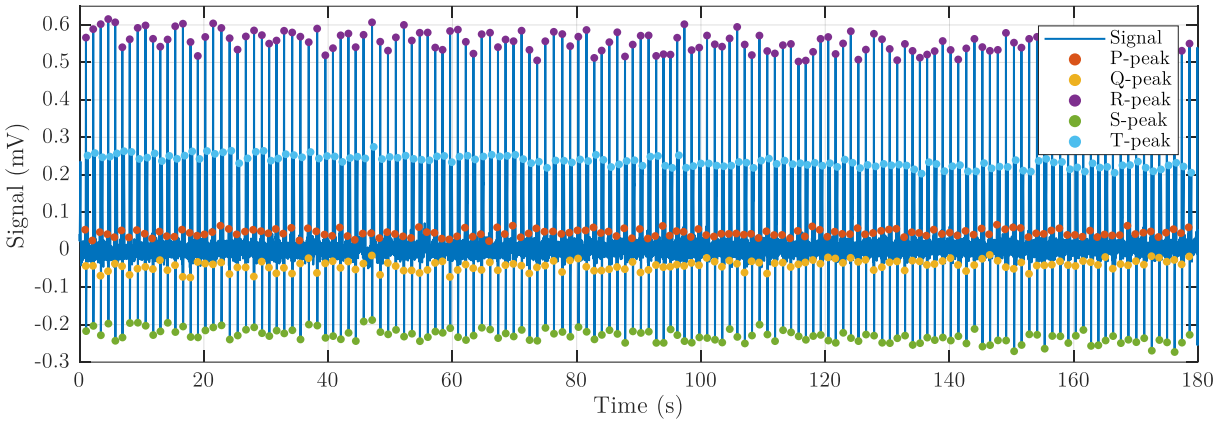

Figure 4.49. Three minutes of an ECG recorded by screen-printed silver electrodes on both arms after wavelet transform to remove low-frequencies from the spectrum.

well as Kapton film that was burned on the surface by a laser to form a thin graphite layer. All these electrodes were stuck onto the skin with the previously mentioned skin plaster. The screen-printed electrodes were flat and the printed layer forms a relief on the surface. Therefore, the skin contact was good and additional pressing by hand on the electrodes did not change the amplitude of the signal much. In contrast, the Kapton electrodes were bent due to the thermal stress during preparation and had a bad skin contact. For a comparison, commercial gel-based electrodes of Biopac with a metal knob and a gel pad were also measured.

Of all four electrodes, a sequence of 180 s was measured and sequenced into individual heartbeats. Each sequence starts 0.25 s before the R-peak and ends 0.5 s after it. The average of all sequences was calculated, which comprises 170, 144, 179, and 148 heart beats for the Biopac, the silver-chloride (AgCl), the Kapton, and the carbon electrode, respectively. As the number of heartbeats varied a lot, we decided to stretch all recorded signals to match a heart rate of 48 beats per minute. Figure 4.50 shows the calculated average signals with the stretched time and aligned on the R-peak. Whereas the gel-based Biopac electrode showed by far the highest signal amplitude of about 1.0 mV, the screen-printed AgCl electrode showed at least an amplitude of about 55 % in comparison. The Kapton electrode showed an amplitude of 40 %, whereas the screen-printed carbon electrode had the lowest signal amplitude of only 33 % in comparison to the gel-based electrode. This different behaviour could result from the resistance of the wires. The lowest resistance possesses the Biopac electrode, which can be directly connected to the cable of the ECG device. The AgCl electrodes had a resistance of several tens of Ohms, and the Carbon electrode in the range of Kiloohms. The Kapton electrode was connected via much shorter wires, thus the resistance is in the range of a few hundreds of Ohms.

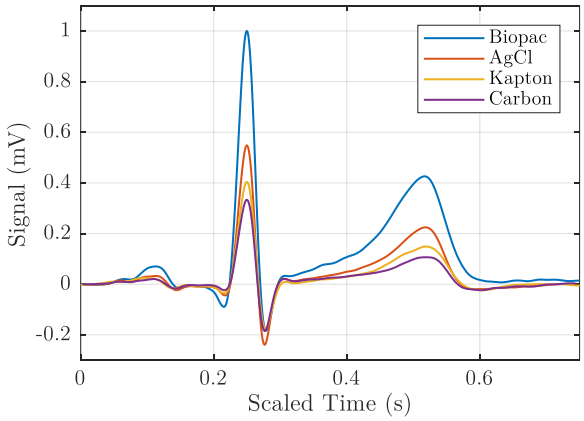

Figure 4.50. Average value of the recorded ECG signals scaled to a heart rate of 48 beats per minute to align the R and the T peaks. Each signal recorded on the four electrodes had an original length of 180 s and comprised 170, 144, 179, and 148 heartbeats.

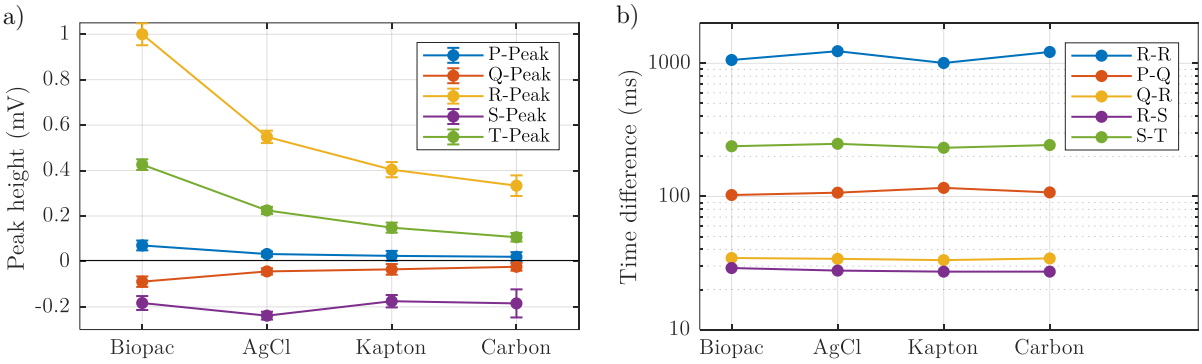

Figure 4.51. a) The average peak height of and b) the average interval between the four selected peaks and the respective standard deviations within three minutes.

The amplitude of the different peaks was evaluated in detail, and the median and the standard deviation are shown in Figure 4.51a. The amplitudes of the P, Q, R, and T-peaks are the highest for the Biopac gel electrode as expected. Surprisingly, the S-peak is most perceivable with the AgCl electrode, which ranks second for all other four peaks. Even the Carbon electrode showed a higher S-peak than the gel electrode. It seems that the shape of the electrode plays a role at this peak, because although the Kapton electrode's peak amplitude range between AgCl and carbon for all peaks, the S-peak amplitude is lower than both. The P and Q peak are hardly detectable in a signal of a single heartbeat because of the noise. Encarnación Castillo employed a 5^{th} and a 6^{th} order wavelet transform to all signals to reduce the high-frequent noise. We found that the 6^{th} order transform hides some of the main peaks of the ECG signal, so the 5^{th} order is the maximum that only reduces noise without interfering with the overall shape of the signal. The removed noise is below 10 µV for all signals with a standard deviation below 1.3 µV. It seems that the major part of the measured traces is real bio-potentials from parts of the body.

The temporal resolution of the electrodes was also investigated. Figure 4.51b shows the average intervals between two subsequent R-peaks as well as the average intervals between the individual peaks for all four electrode materials. No major deviation was found, which means that the capacitive loading of all electrodes is sufficiently low. Our results show, that screen-printed silver-chloride and carbon electrodes are dry alternatives to gel-based electrodes, but the signal amplitudes are about 50 % and 33 % lower, respectively. Both kinds of electrodes are well suitable for measuring the heart rate. If several cycles are recorded and digital filters are applied, the characteristic peaks of an ECG signal are recoverable with all electrodes.

4.5.2 Electrooculography

Electrooculography (EOG) is a method for monitoring the eye position and movement by recording the resting dipole between cornea and retina of the eyes. [332] The potential of this dipole is independent of the orientation of the eye. EOG is a method to detect eye movements also in the dark when other methods like video-oculography and eye trackers fail. [333], [334] Stationary electrodes positioned around the eye can measure a potential depending on the orientation of the eye. For most electrode combinations, the measured voltage is linearly depending on the angle of the eye. Typically, five electrodes are used: a ground electrode, two electrodes for horizontal movement and two electrodes for vertical movement. The ground is positioned on the central forehead. The two electrodes for horizontal eye movement are positioned on the outer canthi of each eye. The electrodes for measuring the vertical movement are typically positioned on top and below the eye. [334]

Electrooculography was used as an automatic method to measure human eye movements and for human-computer interfaces. Skotte et al. measured the human eye blink frequency during computer tasks [335]. Barea et al. developed an EOG-based system to control a wheelchair [332] and later a

human-computer interface by implementing electrodes into a virtual reality eyewear [336]. Chen et al. also developed a human-robot interface that could evaluate the eye position stable enough to reconstruct words [337]. Bulling et al. built a wearable EOG and used it to detect different activities in daily-life scenarios [338], [339]. All these systems have in common a lot of wiring to connect the silver-silver-chloride electrodes to the reading device.

Our approach was avoiding the many cables by screen-printing electrodes and wires onto a flexible PET film. Figure 4.45 on page 134 shows the multilayer approach that was employed for each electrode in this work. The wire from each electrode leads away from the eye and then towards the left ear. This is important to achieve a maximum flexibility of the electrodes so that the skin patch lies conformably on the head of the patient. Figure 4.52 shows the finished EOG patch comprising screen-printed silver silver-chloride onto a PET film that is embedded between an adhesive skin patch with the back cover and a wax paper front cover, which can be seen below the patch. To attach it to the head, first the white wax paper has to be peeled off. Then the electrodes are attached to the head with electrode 3 positioned exactly centrally of the forehead.

The electrodes 2 and 4 have to be positioned above the eyebrows. If done correctly, electrodes 1 and 5 are located in the outer canthi. Last, electrode 6 is pressed onto the bone below the eye. Figure 4.53 shows the attached skin patch to the head of the author. In our approach, the electrode below the eye showed to be not necessary, as the vertical signal may also be recorded between the horizontal electrode and the top vertical electrode. This reduces the overall number of electrodes and measurement channels as well as increases the comfort for the human. Anyway, we included the electrode onto the layout for comparison.

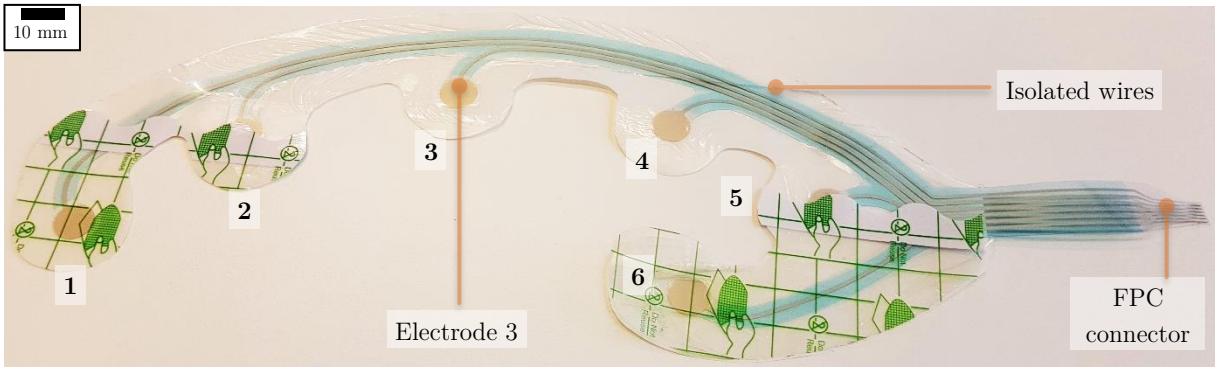

Figure 4.52. Readily assembled EOG patch with six electrodes (numbered) and isolated wires leading to a flexible printed circuit (FPC) connector. The back cover of the skin patch was partially peeled off to better see the screen-printed structure.

Figure 4.53. EOG skin patch with carbon electrodes attached to the forehead of the author.

Table 4.4. Set of movements during EOG recording from the view of the human carrying the patch.

Movement	Description	Repetitions
look right	Looking right for ~0.5 s, then looking straight	5
look left	Looking left for ~0.5 s, then looking straight	5
look up	Looking up for ~0.5 s, then looking straight	5
look down	Looking down for ~0.5 s, then looking straight	5
wink right	Wink slowly with the right eye	5
wink left	Wink slowly with the left eye	5
close eyes	Close eyes for ~0.5 s, then open them. Always looking straight.	5

A set of movements according to Table 4.4 was defined. The human carrying the patch looked straight before starting any of the movements. For the movement "look right", the human looked to the rightmost he can do, hold this position for about half a second, and then look straight. This was repeated five times. Then a break of a few seconds followed. For the movement "look left", "look up", and "look down" the same procedure with the respective directions applies. For "wink right" and "wink left", the human had to slowly wink with the right or left eye approximately once per second. The seventh movement was "close eyes" when the human had to keep his eyes straight while closing and opening his eyes alternately every approximately 0.5 s.

The patch was then attached via a male connector strip and custom made adapter wires to a Biosignals Researcher of Biosignalsplux (Portugal) in the EEG mode. Electrode three was used throughout this work as the ground electrode. Figure 4.54 shows a selection of the recorded EOG signals $V_{i,j}$ between electrodes i and j for a time span of ten seconds. The zero point of the time was set to the manually-identified starting points of the signals and one second before and nine seconds after that point are shown. Each electrode combination was measured separately, which leads to the temporal shifts between the signals on each electrode pair. The first row of Figure 4.54 shows the recorded signals for the human looking right and then to the centre again. In accordance with theory, the signal of all electrode pairs on the side of the eye (1:2 and 4:5) only measure a small signal amplitude that almost disappears in noise. All electrode pairs having one electrode on the right side

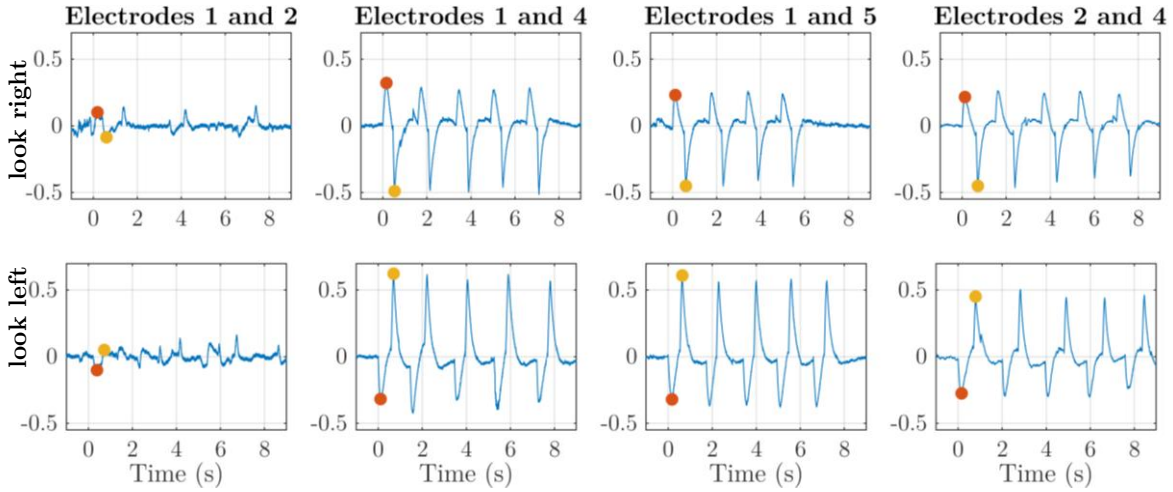

Figure 4.54. Selected EOG recordings $V_{i,j}$ between electrodes i and j over a time span of 10 s for two eye movements, looking right and looking left from the view of the human carrying the patch. Red and yellow markers indicate the two extrema within the first second after the manually selected starting point of the signal. Red indicates the first and yellow the second extremum. The complete recordings with all six electrode combinations and other eye movements can be found in the appendix in Figure B.1.

of the nose and one electrode on the left showed a signal of several hundreds of nanovolts. See Figure B.1 in the appendix for all recorded signals.

For example, the signal $V_{1,4}$ measured between electrode 1 and 4 shows a clear positive peak when the human looks left and a clear negative peak when the human looked straight again. Both peaks were marked by a red and yellow marker, respectively. Actually, the potential of the electrodes is constant, but due to the strict low-pass filtering of the signal, it is pulled to the zero line. The low-pass filtering has the advantage to quickly recover from any other motion artefacts or low-frequent noise. For the movement "look right", the signal looks opposite with a minimum (red marker) followed by a maximum (yellow marker). For all electrode pair combinations and all movements, the first two extrema were identified and marked in Figure B.1 in the appendix. The red marker shows the first extremum and the yellow marker the second.

To evaluate the quality of the electrodes, a scheme was developed and is explained in the following. Figure 4.55 shows the positions of the electrodes on the planar patch as numbered blue markers. Vectors in the graph visualize the potential differences between each electrode pair. The vectors are coloured in green and red if the amplitude is positive or negative, respectively and point towards the electrode with the higher potential. The vectors are weighted with the square root of the amplitude of the red marker in Figure B.1. For example, for the "look right" eye movement, the amplitude $V_{1,4}$ between the electrodes 1 and 4 was high (322 nV) and positive. Thus, a strong green arrow points from electrode 1 to electrode 4 in Figure 4.55a. The negative signal $V_{4,5}$ with an amplitude of only -52 nV is visualized by a thin, red arrow. The directions and amplitudes of the return signals were taken from the yellow markers that indicate the second extrema within the first second of the signals.

For the movements "look right" and "look left", a clear trend of the vectors is visible from left to right and right to left, respectively. All vectors for the two opposite movements are opposite. Furthermore, the vectors at the return movement, i.e. when the human looks straight again, are clearly opposite of the first movements. This indicates, that the quality of the electrodes is sufficient to measure the EOG signal with a sufficient signal to noise ratio (SNR). A further investigation showed, that the weighted sum of all normalized vectors is a good indicator for the conducted movement. The position vectors in Figure 4.55 were normalized to a length of 1 and then multiplied by the

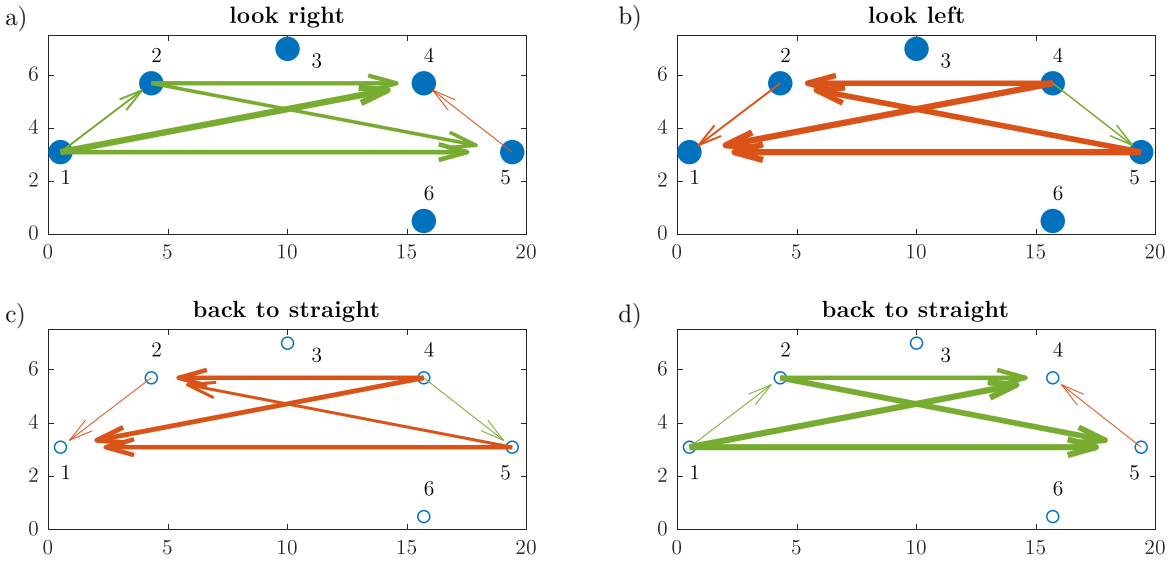

Figure 4.55. Schematic of the position of the six electrodes and the voltages measured between them indicated by a vector pointing towards the electrode with the higher potential. The vectors are coloured in green and red depending on the direction and are weighted with the amplitude. a) Vectors for the eye movement "look right", b) eye movement "look left", c) for the return movement back to looking straight after "look right", and d) the return movement after "look left".

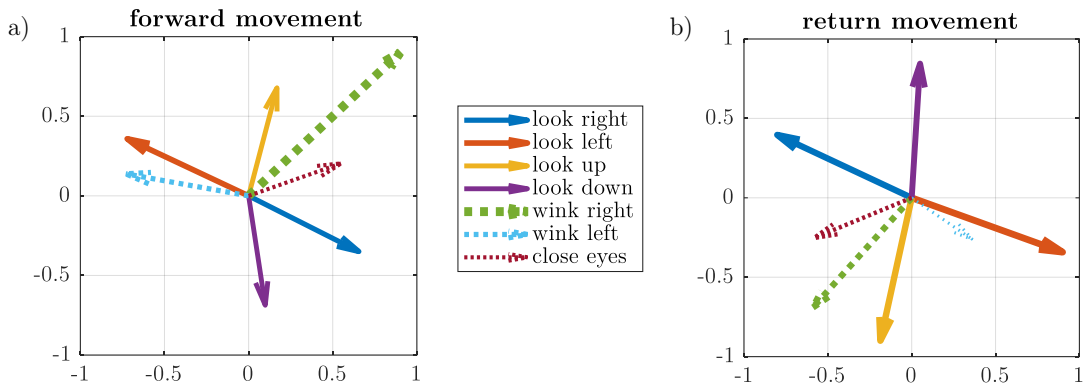

Figure 4.56. Summed vectors of theEOG signals with flipped y-direction to match the intuitive direction. a) Vectors for the forward movement according to the legend and b) for the return movement thereafter, which is looking back to a straight position and opening both eyes.

square root of the amplitude. The sum was then normalized again. Figure B.2 in the appendix shows the evaluations and the summed vectors direction for all seven movements.

A comparison of all summed vectors is shown in Figure 4.56. Here, the summed vectors without normalizations are were used and divided by the maximum value of each direction. Furthermore, the vertical direction is flipped in comparison to the previous figures to fit the intuitive direction. It should be remarked, that actually the horizontal direction of this and all previous figures is also flipped as our drawing was from in front of the human. Figure 4.56a shows the vectors for the forward movement according to the legend. The vectors for horizontal eye movements are almost opposite with angles of 28° for “look right” and 26° for “look left” with respect to the horizontal axis. The same applies with less accuracy to the vertical directions with the angles of 76° for “look up” and 98° for “look down”. The vectors for “wink right”, “wink left”, and “close eyes” point to different positions and can be determined, too. However, one of the latter movements may be confused with a diagonal eye movement, which was not tested here. The return movement of the eye may be helpful to determine different eye movements as well and the respective vectors are shown in Figure 4.56b. Most vectors point to almost opposite directions ($< 6°$) of the forward movements. Only the wink with left eye movement is pointing to a 25° different direction.

Some remarks on future work in this field should be mentioned. Especially the electrodes on the canthi are sensitive to the movement of the skin at the canthi. A strong closing of the eye or an intense smile causes the skin to wrinkle and probably lose contact with the electrodes. This results in a noisy recording. In a new layout, the electrodes should be positioned more towards the temples. Furthermore, the wires of the patch act as antennas capturing temporally and spatially changing noise sources, for example, a non-grounded person moving around the patient. A solution to that could be the printing of some more conductive and isolating layers. An isolated conductive layer below the wire and the electrode can shield electromagnetic noise from the front and sides of the head. Furthermore, the wires could be shielded by a conductive and another isolating layer from signals inside the body or from the rear of the person.

4.6 Summary

This chapter of the thesis presented a variety of mechanical, environmental, chemical, and medical sensors. The first section showed the production of stretchable wires on a silicone rubber film. These showed to be conductive until about 7 % and their resistance recovers to the original value after stretching. The increase of the resistance and the recovery are repeatable and make these wires candidates for sensors with a rather low resolution. A dedicated stretching setup was built for the

characterization of the strain sensors with a resolution of 14 µm per step.The sensors have proven resistant to thousands of stretching cycles even if the strain is much higher than the sensing limit. The maximum strain of the substrate was 330 %. When temporarily stretching the wires up zo this limit, the wire was conductive after less than a second after releasing it to the idle position. We were able to integrate the strain sensors as binary threshold sensors onto a wearable to measure the strain in the textile. An assembled LED indicates the current state and reliably switches on and off for small strains and large strains, respectively. The sensors have a small resistance of only 1 Ω/sq in the idle position, which is much lower than many other suggested methods for stretchable wires [243].

The second section includes the major advances this thesis offers. Different force sensing technologies are discussed and compared experimentally. For the characterization, a special force and pressure setup was built that can apply forces between 0.1 N and 15 N. On the round plate with a diameter of 5 mm, this corresponds to a pressure ranging from about 0.5 kPa to 750 kPa. Resistive pressure sensors were characterized and found suitable to measure pressures precisely but in a limited range of a small range of up to two orders of magnitude. Novel capacitive pressure sensors were produced and characterized. They offer a measurement range of at least five orders of magnitude. The sensitivity at the maximum pressure we could achieve with our measurement setup (750 kPa) was still above 20 %/dB. This maximum is about the pressure of a human (75 kg) standing only on his heel (10 cm^2). On the other end of the measurement range are slight touches (< 1 kPa). Our sensor covers the entire range and with it most of the interesting region of human-machine interaction. The sensitivity is the highest (up to 80 %/kPa) for small pressures (0.5 kPa) and then decreases approximately with the square root of the force. This enables the large measurement range and is similar to our human force perception, which is approximately logarithmic.

The pressure sensors are built of a dielectric that was micro-structured by screen printing. We investigated different dimensions for the hills that form the dielectric spacer between the two electrodes. The hills were varied in radius between 125 µm and 375 µm, while the centre-to-centre distance was kept constant at 1 mm. The radius is linearly proportional to the height of the hills that are between 40 µm and 180 µm. A theoretical model was developed that was able to precisely predict the measured capacitance values. According to the model, the top electrode is deflected by 80 % of its theoretical maximum deflection under the assumption that the volume of the dielectric is not compressible. This fits all produced sensors and predicted a higher sensitivity at smaller hills. We could validate an increase of the maximum response from 300 % for large hills to 420 % for smaller hills. However, smaller hills were eventually compressed so much that a short occurs between both electrodes. This limits the maximum pressure. Furthermore, we found that smaller pillars show a significant hysteresis for decreasing pressures, while all sensors had almost no hysteresis for increasing or pulsed pressures. The amplitudes and the sensitivities are substantially higher than for other sensors presented in literature, among them the Nature Materials publication of Mannsfeld et al. [279], [287], [293], [294], [340]–[342]. None of the publications investigated the hysteresis in detail and it has to be assumed that these sensors show a substantial hysteresis. Our sensors with large hills show a rather small hysteresis of below 10 %.

This chapter presented three-axial shear force sensors, too. They are built of two half-overlapping finger structures separated by an elastic dielectric. While a normal force decreases the distance similar to the pressure sensors above, a shear force perpendicular to the orientation of the fingers increases or decreases the overlap area of the electrodes. Both influences the capacitance between the two electrodes. A force in the direction of the fingers has no impact on the capacitance. If such a configuration is employed four times in the following way, three-axial forces can be measured. Four electrode pairs are oriented so that a shear force always increases the overlap area of one and reduces it of another while the other two show the same response to perpendicular forces. We simulated, produced, and characterized one electrode pair and found a small but almost linear relation between the force and the pressure. The sensitivity to normal force is slightly higher and the sensitivity to shear

forces is about twice that of comparable work [297]. The last of the pressure sensors focuses on the sensing of pressure waves and sound. A piezo-electric vibration sensor was constructed from an amplifying electrode that was mounted on top of piezo-electric PVDF. The pressure is amplified by a factor of 16 due to a large impact area for the pressure and only a small contact region to the PVDF film. However, the employed PET film dampens especially high frequencies. The sensitivity drops significantly at frequencies above 13 kHz.

The next section focused on temperature and humidity sensors. After a general overview of temperature sensors in the literature, semi-transparent thermocouples are investigated. These were made from nanomaterials like silver nanowires, carbon nanotubes, and the conductive polymer PEDOT:PSS. Different combinations of these three materials were systematically evaluated in a specifically developed measurement setup. A linear response for all combinations with Seebeck coefficients up to 55 µV/K makes the thermocouples suitable as temperature sensors. Energy harvesting was also investigated, but the rather high resistance, especially for CNT-containing thermocouples, made the maximum power output only to about 0.55 nW for a gradient of 100 °C. The main difference to literature is the transparency of up to 90 % of the thermocouples. To our knowledge, no such thermocouples have been presented so far. Wireless temperature and humidity sensors based on the change of an inductively coupled resonance circuit were produced and characterized. The first uses a thermosetting paste in series with the coil inductor and the humidity sensor bases on the change of the relative permittivity in the polyimide substrate. Both sensors can be read with a 13.56 MHz antenna similar to the ones in use for near field communication (NFC). Temperature or humidity changes the resonance frequency slightly, but one has to make sure that the distance between the reader and the sensor does not change. In a short section, screen-printed electrodes for organic solar cells are presented together with a discussion why our other printing processes are not suitable.

Section 4.4 discusses inkjet-printing and screen-printing of electrodes for chemical and biomedical sensors. A production method for chlorination of printed silver layers is shown to produce Ag-AgCl reference electrodes. The conventional galvanostatic method is not applicable to thin-film electrodes. Furthermore, printing of interdigitated electrodes (IDEs) is discussed and printed IDEs are presented and characterized. Unfortunately, the printed layers could not withstand the harsh treatments during functionalization of the biosensors that are required to make them selective to certain substances. For gas sensors, the electrodes could be readily employed and an exemplary measurement curve is shown. In comparison to the conventional gold evaporation, the production is faster and first results indicate that the sensor response even benefits.

The last part of this chapter focuses on medical applications and skin electrodes in particular. Dry electrodes were screen-printed with silver-chloride and carbon paste and compared to gel-based electrodes and a conductive, laser-ablated Kapton film. All four electrodes are capable of recording electrocardiographic signals from the hearts activity and the main peaks are perceivable. The signal of the dry electrodes is more than 55 % in comparison to the gel electrode, whereas the graphite-containing electrodes perform less. One of the reasons could be the pressure to the skin, which is higher for the gel-assisted electrode and the higher resistance in the wires of the dry electrodes. Similar silver-chloride and carbon electrodes were employed for electrooculography, the measurement of the resting potential of the eyes. We showed the production of a complete skin patch that bases on a skin adhesive and a liner between which the printed electrodes are embedded. These are printed onto a PET foil, which was cut into a shape that allows a high degree of movement in different directions to attach conformably onto the skin. The stretchable and breathable skin adhesive is suitable for a long-term stable and comfortable wearing.

During this thesis, many sensors were produced that may be useful for sensing devices in the Internet of Things. The next chapter focuses on the integration of some of them into hybrid smart systems that implement evaluation electronics onto the imprinted substrates.

Chapter 5

Hybrid Integrated Sensor Systems

Hybrid electronics or hybrid systems is a term that appears more and more in the industrial area of PE, possibly inspired by the leading industry organization OE-A, which recently created an own working group on hybrid systems. They define hybrid systems as the combination of the advantages of both, printed and silicon-based components. Flexible, thin, and light-weight organic and printed electronics will not reach the processing-power of silicon-based electronics and not vice versa. This requires that we combine the best from both worlds, which enables a broad range of new applications. Figure 5.1 summarizes the distinct advantages of both production techniques. Our everyday electronic devices possess more and more functionalities and are shrinking in size due to progress in the silicon industry and the thin-film production. Already today, these two fields cannot be separated anymore and in the future, more and more hybrid systems will appear that can be interconnected in the Internet of Things. [15], [343]–[345]

This chapter shows some of our hybrid integrated systems that were developed, produced, and characterized during the work on this thesis. Section 5.1 introduces into the production of the circuit board and the assembly of hybrid systems. The simplest form of a hybrid system is a RFID tag that contains only one chip. Section 5.2 presents different RFID antennas, like near field communication (NFC), ultra-high-frequency (UHF), a Gigahertz antennas that can be combined to wireless systems by adding an integrated silicon-based chip (IC). For more complex integrated systems, the wiring on the flexible substrate plays a major role. Several different hybrid integrated sensor systems employing the force sensors described in the previous chapter are presented in Section 5.3. Section 5.4 summarizes this chapter and highlights the main conclusions.

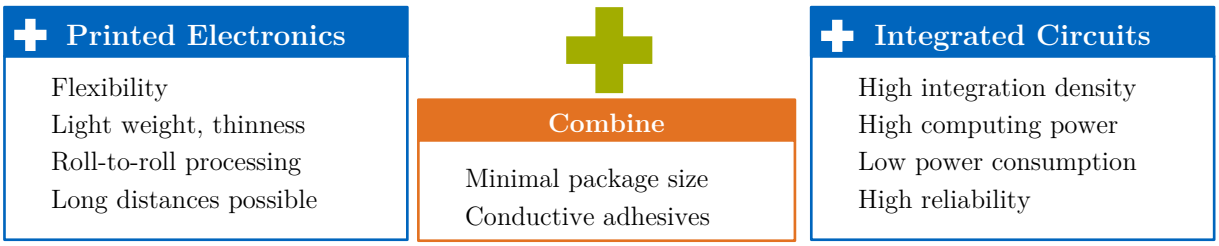

Figure 5.1. Hybrid systems combine the advantages of Printed Electronics and silicon-based Integrated Circuits to create attractive new devices.

5.1 Production of Hybrid Systems

Wiring is one of the most important components of any electronic device. Therefore, we want to show some aspects on the printing of plain wiring for the use as circuit boards including multilayer printing and the assembly of other non-printed components. A certain print quality is required for the small footprints of surface mount devices. The printing of the pads and wires for the circuit boards are investigated in the first subsection 5.1.1. The second subsection 5.1.2 highlights several aspects of multilayer printing. Finally, the assembly of components is discussed in subsection 5.1.3. All these steps are important for the examples of hybrid integrated systems shown in the next section.

5.1.1 Print Quality

There are several kinds of chip packages. Some have rather a rather large pitch and their pads are easy to print and assemble. Others packages like ball grid arrays (BGA) require precise machinery to place the chips and often require multiple circuitry layers that were not yet shown by printing techniques. This section picks some of the smallest packaging forms that are at the edge of what can be done manually. All ICs with pins outside of the package can be assembled as was shown multiple time. Quad-Flat No-Leads (QFN), Micro Lead Frames (MLF), Lead Frame Chip Scale Package (LFCSP) or similar ones are desirable because of their small size. Typical pitches are down to 400 µm of which it is recommended to print 250 µm and leave a gap of 150 µm.

Figure 5.2 shows three different footprints of packages used during the work on this thesis. In the microscope image on the left, eight screen-printed pads designated for a microcontroller can be seen. As the recommended footprint of the manufacturer was directly applied on the screen, we can see, that the gap between the pads is smaller than designed. This small gap can easily cause shorts. Therefore, we recommend to edit the footprint recommendation of manufacturers and reduce the width of the wires regardless which printing technique is used. This was done in the inkjet-printed footprint in the central photo. Here, a clear gap can be seen between the individual pins and simplify the assembly. On the right photo, the footprint was screen-printed but apparently, the paste still flows and makes it hard to attach an SMD component on top. Also, the gap between the isolating layer and the chip footprint is small and makes it almost impossible to verify if a connection was made. These examples show the importance of a modification of the footprint and the necessity for space around the patterns.

5.1.2 Multi-Layer Printing

When designing more complex PCBs, multiple wiring layers are necessary that are separated by isolating layers. Therefore, multi-layer printing is a must and at least one more layer has to be printed. We want to highlight a few differences to conventional PCB making here. The first layer

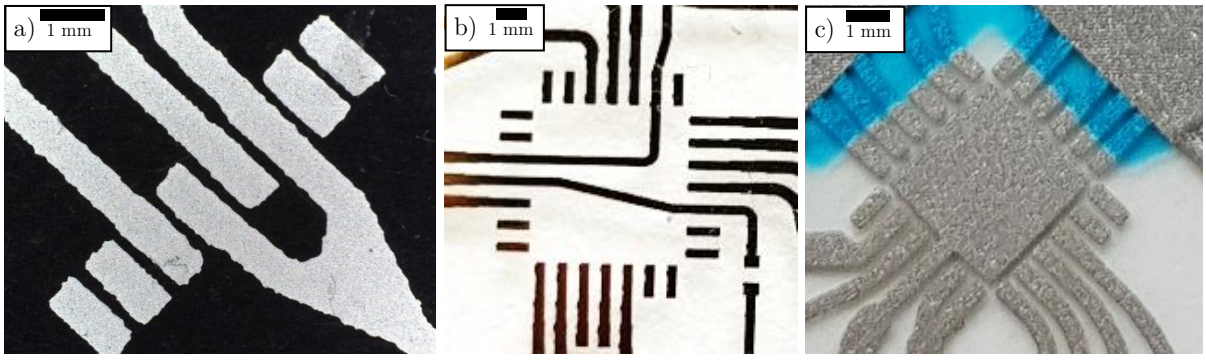

Figure 5.2. a) An optical microscope image of screen-printed pads, b) a photograph of an inkjet-printed footprint, and c) a photograph of contact pads for surface mount ICs.

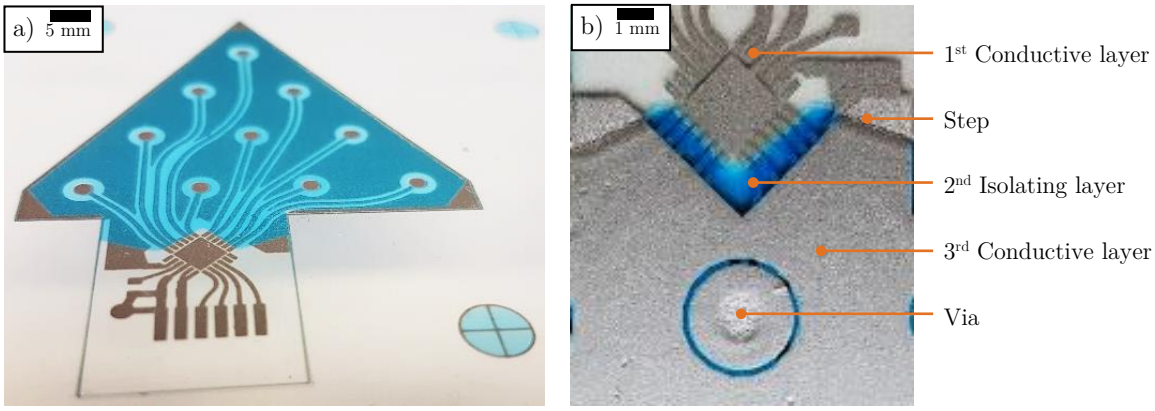

Figure 5.3. a) Printed bottom layer (silver) of a PCB with isolation layer (blue). b) Magnification of a section of the final print showing some distinct differences to conventional PCBs.

can be printed as discusses onto the substrate. The second layer, for example, an isolating layer as shown by the blue layer in Figure 5.3a. In contrast to conventional PCB-design, an isolating layer does not need to cover the entire area of the circuit board. Usually, only the regions where it is important to have an isolation are printed. In the example, it was desirable to achieve a homogeneous thickness across the upper triangle, so most of the area is covered. Only the corners of the triangle and the ten circles within the triangle are not covered because they should make the connection to another conductive layer on top as can be seen in Figure 5.3b.

We found that at least three layers of the thermal curable paste with intermediate drying are required to achieve a homogeneous layer that is not shorted by another conductive layer on top. This is not convenient as before printing each layer, the substrate needs to be aligned again. It is partially related to the rather high mesh count of 80 that we used. Furthermore, the paste is sticky and attracts a lot of dust during printing and drying that cannot be wiped away after drying. The high number of printing cycles may be decreased if a lower mesh count or a thicker emulsion is employed that allows the printing of a much thicker layer. However, it is rather desirable to obtain thin layers, because the step heights as indicated in Figure 5.3b should be low. During the design phase of this pattern, we estimated the necessary thickness of the dielectric as negligible for the final design. However, it can be seen by visual inspection, that the via indicated in the figure is not filled by another layer on top. During drying, the printed silver paste's volume shrinks, and the recession appears. Thinner isolating layers may be printed by using UV-curing dielectrics as the one we also investigated. For this, it was at least possible to conduct multiple wet-in-wet printing cycles without intermediate curing to reach a pinhole-free layer with only one curing step. Unfortunately, our institute did not possess an own UV-curing tool, so it was difficult to pursue this in depth.

We were able to design and screen-print multilayer circuit boards using thermal and UV-curable dielectric pastes. The wires were reliably well-conductive and non-interrupted. A selection of a combination of screen and emulsion that allows a thicker layer to be printed with only one or two passes would be desirable and is within close reach.

5.1.3 Sensor Integration

The printing of sensors was described in detail in Chapter 4. Such printed sensors can be integrated into smart hybrid systems in two ways: horizontal or vertical integration. Horizontal integration places the sensor away from the other printed layers and connects it only by wiring. This is a reproducible way to integrate sensors because the printing process is almost independent of the rest of the system. Still, some conductive and isolating layers can be combined to reduce the number of printing steps. Vertical integration integrates the sensor directly into the printed wiring. These can be resistive or capacitive sensors for temperature, humidity, pressure, and many more. They can be integrated

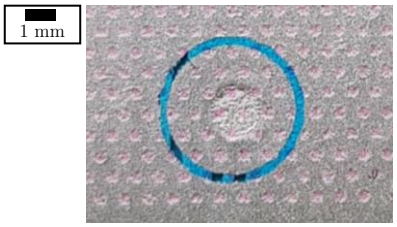

Figure 5.4. Vertically integrated sensor with a structured dielectric that was printed on top of an uneven surface and may be detrimental to the sensors behaviour.

either below all printed structures, on top of the multi-layer stack, or in-between. Figure 5.4 shows an example of vertical integration of our capacitive force sensors on top of the already shown multi-layer circuit. The printing of the structured dielectric is possible as can be seen by the rose speckles distributed all over the image. However, the electrode is not flat because of the via that we used to connect the top conductive layer to the bottom. This may influence the sensor's behaviour and has to be either avoided or investigated in more detail.

How the sensor integration is done for a specific application has to be carefully evaluated. If this is done, sensor integration into smart hybrid systems offers completely new design possibilities that enhance the wiring board with a much more diverse functionality. The protection of intellectual property of printed sensors may also be a reason for a vertical integration, as the disassembly and reverse engineering are made much more complex.

5.1.4 Assembly of Components

For the assembly of conventional SMDs, it is important to discuss the way of interconnection. The important requirements for printed electronics are the following. A low temperature of below 120 °C and ideally below 80 °C is desirable to be compatible with a wide range of substrates. The working time with the interconnection material should be between a few seconds or less for automatic assembly and a few minutes for prototyping and manual assembly. The resistance should be rather low, but up to a few Ohms of contact resistance are often negligible in comparison to the wire's resistance. Soldering would fulfil the last three requirements, but even low-temperature solders like Sn-58Bi or Bi-51In alloys require temperatures above 100 °C. A possible solution could be laser soldering systems that heat the solder paste locally to higher temperatures than are possible with the bulk substrate. [38]

The currently best choice for PE products is conductive adhesive pastes that comprise a stable adhesive matrix fixed with conductive fillers. Conductive adhesive pastes and screen-printing pastes are similar, except that for glueing solvents are often detrimental. Still, screen-printing pastes and conductive paints can be used for glueing. Solvent-free adhesives are usually either cooled to low temperatures or are consisting of two components that need to be mixed. After defrosting or mixing, the adhesives can be used for a certain time until the cross-linking in the material increased the viscosity too much. The most commonly used matrix adhesive is epoxy that can come premixed and frozen or as two separate materials. In recent years, the development of epoxies enabled more and more elastic adhesives by employing different polymers or modifying the matrix. [38] Conductive adhesives can be either isotopically conductive (ICA) or anisotropically conductive (APA).

We found that the ICA Conductive Epoxy 60 Minutes of CircuitWorks (US) provides connections that are often more stable than the coating layers of the substrate and has a decent working time of about 30 min that is comfortable for manual assembly. The curing at room temperature takes several hours. A reduction in elevated temperatures can be achieved, but the viscosity of the epoxy drops at higher temperatures and the glue may flow away from its current location and cause shorts. The same company offers another version of the glue that can be used for about 5 min, which we can

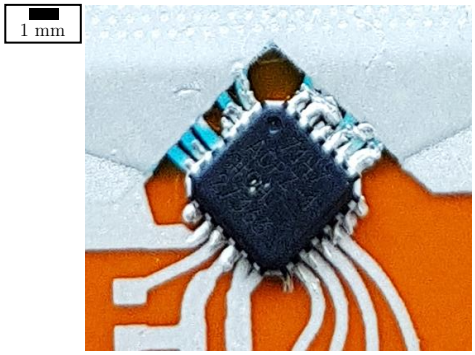

Figure 5.5. Assembled integrated circuit with dimensions of only 4 x 4 mm² using epoxy glue.

recommend if fast hardening at room temperature is desirable. It is stable after about one hour. Both pastes and others that we investigated can be applied by hand as well as by stencil printing. We laser-cut PET and PI films with openings for all areas where glue shall be applied. A screen-printing squeegee can distribute the paste and press it through the openings. Figure 5.5 shows an assembled integrated circuit with dimensions of only 4 x 4 mm² and a pin pitch of 0.5 mm. APA pastes consist of a matrix with an amount of fillers well below the percolation threshold and is only conductive if a filler material is pressed between two conductive contacts. For common APA pastes, high pressure and elevated temperatures are required to stabilize the matrix around the contact region. The attracting properties of ACAs are that they can be applied on a large area and are only conducting in the perpendicular direction. Thus, shorts between adjacent pins of SMD components can be excluded.

Another option is conductive adhesive tapes that exist in three configurations. The first is only conductive on the surface, the second is conductive in all direction (isotropic), and the last one is anisotropic conductive tapes that only conduct perpendicular to their plane. All tapes are available as pressure-sensitive, temperature-sensitive, or a mixture of both, which refers to the necessary conditions for applications. We employed isotropic conductive tapes for some larger contacts as one can solder a wire onto it and then stick it to the printed circuit. Furthermore, we employed the pressure-sensitive adhesive anisotropic conductive tape 9703 of 3M. It can be applied to a large area and, then, components can be pressed onto printed pads below the tape. It is suitable for components with rather large footprints of at least 0.1 mm² as the density of the particles is rather low and inhomogeneous in size. Small footprints, as well as connections with a high current, may lead to a high current density in the few particles.

Table 5.1 summarizes selected properties of all conductive adhesives that were used during the work on this thesis. The book of Suganuma [38] gives a good overview of different techniques for assembly and interconnection in hybrid systems.

Table 5.1. Summary of selected properties of the tested electrically conductive adhesives.

Product	Mixing	Usability	Dry time	Mechanical Stability	Electrical Resistance
Silver Conductive Paint	no	easy	15 min	very low	very low
CircuitWorks Epoxy	yes	hard	15 min	very high	very low
CircuitWorks Epoxy 60 Min.	yes	easy	12 h	very high	very low
WireGlue	no	easy	2 h	low	medium
BarePaint	no	medium	2 h	medium	medium
9703 Tape	no	easy	pressure	high	low

5.1.5 Rapid prototyping

Figure 5.6 shows one of our largest assembled circuit boards consisting of five modules that can be connected to form a modular battery-powered system. It can be extended in every direction by other modules, for example, some that contain a sensor. The central module is printed on two PET foils and the interconnection was done by stamping holes in the top layer and filling them with epoxy. All components, the microcontroller, two capacitors, two resistors, an LED, and the eight connectors were assembled with epoxy too. The other modules, a battery holder, a programming adapter, a USB communication module, and a LED stripe were produced in a similar way.

The circuit boards were designed with a commercial PCB design tool and printed by an inkjet printer with Ag-NP paste. Most components can be assembled by only little-trained persons, only the microcontroller and the USB-controller require experience. The reason for the modular system was that the central unit can be used for many applications. This shows that printed electronics for prototyping of circuit boards is feasible already today.

5.2 Chip-based Wireless Systems

This section focuses mainly on the printing of antennas for chip-based wireless systems. Antennas on a flexible substrate may play an important role in the future applications of printed and flexible electronics. They allow the placing of systems remotely or on movable devices where wiring is difficult or impossible. Examples for sensor systems in remote positions are on the outside of a car or plane, in the soil of a field, inside tanks, and inside the body. Movable devices can be packages, parts of board games, or any other mobile thing enhanced by an electronic functionality. Antennas can overcome the mostly non-trivial connection of a printed device to the rest of the system. The standard method of open connection pads that are connected by conductive glue, spring pins, or a zero-input-force (ZIF) connector is susceptible to mechanical stress, abrasion, and destruction of the pads by environmental conditions. A system employing antennas can be completely sealed and easily exchanged to a new one. Furthermore, antennas allow communication among different printed devices without the need to connect them. Multiple antennas within one device may reduce the complexity as many printed devices are limited in the number of signal layers. An example could be the placement of two matching antennas on each side of the substrate to avoid a through contact.

In the following, antennas across a large range of frequency are shown. Near-Field Communication (NFC) antennas working at 13.56 MHz are available in most smartphones to communicate with

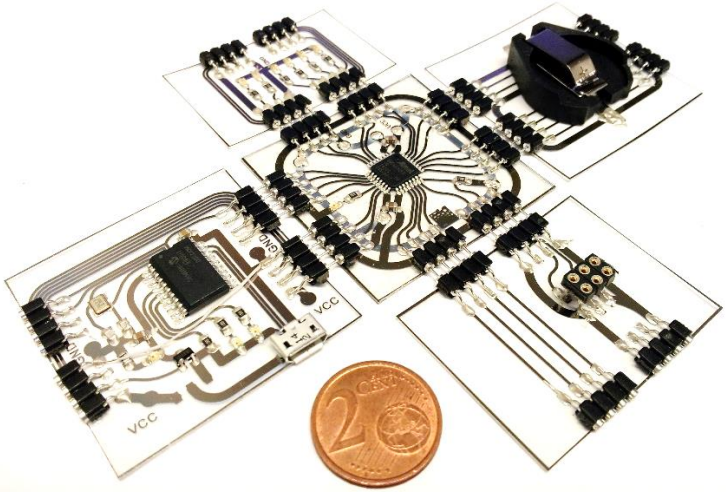

Figure 5.6. Five different modules of inkjet-printed circuitry with assembled SMD components connected to a modular battery-powered system.

external devices. For longer read ranges, ultra-high frequency (UHF) antennas are used to operate at 850 – 950 MHz. Gigahertz antennas in the band of Wi-Fi or Bluetooth can be designed as small patch antennas that are easy to print.

5.2.1 Near-Field Communication (NFC)

As the printed structures, especially inkjet-printed ones, have a rather high resistance, the formula for the resonance frequency has to be extended by a term that regards the resistance. Eq. 5.1 shows the equation for the resonance circuit of a capacitor C, an inductor L, and a resistor R. The capacitance is mainly given by the employed chip (SL13A of AMS AG, Austria) and, here, is 25 pF at 13.56 MHz. The inductance and the resistance mainly depend on the length and the width of the printed antenna.

$$f_{Res} = 2\pi \cdot \sqrt{\frac{1}{LC} - \left(\frac{R}{L}\right)^2} \qquad \text{Eq. 5.1}$$

For the near-field communication (NFC), the frequency should be as close as possible to the defined 13.56 MHz. As this thesis does not focus on antenna characterization, we refrain from showing simulation and measurement results in this section and directly show potential layouts that proved well. Figure 5.7a shows a CuO antenna after IPL-curing and assembly of the bridge. The total area of the coil antenna is about 4.7 x 6.0 cm² and the line width is 600 µm. This leads to a total length of the inductor of about one metre. This results in a high resistance of more than 1 kΩ for the copper-antenna. This is the main reason, why only five loops of the antenna are used because, for more loops, the resistance is too dominant. We achieved a reading of the identification number from the chip, but only at small reading distances of about 1 cm or less. We found the only 100 nm to 200 nm thin copper layers as too resistive to achieve a high antenna performance.

Inkjet-printed silver antennas as shown in Figure 5.7b are more suitable as the resistance is significantly lower at around 300 Ω for 7 loops in the 5.2 x 6.0 cm² area leading to a total length of about 1.4 m. This is still slightly higher than predicted by the measurements in Section 3.1.3 (about 200 Ω) because of the inhomogeneous light distribution in the IPL-tool's process chamber. These antennas are suitable for a measuring range above 1 cm, however not more than 5 cm. Still, the resistance is too high but can be decreased by using screen-printing as was previously shown by other researchers. [101], [316], [346] A screen-printed antenna produced during the work on this thesis is shown in Figure 5.8. It also consists of seven loops, but the size is larger (5.1 x 9.9 cm²), leading to a total length of almost 2 m. The screen-printed antenna's resistance was now a few tens of Ohms.

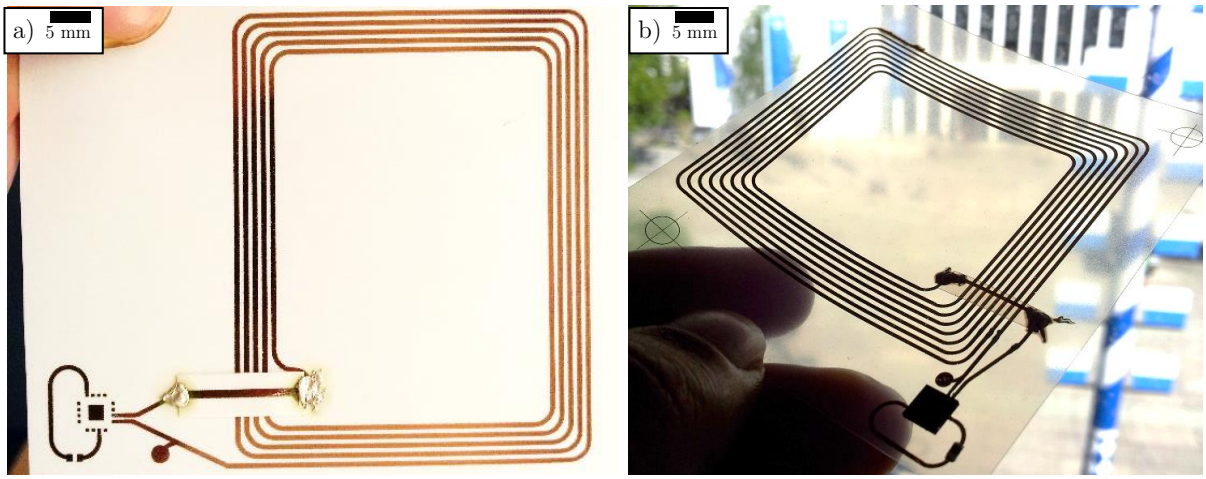

Figure 5.7. a) Inkjet-printed NFC coil with copper NPs and the assembled bridge. On the bottom left corner, a chip and a capacitor have to be assembled. b) Readily assembled NFC tag on semi-transparent PET substrate with only a small chip and a capacitor assembled with conductive epoxy.

Figure 5.8. Screen-printed NFC antenna with the assembled chip.

The main conclusions from this section are rather based on the production technique. It is possible to print non-interrupted silver and copper layers of the length of more than a metre. Except for some obvious printer failures, all our antennas were printed reliably with a similar resistance. The printed wire with the highest aspect ratio was about 2.7 m long and only 200 µm wide and was printed with the Epson printer without any modifications. This shows, that inkjet-printed is a reliable technique also for a large volume at a rather low price. The printing speed of the Epson printer is comparable to a photo print at home. As expected, screen-printing is able to reduce the resistance significantly by applying a thicker layer and the reliability is higher, too.

5.2.2 Ultra-High Frequency (UHF)

The second type of antennas that were investigated during the thesis is ultra-high frequency (UHF) antennas that feature a much larger reading range and a more compact design. The frequency range that is used for RFID is defined as between 865 MHz and 869 MHz in Europe and 950 MHz in the US. Again, different patterns have been simulated and inkjet-printed, screen-printed, and spray-deposited. The tag shown in Figure 5.9 was inkjet-printed on a transparent PET foil within the area of 5 x 5 cm^2. This specific example consists of a dipole antenna, an assembled chip, a capacitor, and a spray-deposited photodiode and is described in detail in the publication of Falco et al. [34]. This work shows for the first time that is feasible to embed thin-film photodetectors into inkjet-printed RFID tags. Both technologies, inkjet printing and spray deposition are roll-to-roll compatible and can produce such systems at low cost and high speed.

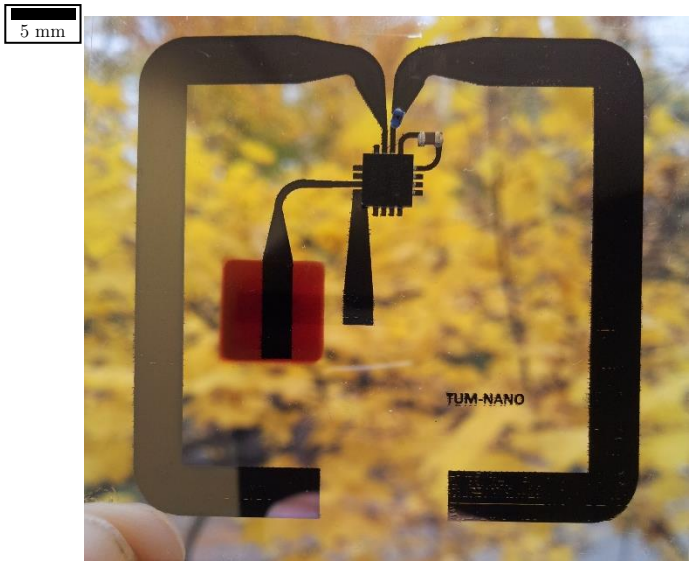

Figure 5.9. Inkjet-printed UHF antenna with integrated photo-detector which was spray-deposited and a chip and a capacitor assembled. Presented in [34]

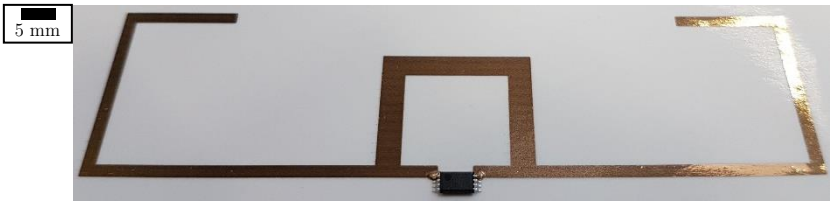

Figure 5.10. Inkjet-printed UHF antenna on photo paper using Au-NPs and an assembled EM4325 chip.

Figure 5.10 shows an inkjet-printed gold antenna on paper. The main reason for using gold was its biocompatibility and the use of paper because of its biodegradability. This tag was produced for research on biodegradable and biocompatible RFID tags. However, on normal paper, we were not able to achieve a conductive layer, so we had to use non-biodegradable photo-paper. We printed four layers of gold ink to be sure to reach a low resistance and sintered it with intense pulsed light. The photo shows the assembled tag with the EM4325 chip of EM Microelectronic with an impedance of 23.3 – 145j Ω.

Figure 5.11 shows exemplary measurement results of the S11 parameter of an inkjet-printed UHF tag. The simulated magnitude and phase are shown in blue and predicted a resonance frequency at 865 MHz. The measured values are shown as red markers and give a resonance frequency between 871 MHz and 891 MHz, which is slightly above the target, but still accurate. The amplitude of the measured tag is about 1 dB lower than the simulation and also in good accordance. The main difference is the much larger bandwidth. This may be partially influenced by the measurement environment, as all magnitudes are rather low.

5.2.3 Gigahertz Antennas

Gigahertz antennas are resonant patterns with a resonance frequency in the gigahertz range. An interesting application is the creation of antennas that resonate at around 2.4 GHz, which is the IEEE 802.11 defined standard for wireless local area networks (WLAN) and employed in Bluetooth devices, some cordless phones, and some radio-controlled toys. This section bases on the publication together with my colleague, Michael Haider, and a student, Quirin Hirmer, presented at the PRIME 2017 conference. [347]

A patch antenna was inkjet printed with Ag-NPs onto the photo paper P4 (thickness 200 µm) and the coated PET T6 (thickness 150 µm) by the Epson printer. The dimensions of the antenna were simulated in CST Microwave Studio 2016 to achieve a resonance frequency of 2.0 GHz. A resonance frequency of 2.11 GHz for the paper antenna and 2.06 GHz for PET was predicted. Before printing, both dimensions were reduced by 100 µm to compensate the drop gain of the inkjet-printer and the pattern was printed twice to decrease the sheet resistance.

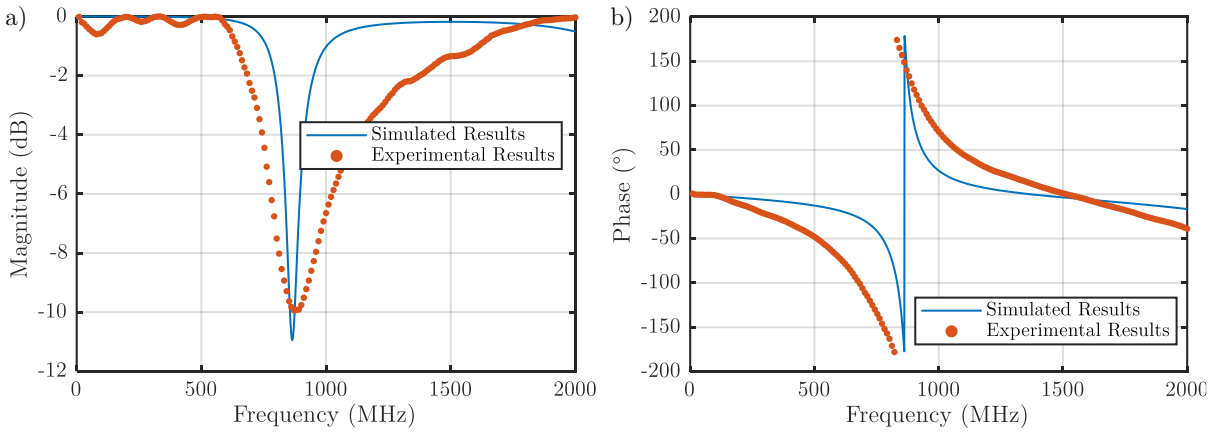

Figure 5.11. Simulation and measured S11 parameter of the UHF antenna with a) magnitude and b) the corresponding phase

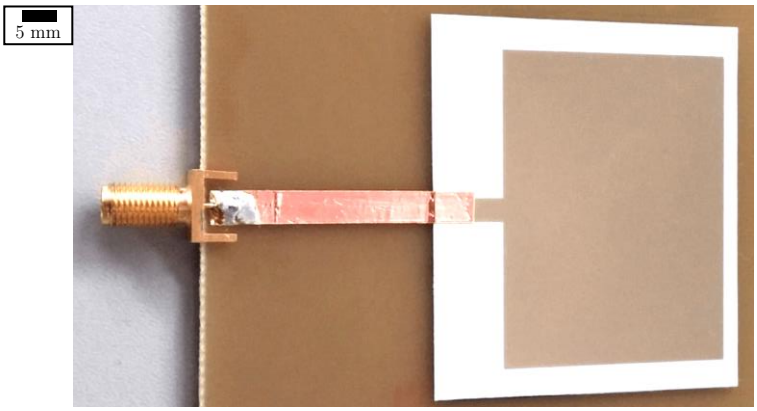

Figure 5.12. Inkjet-printed Gigahertz patch antenna mounted on top of a copper-plated FR4 board.

The final patch antenna was about 46 x 36 mm² with a feed line of 3.5 x 10 mm² and is shown in Figure 5.12. The silver thickness was 1.93 µm and had a sheet resistance of 210 mΩ/sq on paper and 380 mΩ/sq on PET after IPL sintering with two pulses of 500 µs and 750 µs at 2.5 kV. The measured antennas showed a resonance frequency of 2.14 GHz for the paper antenna and 2.09 GHz for the PET antenna. The curves can be found in the publication of Hirmer et al. [347] The close match of the resonance frequencies shows the potential for printed antennas. The small mismatch can be explained by the completely different film morphologies in simulation and real device. Whereas in the simulation a perfectly flat layer out of bulk material with a certain resistivity was assumed, the real device consists of a porous and rough Ag-NP film.

5.2.4 RFID Tag with Security-Button

Radio frequency identification (RFID) tags or systems are increasingly used in day-to-day situations to provide information or handles to information stored elsewhere. In many use cases, the information or handles stored within the tag can be used to track the location of the tag or the person carrying it, eavesdropping on tag-to-reader communication, cloning and pretending to be another tag or person, or misuse the information. [348] It would be desirable to use the advantages of wireless data transfer with a control over it. Our idea was to implement a button into the RFID antenna that is open by default and closes the loop antenna on pressure. We investigated the use of our thin pressure sensors without a dielectric as these are shorted at a certain pressure. The implementation in an NFC circuit is shown in Figure 5.13a with a magnification of the chip and the sensor in Figure 5.13b. The latter shows the structured dielectric as dots around and between the contact area of the bridge to the bottom contact wired to the chip.

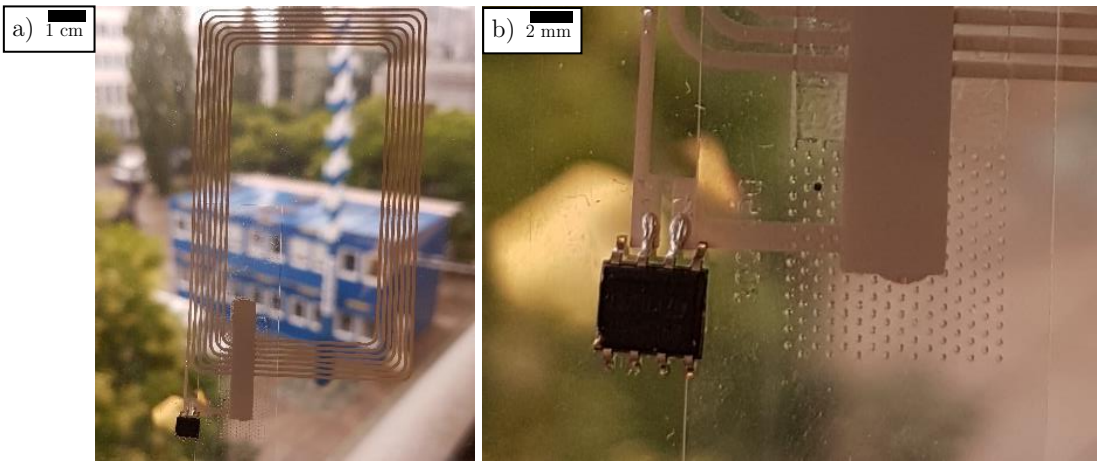

Figure 5.13. a) Screen-printed one-chip RFID tag with a pressure-activated button. b) Magnification of chip and pressure-sensing button.

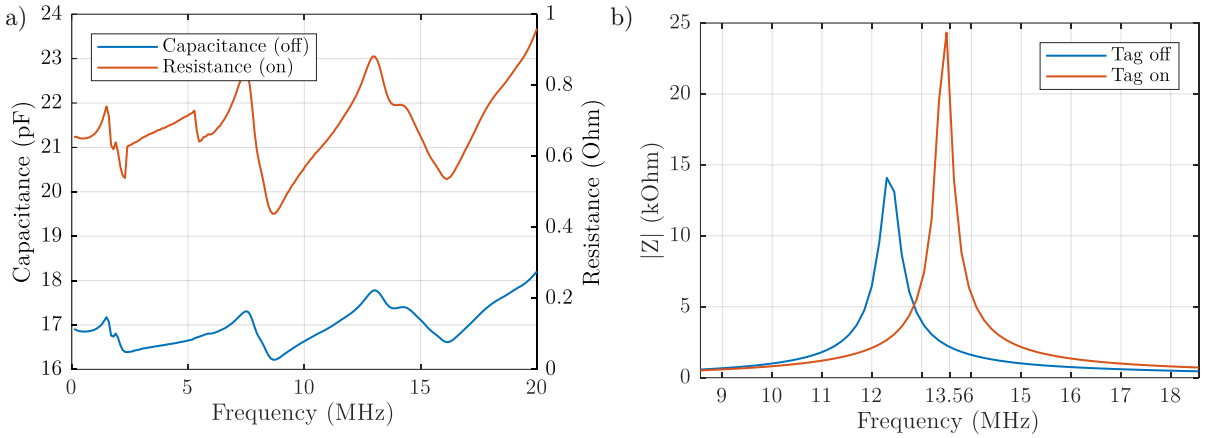

Figure 5.14. a) Capacitance in the off-state and resistance in the on-state of the pressure-sensing button. b) The shift in resonance frequency of the printed RFID tag with security button.

Preliminary results show that the button works as intended and changes from a capacitance of about 17.5 pF to a resistor of about 0.8 Ω at the desired frequency of 13.56 MHz (see Figure 5.14a). The latter should not have a large influence on the antenna behaviour as intended. The first one introduces a second large capacitance next to the internal capacitance in the microcontroller and decreases the coupling of reader and antenna. We used an FR4 antenna resonating at approximately 13.56 MHz and brought the safe tag close to the reader. When the button was pressed by a plastic clamp, the resonance frequency was matching the 13.56 MHz as can be seen in Figure 5.14b. The shift in resonance frequency of the circuit is more than 1 MHz if the clamp was removed and the button was not pressed. This should reliably inhibit the coupling of the reader and the tag. Unfortunately, our tag was never recognized by an NFC reader independently of the pressing state and the measurement with the network analyser gave no satisfactory results. Still, we think it should work and want to pursue this topic in the near future.

This was already showing one implementation using our micro-structured dielectric in a hybrid smart system, the next section focuses on more systems that employ our capacitive pressure sensors.

5.3 Force- and Pressure Sensing Systems

In Section 4.2.5 of this thesis on page 119, we showed the performance of standalone pressure sensors. In this section, we want to integrate these into a hybrid system of an inkjet printed circuit board assembled with conventional surface mount components. The first prototype shows the basics on how to measure capacitances with microcontrollers (Subsection 5.3.1). In the second subsection 5.3.2, we investigate the use of the pressure sensors as weighting scales for evaluating the filling state of a drinking glass. Section 5.3.3 focuses on large-area sensing with a hexagonal patch that can be attached to others for forming a large force sensing “blanket”. This work eventually resulted in the use of a capacitance-to-digital converter chip and the change of the shape to a triangle. Section 5.3.4 presents the most recent work on this pressure sensing “triangle”.

5.3.1 Smart Pressure-Sensing Systems

The first prototype consists of a simple circuit with a microcontroller that is able to read two sensors. A schematic of the assembled circuit is shown in Figure 5.15. From top left to bottom right, it contains a connector for power supply, programming the system and retrieving the measured values. The microcontroller (µC) is shown in the centre surrounded by voltage stabilizing capacitors. Four light emitting diodes (LEDs) with their corresponding serial resistors (R) were placed as visual pressure indicators. Finally, the two sensor electrodes at the bottom of the figure. For this first

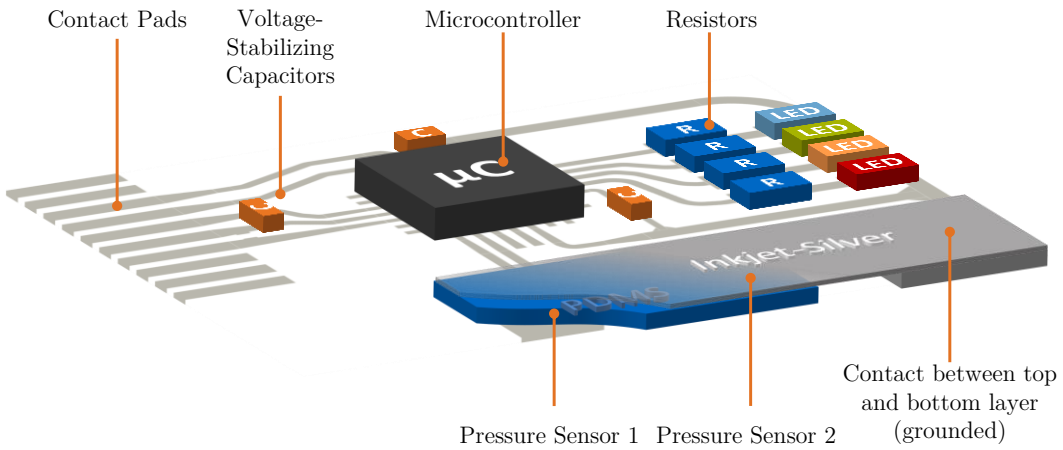

Figure 5.15. Schematic of the first pressure sensing circuit comprising two sensors, a microcontroller, and several LEDs for pressure level indication.

prototype, a non-structured 100 µm thick PDMS film was placed above the sensor. Another PET substrate with an inkjet-printed electrode was put on top with the electrode facing down and glued on the contact area. These two electrodes touching the PDMS layer on each side form the capacitive sensor. All electrical connections were done with electrically conductive epoxy.

The circuit board was inkjet-printed with Ag-NP ink in the Epson printer on a coated PET-based substrate. A photo of the plain circuit board is shown in Figure 5.16a. This was then assembled with SMD components, a 1.27-pitch connector, a PIC24FJ64GA202 microcontroller of Microchip (US), four conventional LEDs, five resistors, and two capacitors. The grounded top electrode was expanded and a grid was added to shield stray capacitances by a grounded human body. If the electrode would not be shielded, the sensor would rather work as a simple touch sensor than a pressure sensor. With the grounded electrode, we noticed no signal change in proximity or light touch by a human finger.

The microcontroller PIC24FJ64GA202 is equipped with a charge time measurement unit (CMTU), which was used to measure the capacitive sensor. The entire circuit was operated at 3.25 V. We used a current of I = 55 µA to charge the capacitor for t = 1.5 µs with the charge Q=I·t. The resulting voltage V at the electrodes was then converted to a digital value D using the internal 12-bit analogue-to-digital converter of the microcontroller with the supply and the reference voltage at V_{ref} = 3.25 V. This procedure allows us to calculate the measured capacitance according to Eq. 5.2.

$$C = \frac{Q}{V} = \frac{I \cdot t}{D \cdot \frac{2^{12}}{V_{ref}}} \qquad \text{Eq. 5.2}$$

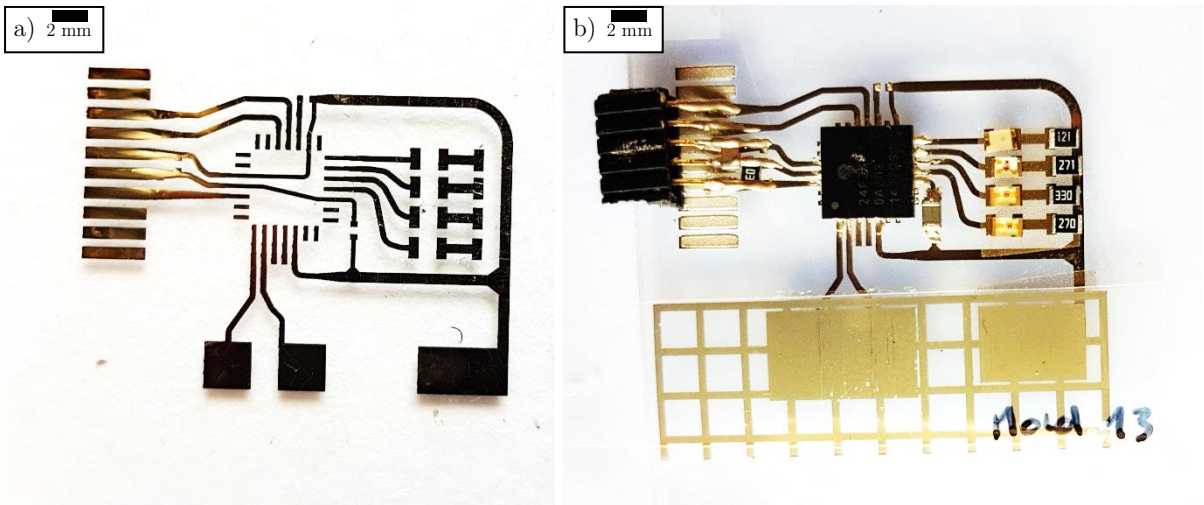

Figure 5.16. a) Printed circuit board of the first pressure sensing system and b) fully assembled tag.

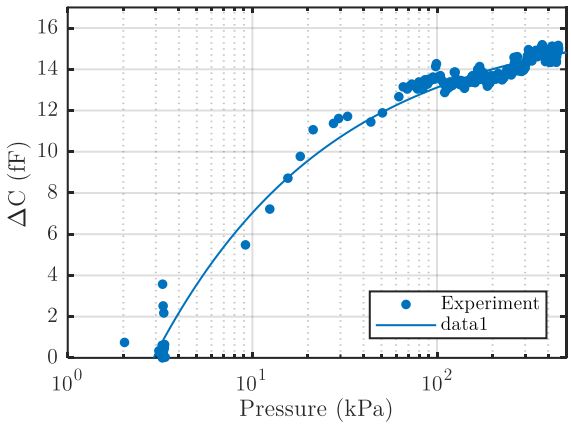

Figure 5.17. Change of the capacitance of the first prototype employing a flat silicone rubber.

The measured force profile consists of a ramp with increasing force. Every 30 s the force was increased by 20 % from 5 mN to 1300 mN. Force and average capacitance values were taken 25 s after each step to allow both values to stabilize. We measured the voltage 100 times and averaged it to increase the signal to noise ratio. The average capacitance in the idle position was 25.635 pF. Figure 5.17 shows a small change of capacity and a clear trend to a higher capacitance at higher force. The relation between the capacitance C and the pressure P can be approximated by Eq. 5.3 with the parameter values a = –26.7 fF, b = -0.455, and c = 16.4 fF at an R^2=0.987.

$$C = a \cdot P^b + c \qquad \text{Eq. 5.3}$$

In comparison to direct capacitive measurements of the sensor, the microcontroller includes the parasitic capacitances of its input pins and the wires to the sensor. Based on the results presented in [257], this parasitic capacitance is in the order of 20 pF. The relative change of the capacitance of this experiment is small and touches the limits of the measurement capabilities of the microcontroller. One reason is the small sensor capacitance compared to the parasitic capacitance. Still, we were able to find suitable threshold voltages to build a small prototype that indicates the pressure level of a pressing finger. Figure 5.18 shows three photos with a finger pressing one of the sensors with four different pressure levels. On the left photo, the sensor is touched gently below the first threshold, which is indicated by switching off all LEDs. On the second photo, a slight pressure is exerted on the sensor to reach the first threshold, which is indicated by a green LED. A medium pressure applied to the sensor was programmed to switch on a yellow LED and strong pressures turn on the red LED. When releasing the pressure slowly, it is possible to turn off the LEDs one after each other in the same order. A sudden release switches off all LEDs almost instantaneously.

With this demonstrator, we could show the basic functionality, the complete production process, and the reliability of printed capacitive force sensors. However, the signals of the five defined pressure

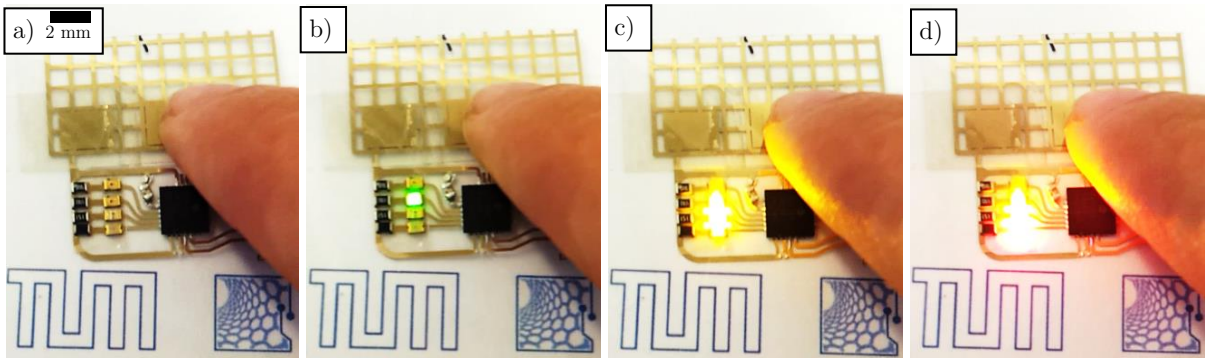

Figure 5.18. Pressure sensing system with two sensors and four-step LED indicators. a) Pressures below a certain value are ignored, which also include gentle touch, and all LEDs are off. b) Light pressure is indicated by a green LED, c) medium pressure by a yellow LED, and d) strong pressure by a red LED.

regions were close together mainly caused by the high parasitic capacitance within the microcontroller. As it is difficult to decrease this, it is necessary to increase the sensor capacitance to rise sensitivity. Our research about capacitive pressure sensors in Section 4.2 showed, that micro-structured silicone rubber films show a much higher relative change of the sensor capacitance of up to 10 pF in the same region. Including the parasitic capacitances, this should result is a change of the measured capacitance of up to 50 %, which is more than 100-times larger than for the previous prototype.

5.3.2 Arduino-Based Weighing Scale

Starting from an idea of Prof. Moosheimer of the University of Applied Sciences, we employed the capacitive pressure sensors as a weighing scale for a liquor glass. He developed a drinking game together with his students that involved a box containing a liquor glass that is passed in circles around until certain conditions are fulfilled and one person has to drink it. The box contains only printed graphical and electronic components and assembled SMD components. The electronic components are an Arduino microcontroller, a few sensors, a speaker, resistors, LEDs, and capacitors. For an improved gaming experience, it would be useful to know, whether there is a glass inside the box or not. The position of the glass is well defined, so we decided to employ only three sensors in a triangular configuration on the ridge of the glass as shown schematically in Figure 5.19a. The glass has an outer diameter of 3.5 cm and the ridge is about 1 cm, so we decided to put our pressure sensors with a diameter of 4 mm equidistant on a circle measuring 3 cm in diameter. The glass weights about 100 g and additional 20 g if filled with water. The pressures will only be about 8 kPa for the empty and 9.5 kPa for the full glass.

The first version of the produced wiring and the sensors can be seen in Figure 5.20a. It consists of three fore sensors that are hidden below the three black bumpers on which the glass stands. These are realized similar to most of our capacitive force sensors on two different sheets of PET of which one was flipped on top of the other. The wiring on the bottom side leads directly to a flexible printed connector (FPC). The wires on the top layer are guided towards the FPC, too, without crossing the bottom layer to avoid shorts. In the middle between the closest sensor and the FPC, the wires are enlarged to a dot that is printed on both, the top and the bottom layer and electrically connected there with conductive epoxy. The FPC is plugged into a zero input force (ZIF) connector mounted onto a conventional PCB. From there, wires lead to the analogue inputs of a commercial Arduino. The final prototype with a glass on top is shown in Figure 5.19b.

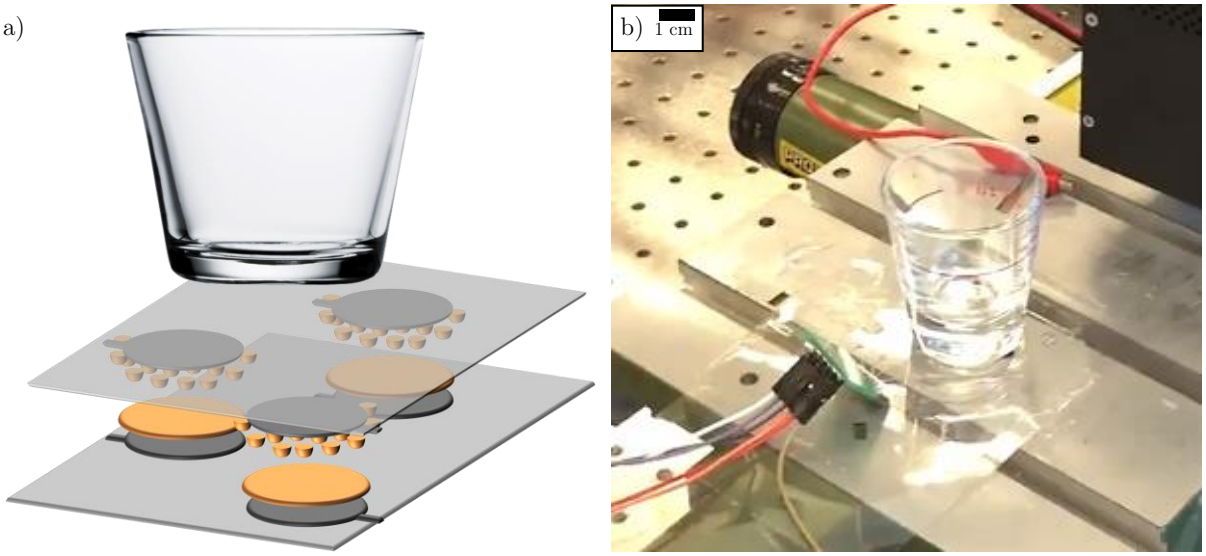

Figure 5.19. a) Schematic of the construction principle of the Arduino-based weighting scale for a glass. A structured and plain silicone rubber films are sandwiched between two electrodes printed on a flexible Substrate. The glass is aligned to stay exactly on the sensors. b) Real sensors under an empty glass.

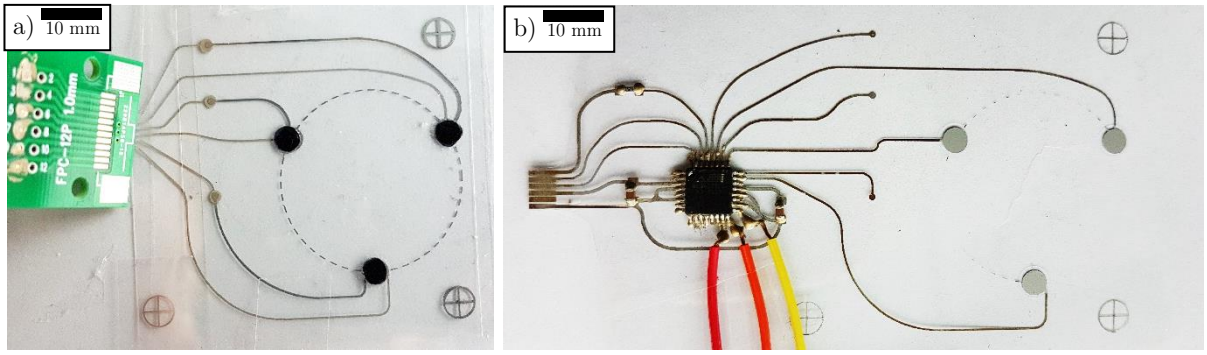

Figure 5.20. a) Weighting scale for a glass with an adapter board connected to an Arduino. b) Arduino chip, a few capacitors and the pull-up resistor assembled onto the printed board.

A second version of the sensing tag was built simultaneously that contains the Arduino chip directly on top of the printed layer and is shown in Figure 5.20b. The layout of only the bottom layer can be seen in on the right side of the image, which already contains the flat printed silicone layer. The Arduino chip ATMega328PB is assembled with conductive epoxy similar to the two capacitors and the resistor. Unfortunately, the chip did not have the bootloader included and therefore, the three colourful wires had to be attached to upload the bootloader.

After carefully checking all printed electronic wires, a surface profilometry of the printed structured dielectric was conducted. The generated 3D topography plot is shown in Figure 5.21. We can see that the hills in the centre are homogeneous with a total height of about 75 µm. The reason for the higher hills in the centre is that, in this place, the electrode is underneath. A small fraction of the connecting wire can be seen at $x = 7$ and $y \approx 5$. The higher hills in the centre are an advantage, as the top layer will preferably be in touch to only these, which reduces the effective area of the sensor. We decided to increase the circle with the structured hills over the electrode to compensate possible shrinking of the substrate. This was a good decision as the silver layer printed with the low-cost screen printer was often distorted slightly. The pressure variations of the operator lead to a small strain of the screen resulting in the distortion. With our larger structured dielectrics, this could be easily compensated.

At first, we characterized the printed sensors according to our standard procedure with our force setup described in Section 4.2. The resulting sensor response with respect to different pressures is shown in Figure 5.22a. A response of 63 % was measured with a rather flat increase for the lower region. Still, the slope at the region of interest (5 kPa to 10 kPa) is more than 1.5 pF/dB, which should be sufficient to measure it with the Arduino.

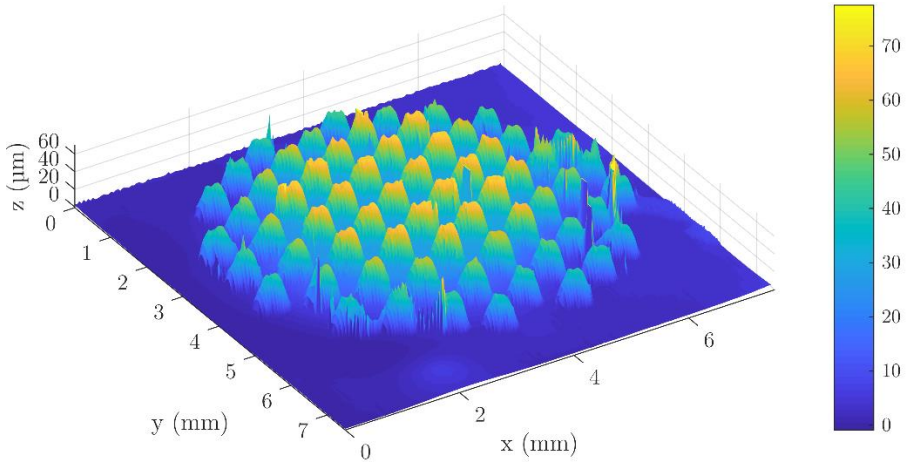

Figure 5.21. 3D surface profilometry of a screen-printed micro-structured dielectric on top of a screen-printed silver electrode, which is located in the centre. The hills are higher on top of the electrode.

Different approaches for the measuring of capacitance for the Arduino have been investigated. The charge time method charges the capacitor across a resistor and measures the time when the voltage at the capacitor exceeds a certain voltage. To achieve a suitable time in the medium microseconds time, we would need a resistor with several tens of Megaohms. This results in a noisy measurement and was not found suitable. A second approach was found in the web that uses several tweaks and multiple charging of the capacitor but was still found unsuitable. The final measurement was conducted with the capacitor directly connected to two pins of the microcontroller. This gave the highest accuracy and had the advantage that no other external components are required. Figure 5.23a shows the schematic with the capacitor C_1 being our sensor. The wires from the sensor are connected to inputs A and B with B being an analogue input. C_2 is the parasitic capacitance of pin B, which is typically around 30 pF and needs to be experimentally found if absolute capacitances shall be measured. This is actually not important for our measurement, but we could easily guess it by comparing the measured value of the Arduino to the value from the force setup, assuming that it does not significantly change over frequency. We found a value for C_2 of 30.46 pF.

The measurement principle of this capacitance meter works as a voltage divider according to Eq. 5.4. Our supply voltage is 5 V and the voltage V_2 is accurately measured with the ADC of the Arduino. The capacitance C_2 we have estimated to 30.46 pF.

$$C_1 = C_2 \cdot \frac{V_2}{5\,V - V_2} \qquad \text{Eq. 5.4}$$

At the beginning of each measurement cycle, both, pin A and B are wired to ground inside the microcontroller by a software command to discharge all capacitors. Then, pin A is wired to the reference voltage of 5 V. Quickly after, the voltage at C_2 settles, and the voltage V_2 is read by the ADC. This cycle is repeated 100 times and the average ADC value is used to calculate the capacitance value from the calculated voltage.

Figure 5.23b shows the sensor response in the resting position, after putting a glass, filling it with water, and taking it off the sensor. Eleven seconds after the start of the measurement, we put the empty liquor glass on top of the sensor. A glitch can be seen for the first trial, but after the second trial a few seconds later, the glass stood stable on the sensors. The capacitance increased from about 5.6 pF to about 6.05 pF and was then stable. After another 10 s, we started to fill the glass slowly with water and it can be seen, that the capacitance increases steadily to almost 6.2 pF. After waiting for a few seconds, we removed the glass and the capacitance decreased to the initial range. Our sensors proved stable and repeatable as well as compatible with the capacitance metering of an Arduino. We found the thresholds marked in the figure reliable to achieve this measurement.

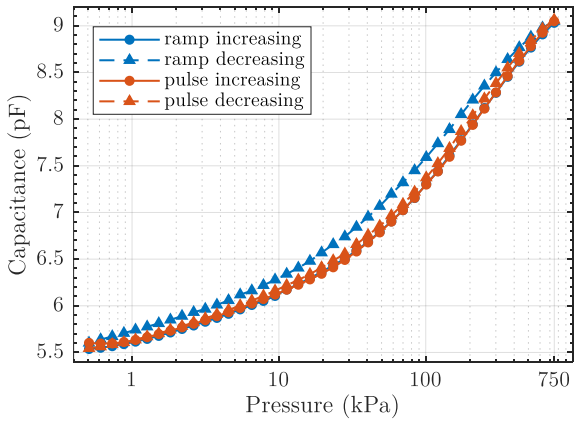

Figure 5.22. Sensor responses measured with a lab-scale LCR meter and applying the force profiles from Section 4.2.

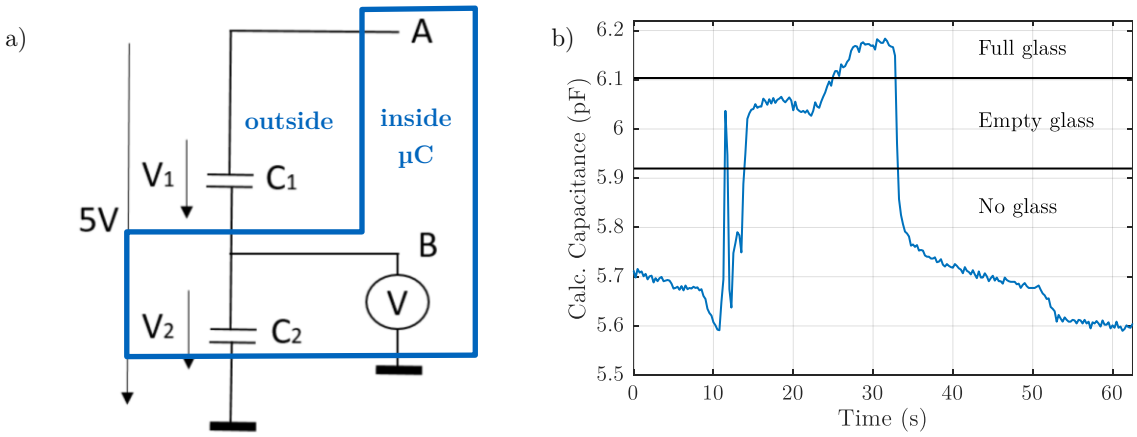

Figure 5.23. a) Schematic of the measurement principle with all components in the blue frame being inside the Arduino microcontroller. b) Sensor response during putting (t = 15 s), filling (23 s < t < 28 s), and removing (t = 33 s) a glass. The experimentally found thresholds are indicated.

The major problem was that the sensor signal in the idle position is not perfectly stable because the sensor electrodes are not pressed together. In Section 4.2, we used a small pressure to achieve a better baseline. Here, we could glue together the sheets of PET around the sensors to obtain a more stable configuration. This would improve the sensor performance significantly. Furthermore, at the beginning of the program, a reading of the capacitance may measure the baseline depending on the environment and adjust the thresholds accordingly. The sensor response could be increased by our latest findings in Section 4.2.3, which do not need an isolating layer between the electrodes because the structured dielectric is already sufficiently thick.

In conclusion, we could reliably detect the three states of the sensor: no glass present, empty glass present, and full glass present. The differences of the signal in the three states are about 0.25 pF and we showed that it may even be possible to measure more distinct filling levels of the glass. The liquor glass filling was especially difficult because the weight changes are only 20 % of the original weight. With larger types of glasses, the change in capacitance may be much higher. Larger glasses would lead to an operation in a response region with a higher sensitivity.

5.3.3 Large Area Sensing

Simultaneously to the structuring of the dielectrics, we also approached large area pressure sensing for an artificial skin for humanoid robots and eventually humans [349], [350] with patches that can be attached to each other similar to the work of Mittendorfer et al. [351]. Therefore, a hexagonal design with four pressure sensors as shown in Figure 5.24 was chosen. Additionally, the electrical wiring to the microcontroller was changed and both electrodes are directly connected to microcontroller pins. To exclude effects of the environment, we wanted to be able to switch the charged electrode and the ground electrode. The microcontroller was exchanged for the same model with a large packaging that simplified the assembly significantly. This applies mainly to the manual assembly that requires a quiet hand. Automatic assembly systems have a sufficient precision to place smaller packages as well. Figure 5.24a shows the patch without the top electrodes to visualize the structured dielectrics on the electrodes. In Figure 5.24b, the top electrodes have been cut to leave a central area for the microcontroller and were attached by conductive epoxy on the designated pads.

We characterized the hexagon with the force profiles introduced in Section 4.2. The microcontroller was programmed to first discharge the capacitor and then charge the capacitor with a current of I = 55 µA for seven processor cycles, which is t = 1.75 µs. Then the analogue-to-digital converter (ADC) measures the voltage at the capacitor. This cycle was repeated 50 times per sensor and the average value for each of the four sensors is shown in Figure 5.25a. It can be seen that only the sensor on which pressure was applied, shows a signal and the three others remain at the same level.

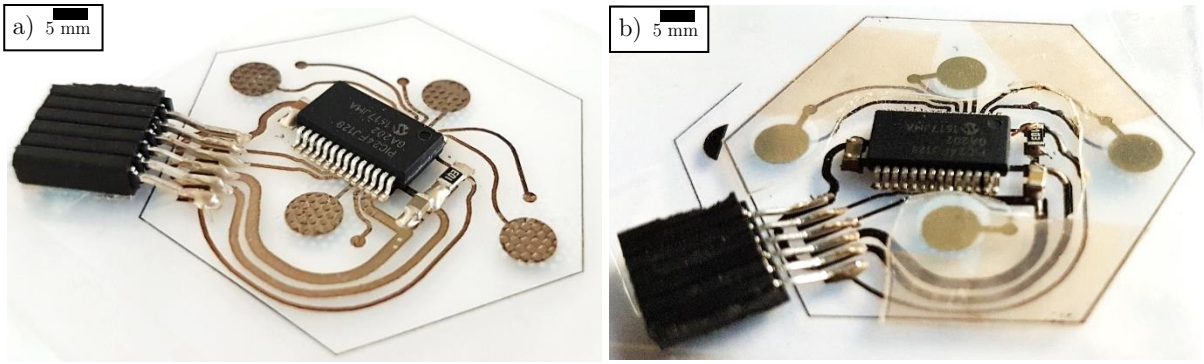

Figure 5.24. a) Assembled bottom layer and b) assembled top electrodes of a pressure sensing system with four pressure sensors (only bottom layer shown here). Both electrodes of each of the four sensors are connected to the microcontroller and can be reversed by software to compensate stray capacitances from the environment.

The signal change is about 130 digits of the ADC. The hysteresis of the measured sensors is below 14 digits, which allows a rather precise pressure measurement with an accuracy of about 10 %. The ADC digits can be converted to a capacitance value C that includes the parasitic capacitance of the microcontroller. Eq. 5.2 on page 156 shows the formula for ideal conditions and an operation voltage of V = 3.25 V.

Figure 5.25b shows the calculated capacitance that is much higher than the values shown in Section 4.2 and the maximum change is only about 1.25 pF. Anyway, the change is much higher than for the pressure sensing tag presented in Section 5.3.1. The printed sensors that were used for this demonstrator did not have the maturity of our last results, so there is still a good chance to increase the sensitivity of the sensors. If we can achieve a change in capacitance of several Picofarads, the parasitic capacitance of about 25 pF will play a smaller role.

Finally, after the tests, the microcontroller-package was switched back to the initial model as shown in Figure 5.26a without the top layer to uncover the structured dielectric on the electrodes. Such patches can be combined to a large-area, pressure-sensing "blanket" as shown in Figure 5.26b. The distribution of the pressure sensors shown as the black circles is homogeneous with equal distances between each sensor and the neighbouring six sensors. The "blanket" can be formed around one-dimensional curvatures, e.g. it can be rolled up. Spheres can be approximated by a football-like patterning with a loss of the exactly equally spaced sensors, which may be compensated by software. To bring the "blanket" to a robot, two important steps were neglected so far, which is the wiring of the individual patches and the force and counter-force application. The wiring may occur in a second layer that only requires two wires for the power supply and two wires for the UART connection. For large- area pressure-sensing, it is important to have a smooth surface. It is possible to attach even smaller chips as many research groups have shown, especially for RFID applications. This reduces

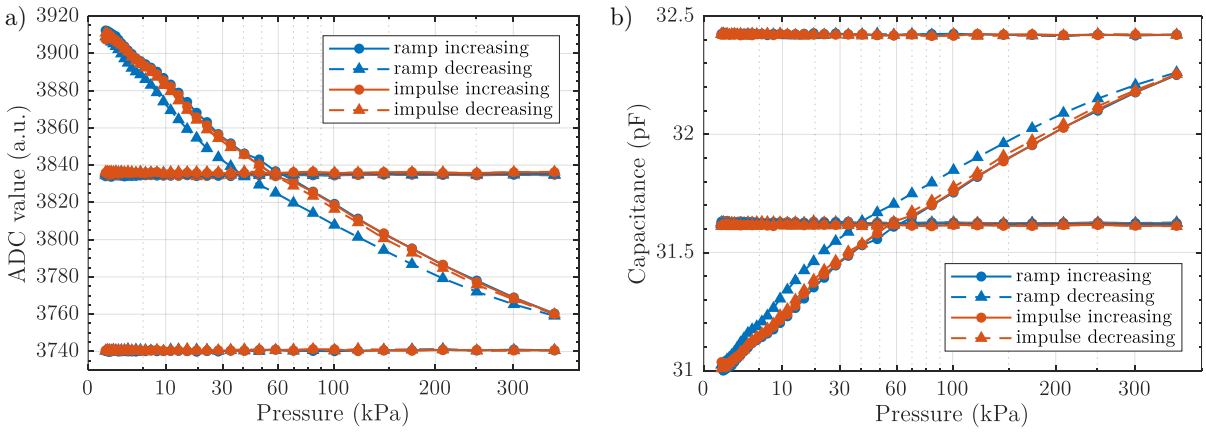

Figure 5.25. Signals of the four sensors while pressing on one of them. Incidentally, two sensors have almost the same signal. a) Direct ADC values, and b) the calculated capacitance including parasitic capacitances.

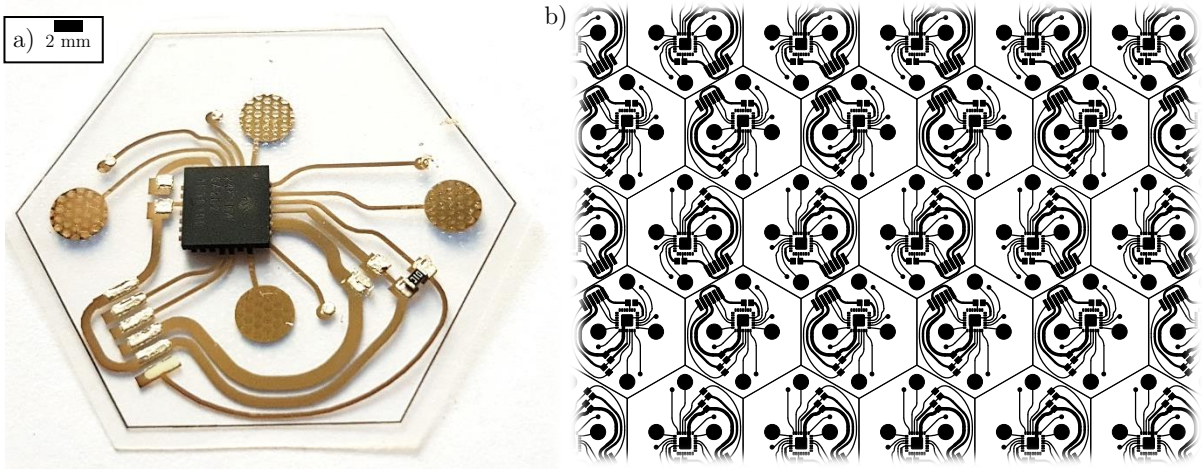

Figure 5.26. a) The final iteration of smart, hexagonal pressure sensing systems with a much smaller microcontroller that can be attached to a b) large area sensing "blanket" just requiring a second layer that interconnects the patches for power supply and bus communication.

the thickness of the patch and may not require a moulded silicone rubber that Mittendorfer and Cheng [351] employed. It should feature a force transition to the pressures and connect to a hard part of the robot to obtain a counter-force to the to-be-measured pressure.

The main advantage in comparison to the rigid hexagons presented by Mittendorfer and Cheng [351] is that the substrate is flexible, cuttable, and transparent. The flexibility allows a much smaller bending radius because the patch can bend within itself and does not realize the entire bending at the intersections. This makes the "blanket" much more conformable to the underlying or superposed layers of the "skin" of a humanoid or human. The cuttable substrate allows certain modifications in size of each of the patches to enable the covering of more complex shapes, e.g. a sphere. The transparent substrate allows the use of backlighting LEDs so that the side with the assembled components can be on the inside of a skin and the entire patch is protected by the outfacing main substrate. We suggest this configuration independently if LEDs are employed or not.

Another advantage is the 33 % lower number of microcontrollers per sensor that can either be used to increase the sensor density of increase the patch size. Actually, the employed microcontroller supports up to ten sensors if we refrain from the option to switch between charge and ground electrode for compensation of stray capacitances. Figure 5.27 shows a proposal for a design with nine sensors per microcontroller, which would reduce the number of necessary microcontrollers by 66 % in comparison to Mittendorfer and Cheng. However, this means that almost all analogue channels of the microcontroller are used for pressure sensing and are not available for other parameters that the patch of Mittendorfer and Cheng includes like temperature, acceleration, and proximity. [351]

5.3.4 Pressure Sensing Triangle

The disadvantage of the previously proposed designs is the placing of the microcontroller inside the patch, which requires a large distance between the sensors if a homogeneous distribution is wanted. The option to leave out one sensor at the position was never seen as a desirable solution. In the following, we want to present another approach with a new design that is inspired by the work of Schmitz et al. [352]. Unfortunately, the work could not be completed before the submission of the thesis, so the intermediate progress is shown in the following. The novelty of our work is the production by means of screen-printing and a lamination of the top electrode. Furthermore, we developed a new design that allows truly homogeneous distribution of the force sensors in a "blanket" by adding many of the triangles either at the design stage or later during the assembly on a specific surface.

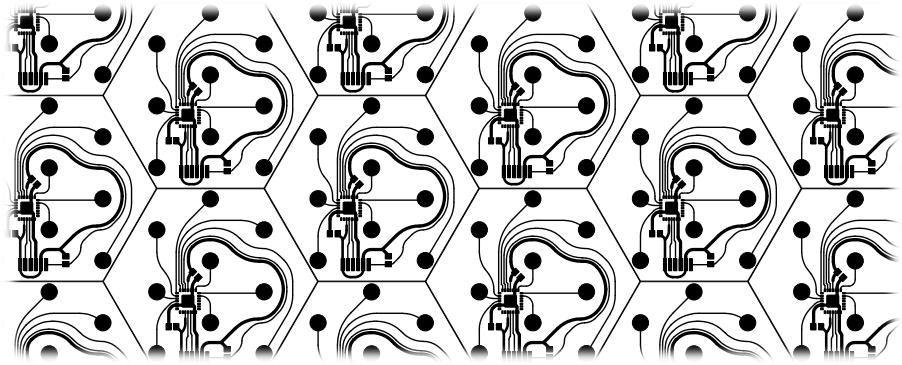

Figure 5.27 Proposal for a force-sensing "blanket" with nine sensors per microcontroller.

Figure 5.28a shows the fully screen-printed force sensing triangle from the bottom side with a mirrored photo. In the upper two-thirds of the photo, the triangle can be seen and in the lower part the readout circuitry. Ten circles show the central position of each of the sensors and are distributed equidistantly on a triangular area with two cut corners. A wire leads from each sensor down to the computing unit at the bottom. There, they are connected to the pads for a capacitance-to-digital converter (CDC). The major part of the triangle is filled with a conductive layer that is connected to the active shield of the CDC. The power supply wires were printed thicker than the communication-related wires and connect the CDC to the contact pads at the bottom of the photo. The entire circuit board was screen-printed with silver paste through a screen with 120 threads per centimetre. On top of the silver layer, multiple layers of the blue, thermal-curable dielectric were printed. We found, that at least five layers were necessary with a screen having a mesh count of 80. Aside from the necessity to achieve a pin-hole free isolating layer, the reason for the high number is the sticky surface of the dielectric that attracts dust during curing and transport, which creates many pinholes. The isolating layer covered the entire triangle except for the silver circles that shall serve as vias to the next conductive layer. The second silver layer as can be seen at the top of the front side shown in Figure 5.28b. It consists of the sensor electrodes that are 4 mm in diameter and the active shielding that is connected to the bottom layer at all corners of the triangle. Figure 5.29 shows a 3D profile of the surface of the sensor area that is within the perceivable circle (0.5 mm $<$ x|y $<$ 4.5 mm). The

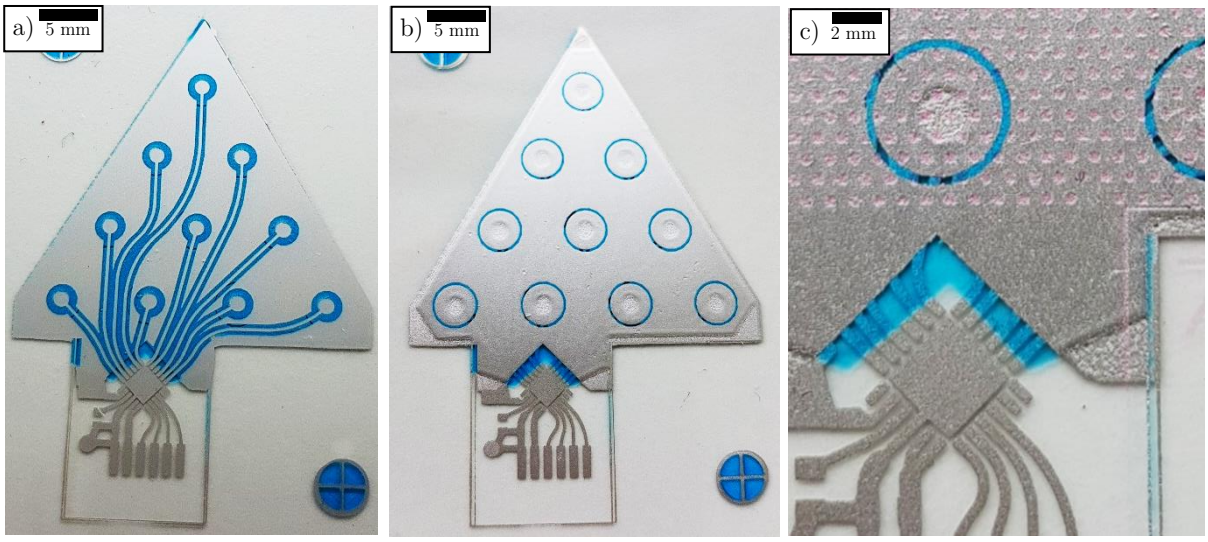

Figure 5.28. Photos of the force sensing triangle with ten sensors on a flexible transparent PET film. The screen-printed silver is shown in grey, the screen-printed dielectric in blue, and the silicone rubber as speckles in a slight rose colour. a) Bottom view (mirrored) with pads for connection and the microcontroller (bottom) and wiring towards the b) Top view with sensor electrodes and shielding. c) Magnification of one sensor and the pads for the microcontroller showing the silicone rubber micro-structuring.

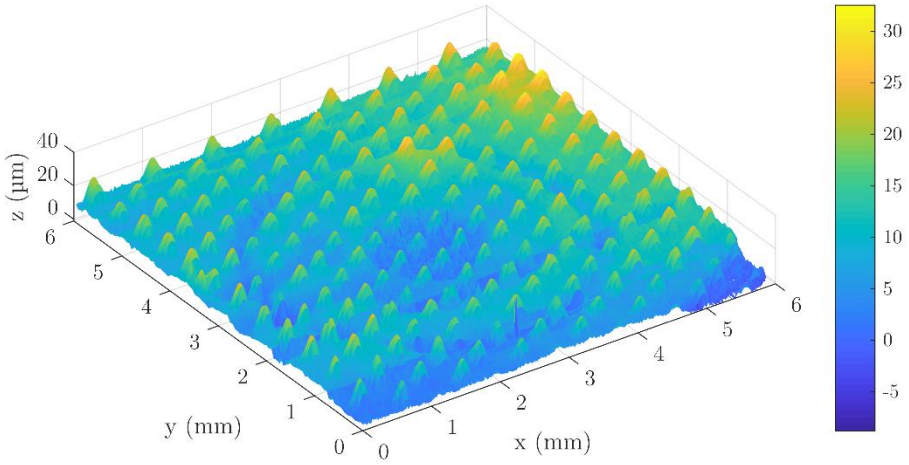

Figure 5.29. 3D surface profilometry on one of the sensor electrodes. The silicone rubber hills are low and inhomogeneous. The electrode has a hole in the centre, where no dielectric was printed.

recessing via is clearly visible. In the future, we have to apply our most recent knowledge from the printing of silicones, to increase the height of the hill and reduce the influence of the via.

All upper layers leave free the part, where the CDC will be placed. This can be seen in the magnified image in Figure 5.28c, which also shows the last printed layer, the microstructured silicone rubber. We tried to mix the transparent silicone rubber before printing with a strong colourant to make it visible on the photos. However, we only achieve a slight rose colour and the dots on the photo are mainly perceivable because of their shape. The silicone hills were printed all over the triangle area to keep the planarity of the entire design. Figure 5.30 shows the finished force sensing triangle with the attached chip using epoxy glue.

The employed programmable CDC is an AD7147 of Analog Devices. It supports up to 13 capacitance sensor inputs of which we used 10. It can update the values at a frequency up to 100 Hz and has an on-chip automatic calibration logic and compensation for environmental changes, adaptive threshold and sensitivity levels. Unfortunately, the only available package is a 4 x 4 mm² small package with 24 leads. The wiring to the triangle was done by a commercial USB-to-I2C converter cable. The standard LabView library provided with the employed FTDI chip was found not usable due to too high glitches in the signal. Therefore, a Beta version was sent from the manufacturer that

Figure 5.30 Bottom layer of the force sensing triangle with attached CDC.

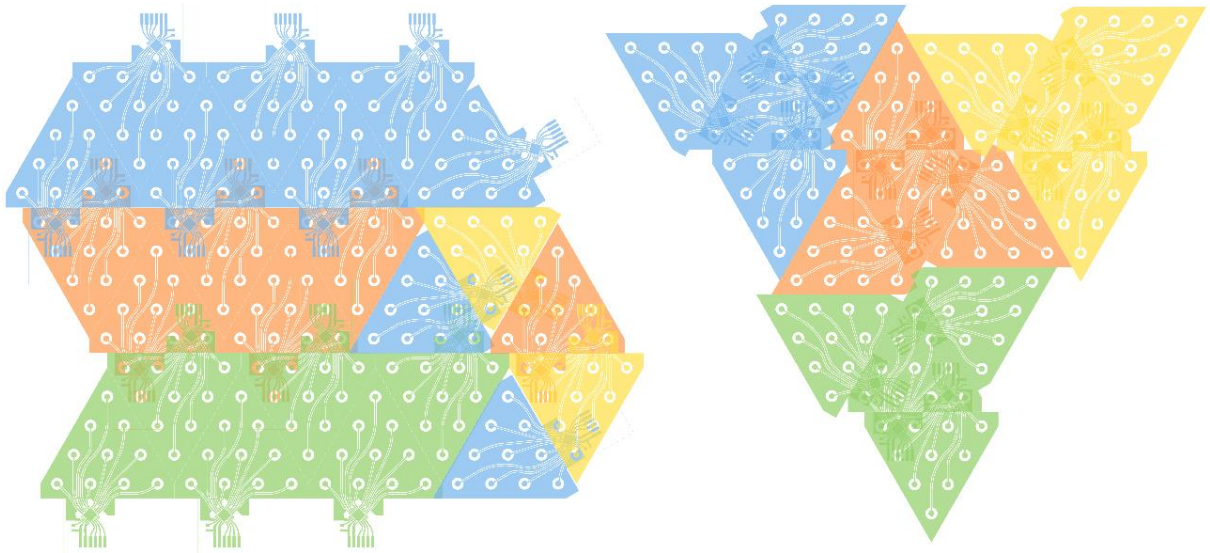

Figure 5.31. Three different methods to arrange the force sensing triangles in the plane. Left: Row-configuration with alternating triangles put in rows. Middle: Random orientation. Right: Grouping by four triangles that can be connected to one bus to the host system.

solved the problems. A LabView program was developed that offers full control over the employed parameters and the measured values.

The assembly of the triangle showed major difficulties as many wires were shorted. Therefore, it was not possible to characterize a complete triangle and more research needs to be conducted. The detailed characterization may be conducted in near future and the reader is referred to a future publication. This section is concluded by the discussion about the arrangement of the triangles. Figure 5.31 shows three different methods that are possible and all place the force sensors equidistant to each other. The computing unit is assumed to be bent slightly to move below another overlapping triangle. On the left, an arrangement in rows is visualized. The orientation alternates with the computing unit up and down. Then, there is a straight top and bottom line, so multiple of these rows can be employed to cover large areas. In the centre, a random distribution is visualized, which may be necessary at covering more complex shapes. Still, the sensors are placed equidistant. Some of the corners of the triangles may have to be cut to form a flat layer. On the right side, we visualize a suggestion for a combination of four triangles. The employed CDC chip supports up to four chips connected to one I2C bus. Therefore, it makes sense to combine four triangles and their wiring. The shape shown by the orange four triangles can be reproduced in all three directions keeping the sensor locations equidistant to each other.

5.4 Summary

This chapter showed several applications of printed electronics in hybrid integrated systems for the Internet of Things. Hybrid systems combine the advantages of printed electronics and silicon-based components. This allows lightweight, thin, and flexible devices with high computing capabilities, low power, and high integration. The first section of this chapter shows the basics about printing multilayer wiring, sensor integration, and assembly of surface mount devices (SMD). Several key aspects have to be kept in mind. In contrast to conventional wiring on an FR4 board, additive manufacturing offers a structuring of the isolating layers, too. This structuring is often employed to save material and reduce the number of interconnects between the layers. However, this leads to a three-dimensional design with steps and recesses within one printed layer. This can influence sensors if they are vertically integrated onto the wiring. We showed an example of a pressure sensor electrode

that was not flat because of underlying layers. The assembly of SMD components can be conducted by conductive adhesive pastes and by conductive adhesive pressure-sensitive tapes. We used both techniques to assemble microcontrollers, resistors, capacitors, LEDs, and other components onto inkjet-printed and screen-printed wiring boards and show several examples.

The rest of the chapter focuses on prototypes of sensor systems that we produced in our labs. We fabricated mainly two different kinds of hybrid systems. The first group comprises chip-based wireless systems including NFC-tags and UHF-tags. We showed the possibility to use inkjet and screen printing for the production of such tags as well as the different methods to integrate sensors. We printed RFID tags with silver, gold, and copper. Other materials were found to have a too high resistivity to be employed in effective antennas. We show tags with integrated photodiodes and pressure sensors produced at our labs as well as chips with integrated temperature sensors. The RFID tag made by printed gold on paper goes one step towards biodegradable electronics, and the pressure-sensitive button in an RFID tag can increase its security by inhibiting unwanted readings.

We have proven that our capacitive pressure sensors are not only well-performing in specific characterization setups but also in smart hybrid sensor systems with microcontrollers. Four different systems were described starting from a basic pressure-sensing microcontroller-based circuit. The second prototype used Arduino to measure weights on three different sensors and combine the values to determine the filling of a glass that only changes its weight slightly. The next prototypes focus on large-area force sensing. Hexagonal and triangular structures were printed and characterized that can be combined to form a force sensing "blanket" with equidistant pressure sensors of unlimited size. This may find interest in security applications, robotics, and healthcare. The advances in the force sensing can produce a truly flexible skin for humanoids. In contrast to previous work on these skins, flexible patches are bendable to follow round contours and can be cut to cover more complex shapes. Still, customized patterns are easy to produce that fit perfectly the desired shape. One day, such an artificial skin may be also employed in healthcare to support paralysed people. There is still a long way that requires the reduction of the number of computing components and a decrease the power consumption. We employed low-power capacitance to digital converters that can read up to 13 sensors, which potentially could decrease the number of chips and with it the power consumption significantly. We could reduce the number of chips by more than two thirds necessary for pressure sensors but comparable skins usually employ many other sensors, which were not regarded here.

This chapter showed several examples of hybrid electronics that merge the advantages of printed electronics and silicon-based electronics for lightweight and flexible devices with the required computing power and means of communication. Such devices are required for remote sensing and can be part of the Internet of Things.

Chapter 6

Conclusion and Outlook

This thesis contributed many new aspects to the field of printed electronics, sensors, and smart systems. This chapter summarizes the main findings in Section 6.1. The results of this thesis are then compared to other works in the field and the main novelties are highlighted in Section 6.2. The integration of printed electronics is an ongoing and exciting research field. Section 6.3 picks selected promising topics on which the work of this thesis could be continued.

6.1 Summary of the Thesis

The thesis was structured in the typical workflow that is needed to produce and characterize printed smart systems for the Internet of Things. Chapter 1 started with the idea and the motivation of printed electronics in general and this thesis in particular. Printed Electronics (PE) includes processes that employ printing techniques known in the graphical industry since many decades the additive application of materials on a wide range of substrates. These substrates can possess desirable functionalities like soft and conformable textiles, bio-degradable paper, bio-compatible and implantable polymers, transparent glass, and many more. Such materials form many objects on which we don't expect electronics today, but many of them are already in development or are imaginable. Long-time ECG electrodes may be directly integrated into your shirt and tell you how to optimize your training or detect rare heart problems. The plaster on your wound checks automatically whether there is an infection below without opening it. Organic light emitting diodes on your window let the light come from the same direction day and night and organic photovoltaics generate energy in your window shades.

All these applications require the deposition of functional material on flexible substrates and printing techniques are doing exactly this for many years with all kinds of colour and effect inks. Therefore, it is interesting to analyse different techniques, their advantages and disadvantages, and the employed inks and pastes. Chapter 2 depicts several printing techniques and elaborates on inkjet printing, screen printing, and spray deposition. Contactless and digital inkjet printing is able to deposit thin layers on almost any substrate with an adequate roughness. We employed a desktop inkjet printer as well as a high-precision lab-scale printer, but the process is similar to printing photos at

home. It starts with the desired functionality that is dissolved in the ink in the cartridge. We investigated conductive inks based on metal NPs made of silver, gold, and copper-oxide as well as conductive molecules like carbon nanotubes and a conductive polymer blend. The next important factor is the substrate on which the conductive pattern will be printed. We evaluated more than 60 different flexible substrates including a wide range of papers and polymer films but also textiles and speciality materials. The substrate's and ink's properties are crucial for successful inkjet printing, whereas screen printing is more tolerant to both. Screen printing is the second technique employed in this work. It can be used both in a laboratory scale and in an industrial scale with a throughput of several meters per second. We investigated the printing of a variety of conductive pastes including silver, carbon, a conductive polymer and several dielectric pastes like thermal and UV-curable dielectrics and elastic silicones. The last ones are highly viscous and allow the printing of microstructures with a high aspect ratio. It is possible to print structures with ratio of 25 % between the height and width in a single pass. We showed that screen-printing of silicone rubber hills with a height of 180 µm can be reliably printed on both, previously screen-printed silver and flexible substrates like PET or Kapton. The focus of this thesis lies on these two printing techniques, yet also spray coating was employed for some devices. The technique is intended to coat large areas with low film thicknesses and homogeneity. We employed it to coat transparent conductive patterns through a shadow mask with three different materials: Silver nanowires (AgNWs), CNTs, and a conductive polymer. The printed materials were characterized using optical, topographical, and functional characterization tools.

Chapter 3 focuses on the post-treatment and functional characterization of the printed layers. Many different kinds of curing and sintering techniques have been proposed in the literature as alternatives to simple heating, which is often not compatible with temperature-sensitive substrates like PET. We focus on the investigation of an optical technique that employs a flash lamp to produce intense pulsed light (IPL) that heats selectively printed layers whereas the substrate remains cool. Curing and sintering are especially important for particle-based inks as they form a porous layer after printing that still contains stabilizer molecules necessary for the ink formulation. IPL curing showed efficiently to heat the thin films to temperatures that decompose the stabilizer molecules. The heat also increases mater diffusion in the printed layer towards the small contact regions between adjacent particles. This diffusion is favourable for NPs to reduce their overall surface energy and necks between the particles are created. The densification and coarsening of the layers with a better metallic connection between the particles increases the conductivity of the printed films significantly. We were able to achieve almost half of the bulk conductivity in IPL-sintered silver films within two pulses in the microseconds region. IPL curing can also provide the activation energy for the chemical reduction of metal-oxides to their zerovalent metals. This was shown for inkjet-printed fully oxidized copper NPs. A single flash of around a microsecond converted the copper-oxide to copper with a conductivity of about 25 % of bulk copper. These conductivities are high as the films are porous and usually have a density of below 50 % in comparison to the bulk material. Screen-printed silver particles were also IPL-sintered and the conductivity could be increased significantly towards the bulk conductivity. Furthermore, IPL curing was used to increase the adhesion of silver NPs to temperature-sensitive substrates by slightly melting the surface of the substrate. Chapter 3 also presents different conductive patterns with a focus on semi-transparent electrodes and stretchable wires. The semi-transparent electrodes made of AgNWs, CNTs, and a conductive polymer showed a linearly decreasing transparency and a more than linearly decreasing resistance with an increasing amount of sprayed material. The ideal compromise between the transparency and the resistance depends on the designated application. As an application of the spray-coated layers, we showed a large-area (20 x 20 cm^2) transparent heater on a polymer foil.

The printing and curing processes and the gained functionality of the printed layers were subsequently employed in Chapter 4 for a large range of sensors including mechanical, environmental,

chemical, and medical sensors. We produced capacitive pressure sensors and compared them to resistive ones. The capacitive sensors consist of a micro-structured dielectric between two electrodes and all three layers were screen-printed. The sensors have a measurement range (0.5 kPa to 750 kPa) that encompasses almost the entire range of human-machine interaction. This is possible by a sensitivity that starts at 80 %/kPa and is decreasing approximately linear to the square root of the exerted pressure. The sensor response within this range can be up to 420 % of the signal in the idle position. We compared sensors with different micro-structures as our simulation showed an increase in sensitivity for smaller structures. This could be experimentally validated as the maximum sensor response increased with reducing structure radii whereas the baseline capacitance only slightly increased. However, the hysteresis to decreasing forces increased strongly and is higher than the baseline capacitance for small radii. Still, the sensors' response times are below 1 s for pulsed pressures. Next to the normal pressure sensors, also three-axial force sensors were presented that consist of four electrode pairs around a dielectric that change their overlap area selectively on the impact shear forces and their distance on normal forces. A small yet linear relation between force and capacitance could be found that is up to twice as high as in comparable sensors in the literature. The fourth type of pressure sensors is pressure wave or acoustic sensors based on piezoelectric PVDF film. An incoming pressure is amplified by a multilayer screen-printed electrode and the generated voltage indicates the pressure and possibly the frequency. We found that the employed PET film dampens frequencies above 13 kHz significantly. The sensitivity of only –80 dB could be improved by a better adhesion of the electrodes to the piezoelectric film.

Next to pressure sensors, we showed strain sensors that can be inkjet-printed onto a commercially available elastic silicone rubber and can be stretched for some percent of their initial length while increasing the resistance. The main finding here is that they are over-stretching tolerant. The strain sensors can be stretched to up to 330 % of their initial length and regain their conductivity within less than a second after relaxation. Depending on the strain, the remaining viscoelastic deformation of the substrate may cause a temporary resistance increase. For small strains or after some waiting time, the resistance reaches almost exactly its starting value. We showed, that this can be repeated for at least 20000 cycles. The next category of sensors is humidity and temperature sensors. We showed thermocouples made of different materials that have a linear response of up to 55 µV/K and are semi-transparent (up to 90 %). Furthermore, we showed wireless temperature and humidity sensors that change the resonance frequency of a distant reader antenna depending on the environmental conditions at the sensor. The inkjet-printing and screen-printing for the electrodes of chemical and biochemical sensors as well as solar cells were shown and discussed.

Printed electronics may have a large impact on wearables and healthcare. Representatively, we investigated screen-printed silver-chloride and carbon electrodes and employed them for electrocardiography (ECG) and electrooculography (EOG). The dry electrodes for the first applications proved well suited for recognition of the main peaks with signal amplitudes of 55 % in comparison to gel-assisted electrodes. A complete skin patch with screen-printed electrodes, isolator, skin adhesives, and liners was produced for EOG and showed promising results for the recognition of eye movements. All four different directions could be detected as well as blinking.

During this thesis, many sensors were produced that may be useful for sensing devices in the Internet of Things. Figure 6.1 summarizes small pictures of the sensors that we manufactured and characterized.

Chapter 5 focuses on hybrid integrated systems that combine the best of printed electronics with silicon-based electronics. Low-power and highly integrated circuits (ICs) are assembled on top of lightweight, flexible, and thin printed electronics. Precise multilayer printing and the assembly of components is shown and discussed. The simplest hybrid systems are chip-based wireless tags of which we produced several for different communication protocols and some including printed sensors.

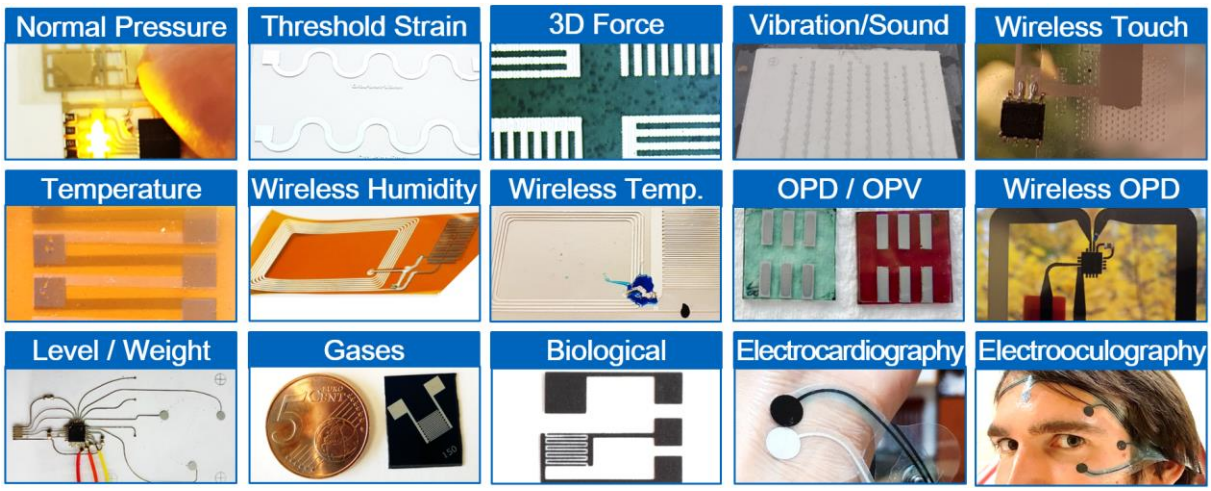

Figure 6.1. Overview of the different sensors produced during the work on this thesis.

An example is an NFC tag with a security button that only allows data transfer when pressed. This combines the comfort of a wireless tag like a credit card with additional security against tracking and eavesdropping. Another example is an inkjet-printed UHF tag with a spray-deposited photodiode for remote light sensing. Only a single IC is necessary for the data acquisition and transfer. The rest of the chapter mainly focuses on different smart hybrid systems employing our capacitive force sensor technology. Different demonstrators using Arduino and other microcontrollers as well as dedicated capacitance-to-digital converters. The Arduino system focuses on the precise weighting of a glass to determine its presence and its filling state. Multiples of another microcontroller-based system in the shape of a hexagon can be arranged next to each other to homogeneously cover large areas and measure pressures on equidistant sensors. Such a pressure sensing "blanket" can be improved by the presented triangular patches that reduce the number of integrated circuits and the power consumption and offers a much higher spatial resolution. Such and other hybrid systems need to be interconnected to other systems (Internet of Things) that make use of the sensed data.

This thesis covers the entire production range for printed sensor systems for the Internet of Things. Several production techniques were combined with different sensing methods. Finally, several prototypes are presented to prove the feasibility of low-cost production of smart systems.

6.2 Progress beyond the State of the Art

This section provides a comparison of selected results from this thesis to literature values. The inkjet-printed lines with 60 µm width that were printed for the shear force sensors are close to the minimum that is achievable with conventional inkjet printing techniques, namely the size of a single drop that can be ejected from a small hole [353]. Still, these lines consist of two adjacent drops at a distance of 20 µm, which means that lines of 40 µm are achievable on the employed porous substrate. Lines below 50 µm or even 25 µm have been shown previously on an unstructured surface [23], [354]–[356]. However, in most practical applications, rather line widths between 150 µm to 300 µm are used [12], [146], [316], [357]. Our thinnest screen-printed conductive lines are about 80 µm and only slightly wider than the inkjet-printed ones. Usually, rather wide lines of at least 100 µm up to several hundreds of micrometres are reported in the literature [57], [251], [358], although thinner lines down to 50 µm or even 30 µm have been shown [38], [359], [360]. The thickness of the screen printed dielectric layers rank highest in literature as mainly conductive lines are printed with high aspect ratios. [361], [362]

Our achieved conductivities after IPL sintering rank high for silver NP inkjet inks (42 %) [165], [172], [363] and for copper-oxide not many publications are available but all [175], [364] are lower than our 23 % in comparison to the bulk conductivity. Many of the publications required more than only one or two pulses to achieve these conductivities. The destruction of the sintered samples is almost never investigated. To our knowledge, IPL sintering of gold was only conducted by Liana et al. [177] and their conductivity was much lower than ours although it is not really comparable.

Strain sensors have been investigated in the paste with a large variety of construction mechanisms. Printed strain sensors often involve the creation of new material composites [243], [245], [251], [252]. Our engineering approach was the use of only commercially available inks and substrates. We selected silicone rubber film as the substrate because it recovers to its initial dimensions after stretching in comparison to the commonly used polyurethanes. Printing on silicone rubber is non-trivial due to its low surface energy [106], [365]. We could increase it by oxygen-plasma and then print homogeneous and conductive silver films with an arbitrary length that can be employed as strain sensors up to a certain extent. The wire's resistance increases and decreases in a repeatable manner similar to previously presented ones. The main difference is the regaining of the conductivity within less than a second after relaxing from strains as high as 330 %. This value cannot be achieved with polyurethanes.

Semi-transparent thermocouples (TCs) have been presented before [366], [367], but to our knowledge never by printing techniques. The Seebeck coefficients of our TCs are rather low (55 µV/K) and the energy harvesting properties are poor (55 fW/K² per thermocouple) in comparison to the literature [17], [301], [368], [369]. Still, there may be applications for transparent temperature sensors and possibly for energy harvesting if the resistance of the layers can be reduced.

The main progress of this thesis in the field of printed sensors was done for capacitive pressure sensors. Our sensors are applicable in the entire range necessary for human-machine interaction and have sensitivities of up to 80 %/kPa in the "light-touch"-region of around 1 kPa and below. They have a high response of up to 420 % at pressures at 750 kPa, which corresponds to the pressure range at the human heel. We could not yet see a decrease in the logarithmic sensitivity of the sensors but were limited with our measurement setup, so we expect them to be usable at higher pressures, too. All these values are considerably higher than previously presented sensors including the Nature publications of Mannsfeld et al. and Lipomi et al. [279], [287], [293], [294], [340]–[342]. In contrast to many publications in the field, we also investigated the accuracy of the sensors, which was found to be more than 90 % for some configurations for pressures across the entire range between 0.5 kPa and 750 kPa. For smaller ranges, the accuracy can be even as high as 99 %. The only condition, when the sensor is showing a hysteresis is after gradually decreasing the pressure from medium to high pressures. When releasing the pressure completely, the signal is reset within less than a second. This shows the high response speed that was above the capabilities of our measurement setup and shows equal or better results than the publications referenced above.

Dry skin electrodes have been printed and used since some time [332], [336], [370], [371]. Yet, they are still an ongoing research field and gain interest as wearables are reaching the market. They are important for many healthcare and fitness applications that require cheap, disposable, and wearable electrodes. We think that the field of wearables will bring the most printed electronics products to the market, therefore it is necessary to follow on this. We could screen-print robust and well-performing skin electrodes with silver-chloride and carbon. We proved that they can measure biopotentials like the cardiac potentials in ECG and the resting potential of the eyes in EOG. For ECG, we could identify the main peaks with an amplitude lower than gel-based electrodes yet still comparable. For EOG, we were able to detect the direction of certain movements of the eye and identify all four different looking directions, as well as blinking with one or both eyes. As an example, we showed the entire production of an EOG patch including the sandwiching between skin adhesive and liner.

In contrast to many other works in the field, we did not stop after characterization of the sensors but also implemented several into hybrid integrated systems to prove that they are actually working outside of specifically designed setups. The focus of the presented demonstrators lies on pressure sensing and we could show four different implementations for weighting, as well as point and large-area pressure sensing. The sensors can also be employed as buttons for secure RFID tags. This idea was presented before [348] but never shown by printing techniques and an as simple integration. We showed different smart systems employing our novel force sensing technology for weighting as well as large area force sensing for artificial skins. In contrast to work in the field employing conventional PCBs [349]–[351], our patches are flexible, bendable and employ fewer microcontrollers. On the other side, they are not yet mature enough to be employed in large scale and the sensor response in the bent state has to be investigated first. Also, they implement only pressure sensor in contrast to the variety of sensors that are employed by Mittendorfer and Cheng [351].

6.3 Outlook

The work on the integration of printed sensors into hybrid smart sensor system is an ongoing, exciting, and challenging field. In the future, we would like to continue the work on the artificial skin and improve the production of the patches for large areas. Furthermore, other sensors like temperature and chemical sensors should be printed on the same patches as well. Other sensors like accelerometers, vibration sensors, and others may be too difficult to print and can be assembled on top of printed structures. Also the interconnection and processing of all acquired data by the IoT devices is an interesting research topic.

The second interesting research field, from our point of view, are medical sensors including skin electrodes. The produced skin patches for EOG are worth a deeper investigation with portable readout electronics. Several works have shown that structured electrode surfaces decrease the skin resistance significantly and may overcome the hair-barrier. A second improvement can be the use of additional printed shielding layers to decrease noise from the environment and capacitive coupling. Printed skin electrode may be truly wearable if the right substrate, paste, and adhesive combination is found. They may be used for long-term ECG or EEG measurements to detect rarely occurring health problems or support research of human emotions and reactions outside of a lab atmosphere.

In the section of sensors, many other types of sensors are imaginable and the presented ones can be still improved. The pressure sensors require a thorough investigation of their response during bending and the reading of them in a matrix configuration would be beneficial for large-area pressure sensing. The materials or processes for the production of biosensors should be investigated in detail on how to employ printed electrodes for these applications. Printing would be much cheaper, faster, and more customizable than the existing evaporation.

Independently of the specific application, research in the business-related fields is necessary to investigate the potential markets and products that printed electronics can achieve. Electronics could change many other fields like architecture (OLED or OPV in windows), civil engineering (environmental sensors), mechanical engineering (strain sensors in turbines, et cetera.), healthcare (wound-healing sensors), food industry (degradation sensors), and many more. Many engineers and persons working in other fields are not aware of the opportunities of printed electronics. These opportunities, however, can only lead to innovations if certain unique improvements can be made in comparison to the current state. These may be cost reductions and completely new functionalities that printed electronics offers. Many electronic applications today could benefit from light-weight, thin, and flexible imprinted substrates that may even be transparent, stretchable, soft, or conformable. New designs and use cases may be created that make electronics, even more, a useful part of our daily life.

Materials and Methods

M.1 Inks, Pastes, and Cleaning Agents

The used inks can be found in Table 2.2 on page 31. The conductive screen-printing pastes are listed in Table 2.5 on page 47 and all isolating and dielectric pastes in Table 2.6 on page 51.

Table M.1 lists the cleaning agents and their applicability on the different kinds of screen-printing pastes that were used during the work on this thesis. Most of these have a safety classification and should only be used in proper ventilation, ideally under the fume hood. The K3x cleaner is the most dangerous according to the materials safety datasheet, but the evaporation rate is rather low and it has a pronounced smell, which limits its danger. The low evaporation rate is beneficial during cleaning, because it allows a long cleaning with only a little amount. This is especially useful for cleaning of the silicone rubber pastes. However, it does not clean the Henkel pastes. For this pastes, we recommend the Vx cleaner. It is less dangerous but has a faster drying time. If ever cleaning outside the fume hood is necessary, we recommend Isopropanol or small amounts of 10-063 cleaner. Water cleans the PEDOT:PSS pastes well.

We recommend a quick cleaning after finishing screen-printing and remove all remaining paste with a spatula. Then apply a generous amount onto the screen and rub the entire screen with tissues until the tissues keep their original colour.

Table M.1. List of cleaning agents and their usage for the different kinds of pastes.

Product	Manufacturer	Applicable to	Remarks
Screen Cleaner K3x	CPS Chemical Products and Services	Ag-510, C-220, CI-1036, CI-2051, Silicones	Very dangerous, only in fume hood, long working time
Screen Cleaner Vx	CPS Chemical Products and Services	1010, 1011, 6038E, 455BC, CI-1036, CI-2051	Short working time
10-063	Printcolor	1010, 1011, 6038E, 455BC, CI-1036, CI-2051	Very short working time, may be used outside of fume hood
Isopropanol		Spilled paste before drying	
Water		PEDOT:PSS	

M.2 List of Substrates

Table M.2. List of substrates used in this thesis. The substrates will be mentioned by their abbreviation.

No.	Manufacturer	Product Name
P1	Mitsubishi Paper Mills	Nano Benefit Series NB-RC-3GR120
P2	Schoeller Technocell	p_e:smart type 2
P3	Schoeller Technocell	p_e:smart type 3
P4	Dataplot	Emblem WAPUM Glossy 240g
P5	Pelikan	Geha Photo paper P05
P6	Canon	Glossy Photographic Paper
P7	HP	Universal Semigloss Photographic Paper
P8	Canon	Semi-Matte Photographic Paper
P9	Dataplot	Emblem WAPUM Semimatte 240g
T1	Mitsubishi Paper Mills	Nano Benefit Series NB-TP-3GU100
T2	Novacentrix	Novele IJ-220
T3	Mitsubishi Paper Mills	InkJet Film UC100
T4	Folex	Reprojet P HD
T5	Folex	Reprojet P HDM
T6	ColorGATE	Reprofilm HD
T7	ColorGATE	Screenfilm Waterbased
T8	ESC	ScreenJet Film
T9	R. Rauch	Repro-UV
T10	R. Rauch	Repro-UV II
W1	Mitsubishi Paper Mills	Nano Benefit Series NB-WF-3GF100
W2	Unknown	Greyback
N1	Schoeller Technocell	p_e:smart type 1
N2	Arjowiggins	Powercoat HD 230
N3	Stora Enso	LumiArt
N4	Konica Minolta	Photo Paper
N5	Stora Enso	LumiSilk
M1	MGW Office Supplies	Clear Laser & Copy Foil
M2	Viking	Transparency Film
M3	Folex	GO-HC

M.3 Production Equipment

For inkjet printing, a Workforce 2010W of Epson (Tokio, Japan) and a DMP-2831 (Dimatix) of Fujifilm Dimatix Inc (Santa Clara, CA, USA) were used. They are described in more detail in Section 2.2.1. The modification of a consumer desktop inkjet-printer into a flatbed printer, which was done during the work on this thesis, is also described in Section 2.2.1

For screen printing, the basic screen printer FLAT-DX 200 ordered at Siebdruck Versand (Magdeburg, Germany) and the high-precision screen printer Nino of Coruna Printed Electronics (Bettwil, Switzerland) were used. They are described in more detail in Section 2.3.2. The screens and squeegees for both printers were ordered at the respective companies. The large screens for the basic printer were patterned by Siebdruck Versand and the smaller one for the high precision printer by the author in the laboratory of Prof. Moosheimer at the Hochschule München. The detailed process is described in Section 2.3.1. The screen for the structured dielectric of the capacitive pressure sensors was patterned by Markus Engel of industrial print solutions (ips, Taufkirchen, Germany).

The curing of the patterns was conducted in the universal oven UF55plus of Memmert (Schwabach, Germany) and the photonic sintering tool Sinteron 2010-S of Xenon Corporation (Wilmington, Massachusetts, US). The latter is described in detail in Section 3.1.2.

M.4 Characterization Tools build during the Thesis

This section shows some of the measurement tools that were specifically designed for the characterization of the printed sensors. These include the Bending and Stretching Setup in Section M.4.1, the Force and Pressure Setup in Section M.4.2, the Shear Force Setup in Section M.4.3, and the Thermocouple Setup in Section M.4.4.

M.4.1 Bending and Stretching Setup

During the work on this thesis, a new setup was built to conduct the bending and stretching tests. Figure M.1 shows a photo of the setup that consists of a power supply, a step motor and two carriages on a rail. One of the carriages is fixed and the other one can be moved by the belt on a length of up to 25 cm. Both carriages are made of two blocks each of which the top one can be removed to mount a sample. On the photo, a stretchable wire is mounted in the setup. All four

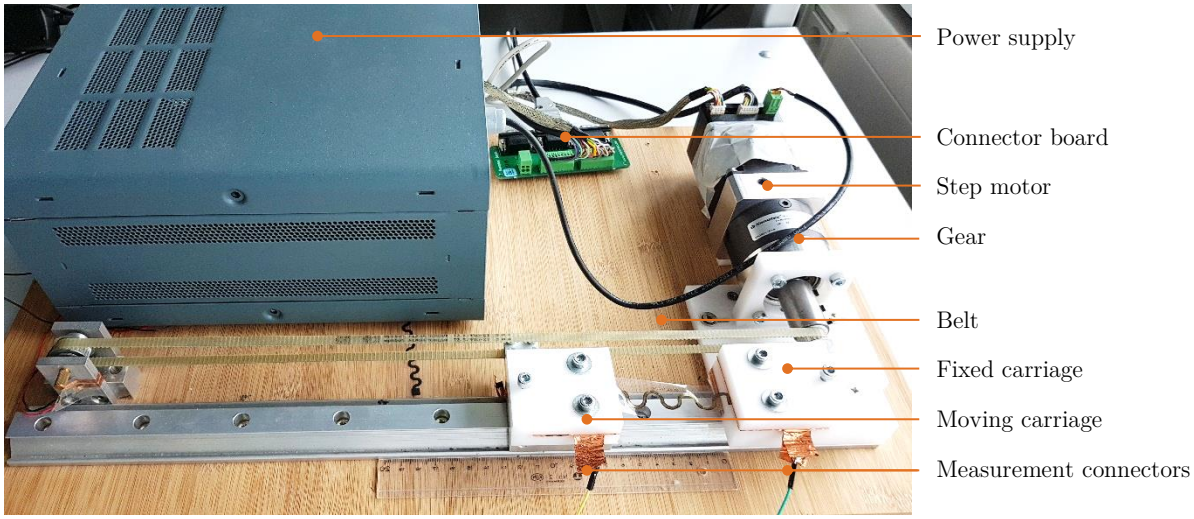

Figure M.1. Bending and Stretching Setup built during the thesis and used for bending tests and the characterization of strain sensors.

blocks are covered with conductive copper tape to make contacting as simple as possible. Onto the copper wire, connectors are soldered that can be connected to a multimeter or any other measurement device. The resistance of the wires and the connectors are below 1 Ω. The motor consists of a full step angle of 1.8° and was operated in half step mode. It is connected to a 1/8 gear, which results in an angle of 0.1125° per step. The diameter of the mounted wheel with the belt was experimentally found and calibrated to 14.34 mm. This results in a step length of 14.08 µm.

Figure M.2 shows the settings bar of the Labview programme that was developed. The settings bar starts from left with the Communication & Status Section including a debug window with the last commands sent to the motor and the received responses. Next to it, the communication port has to be selected, to which the setup is connected. Custom commands can be sent to the motor, if necessary. Below, three LEDs indicate whether the motor is ready to move, it reached the zero position, or a position error occurred. Below, the entire programme can be stopped. It is recommended to always use this button instead of stopping it in the LabView interface because only then the communication port is properly closed. The next Section includes the profile settings. The speed and the set position can be either entered in millimetres or in steps. The programme converts between both automatically and always uses the values shown in the selected tab. The current position is indicated and can be reset to zero. The repetitions field offers the opportunity to repeat the current profile for the given number. If moving back and forth is wanted, the "change of direction" button has to be activated and the number of repetition gives the number of movements. For one cycle, two repetitions are necessary. A break between the repetitions can be set as well. The operation mode can be selected, but we think that relative positioning is the most used mode. A click on the Start Profile button runs the current profile and may be stopped if wanted by the Stop Profile button.

The software allows running scripts defined in the "program settings" fully automatically. An input text file can be selected that contains one header row and then the following values separated by tabulators: Delay (s), Position (mm/steps), speed (mm/steps), repetitions. After initializing the motor, the first line is read and the given delay time is awaited. Then, the position, the speed, and the number of repetitions are filled into the designated fields in the front panel depending on the switch next to the input file location. Then the start command is sent to the motor. After reaching the desired position, the ready command is on and the next line is read. It has to be regarded, that the file should contain one more line with zeros at the position and speed. After reading the last line, the programme stops. The elapsed and the remaining time are shown. After each measurement, the set position, the current position, and the measured resistance value are saved to the output file.

On the last settings window, the measurement can be switched on and off, the measurement period set and the Multimeter connection selected. The desired measured property can be selected from the functions list, the current measured value is displayed, and a maximum value can be set. The last only applies to the graphs below the bar that show the position of the motor and the currently measured resistance value over time. A tab offers a third plot that displays the resistance over the position for each time step.

This programme does not offer a synchronization between the moving motor and the measurement. Therefore, a second programme was built to that looks similar and allows cyclic measurements. The number of cycles, the position, the speed, and a wait time in the stretched and in the idle position can be set. The programme stretches the sample to the desired position, waits for the given time and

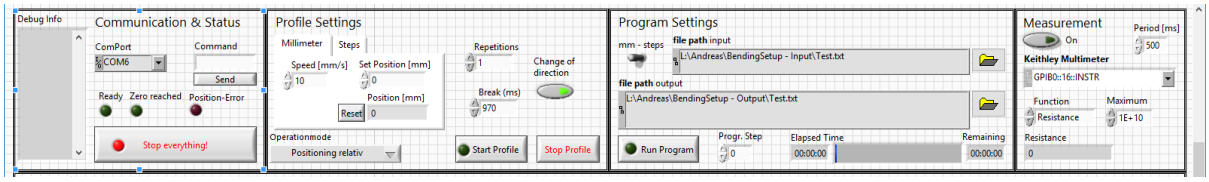

Figure M.2 Labview Programme for the Bending and Stretching Setup

then returns to the initial position. Then the second wait time is excuted and then, the measurement is conducted before the next cycle starts.

M.4.2 Force and Pressure Setup

For the force measurements conducted in this thesis, a new force setup was custom-built. Figure M.3 a shows the central part of the setup with the force actuator and the stage. The setup consists of a stage, a linear actuator, and several measurement devices. The stage is formed by the drilling and milling bank BFB 2000 (Article number 20 000) of Proxxon (Luxemburg). It is a stable tool that withstands the forces applied during the tests without deforming too much. It has a holder for 43 mm spindles that can be moved in the z-direction as well as be rotated. A manual positioning stage KT 150 (no. 20 150) of the same company was employed to simplify the alignment of the force actuator with the sensor. A 43 mm cylinder of hard plastic was cut to screw the motor to and fix it in the holder.

The force actuator is a V-275 PIMAG voice coil actuator of Physik Instrumente (PI) GmbH & Co. KG (Germany) that can apply forces up to 15 N with a moving range of 10 mm. It has an integrated force and position sensor with resolutions of 1 mN and 10 nm, respectively. The smallest step sizes are 5 mN and 100 nm with speeds of up to 600 mm/s. The force is applied through an aluminium rod with a diameter of 5 mm. Its precision-cut bottom side presses on top of a sensor while the stiff stage exerts the counter force. The stage and the force applicator are wired to ground potential. To easily control the force actuator a C-413.20GA PIMag Motion Controller is employed that supports up to 2 motors and 2 sensor pairs (position and force) and can be connected by USB to a computer.

A LabView program (Figure M.4) was developed to send the commands to the actuator as well as read measurement values from a variety of devices: An impedance analyser E4980A of Agilent, a multimeter 2700 of Keithley, and a source-meter 2602B of Keithley are available. These instruments can be multiplexed with a multiplexer/switch 34980A of Keysight. Furthermore, the LabView programme supports the reading and processing of digital measurements transmitted via serial communication ports (COM) and the inter-integrated circuit (I2C) bus with support for the AD7147 capacitance to digital converter chip. The read measurement values are then can be saved together with the current position and force to an output file. The current pressure on the sensor is calculated after each force measurement. If necessary, moving average values of force, position, and measurement values can be computed.

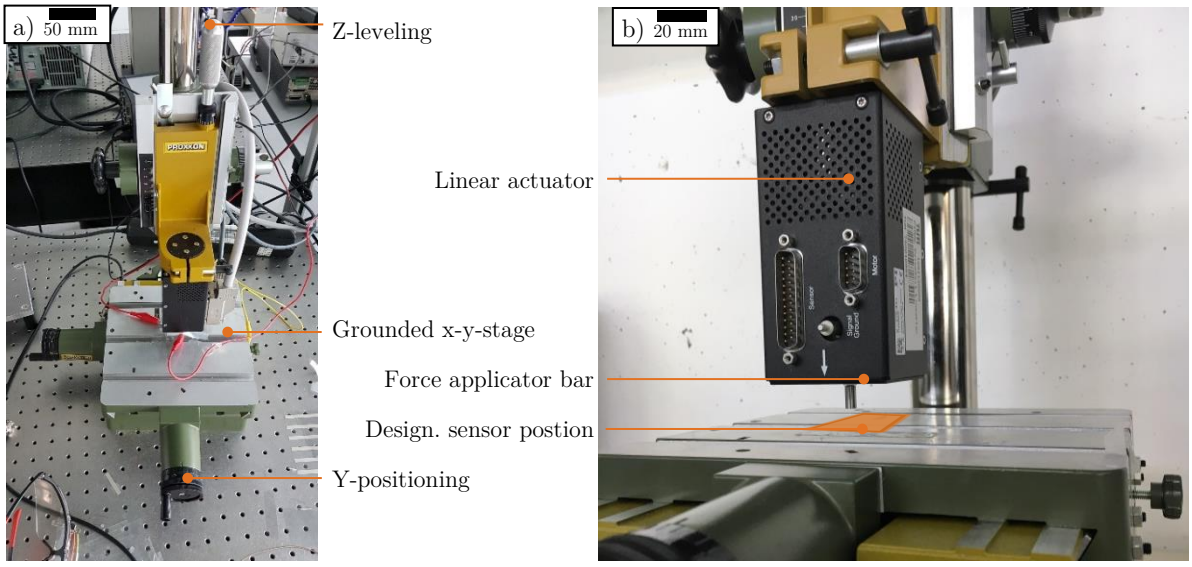

Figure M.3 a) Stage and linear actuator of the normal force setup with labelled components without wires.

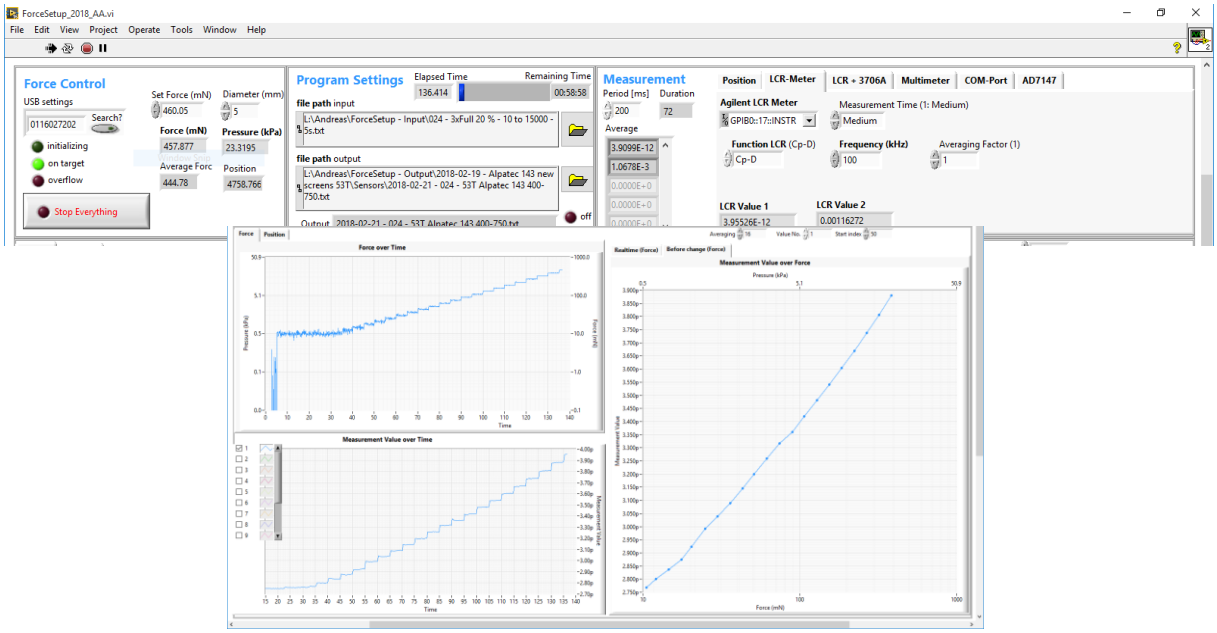

Figure M.4. The Labview program for the force and pressure setup build during the work on this thesis. The top image shows the magnified settings bar and the bottom one the live graphs.

In the Force Control section, the USB connection can be set and the current status is indicated. A yellow flashing LED indicates the initialization, which may take several seconds after starting the programme. Make sure that the linear actuator is free to move at this point. The desired force can be set and is transferred to the motor as soon as the operator leaves the field or presses enter. The diameter is used for conversion of force to pressure. A script can be run in the program settings Section with the following three inputs: Time (s), Force (mN), and Signal Frequency (Hz). When the elapsed time of the programme passes the value set in the first column of the input file, the force value and the signal frequency are inserted into the set force field and the respective field of the LCR meter and executed. The output file contains the current time, set force, current force, position, corrected position, and all measurement values. The measurement settings of the different devices are not explained here as this exceeds the frame of this thesis.

The current force, pressure, position, and measurement values are shown in graphs over time on the left side of the program window. On the right side, it is possible to select one measurement value that will be shown on the y-axis while on the x-axis, the force and pressure are shown. This helps to directly interpret the sensor behaviour during the program execution. A second graph shows the last moving average value at the time steps defined in the spreadsheet. This reduces the complexity of the graph because time-effects disappear.

M.4.3 Shear Force Setup

The normal force setup was extended by a stage measure shear force that is shown in Figure M.5. In the shear force setup, the linear actuator described above is mounted horizontally on an aluminium plate. Close to the tip of its force applicator, the sensor holder is placed so that the force is exerted exactly horizontally on the sensor. The sensor is shown in the schematic with four sensing areas and some wiring. It is glued with one side onto an aluminium block of the dimensions 30 x 30 mm^2. Its height matches exactly with the centre of the force applicator be able to exert only a shear force. The other side of the sensor is glued to an aluminium cap which is shown transparent blue in the schematic. It has downward-oriented notches at which the force will be applied. The gaps between the notches were left free to allow wiring of the sensor. The combination of the bottom block and the top cap with the sensor can be rotated in steps of 45° and then be fixed. Therefore, the top cap

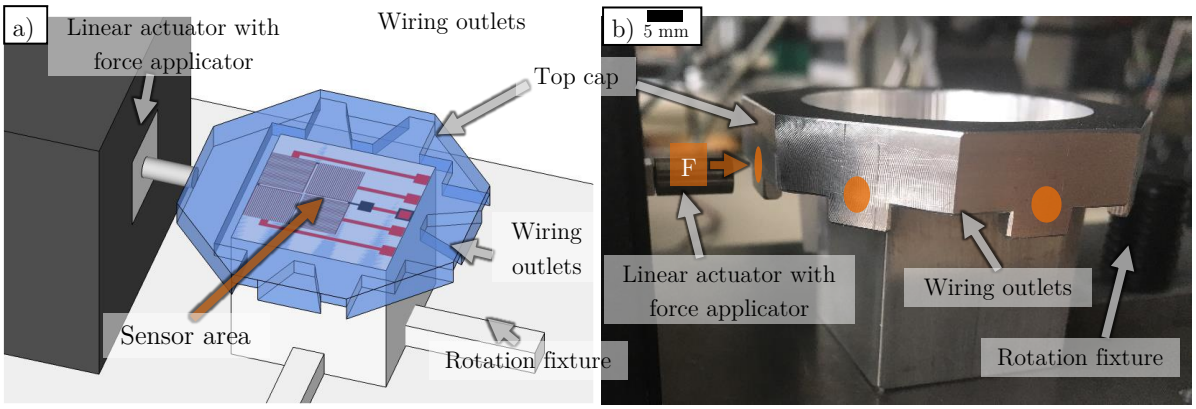

Figure M.5. a) Schematic and b) a photo of the shear force setup with labelled components. The top aluminium cap is shown semi-transparent in the schematic to make the shear force sensor visible that sits between it and the bottom aluminium block. The force application areas are marked in orange.

is hexagonally shaped to allow force application on each of the eight sides. The force application areas are marked in orange in Figure M.5b. This setup makes it possible to measure the sensor for shear forces in eight different directions without removing it and maybe change its properties or destroy it.

M.4.4 Thermocouple Setup

For the measurement of the produced thin-film thermocouples (TC), the characterization setup shown in Figure M.6 was purposely developed and custom-built. The main components are labelled in the figure and the position of the thermocouples under test are shown by orange lines. The setup was built on top of a heat sink to maintain parts of the setup at room-temperature. An aluminium plate mounted on top serves as a stable ground to the overlying components. To avoid unnecessary heat flow to the environment and press the thin-film TCs flat, two blocks of foam glass with a height of 30 mm from D&I GmbH Handel & Logistik (Germany) were used that can support temperatures up to 450 °C. Into the bottom foam glass, the heater and the cooler are integrated at a distance of 20 mm and into the top one, the measurement system. Both layers were held in place by pins in the corners.

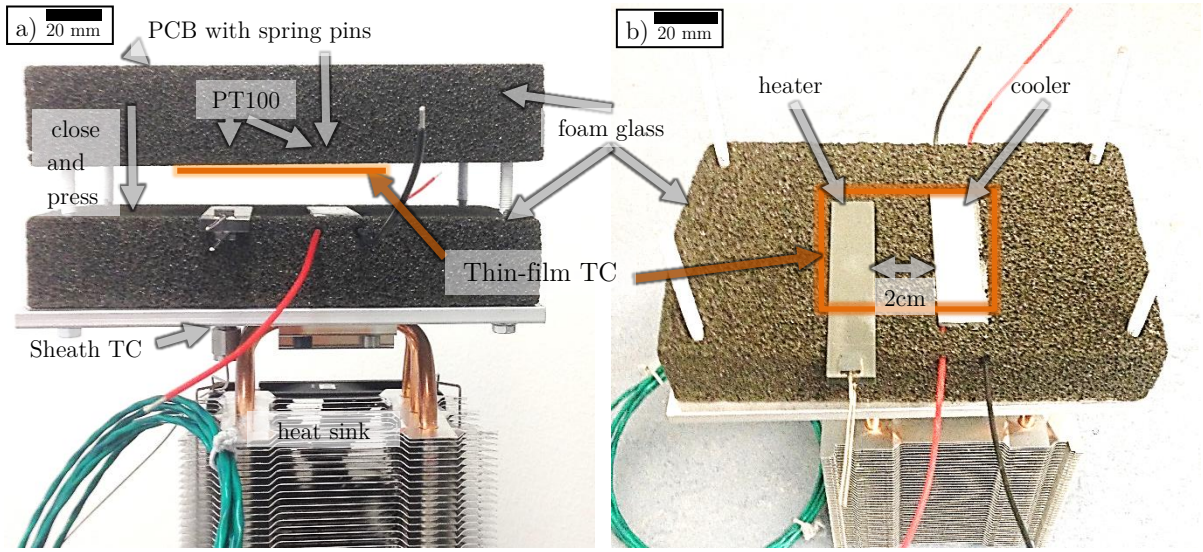

Figure M.6 a) Characterization setup for thin-film thermocouples (TC) with labelled components and the orange-marked position of the TC under test from a) side view with lifted top-cover and b) top view without top cover. Reprocessed from original files published in [22].

The flat, full-ceramic heater from Bach Resistor Ceramics GmbH (Germany) supports temperatures up to 1000 °C with a limitation of 500 °C at the contacts. The heated area is approximately 50 x 14.7 mm², can be operated with a voltage up to 48 V, and has a resistance of 8 Ω ± 25 %. A notch was milled into the foam glass to place the heater's upper surface in line with the top of the foam glass and position the heater's contacts outside to avoid troubles with overheating. The contact wires were partially isolated so that they can be connected via crocodile clamps to a power supply. The heater has a hole to measure the inside temperature with a sheath thermocouple type K. Such a thermocouple was mounted with a fixture into the bottom plate of the setup and can be connected to a multimeter with the green and white cable. In the final setup, the heater was lowered by two millimetres and covered with an aluminium plate to homogenize the heat distribution.

The active part of the cooler consists of two Peltier elements QC-63-1.0-3.9M of QuickCool (Germany) with the dimensions 30 x 15 mm², which were put in a row to create a 60 mm long cooler. They have a resistance of 1.5 Ω and can support a maximum voltage of 7.6 V and a current of 3.9 A to reach a temperature difference of up to 70°C at a maximum heat flow of 16.2 W. The Peltier elements where put onto an aluminium block that was mounted onto the bottom plate and is integrated into the foam glass. To homogenize the temperature distribution, they were covered with a 2 mm aluminium plate of the same dimensions. A thermally-conductive paste was used to improve the heat flow. The red and black cables appearing through the foam glass are the leads to the Peltier elements and were connected in series to a power supply.

The top foam glass can be removed to place the thermocouples to be tested. The top of this foam glass block is glued onto a copper-coated printed circuit board (PCB) that serves as a wiring board. A 40-pin connector is placed for all connections to the multimeter, a 10-pin connector allows the recording of the voltage-current characteristics by a source meter. A 2-pin connector can be used to couple the sheath thermocouple voltage to the multimeter. Five spring-loaded pins with a length of 32.3 mm and a diameter of 2 mm were soldered into the PCB and wired to the multimeter connector. These pins are positioned exactly on the location of the overlapping layers of the TC under test on the cold side. Spring pin 1 serves as the low potential and is connected to the low input of channel 1 of the multimeter. The other pins n are connected to the high input of channel n-1 and the low input of channel n.

To monitor the current temperature on top of the thermocouple, two PT100 thermoresistors were placed on top of the hot and cold side approximately in the middle of the areas. They were soldered to the PCB and were measured by the four-point method by the multimeter. Furthermore, they were used to control the temperatures of the heater and the cooler. All electrical connections are summarized in Figure M.7, which shows the device under test in the centre and the two measurement devices as well as the two power supplies and the PC in the corners. Schematically, the measurement functions are visualized in the devices. A detailed description of the four devices can be found in the next section.

A Labview program was developed to automate the measurement with the program steps indicated in the flow diagram in Figure M.8 of the Appendix. After initialization, the multimeter was addressed to read out the current values of the two PT100 temperature sensors on the hot and the cold side of the setup as well as the safety sheath thermocouple. The first two were used to feed the PID controller of the heater and the cooler, respectively, to reach the desired setpoint. The last was used to identify an exceeding temperature and shut down the setup before any destruction occurs. Together with these three values, the current voltages at the thermocouples were measured. The reading of the temperatures and the writing of the new voltage values to the power supplies took about 3 s. Then, the loop was repeated. After exemplary 5 minutes, the temperatures were stable and the voltages at the thermocouples under test were read, displayed, and saved to a file. To avoid electrostatic charging of the thermocouple pins, the voltages were actively set to ground about 2 s before the measurement.

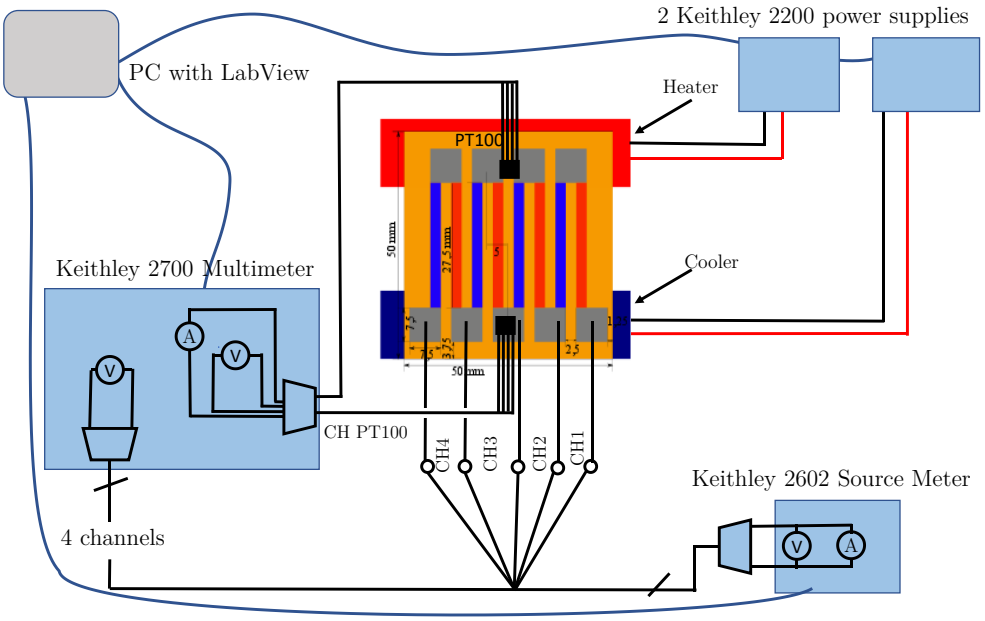

Figure M.7 Electrical connection diagram of thermocouple setup consisting of the five measurement points of the four legs of the thermocouples (blue, red) that contact to the overlap area (grey) on the cold side. For each thermocouple, one voltage sensing channel is configured in the multimeter. Recording of the I-V-curve of each thermocouple or a series connection of them is possible with the Source Meter. The heater and cooler to generate the temperature gradient are each powered by a power supply. All measurement devices and power supplies are connected to the PC and controlled through a Labview program.

After this, the I-V curve was recorded with the source meter to check, if the resistance curve is linear and find the maximum power point. Subsequently, the next temperature set point was loaded from a file and the loop repeated until reaching the last set point.

To improve the response of the PID controller, the two formulas in Eq. 6.1 were fitted to the measured values to reach the desired temperatures quickly and only use the PID controller for a higher accuracy.

$$V_{Heater} = \frac{T_{Set}+36°C}{32°C} \quad V_{Cooler} = \frac{T_{Set}+18°C}{19°C} \qquad \text{Eq. 6.1}$$

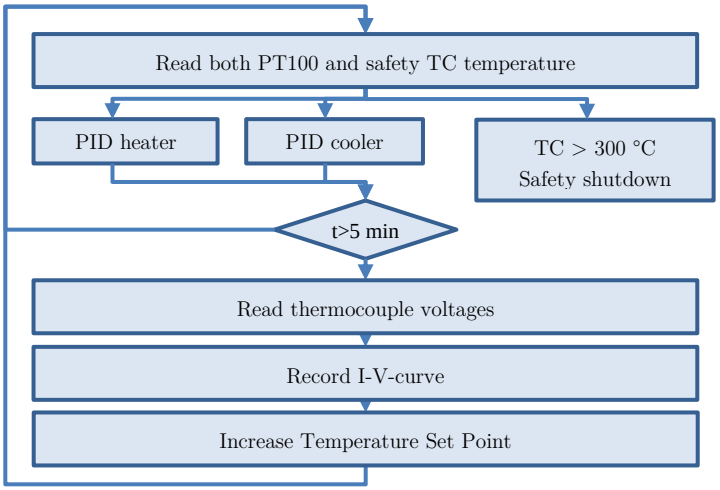

Figure M.8 Flow diagram of the Labview program used to control the thermocouple setup.

M.5 Optical and Surface Analysis

Optical microscope images of small patterns were taken with an Axiolab A1 MAT equipped with an Axiocam 105 colour camera, both of Carl Zeiss AG (Germany). It is equipped with EC Epiplan M27 objectives and light emitting diodes for illumination. Contrast, brightness, and white balance of the images have been adjusted afterwards.

Optical microscope images of larger patterns and screen-printing screens were taken with an AM4115ZT Dino-Lite Edge Microscope. Depending on the working distance, it has up to two focus points. One is in the magnification range of 50x – 70x and the other is between 210x and 230x. We used two of these microscopes in the Nino screen-printer. Before taking a picture, the camera was focused and a ruler provided by the manufacturer was used to determine the magnification factor that needs to be inserted in the DinoCapture software. This software was used to show the images of both cameras while printing and to capture images and perform measurements on them. Contrast, brightness, and white balance of the images have been adjusted afterwards.

Profilometer studies have been done with a Dektak XT of Bruker (US) with the micro-porous vacuum chuck that holds flexible samples flat. Always the lowest measurement range was used to measure the samples. Other parameters can be found at the respective locations in this work. Data levelling was used to compensate tilt, modal tilt, and cylindrical or spherical bending of the substrate on the table.

Atomic Force Microscope (AFM) images were taken with a JSPM 5200 of Jeol (Japan). It was used in the scanning probe mode (SPM) and the images have been processed using the software Gwyddion. Field Emission Scanning Electron Microscope (FESEM) images have been taken with a Nvision 40 of Zeiss (Germany) at 5.0 kV beam energy. Due to the pre-alignment of the electron beam prior to entering the electron optics, FESEM-imaging offers a higher spatial resolution than conventional SEM-imaging. The aperture size for all measurements was 30 µm. The working distance was optimized for the best image quality around 7 mm. Contrast, brightness, and sharpness of the images have been adjusted afterwards.

Static water contact angles of 4 µL droplets of deionized water were measured under ambient conditions by the sessile-drop method using an OCA15 of Dataphysics (Germany). For the contact angles of the silver ink, micropipettes with the same volume were used and the drop was carefully put onto the substrate.

The transmittance of the spray-coated films on glass was evaluated using a 300W xenon arc lamp chopped at 210 Hz, passing through an Oriel Cornerstone 260 ¼m monochromator and a calibrated photodetector. The output signal was connected to a transimpedance amplifier and fed to a lock-in amplifier. Before each characterization, the substrate was characterized and used for calibration in the data acquisition and spectrometer software TracQ Basic of Newport Corporation (US).

M.6 Electronic Precision Meters and Power Sources

A Keithley 2700 multimeter with 20 input channels was also used for measuring the resistances and open-circuit voltages in the bending setup and in the thermocouple setup. A Keithley 2602B source meter was employed in the thermocouple setup. The LCR meter E4982A of Keysight was employed for all capacitance measurements at an amplitude of 1 V at a frequency of 100 kHz, if not indicated otherwise. A calibration of the wires was done after each change of the setup. The impedance analyser E4990A was employed to measure the frequency depended response of the wireless tags and an E5061B ENA Vector Network Analyzer of Keysight for the S11 parameter measurements.

Sheet resistance measurements were conducted on the printed films with two different probes. A linear four point probe head of Jandel (UK) with a probe spacing of 635 µm and a spherical probe tip with a diameter of 150 µm and a curvature diameter of 1 mm was used. The contact force on the sample was adjusted to 10 g. If this probe was not applicable because of film or substrate properties, a self-made linear four-point probe was used that has a pin spacing of approximately 1.6 mm. The electrical measurements were conducted with a Keysight B2900 source meter or a Keithley 2700 multimeter. A correction factor was applied to compensate the effect of limited boundaries according to Smits et al. [126]

References

[1] A. S. Brown, “Flexible electronics could transform the way we make and use electronic devices”, *Penn State University News*, 2013.

[2] D. Tobjörk and R. Österbacka, “Paper electronics.”, *Adv. Mater.*, vol. 23, no. 17, pp. 1935–61, May 2011.

[3] C. Zheng, *Printed Electronics: Manufacturing Technologies and Applications*. Singapore: John Wiley & Sons Singapore Pte. Ltd, 2014.

[4] D. R. Gamota, P. Brazis, K. Kalyanasundaram, and J. Zhang, *Printed Organic and Molecular Electronics*. Springer Science & Business Media, 2004.

[5] L. Xie, “Heterogeneous Integration of Silicon and Printed Electronics for Intelligent Sensing Devices”, KTH School of Information and Communication Technology, Stockholm, 2014.

[6] P. Teunissen, R. Abbel, T. Eggenhuizen, M. Coenen, and P. Groen, “Inkjet Printing for Printed Electronics”, in *Handbook of Industrial Inkjet Printing*, Weinheim, Germany: Wiley-VCH Verlag GmbH & Co. KGaA, 2017, pp. 599–616.

[7] I. Yun, *Printed Electronics - Current Trends and Applications*. InTech, 2016.

[8] U. Caglar, “Studies of Inkjet Printing Technology with Focus on Electronic Materials”, Tampere University of Technology, 2010.

[9] M. Pudas, N. Halonen, P. Granat, and J. Vähäkangas, “Gravure printing of conductive particulate polymer inks on flexible substrates”, *Prog. Org. Coatings*, vol. 54, no. 4, pp. 310–316, Dec. 2005.

[10] S. S. L. Merilampi, T. Bjorninen, A. Vuorimaki, L. Ukkonen, P. Ruuskanen, and L. Sydanheimo, “The Effect of Conductive Ink Layer Thickness on the Functioning of Printed UHF RFID Antennas”, *Proc. IEEE*, vol. 98, no. 9, pp. 1610–1619, Sep. 2010.

[11] J. Fernández Salmerón, “Desarrollo de capacidades sensoras en tecnología RFID = Development of sensing capabilities in RFID technology”, Editorial de la Universidad de Granada, 2014.

[12] A. Rivadeneyra Torres, J. Fernández-Salmerón, J. Banqueri, J. A. López-villanueva, L. F. Capitan-Vallvey, and A. J. Palma, “A novel electrode structure compared with interdigitated electrodes as capacitive sensor”, *Sensors Actuators B Chem.*, vol. 204, pp. 552–560, 2014.

[13] V. Akhavan, K. Schroder, and S. Farnsworth, “Photonic Curing Enabling High-Speed Sintering of Metal Inkjet Inks on Temperature-Sensitive Substrates”, in *Handbook of Industrial Inkjet Printing: A Full System Approach*, Weinheim, Germany: Wiley-VCH Verlag GmbH & Co. KGaA, 2018, pp. 557–566.

[14] G. Bai, “Low-Temperature Sintering of Nanoscale Silver Paste for Semiconductor Device Interconnection”, Virginia Polytechnic Institute and State University, 2005.

[15] J. Burroughes and K. Hecker, “Organic and Printed Electronics: Application, Technologies and Suppliers, 7th Edition”, *OE-A Broch.*, p. 108, 2017.

[16] S. Kirchmeyer and K. Hecker, “Organic and Printed Electronics: Application, Technologies and Suppliers, 5th Edition”, *OE-A Broch.*, p. 34, 2013.

[17] Z. Cao, E. Koukharenko, R. N. Torah, and S. P. Beeby, “Exploring Screen Printing Technology On Thermoelectric Energy Harvesting With Printing Copper-Nickel And Bismuth-Antimony Thermocouples”, *2013 Transducers Eurosensors XXVII 17th Int. Conf. Solid-State Sensors, Actuators Microsystems*, no. June, pp. 478–481, 2013.

[18] E. P. M. Bischur, “Energy Harvesting auf Basis monoaxial gereckter PVDF-Folie und der Technologie von Folienkondensatoren”, Technical University of Munich, 2016.

[19] Y. Qi, N. T. Jafferis, K. Lyons, C. M. Lee, H. Ahmad, and M. C. McAlpine, “Piezoelectric Ribbons Printed onto Rubber for Flexible Energy Conversion”, *Nano Lett.*, vol. 10, no. 2, pp. 524–528, Feb. 2010.

[20] M. E. Karagozler, I. Poupyrev, G. K. Fedder, and Y. Suzuki, “Paper Generators : Harvesting Energy from Touching , Rubbing and Sliding”, *UIST’13*, 2013.

[21] A. Georgiadis, A. Collado, S. Via, and C. Meneses, “Flexible hybrid solar/EM energy harvester for autonomous sensors”, in *IEEE MTT-S International Microwave Symposium Digest*, 2011, pp. 1–4.

[22] A. Albrecht, M. Bobinger, J. B. Calia, A. Falco, *et al.*, “Transparent Thermocouples based on Spray-coated Nanocomposites”, *2017 IEEE SENSORS*, pp. 4–6, Oct. 2017.

[23] G. Nisato, D. Lupo, and S. Ganz, *Organic and Printed Electronics: Fundamentals and Applications*. CRC Press, 2016.

[24] H. Andersson, B. Andres, A. Manuilskiy, S. Forsberg, *et al.*, “Contacting paper-based supercapacitors to printed electronics on paper substrates”, *Nord. Pulp Pap. Res. J.*, vol. 27, no. 2, p. 476, 2012.

[25] S. Yao and Y. Zhu, “Nanomaterial-enabled stretchable conductors: Strategies, materials and devices”, *Adv.*

Mater., vol. 27, no. 9, pp. 1480–1511, 2015.

[26] A. Albrecht, "KEYNOTE: Printed Sensors for the Internet of Things", in *Advanced Functional & Industrial Printing 2016*, 2016.

[27] S. Harada, K. Kanao, Y. Yamamoto, T. Arie, S. Akita, and K. Takei, "Fully Printed Flexible Fingerprint-like Three-Axis Tactile and Slip Force and Temperature Sensors for Artificial Skin", *ACS Nano*, vol. 8, no. 12, pp. 12851–12857, Dec. 2014.

[28] L. Seminara, L. Pinna, M. Valle, L. Basirico, *et al.*, "Piezoelectric polymer transducer arrays for flexible tactile sensors", *IEEE Sens. J.*, vol. 13, no. 10, pp. 4022–4029, 2013.

[29] H. Andersson, A. Manuilskiy, and J. Gao, "Investigation of humidity sensor effect in silver nano-particle ink sensors printed on paper", *IEEE Sens. J.*, vol. 14, no. 3, pp. 623–628, 2014.

[30] J. Ahmad, H. Andersson, and J. Sidén, "Sitting Posture Recognition using Screen Printed Large Area Pressure Sensors", *2017 IEEE SENSORS*, pp. 8–10, Oct. 2017.

[31] K. Chen, W. Gao, S. Emaminejad, D. Kiriya, *et al.*, "Printed Carbon Nanotube Electronics and Sensor Systems", *Advanced Materials*, vol. 28, no. 22. pp. 4397–4414, 01-Jun-2016.

[32] K. D. Harris, A. L. Elias, and H.-J. Chung, "Flexible electronics under strain: a review of mechanical characterization and durability enhancement strategies", *J. Mater. Sci.*, vol. 51, no. 6, pp. 2771–2805, Mar. 2016.

[33] J. F. Salmerón, F. Molina-lopez, A. Rivadeneyra Torres, A. V. Quintero, *et al.*, "Design and Development of Sensing RFID Tags on Flexible Foil Compatible With EPC Gen 2", *IEEE Sens. J.*, vol. 14, no. 12, pp. 4361–4371, 2014.

[34] A. Falco, J. Salmerón, F. Loghin, P. Lugli, and A. Rivadeneyra, "Fully Printed Flexible Single-Chip RFID Tag with Light Detection Capabilities", *Sensors*, vol. 17, no. 3, p. 534, Mar. 2017.

[35] K. Cherenack and L. van Pieterson, "Smart textiles: Challenges and opportunities", *J. Appl. Phys.*, vol. 112, no. 9, p. 091301, Nov. 2012.

[36] M. Stoppa and A. Chiolerio, "Wearable Electronics and Smart Textiles: A Critical Review", *Sensors*, vol. 14, no. 7, pp. 11957–11992, Jul. 2014.

[37] B. Geffroy, P. le Roy, and C. Prat, "Organic light-emitting diode (OLED) technology: materials, devices and display technologies", *Polym. Int.*, vol. 55, no. 6, pp. 572–582, Jun. 2006.

[38] K. Suganuma, *Introduction to Printed Electronics*, vol. 74. Springer Science & Business Media, 2014.

[39] A. Karwa, "Printing studies with conductive inks and exploration of new conducting polymer compositions", Rochester Institut of Technology, 2006.

[40] A. Blayo, B. Pineaux, L. De Génie, P. Lgp, P. B. P. Saint-martin, and H. Cedex, "Printing Processes and their Potential for RFID Printing", *Jt. sOc-EUSAI Conf.*, pp. 7–10, 2005.

[41] K. Reuter, H. Kempa, N. Brandt, M. Bartzsch, and A. C. Huebler, "Influence of process parameters on the electrical properties of offset printed conductive polymer layers", *Prog. Org. Coatings*, vol. 58, no. 4, pp. 312–315, Mar. 2007.

[42] M. Kim, J. Bon Koo, K.-J. Baeg, S.-W. Jung, B.-K. Ju, and I.-K. You, "Top-gate staggered poly(3,3‴-dialkyl-quarterthiophene) organic thin-film transistors with reverse-offset-printed silver source/drain electrodes", *Appl. Phys. Lett.*, vol. 101, no. 13, p. 133306, Sep. 2012.

[43] H. Kipphan, *Handbook of print media : technologies and production methods*. 2001.

[44] H. Yan, Z. Chen, Y. Zheng, C. Newman, *et al.*, "A high-mobility electron-transporting polymer for printed transistors.", *Nature*, vol. 457, no. 7230, pp. 679–86, Feb. 2009.

[45] Sefar, "Product Information Guide for Precision Electronic Screens (11.09)." .

[46] S. Khan, L. Lorenzelli, and R. S. Dahiya, "Technologies for printing sensors and electronics over large flexible substrates: A review", *IEEE Sens. J.*, vol. 15, no. 6, pp. 3164–3185, Jun. 2015.

[47] R. Abbel, P. Teunissen, E. Rubingh, and T. J. Van Lammeren, "Industrial-scale inkjet printed electronics manufacturing — production up-scaling from concept tools to a roll-to-roll pilot line", *Transl. Mater. Res.*, vol. 1, no. 1, p. 015002, 2014.

[48] J. F. Salmerón, F. Molina-Lopez, D. Briand, J. J. Ruan, *et al.*, "Properties and Printability of Inkjet and Screen-Printed Silver Patterns for RFID Antennas", *J. Electron. Mater.*, vol. 43, no. 2, pp. 604–617, Nov. 2013.

[49] M. Singh, H. M. Haverinen, P. Dhagat, and G. E. Jabbour, "Inkjet printing-process and its applications.", *Adv. Mater.*, vol. 22, no. 6, pp. 673–85, Feb. 2010.

[50] M. Nir, D. Zamir, I. Haymov, and L. Ben-Asher, "Electrically conductive inks for inkjet printing", in *The Chemistry of Inkjet Inks*, S. Magdassi, Ed. 2010, pp. 225–254.

[51] G. Cummins and M. P. Y. Desmulliez, "Inkjet printing of conductive materials: a review", *Circuit World*, vol. 38, no. 4, pp. 193–213, 2012.

[52] R. D. Deegan, O. Bakajin, T. F. Dupont, G. Huber, S. R. Nagel, and T. A. Witten, "Contact line deposits in

an evaporating drop", *Phys. Rev. E - Stat. Physics, Plasmas, Fluids, Relat. Interdiscip. Top.*, vol. 62, no. 1 B, pp. 756–765, Jul. 2000.

[53] † and Hua Hu* and R. G. Larson, "Marangoni Effect Reverses Coffee-Ring Depositions", 2006.

[54] A. Kamyshny, J. Steinke, and S. Magdassi, "Metal-based Inkjet Inks for Printed Electronics", *Open Appl. Phys. J.*, vol. 4, pp. 19–36, 2011.

[55] K. C. Yung, X. Gu, C. P. Lee, and H. S. Choy, "Ink-jet printing and camera flash sintering of silver tracks on different substrates", *J. Mater. Process. Technol.*, vol. 210, no. 15, pp. 2268–2272, Nov. 2010.

[56] D. Lupo, C. N. Hoth, J. H. Kwon, C. Verschuren, *et al.*, *Applications of Organic and Printed Electronics*. Springer, 2013.

[57] F. C. Krebs, "Polymer solar cell modules prepared using roll-to-roll methods: Knife-over-edge coating, slot-die coating and screen printing", *Sol. Energy Mater. Sol. Cells*, vol. 93, no. 4, pp. 465–475, Apr. 2009.

[58] A. Falco, "Printed Components for Organic Optoelectronics", Technical University of Munich, 2016.

[59] A. Abdellah, "Thin-Film Manufacturing Technologies for Organic Electronics", Technical University of Munich, 2012.

[60] A. Abdelhalim, "Fabrication and Characterization of Carbon Nanotube Thin-Films for Gas Sensing Applications", Technical University of Munich, 2015.

[61] A. Falco, A. M. Zaidi, P. Lugli, and A. Abdellah, "Spray deposition of Polyethylenimine thin films for the fabrication of fully-sprayed organic photodiodes", *Org. Electron. physics, Mater. Appl.*, vol. 23, pp. 186–192, 2015.

[62] P. Lugli, A. Abdellah, A. Abdelhalim, A. Albrecht, *et al.*, "Fabrication, characterization and modeling of flexible electronic components based on CNT networks", in *Proceedings - IEEE International Symposium on Circuits and Systems*, 2016, vol. 2016–July, pp. 1362–1365.

[63] A. Abdelhalim, M. Winkler, F. Loghin, C. Zeiser, P. Lugli, and A. Abdellah, "Highly sensitive and selective carbon nanotube-based gas sensor arrays functionalized with different metallic nanoparticles", *Sensors Actuators, B Chem.*, vol. 220, no. 2, pp. 1288–1296, 2015.

[64] A. Albrecht, A. Rivadeneyra Torres, J. F. Salmerón, A. Abdellah, and P. Lugli, "Inkjet Printing and Photonic Sintering of Silver and Copper Oxide Nanoparticles for Ultra-Low-Cost Conductive Patterns", *J. Mater. Chem. C*, Mar. 2016.

[65] H. P. Le, "Progress and Trends in Ink-jet Printing Technology", *J. Imaging Sci. Technol.*, vol. 42, no. 1, 1998.

[66] J. Eggers, "Nonlinear dynamics and breakup of free-surface flows", *Rev. Mod. Phys.*, vol. 69, no. 3, pp. 865–930, 1997.

[67] P. Gregory, Ed., *Chemistry and Technology of Printing and Imaging Systems*. Dordrecht: Springer Netherlands, 1996.

[68] H. Ujiie, *Digital Printing of Textiles*. Elsevier Science, 2006.

[69] Kodak, *Kodak Stream Inkjet Technology Overview - YouTube*. 2009.

[70] J. R. Castrejon-Pita, W. R. S. Baxter, J. Morgan, S. Temple, G. D. Martin, and I. M. Hutchings, "Future, Opportunities and Challenges of Inkjet Technologies", *At. Sprays*, pp. 1–13, 2013.

[71] Videojet Technologies GmbH, "Videojet Tintenstrahldrucker sind wartungsarm und leicht zu bedienen." [Online]. Available: http://www.videojet.de/de/homepage/products/continuous-inkjet-printers.html. [Accessed: 09-Mar-2018].

[72] D. A. Inc, "Product printing - Products." [Online]. Available: https://www.domino-printing.com/en-us/products/product-printing.aspx. [Accessed: 09-Mar-2018].

[73] L. P. Technologies, "CIJ-Drucker | Linx Printing Technologies." [Online]. Available: https://www.linxglobal.com/de/produkte/cij-drucker/. [Accessed: 09-Mar-2018].

[74] Kodak, "White Paper: Kodak Ultrastream."

[75] I. M. Hutchings and G. D. Martin, *Inkjet Technology for Digital Fabrication*. 2012.

[76] Canon Inc., "Canon : Technology | Technology Used in Inkjet Printers." [Online]. Available: http://www.canon.com/technology/now/output/ijp.html. [Accessed: 16-Mar-2018].

[77] H. Wijshoff, "Structure- and fluid-dynamics in piezo inkjet printheads", 2008.

[78] M. Caironi, "Printed Electronics: from fundamentals to advanced processing techniques." 2011.

[79] S. F. Pond, *Inkjet Technology and Product Development Strategies*. 2000.

[80] J.-U. Park, M. Hardy, S. J. Kang, K. Barton, *et al.*, "High-resolution electrohydrodynamic jet printing", *Nat. Mater.*, vol. 6, no. 10, pp. 782–789, Oct. 2007.

[81] D. K. Murata, "Super-fine ink-jet printing for nanotechnology", in *MEMS, NANO and Smart Systems*, 2003.

[82] D. K. Murata and D. K. Masuda, "Super Inkjet Printer Technology and Its Properties", *Convert. e-Print*, no. July/August, pp. 74–78, 2011.

[83] J. Ledesma-Fernandez, C. Tuck, and R. Hague, "3D high viscosity jetting of functional materials", *32nd Int. Conf. Digit. Print. Technol. NIP 2016*, pp. 41–47, 2016.

[84] M. Fujii, "Issues and Approaches Imposed on Ink Jet Technologies for the Progress of Printed Electronics", *Trans. Japan Inst. Electron. Packag.*, vol. 3, no. 1, pp. 35–39, 2010.

[85] T. Sekitani, Y. Noguchi, U. Zschieschang, H. Klauk, and T. Someya, "Organic transistors manufactured using inkjet technology with subfemtoliter accuracy.", *Proc. Natl. Acad. Sci. U. S. A.*, vol. 105, no. 13, pp. 4976–80, Apr. 2008.

[86] S. A. Elrod, B. Hadimioglu, B. T. Khuri-Yakub, E. G. Rawson, *et al.*, "Nozzleless droplet formation with focused acoustic beams", *J. Appl. Phys.*, vol. 65, no. 9, pp. 3441–3447, May 1989.

[87] E. Gili, M. Caironi, and H. Sirringhaus, "Picoliter Printing", in *Academic Press*, G. Wiederrecht, Ed. 2009, pp. 183–208.

[88] Kazuhiro Murata, "Collective Transfer Inkjet Nozzle Plate and Method of Producing the Same", US7971962B2, 05-Jul-2011.

[89] O. D. Trier and T. Taxt, "Evaluation of binarization methods for document images", *Pattern Anal. Mach. Intell. IEEE Trans.*, vol. 17, no. 3, pp. 312–315, Mar. 1995.

[90] M. L. Sham, J. Li, P. Ma, and J.-K. Kim, "Cleaning and Functionalization of Polymer Surfaces and Nanoscale Carbon Fillers by UV/Ozone Treatment: A Review", *J. Compos. Mater.*, vol. 43, no. 14, pp. 1537–1564, Jul. 2009.

[91] B. T. Ginn and O. Steinbock, "Polymer surface modification using microwave-oven-generated plasma", *Langmuir*, vol. 19, no. 19, pp. 8117–8118, 2003.

[92] H. Hillborg and U. W. Gedde, "Hydrophobicity recovery of polydimethylsiloxane after exposure to corona discharges", *Polymer (Guildf).*, vol. 39, no. 10, pp. 1991–1998, May 1998.

[93] M. J. Owen and P. J. Smith, "Plasma treatment of polydimethylsiloxane", *J. Adhes. Sci. Technol.*, vol. 8, no. 10, pp. 1063–1075, Jan. 1994.

[94] K. Efimenko, W. E. Wallace, and J. Genzer, "Surface modification of Sylgard-184 poly(dimethyl siloxane) networks by ultraviolet and ultraviolet/ozone treatment", *J. Colloid Interface Sci.*, vol. 254, no. 2, pp. 306–315, Oct. 2002.

[95] G. S. Ferguson, M. K. Chaudhury, H. A. Biebuyck, and G. M. Whitesides, "Monolayers on disordered substrates: self-assembly of alkyltrichlorosilanes on surface-modified polyethylene and poly(dimethylsiloxane)", *Macromolecules*, vol. 26, no. 22, pp. 5870–5875, Oct. 1993.

[96] N. Y. Adly, H. Hassani, A. Q. Tran, M. Balski, *et al.*, "Observation of chemically protected polydimethylsiloxane: towards crack-free PDMS", *Soft Matter*, vol. 13, no. 37, pp. 6297–6303, Sep. 2017.

[97] Tri-Star Technologies, "PT-2000P Duradyne Plasma Treatment System." [Online]. Available: http://tri-star-technologies.com/catalog/plasma/pt-2000p.php. [Accessed: 22-Mar-2018].

[98] T. Huiskamp, W. J. M. Brok, A. A. E. Stevens, E. J. M. Van Heesch, and A. J. M. Pemen, "Maskless patterning by pulsed-power plasma printing", *IEEE Trans. Plasma Sci.*, vol. 40, no. 7 PART 2, pp. 1913–1925, Jul. 2012.

[99] M. van Dongen, J. Bernards, E. Niewenhuis, R. Verkuijlen, and L. Verbraeken, "µPlasma printing of hydrophobic and hydrophilic patterns to improve wetting behaviour for printed electronics", *LOPEC Proc. 2012*, pp. 1–5, 2012.

[100] K. Haubert, T. Drier, and D. Beebe, "PDMS bonding by means of a portable, low-cost corona system", *Lab Chip*, vol. 6, no. 12, p. 1548, Nov. 2006.

[101] K. Shin, M. Lee, H. Kang, K. Kang, *et al.*, "Characterization of Inkjet-Printed Silver Patterns for Application to Printed Circuit Board (PCB)", vol. 8, no. 3, pp. 603–609, 2013.

[102] D. Tian, Y. Song, and L. Jiang, "Patterning of controllable surface wettability for printing techniques", *Chem. Soc. Rev.*, vol. 42, no. 12, p. 5184, May 2013.

[103] Christopher J. Campbell, Stoyan K. Smoukov, and Kyle J. M. Bishop, and B. A. Grzybowski*, "Reactive Surface Micropatterning by Wet Stamping", 2005.

[104] D. Maji, S. K. Lahiri, and S. Das, "Study of hydrophilicity and stability of chemically modified PDMS surface using piranha and KOH solution", *Surf. Interface Anal.*, vol. 44, no. 1, pp. 62–69, Jan. 2012.

[105] J. H. Park, Y. G. Kim, C. Oh, S. Il Shin, *et al.*, "Fabrication of hollow silver spheres by MPTMS-functionalized hollow silica spheres as templates", *Mater. Res. Bull.*, vol. 40, no. 2, pp. 271–280, 2005.

[106] J. Wu, R. C. Roberts, N. C. Tien, and D. Li, "Inkjet printed silver patterning on PDMS to fabricate microelectrodes for microfluidic sensing", *Proc. IEEE Sensors*, vol. 2014–Decem, no. December, pp. 1100–1103, Nov. 2014.

[107] J. Wu, R. Wang, H. Yu, G. Li, *et al.*, "Inkjet-printed microelectrodes on PDMS as biosensors for functionalized microfluidic systems", *Lab Chip*, vol. 15, no. 3, pp. 690–695, 2015.

[108] H. Andersson and C. Lidenmark, "Evaluation of coatings applied to flexible substrates to enhance quality of ink jet printed silver nano-particle structures", *IEEE Trans. Compon. Packaging. Manuf. Technol.*, vol. 2,

no. 2, pp. 342–348, 2012.

[109] A. S. Diamond, *Handbook of Imaging Materials*. 2002.

[110] J. Kettle, T. Lamminmäki, and P. Gane, "A review of modified surfaces for high speed inkjet coating", *Surf. Coatings Technol.*, vol. 204, no. 12–13, pp. 2103–2109, Mar. 2010.

[111] T. Lamminmäki, J. Kettle, and P. Gane, "Absorption and adsorption of dye-based inkjet inks by coating layer components and the implications for print quality", *Colloids Surfaces A Physicochem. Eng. Asp.*, vol. 380, no. 1–3, pp. 79–88, May 2011.

[112] M. Frenkel, "Tailoring substrates for inkjet printing", in *The chemistry of inkjet inks*, 2009, pp. 73–97.

[113] E. Svanholm, *Printability and Ink-Coating Interactions in Inkjet Printing*. 2007.

[114] R. Torah, Y. Wei, Y. Li, K. Yang, S. Beeby, and J. Tudor, "Printed Textile-Based Electronic Devices", in *Handbook of Smart Textiles*, 2014, pp. 1–28.

[115] J. E. Morris, *Nanopackaging*. 2008.

[116] D. Soltman and V. Subramanian, "Inkjet-Printed Line Morphologies and Temperature Control of the Coffee Ring Effect", *Langmuir*, vol. 24, no. 5, pp. 2224–2231, 2008.

[117] M. Layani, M. Gruchko, O. Milo, I. Balberg, D. Azulay, and S. Magdassi, "Transparent conductive coatings by printing coffee ring arrays obtained at room temperature.", *ACS Nano*, vol. 3, no. 11, pp. 3537–42, Nov. 2009.

[118] D. J. Finn, M. Lotya, and J. N. Coleman, "Inkjet Printing of Silver Nanowire Networks", *ACS Appl. Mater. Interfaces*, vol. 7, no. 17, pp. 9254–9261, May 2015.

[119] H. Lu, J. Lin, N. Wu, S. Nie, *et al.*, "Inkjet printed silver nanowire network as top electrode for semi-transparent organic photovoltaic devices", *Appl. Phys. Lett.*, vol. 106, no. 9, p. 093302, Mar. 2015.

[120] A. Kamyshny and S. Magdassi, "Conductive Nanomaterials for Printed Electronics", *Small*, no. 17, 2014.

[121] National Center for Biotechnology Information, "Triethylene glycol monoethyl ether (CID=8190)", *PubChem Compound Database*. [Online]. Available: https://pubchem.ncbi.nlm.nih.gov/compound/triethylene_glycol_monoethyl_ether#section=Top. [Accessed: 23-Apr-2018].

[122] ANP Advanced Nano Products Ltd., "Silver Jet Ink | Nano-Silver Ink for Inkjet Printing | ANP Co., Ltd." [Online]. Available: http://anapro.com/eng/product/silver_inkjet_ink.html. [Accessed: 29-Sep-2014].

[123] Sigma Aldrich, "Silver, dispersion." [Online]. Available: http://www.sigmaaldrich.com/catalog/product/aldrich/736465?lang=de&region=DE. [Accessed: 13-Aug-2015].

[124] NovaCentrix, "Metalon ICI-002HV", 2012.

[125] S. Magdassi, Ed., *The Chemistry of Inkjet Inks*. The Hebrew University of Jerusalem, 2009.

[126] F. M. Smits, "Measurement of Sheet Resistivities with the Four-Point Probe", *Bell Syst. Tech. J.*, vol. 37, no. 3, pp. 711–718, May 1958.

[127] K. Schroder, S. C. McCool, W. F. Furlan, and K. Lane, "Broadcast Photonic Curing of Metallic Nanoparticle Films", *NSTI-Nanotech*, vol. 3, no. 512, pp. 198–201, 2006.

[128] D. Tobjörk, H. Aarnio, P. Pulkkinen, R. Bollström, *et al.*, "IR-sintering of ink-jet printed metal-nanoparticles on paper", *Thin Solid Films*, vol. 520, no. 7, pp. 2949–2955, Jan. 2012.

[129] S. Seipel, J. Yu, A. P. Periyasamy, M. Viková, M. Vik, and V. A. Nierstrasz, "Resource-Efficient Production of a Smart Textile UV Sensor Using Photochromic Dyes: Characterization and Optimization", in *Narrow and Smart Textiles*, Cham: Springer International Publishing, 2018, pp. 251–257.

[130] T. Gebel, L. Rebohle, R. Fendler, W. Hentsch, *et al.*, "Millisecond Annealing with Flashlamps: Tool and Process Challenges", in *2006 14th IEEE International Conference on Advanced Thermal Processing of Semiconductors*, 2006, pp. 47–55.

[131] J.-H. Kim, J. Choi, J. Bae, M. Kim, and T. Oh, "Thermoelectric Characteristics of n-Type Bi2Te3 and p-Type Sb2Te3 Thin Films Prepared by Co-Evaporation and Annealing for Thermopile Sensor Applications", *Mater. Trans.*, vol. 54, no. 4, pp. 618–625, 2013.

[132] X. Song, D. Wei, T. Sun, L. Yu, *et al.*, "A stably enhanced transparent conductive graphene film obtained using an air-annealing method", *Mater. Res. Express*, vol. 3, no. 8, p. 085003, Aug. 2016.

[133] J. Perelaer, C. E. Hendriks, A. W. M. de Laat, and U. S. Schubert, "One-step inkjet printing of conductive silver tracks on polymer substrates.", *Nanotechnology*, vol. 20, no. 16, p. 165303, Apr. 2009.

[134] B.-Y. Wang, T.-H. Yoo, Y.-W. Song, D.-S. Lim, and Y.-J. Oh, "Cu Ion Ink for a Flexible Substrate and Highly Conductive Patterning by Intensive Pulsed Light Sintering", *ACS Appl. Mater. Interfaces*, vol. 5, no. 10, pp. 4113–4119, May 2013.

[135] D. A. Pardo, G. E. Jabbour, and N. Peyghambarian, "Application of Screen Printing in the Fabrication of Organic Light-Emitting Devices", *Adv. Mater.*, vol. 12, no. 17, pp. 1249–1252, Sep. 2000.

[136] G. Korotcenkov, "Materials for Thick Film Technology," 2013, pp. 249–254.

[137] Sefar, *Siebdruck Handbuch*. 2006.

[138] S. Khan, L. Lorenzelli, and R. S. Dahiya, "Screen printed flexible pressure sensors skin", *ASMC (Advanced Semicond. Manuf. Conf. Proc.*, pp. 219–224, 2014.

[139] A. H. (Arthur H. Lefebvre, *Atomization and sprays*. Hemisphere Pub. Corp, 1989.

[140] E. J. Lavernia and Y. Wu, *Spray atomization and deposition*. John Wiley, 1996.

[141] M. R. Bobinger, "Solution-processing of Transparent Electrodes for Novel Electronic Devices", Technical University of Munich, 2018.

[142] M. Bobinger, D. Angeli, S. Colasanti, P. La Torraca, L. Larcher, and P. Lugli, "Infrared, transient thermal, and electrical properties of silver nanowire thin films for transparent heaters and energy-efficient coatings", *Phys. status solidi*, vol. 214, no. 1, p. 1600466, Jan. 2017.

[143] W. Cao, J. Li, H. Chen, and J. Xue, "Transparent electrodes for organic optoelectronic devices: a review", *J. Photonics Energy*, vol. 4, no. 1, p. 040990, Oct. 2014.

[144] A. Abdellah, A. Abdelhalim, M. Horn, G. Scarpa, and P. Lugli, "Scalable spray deposition process for high-performance carbon nanotube gas sensors", *IEEE Trans. Nanotechnol.*, vol. 12, no. 2, pp. 174–181, 2013.

[145] S. Wünscher, R. Abbel, J. Perelaer, and U. S. Schubert, "Progress of alternative sintering approaches of inkjet-printed metal inks and their application for manufacturing of flexible electronic devices", *J. Mater. Chem. C*, vol. 2, no. 48, pp. 10232–10261, 2014.

[146] J. Niittynen, "Comparison of Sintering Methods and Conductive Adhesives for Interconnections in Inkjet-Printed Flexible Electronics", 2015.

[147] J. Niittynen, E. Sowade, H. Kang, R. R. Baumann, and M. Mäntysalo, "Comparison of laser and intense pulsed light sintering (IPL) for inkjet-printed copper nanoparticle layers.", *Sci. Rep.*, vol. 5, p. 8832, Jan. 2015.

[148] S. H. Ko, H. Pan, C. P. Grigoropoulos, C. K. Luscombe, *et al.*, "All-inkjet-printed flexible electronics fabrication on a polymer substrate by low-temperature high-resolution selective laser sintering of metal nanoparticles", *Nanotechnology*, vol. 18, no. 34, p. 345202, Aug. 2007.

[149] J. Perelaer, R. Abbel, S. Wünscher, R. Jani, T. Van Lammeren, and U. S. Schubert, "Roll-to-roll compatible sintering of inkjet printed features by photonic and microwave exposure: From non-conductive ink to 40% bulk silver conductivity in less than 15 seconds", *Adv. Mater.*, vol. 24, no. 19, pp. 2620–2625, 2012.

[150] Y. Galagan, E. W. C. Coenen, R. Abbel, T. Van Lammeren, *et al.*, "Photonic sintering of inkjet printed current collecting grids for organic solar cell applications", *Org. Electron.*, vol. 14, no. 1, pp. 38–46, Jan. 2013.

[151] V. Akhavan, K. Schroder, D. Pope, and S. Farnsworth, "Processing thick-film screen printed Metalon® CuO reduction ink with PulseForge® tools", 2013.

[152] E. Sowade, H. Kang, K. Y. Mitra, O. J. Weiß, J. Weber, and R. R. Baumann, "Roll-to-roll infrared (IR) drying and sintering of an inkjet-printed silver nanoparticle ink within 1 second", *J. Mater. Chem. C*, vol. 3, no. 45, pp. 11815–11826, Nov. 2015.

[153] C. Gaspar, S. Passoja, J. Olkkonen, and M. Smolander, "IR-sintering efficiency on inkjet-printed conductive structures on paper substrates", *Microelectron. Eng.*, vol. 149, pp. 135–140, 2016.

[154] D. Zhai, T. Zhang, J. Guo, X. Fang, and J. Wei, "Water-based ultraviolet curable conductive inkjet ink containing silver nano-colloids for flexible electronics", *Colloids Surfaces A Physicochem. Eng. Asp.*, vol. 424, pp. 1–9, May 2013.

[155] B. C. Riggs, R. Elupula, V. S. Puli, S. M. Grayson, and D. B. Chrisey, "Dielectric Properties of UV Cured Thick Film Polymer Networks through High Power Xenon Flash Lamp Curing", *MRS Proc.*, vol. 1630, pp. mrsf13-1630-o06-38, Jan. 2014.

[156] M. L. Allen, M. Aronniemi, T. Mattila, A. Alastalo, *et al.*, "Electrical sintering of nanoparticle structures.", *Nanotechnology*, vol. 19, no. 17, p. 175201, Apr. 2008.

[157] J. Perelaer, B.-J. de Gans, and U. S. Schubert, "Ink-jet Printing and Microwave Sintering of Conductive Silver Tracks", *Adv. Mater.*, vol. 18, no. 16, pp. 2101–2104, Aug. 2006.

[158] J. Perelaer, M. Klokkenburg, C. E. Hendriks, and U. S. Schubert, "Microwave flash sintering of inkjet-printed silver tracks on polymer substrates", *Adv. Mater.*, vol. 21, no. 47, pp. 4830–4834, 2009.

[159] I. Reinhold, C. E. Hendriks, R. Eckardt, J. M. Kranenburg, *et al.*, "Argon plasma sintering of inkjet printed silver tracks on polymer substrates", *J. Mater. Chem.*, vol. 19, no. 21, p. 3384, 2009.

[160] J. Niittynen, R. Abbel, M. Mäntysalo, J. Perelaer, U. S. Schubert, and D. Lupo, "Alternative sintering methods compared to conventional thermal sintering for inkjet printed silver nanoparticle ink", *Thin Solid Films*, vol. 556, pp. 452–459, Apr. 2014.

[161] S. Magdassi, M. Grouchko, O. Berezin, and A. Kamyshny, "Triggering the sintering of silver nanoparticles at room temperature", *ACS Nano*, vol. 4, no. 4, pp. 1943–8, Apr. 2010.

[162] D. Wakuda, M. Hatamura, and K. Suganuma, "Novel Room Temperature Wiring Process of Ag Nanoparticle Paste", in *Polytronic 2007 - 6th International Conference on Polymers and Adhesives in Microelectronics*

and Photonics, 2007, pp. 110–113.

[163] H. Andersson, A. Manuilskiy, C. Lidenmark, J. Gao, *et al.*, "The influence of paper coating content on room temperature sintering of silver nanoparticle ink", *Nanotechnology*, vol. 24, no. 45, p. 455203, Nov. 2013.

[164] J. Perelaer, P. J. Smith, D. Mager, D. Soltman, *et al.*, "Printed electronics: the challenges involved in printing devices, interconnects, and contacts based on inorganic materials", *J. Mater. Chem.*, vol. 20, no. 39, p. 8446, Sep. 2010.

[165] I. Reinhold, M. Müller, M. Müller, W. Voit, and W. Zapka, "Spectrally Enhanced Photonic Sintering", in *NIP & Digital Fabrication Conference*, 2012, pp. 424–430.

[166] S. Farnsworth and K. Schroder, "Photonic curing for Millisecond-drying of thin films", *Spec. Print. Worldw.*, no. 4, pp. 34–35, 2012.

[167] I. Reinhold, W. Voit, I. Rawson, K. Martin, *et al.*, "Novel Developments in Photonic Sintering of Inkjet Printed Functional Inks", *Int. Conf. Non Impact Print. Digit. Fabr.*, pp. 2–4, 2013.

[168] R. Abbel, T. van Lammeren, R. Hendriks, J. Ploegmakers, *et al.*, "Photonic flash sintering of silver nanoparticle inks: a fast and convenient method for the preparation of highly conductive structures on foil", *MRS Commun.*, vol. 2, no. 04, pp. 145–150, Dec. 2012.

[169] H.-J. Hwang, W.-H. Chung, and H.-S. Kim, "*In situ* monitoring of flash-light sintering of copper nanoparticle ink for printed electronics", *Nanotechnology*, vol. 23, no. 48, p. 485205, Dec. 2012.

[170] M. J. Guillot, S. C. McCool, and K. A. Schroder, "Simulating the Thermal Response of Thin Films During Photonic Curing", in *Volume 7: Fluids and Heat Transfer, Parts A, B, C, and D*, 2012, p. 19.

[171] W.-H. Chung, H.-J. Hwang, and H.-S. Kim, "Flash light sintered copper precursor/nanoparticle pattern with high electrical conductivity and low porosity for printed electronics", *Thin Solid Films*, vol. 580, pp. 61–70, Mar. 2015.

[172] S. Park, S. Jang, D.-J. Lee, J. Oh, and H.-S. Kim, "Two-step flash light sintering process for crack-free inkjet-printed Ag films", *J. Micromechanics Microengineering*, vol. 23, no. 1, p. 015013, 2013.

[173] S. Farnsworth, V. Akhavan, K. Schroder, D. Pope, and I. Rawson, "Reacting Thick-Film Nano-Copper Conductive Inks with Photonic Curing", 2013.

[174] K. Eun, M.-W. Chon, T.-H. Yoo, Y.-W. Song, and S.-H. Choa, "Electromechanical properties of printed copper ink film using a white flash light annealing process for flexible electronics", *Microelectron. Reliab.*, vol. 55, no. 5, pp. 838–845, Apr. 2015.

[175] C. Paquet, R. James, A. J. Kell, O. Mozenson, *et al.*, "Photosintering and electrical performance of CuO nanoparticle inks", *Org. Electron.*, vol. 15, no. 8, pp. 1836–1842, Aug. 2014.

[176] S.-H. Park and H.-S. Kim, "Flash light sintering of nickel nanoparticles for printed electronics", *Thin Solid Films*, vol. 550, pp. 575–581, Jan. 2014.

[177] D. D. Liana, B. Raguse, L. Wieczorek, G. R. Baxter, *et al.*, "Sintered gold nanoparticles as an electrode material for paper-based electrochemical sensors", *RSC Adv.*, vol. 3, no. 23, p. 8683, May 2013.

[178] D. K. Jackson, K. A. Schroder, and S. C. McCool, "Apparatus for curing thin films on a moving substrate", US20110247851A1, 07-Apr-2011.

[179] K. A. Schroder, I. M. Rawson, S. C. McCool, A. E. Edd, and R. I. Dass, "Method for Drying Thin Films in an Energy Efficient Manner", US20120255192A1, 28-Mar-2012.

[180] Seigi Suh, "Photonic sintering of a polymer thick film copper conductor composition", US9637647B2, 23-Sep-2015.

[181] D. Mitra, K. Y. Mitra, M. Hartwig, and R. R. Baumann, "Intense Pulsed Light Sintering of an Inkjet Printed Silver Nanoparticle Ink Depending on the Spectral Absorption and Reflection of the Background", *J. Imaging Sci. Technol.*, vol. 60, no. 4, pp. 404031–404035, Jul. 2016.

[182] M. N. Rahaman, *Ceramic processing and sintering*. M. Dekker, 2003.

[183] W. D. Kingery and M. Berg, "Study of the initial stages of sintering solids by viscous flow, evaporation-condensation, and self-diffusion", *J. Appl. Phys.*, vol. 26, no. 10, pp. 1205–1212, Oct. 1955.

[184] J. C. Kim, K. H. Auh, and D. M. Martin, "Multi-level particle packing model of ceramic agglomerates", *Model. Simul. Mater. Sci. Eng.*, vol. 8, no. 2, pp. 159–168, Mar. 2000.

[185] M. A. Asoro, J. Damiano, and P. J. Ferreira, "Size effects on the melting temperature of silver nanoparticles: In-situ TEM observations", *Microsc. Microanal.*, vol. 15, no. SUPPL. 2, pp. 706–707, 2009.

[186] C. C. Yang and S. Li, "Size-Dependent Phase Stability of Silver Nanocrystals", *J. Phys. Chem. C*, vol. 112, no. 42, pp. 16400–16404, Oct. 2008.

[187] P. Buffat and J. P. Borel, "Size effect on the melting temperature of gold particles", *Phys. Rev. A*, vol. 13, no. 6, pp. 2287–2298, Jun. 1976.

[188] S. L. Lai, J. Y. Guo, V. Petrova, G. Ramanath, and L. H. Allen, "Size-dependent melting properties of small tin particles: Nanocalorimetric measurements", *Phys. Rev. Lett.*, vol. 77, no. 1, pp. 99–102, Jul. 1996.

[189] H.-S. Kim, S. R. Dhage, D.-E. Shim, and H. T. Hahn, "Intense pulsed light sintering of copper nanoink for

printed electronics", *Appl. Phys. A*, vol. 97, no. 4, pp. 791–798, Aug. 2009.

[190] J. S. Kang, J. Ryu, H. S. Kim, and H. T. Hahn, "Sintering of inkjet-printed silver nanoparticles at room temperature using intense pulsed light", *J. Electron. Mater.*, vol. 40, no. 11, pp. 2268–2277, Nov. 2011.

[191] M. J. Mayo, "Processing of nanocrystalline ceramics from ultrafine particles", *Int. Mater. Rev.*, vol. 41, no. 3, pp. 85–115, Jan. 1996.

[192] M. F. Ashby, "First Report on Sintering Diagrams", *Acta Metall.*, vol. 22, no. 3, pp. 275–289, 1974.

[193] T. Enz, "Phasenentwicklung und thermische Stabilität von Nanokompositen des Systems Sm2O3-MgO", Technische Universität Darmstadt, 2009.

[194] A. Albrecht, "Ultra-Low-Cost and Rapid Production of Inkjet-Printed Conductive Patterns using Silver Inks and Copper Oxide Inks", in *Printing Future Days 2015: Proceedings of the 6th International Scientific Conference on Print and Media Technology for Junior Scientists and PhD Students*, 2015, pp. 19–24.

[195] M. Klokkenburg, G. T. van Heck, E. Rubingh, T. J. Van Lammeren, and H. A. J. M. Andriessen, "Device and a method for curing patterns of a substance at a surface of a foil", 12-Mar-2013.

[196] G. Oms-Oliu, O. Martín-Belloso, and R. Soliva-Fortuny, "Pulsed Light Treatments for Food Preservation. A Review", *Food Bioprocess Technol.*, vol. 3, no. 1, pp. 13–23, Feb. 2010.

[197] N. L. Schoenewolf, M. J. Barysch, and R. Dummer, "Intense pulsed light.", *Curr. Probl. Dermatol.*, vol. 42, pp. 166–72, 2011.

[198] P. H. Bitter, "Noninvasive Rejuvenation of Photodamaged Skin Using Serial, Full-Face Intense Pulsed Light Treatments", *Dermatologic Surg.*, vol. 26, no. 9, pp. 835–843, Sep. 2000.

[199] S. Magdassi, M. Grouchko, and A. Kamyshny, "Copper Nanoparticles for Printed Electronics: Routes Towards Achieving Oxidation Stability", *Materials (Basel).*, vol. 3, no. 9, pp. 4626–4638, Sep. 2010.

[200] J. Ryu, H.-S. Kim, and H. T. Hahn, "Reactive Sintering of Copper Nanoparticles Using Intense Pulsed Light for Printed Electronics", *J. Electron. Mater.*, vol. 40, no. 1, pp. 42–50, Sep. 2010.

[201] J. Jiu, T. Sugahara, M. Nogi, T. Araki, *et al.*, "High-intensity pulse light sintering of silver nanowire transparent films on polymer substrates: the effect of the thermal properties of substrates on the performance of silver films", *Nanoscale*, vol. 5, no. 23, p. 11820, Nov. 2013.

[202] J. Jiu, M. Nogi, T. Sugahara, T. Tokuno, *et al.*, "Strongly adhesive and flexible transparent silver nanowire conductive films fabricated with a high-intensity pulsed light technique", *J. Mater. Chem.*, vol. 22, no. 44, p. 23561, Oct. 2012.

[203] D. S. Hecht, L. Hu, and G. Irvin, "Emerging transparent electrodes based on thin films of carbon nanotubes, graphene, and metallic nanostructures", *Advanced Materials*, vol. 23, no. 13. WILEY-VCH Verlag, pp. 1482–1513, 05-Apr-2011.

[204] Y. Leterrier, L. Médico, F. Demarco, J.-A. E. Månson, *et al.*, "Mechanical integrity of transparent conductive oxide films for flexible polymer-based displays", *Thin Solid Films*, vol. 460, no. 1–2, pp. 156–166, Jul. 2004.

[205] A. Axelevitch, B. Gorenstein, and G. Golan, "Investigation of Optical Transmission in Thin Metal Films", *Phys. Procedia*, vol. 32, pp. 1–13, Jan. 2012.

[206] A. J. Morfa, E. M. Akinoglu, J. Subbiah, M. Giersig, and P. Mulvaney, "Transparent metal electrodes from ordered nanosphere arrays", *J. Appl. Phys.*, vol. 114, no. 5, p. 054502, Aug. 2013.

[207] Y. Wang, C. Zhu, R. Pfattner, H. Yan, *et al.*, "A highly stretchable, transparent, and conductive polymer.", *Sci. Adv.*, vol. 3, no. 3, p. e1602076, Mar. 2017.

[208] P. D. Angelo, "Inkjet-Printed Light-Emitting Devices : Applying Inkjet Microfabrication to Multilayer Electronics", University of Toronto, 2013.

[209] J. Tokarský, L. Kulhánková, K. M. Kutláková, P. Peikertová, *et al.*, "Monitoring conductivity and optical homogeneity during the growth of polyaniline thin films", *Thin Solid Films*, vol. 537, pp. 58–64, 2013.

[210] J. Jang, J. Ha, and J. Cho, "Fabrication of water-dispersible polyaniline-poly(4-styrenesulfonate) nanoparticles for inkjet-printed chemical-sensor applications", *Adv. Mater.*, vol. 19, no. 13, pp. 1772–1775, 2007.

[211] B. Chen, T. Cui, Y. Liu, and K. Varahramyan, "All-polymer RC filter circuits fabricated with inkjet printing technology", *Solid. State. Electron.*, vol. 47, no. 5, pp. 841–847, May 2003.

[212] G. Eda, G. Fanchini, and M. Chhowalla, "Large-area ultrathin films of reduced graphene oxide as a transparent and flexible electronic material", *Nat. Nanotechnol.*, vol. 3, no. 5, pp. 270–274, May 2008.

[213] V. C. Tung, M. J. Allen, Y. Yang, and R. B. Kaner, "High-throughput solution processing of large-scale graphene", *Nat. Nanotechnol.*, vol. 4, no. 1, pp. 25–29, Jan. 2009.

[214] K. S. K. S. Kim, Y. Zhao, H. Jang, S. Y. Lee, *et al.*, "Large-scale pattern growth of graphene films for stretchable transparent electrodes", *Nature*, vol. 457, no. 7230, pp. 706–710, Feb. 2009.

[215] M. Bobinger, J. Mock, P. La Torraca, M. Becherer, P. Lugli, and L. Larcher, "Tailoring the Aqueous Synthesis and Deposition of Copper Nanowires for Transparent Electrodes and Heaters", *Adv. Mater. Interfaces*, p. 1700568, Aug. 2017.

[216] D. Langley, G. Giusti, C. Mayousse, C. Celle, D. Bellet, and J. P. Simonato, "Flexible transparent conductive materials based on silver nanowire networks: A review", *Nanotechnology*, vol. 24, no. 45, p. 452001, Nov. 2013.

[217] Z. Wu, Z. Chen, X. Du, J. M. Logan, *et al.*, "Transparent, conductive carbon nanotube films", *Science (80-.).*, vol. 305, no. 5688, pp. 1273–1276, 2004.

[218] T. M. Barnes and J. L. Blackburn, "Carbon Nanotube Transparent Electrodes", in *Transparent Electronics*, Chichester, UK: John Wiley & Sons, Ltd, 2010, pp. 185–211.

[219] M. Bobinger, V. Dergianlis, A. Albrecht, M. Haider, *et al.*, "Solution processing of silver nanowires for transparent heaters and flexible electronics", in *PRIME 2017 - 13th Conference on PhD Research in Microelectronics and Electronics, Proceedings*, 2017, pp. 9–12.

[220] K. Ellmer, "Past achievements and future challenges in the development of optically transparent electrodes", *Nat. Photonics*, vol. 6, no. 12, pp. 809–817, Dec. 2012.

[221] E. Bonderover and S. Wagner, "A woven inverter circuit for e-textile applications", *IEEE Electron Device Letters*, vol. 25, no. 5. pp. 295–297, May-2004.

[222] S. Jung, C. Lauterbach, M. Strasser, and W. Weber, "Enabling technologies for disappearing electronics in smart textiles", *2003 IEEE Int. Solid-State Circuits Conf. 2003. Dig. Tech. Pap. ISSCC.*, vol. 1, pp. 386–387, 2003.

[223] D. Marculescu, R. Marculescu, N. H. Zamora, P. Stanley-Marbell, *et al.*, "Electronic textiles: A platform for pervasive computing", in *Proceedings of the IEEE*, 2003, vol. 91, no. 12, pp. 1995–2016.

[224] Y. Kim, H. Kim, and H. J. Yoo, "Electrical characterization of screen-printed circuits on the fabric", *IEEE Trans. Adv. Packag.*, vol. 33, no. 1, pp. 196–205, Feb. 2010.

[225] J. Edmison, M. Jones, Z. Nakad, and T. Martin, "Using piezoelectric materials for wearable electronic textiles", in *Proceedings - International Symposium on Wearable Computers, ISWC*, 2002, vol. 2002–Janua, pp. 41–48.

[226] E. R. Post, M. Orth, P. R. Russo, and N. Gershenfeld, "E-broidery: Design and fabrication of textile-based computing", *IBM Syst. J.*, vol. 39, no. 3.4, pp. 840–860, 2000.

[227] J. Kaufmann, Y. Kyosev, H. Rabe, K. Gustke, and H. Cebulla, "Investigation of the Elastic Properties of Weft-Knitted Metal-Reinforced Narrow Composites", in *Narrow and Smart Textiles*, Cham: Springer International Publishing, 2018, pp. 49–57.

[228] Y. Kyosev, B. Mahltig, and A. Schwarz-Pfeiffer, *Narrow and Smart Textiles*. Cham: Springer International Publishing, 2018.

[229] T. M. Seeberg, A. Royset, S. Jahren, and F. Strisland, "Printed organic conductive polymers thermocouples in textile and smart clothing applications", *Proc. Annu. Int. Conf. IEEE Eng. Med. Biol. Soc. EMBS*, no. 0314, pp. 3278–3281, 2011.

[230] W. G. Whittow, A. Chauraya, J. C. Vardaxoglou, Y. Li, *et al.*, "Inkjet-printed microstrip patch antennas realized on textile for wearable applications", *IEEE Antennas Wirel. Propag. Lett.*, vol. 13, pp. 71–74, 2014.

[231] T. Öhlund, "Coated Surfaces for Inkjet-Printed Conductors", Mid Sweden University, 2012.

[232] A. Chauraya, W. G. Whittow, J. C. Vardaxoglou, Y. Li, *et al.*, "Inkjet printed dipole antennas on textiles for wearable communications", *IET Microwaves, Antennas Propag.*, vol. 7, no. 9, pp. 760–767, Jun. 2013.

[233] L. M. Castano and A. B. Flatau, "Smart fabric sensors and e-textile technologies: a review", *Smart Mater. Struct.*, vol. 23, no. 5, p. 053001, May 2014.

[234] W. Weng, P. Chen, S. He, X. Sun, and H. Peng, "Smart electronic textiles", *Angewandte Chemie - International Edition*, vol. 55, no. 21. 2016.

[235] T. Q. Trung and N. E. Lee, "Recent Progress on Stretchable Electronic Devices with Intrinsically Stretchable Components", *Adv. Mater.*, vol. 29, no. 3, 2017.

[236] D.-H. H. Kim, J. Xiao, J. Song, Y. Huang, and J. A. Rogers, "Stretchable, curvilinear electronics based on inorganic materials", *Adv. Mater.*, vol. 22, no. 19, pp. 2108–2124, Jan. 2010.

[237] J. Song, H. Jiang, Y. Huang, and J. A. Rogers, "Mechanics of stretchable inorganic electronic materials", *J. Vac. Sci. Technol. A Vacuum, Surfaces, Film.*, vol. 27, no. 5, pp. 1107–1125, Sep. 2009.

[238] H. Jiang, D.-Y. D.-Y. Khang, J. Song, Y. Sun, Y. Huang, and J. A. Rogers, "Finite deformation mechanics in buckled thin films on compliant supports", *Proc. Natl. Acad. Sci.*, vol. 104, no. 40, pp. 15607–15612, Oct. 2007.

[239] N. Bowden, S. Brittain, A. G. Evans, J. W. Hutchinson, and G. M. Whitesides, "Spontaneous formation of ordered structures in thin films of metals supported on an elastomeric polymer", *Nature*, vol. 393, no. May, pp. 146–149, May 1998.

[240] S. P. S. P. Lacour, S. Wagner, Z. Huang, and Z. Suo, "Stretchable gold conductors on elastomeric substrates", *Appl. Phys. Lett.*, vol. 82, no. 15, pp. 2404–2406, Apr. 2003.

[241] E.-H. Ko, H.-J. Kim, S.-M. Lee, T.-W. Kim, and H.-K. Kim, "Stretchable Ag electrodes with mechanically tunable optical transmittance on wavy-patterned PDMS substrates.", *Sci. Rep.*, vol. 7, p. 46739, Apr. 2017.

[242] D. Y. Khang, H. Jiang, Y. Huang, and J. A. Rogers, "A stretchable form of single-crystal silicon for high-performance electronics on rubber subtrates", *Science (80-.).*, vol. 311, no. 5758, pp. 208–212, Jan. 2006.

[243] T. Sekitani and T. T. Someya, "Stretchable, large-area organic electronics", *Adv. Mater.*, vol. 22, no. 20, pp. 2228–2246, May 2010.

[244] N. Matsuhisa, D. Inoue, P. Zalar, H. Jin, *et al.*, "Printable elastic conductors by in situ formation of silver nanoparticles from silver flakes", *Nat. Mater.*, vol. 16, no. May, p. DOI: 10.1038/NMAT4904, 2017.

[245] Y. Kim, J. Zhu, B. Yeom, M. Di Prima, *et al.*, "Stretchable nanoparticle conductors with self-organized conductive pathways", *Nature*, vol. 500, no. 7460, pp. 59–63, 2013.

[246] A. Larmagnac, S. Eggenberger, H. Janossy, and J. Vörös, "Stretchable electronics based on Ag-PDMS composites", *Sci. Rep.*, vol. 4, p. 7254, Dec. 2014.

[247] N. Matsuhisa, M. Kaltenbrunner, T. Yokota, H. Jinno, *et al.*, "Printable elastic conductors with a high conductivity for electronic textile applications", *Nat. Commun.*, vol. 6, 2015.

[248] H. A. Kim, M. S. Kim, S. Y. Chun, Y. H. Park, *et al.*, "Characteristics of electrically conducting polymer-coated textiles", *Mol. Cryst. Liq. Cryst.*, vol. 405, no. 1, pp. 161–169, Jan. 2003.

[249] D.-H. Kim, K.-C. Yu, Y. Kim, and J.-W. Kim, "Highly Stretchable and Mechanically Stable Transparent Electrode Based on Composite of Silver Nanowires and Polyurethane–Urea", *ACS Appl. Mater. Interfaces*, vol. 7, no. 28, pp. 15214–15222, Jul. 2015.

[250] N. Liu, A. Chortos, T. Lei, L. Jin, *et al.*, "Ultratransparent and stretchable graphene electrodes.", *Sci. Adv.*, vol. 3, no. 9, p. e1700159, Sep. 2017.

[251] T. Sekitani, Y. Noguchi, K. Hata, T. Fukushima, T. Aida, and T. Someya, "A Rubberlike Stretchable Active Matrix Using Elastic Conductors", *Science (80-.).*, vol. 321, no. 5895, pp. 1468–1472, 2008.

[252] J. A. Rogers, T. Someya, and Y. Huang, "Materials and Mechanics for Stretchable Electronics", *Science (80-.).*, vol. 327, no. 5973, pp. 1603–1607, 2010.

[253] A. L. Skov and P. Sommer-Larsen, "Phyiscal and Chemical Properties of Dielectric Elastomers", in *Dielectric Elastomers as Electromechanical Transducers*, Elsevier, 2008, pp. 25–32.

[254] A. K. Bhowmick and H. L. Stephens, *Handbook of elastomers*. M. Dekker, 2001.

[255] T. K. Kim, J. K. Kim, and O. C. Jeong, "Measurement of nonlinear mechanical properties of PDMS elastomer", in *Microelectronic Engineering*, 2011, vol. 88, no. 8, pp. 1982–1985.

[256] W. T. S. Huck, N. Bowden, P. Onck, T. Pardoen, J. W. Hutchinson, and G. M. Whitesides, "Ordering of spontaneously formed buckles on planar surfaces", *Langmuir*, vol. 16, no. 7, pp. 3497–3501, 2000.

[257] S. El-Molla, A. Albrecht, E. Cagatay, P. Mittendorfer, *et al.*, "Integration of a Thin Film PDMS-Based Capacitive Sensor for Tactile Sensing in an Electronic Skin", *J. Sensors*, vol. 2016, 2016.

[258] J. N. Lee, C. Park, and G. M. Whitesides, "Solvent Compatibility of Poly(dimethylsiloxane)-Based Microfluidic Devices", *Anal. Chem.*, vol. 75, no. 23, pp. 6544–6554, 2003.

[259] T. Lindvig, M. L. Michelsen, and G. M. Kontogeorgis, "A Flory-Huggins model based on the Hansen solubility parameters", *Fluid Phase Equilib.*, vol. 203, no. 1–2, pp. 247–260, 2002.

[260] C. M. Hansen, *Hansen Solubility Parameters: A User's Handbook, Second Edition*, vol. 2. CRC Press, 2007.

[261] J. Van Den Brand, M. De Kok, M. Koetse, M. Cauwe, *et al.*, "Flexible and stretchable electronics for wearable health devices", *Solid. State. Electron.*, vol. 113, pp. 116–120, Nov. 2015.

[262] S. P. Lacour, S. Wagner, R. J. Narayan, T. Li, and Z. Suo, "Stiff subcircuit islands of diamondlike carbon for stretchable electronics", *J. Appl. Phys.*, vol. 100, no. 1, p. 014913, Jul. 2006.

[263] J. Lee, J. Wu, J. H. Ryu, Z. Liu, *et al.*, "Stretchable Semiconductor Technologies with High Areal Coverages and Strain-Limiting Behavior: Demonstration in High-Efficiency Dual-Junction GaInP/GaAs Photovoltaics", *Small*, vol. 8, no. 12, pp. 1851–1856, Jun. 2012.

[264] M. Senthilkumar and N. Anbumani, "Dynamics of Elastic Knitted Fabrics for Sports Wear", *J. Ind. Text.*, vol. 41, no. 1, pp. 13–24, Jul. 2011.

[265] A. Kaneko, N. Asai, and T. Kanda, "The influence of age on pressure perception of static and moving two-point discrimination in normal subjects", *J. Hand Ther.*, vol. 18, no. 4, pp. 421–425, Oct. 2005.

[266] E. H. Weber, H. E. (Helen E. Ross, D. J. Murray, E. H. Weber, E. H. Weber, and Experimental Psychology Society., *E.H. Weber on the tactile senses*. Erlbaum (UK) Taylor & Francis, 1996.

[267] W. Tiest and A. Kappers, "Haptic perception of force", *Scholarpedia*, vol. 10, no. 4, p. 32732, 2015.

[268] C. Becker-Carus and M. Wendt, "Wahrnehmung", in *Allgemeine Psychologie Eine Einführung*, hEIDELBERG: Springer-Verlag, 2017, pp. 75–150.

[269] R. S. Dahiya, G. Metta, M. Valle, and G. Sandini, "Tactile sensing-from humans to humanoids", *IEEE Trans. Robot.*, vol. 26, no. 1, pp. 1–20, 2010.

[270] M. R. Cutkosky, R. D. Howe, and W. R. Provancher, "19. Force and Tactile Sensors", *Springer Handb. Robot.*, pp. 455–476, 2008.

[271] R. S. Dahiya and M. Valle, *Robotic tactile sensing : technologies and system*. Springer, 2013.

[272] J. Castellanos-Ramos, R. Navas-González, H. Macicior, T. Sikora, E. Ochoteco, and F. Vidal-Verdú, "Tactile sensors based on conductive polymers", *Microsyst. Technol.*, vol. 16, no. 5, pp. 765–776, May 2010.

[273] L. Wang, F. Ma, Q. Shi, H. Liu, and X. Wang, "Study on compressive resistance creep and recovery of flexible pressure sensitive material based on carbon black filled silicone rubber composite", *Sensors Actuators A Phys.*, vol. 165, no. 2, pp. 207–215, Feb. 2011.

[274] Y. Ishigure, S. Iijima, H. Ito, T. Ota, *et al.*, "Electrical and elastic properties of conductor-polymer composites", *J. Mater. Sci.*, vol. 34, no. 12, pp. 2979–2985, 1999.

[275] N. Witt, Y. Tang, L. Ye, and L. Fang, "Silicone rubber nanocomposites containing a small amount of hybrid fillers with enhanced electrical sensitivity", *Mater. Des.*, vol. 45, pp. 548–554, Mar. 2013.

[276] X. Z. Niu, S. L. Peng, L. Y. Liu, W. J. Wen, and P. Sheng, "Characterizing and Patterning of PDMS-Based Conducting Composites", *Adv. Mater.*, vol. 19, no. 18, pp. 2682–2686, Sep. 2007.

[277] J.-B. Lee and D.-Y. Khang, "Electrical and mechanical characterization of stretchable multi-walled carbon nanotubes/polydimethylsiloxane elastomeric composite conductors", *Compos. Sci. Technol.*, vol. 72, no. 11, pp. 1257–1263, Jun. 2012.

[278] L. Wang, X. Wang, and Y. Li, "Relation between repeated uniaxial compressive pressure and electrical resistance of carbon nanotube filled silicone rubber composite", *Compos. Part A Appl. Sci. Manuf.*, vol. 43, no. 2, pp. 268–274, Feb. 2012.

[279] D. J. Lipomi, M. Vosgueritchian, B. C.-K. Tee, S. L. Hellstrom, *et al.*, "Skin-like pressure and strain sensors based on transparent elastic films of carbon nanotubes", *Nat. Nanotechnol.*, vol. 6, no. 12, pp. 788–792, Dec. 2011.

[280] Interlink Electronics, "Data Sheets | Standard Products." [Online]. Available: https://www.interlinkelectronics.com/data-sheets. [Accessed: 15-Feb-2018].

[281] B. Krivopal, "Pressure sensitive ink means, and methods of use", EP0871681B1, 1996.

[282] "Tekscan Technology." [Online]. Available: https://www.tekscan.com/tekscan-technology. [Accessed: 15-Feb-2018].

[283] W. Y. Chang, T. H. Fang, H. J. Lin, Y. T. Shen, and Y. C. Lin, "A large area flexible array sensors using screen printing technology", *IEEE/OSA J. Disp. Technol.*, vol. 5, no. 6, pp. 178–183, 2009.

[284] C. Chiang, C. K. Lin, M.-S. Ju, C.-C. K. Lin, and M.-S. Ju, "An implantable capacitive pressure sensor for biomedical applications", *Sensors Actuators A Phys.*, vol. 134, no. 2, pp. 382–388, 2007.

[285] I. D. Johnston, D. K. McCluskey, C. K. L. Tan, and M. C. Tracey, "Mechanical characterization of bulk Sylgard 184 for microfluidics and microengineering", *J. Micromechanics Microengineering*, vol. 24, no. 3, p. 035017, Mar. 2014.

[286] A. Ali, M. Hosseini, B. B. Sahari, A. Ali, M. Hosseini, and B. B. Sahari, "A Review of Constitutive Models for Rubber-Like Materials", *Am. J. Eng. Appl. Sci.*, vol. 3, no. 1, pp. 232–239, Jan. 2010.

[287] S. C. B. Mannsfeld, B. C.-K. Tee, R. M. Stoltenberg, C. V. H.-H. Chen, *et al.*, "Highly sensitive flexible pressure sensors with microstructured rubber dielectric layers.", *Nat. Mater.*, vol. 9, no. 10, pp. 859–64, 2010.

[288] C. L. Choong, M. B. Shim, B. S. Lee, S. Jeon, *et al.*, "Highly stretchable resistive pressure sensors using a conductive elastomeric composite on a micropyramid array", *Adv. Mater.*, vol. 26, no. 21, pp. 3451–3458, Jun. 2014.

[289] R. J. Young and P. A. Lovell, *Introduction to Polymers*. CRC Press, 2011.

[290] Z. Wang, "Polydimethylsiloxane Mechanical Properties Measured by Macroscopic Compression and Nanoindentation Techniques", p. 68, 2011.

[291] Z. Wang, A. A. Volinsky, and N. D. Gallant, "Crosslinking effect on polydimethylsiloxane elastic modulus measured by custom-built compression instrument", *J. Appl. Polym. Sci.*, vol. 131, no. 22, p. n/a-n/a, Nov. 2014.

[292] K. K. Kärkkäinen, A. H. Sihvola, and K. I. Hikoskinen, "Effective permittivity of mixtures: numerical validation by the FDTD method", *IEEE Trans. Geosci. Remote Sens.*, vol. 38, no. 3, pp. 1303–1308, May 2000.

[293] D. Maddipatla, B. B. Narakathu, M. M. Ali, A. A. Chlaihawi, and M. Z. Atashbar, "Development of a novel carbon nanotube based printed and flexible pressure sensor", in *SAS 2017 - 2017 IEEE Sensors Applications Symposium, Proceedings*, 2017, pp. 1–4.

[294] E. Cagatay, P. Kohler, P. Lugli, A. Abdellah, *et al.*, "Flexible capacitive tactile sensors based on carbon nanotube thin films", *IEEE Sens. J.*, vol. 15, no. 6, pp. 3225–3233, 2015.

[295] A. Albrecht, M. Trautmann, M. Becherer, P. Lugli, and A. Rivadeneyra, "Multi-Layer Printed Shear Force Sensor on Flexible Substrates", in *ALLSENSORS 2018, The Third International Conference on Advances in Sensors, Actuators, Metering and Sensing*, 2018, pp. 70–75.

[296] T. A. T. A. Chase and R. C. R. C. Luo, "A thin-film flexible capacitive tactile normal/shear force array sensor", in *Proceedings of IECON '95 - 21st Annual Conference on IEEE Industrial Electronics*, 1995, vol. 2, pp. 1196–1201.

[297] J. A. Dobrzynska and M. A. M. Gijs, "Polymer-based flexible capacitive sensor for three-axial force measurements", *J. Micromechanics Microengineering*, vol. 23, no. 1, p. 015009, Jan. 2013.

[298] J. E. Mark, *Polymer data handbook*. Oxford University Press, 2009.

[299] M. Zirkl, B. Stadlober, M. Haller, P. Greindl, and C. Rendl, "Printed piezoelectric pressure sensing foil", US9612690B2, 04-Sep-2012.

[300] S. B. B. Riffat and X. Ma, "Thermoelectrics: A review of present and potential applications", *Appl. Therm. Eng.*, vol. 23, no. 8, pp. 913–935, Jun. 2003.

[301] E. Shapira, D. Marchak, A. Tsukernik, and Y. Selzer, "Segmented metal nanowires as nanoscale thermocouples", *Nanotechnology*, vol. 19, no. 12, p. 125501, 2008.

[302] T. Akter and W. S. Kim, "Reversibly Stretchable Transparent Conductive Coatings of Spray-Deposited Silver Nanowires", *ACS Appl. Mater. Interfaces*, vol. 4, no. 4, pp. 1855–1859, Apr. 2012.

[303] J.-W. Song, J. Kim, Y.-H. Yoon, B.-S. Choi, J.-H. Kim, and C.-S. Han, "Inkjet printing of single-walled carbon nanotubes and electrical characterization of the line pattern", *Nanotechnology*, vol. 19, no. 9, p. 095702, Mar. 2008.

[304] J. Liang, K. Tong, and Q. Pei, "A Water-Based Silver-Nanowire Screen-Print Ink for the Fabrication of Stretchable Conductors and Wearable Thin-Film Transistors", *Adv. Mater.*, vol. 28, no. 28, pp. 5986–5996, Jul. 2016.

[305] L. Song, A. C. Myers, J. J. Adams, and Y. Zhu, "Stretchable and Reversibly Deformable Radio Frequency Antennas Based on Silver Nanowires", *ACS Appl. Mater. Interfaces*, vol. 6, no. 6, pp. 4248–4253, Mar. 2014.

[306] S. Yao and Y. Zhu, "Wearable multifunctional sensors using printed stretchable conductors made of silver nanowires", *Nanoscale*, vol. 6, no. 4, p. 2345, Jan. 2014.

[307] G. S. Korotchenkov and G. Sergeevich, *Handbook of gas sensor materials: properties, advantages and shortcomings for applications. Volume 1: Conventional approaches*. 2013.

[308] P. G. Su and C. S. Wang, "Novel flexible resistive-type humidity sensor", *Sensors Actuators, B Chem.*, vol. 123, no. 2, pp. 1071–1076, May 2007.

[309] P. G. Su and C. F. Chiou, "Electrical and humidity-sensing properties of reduced graphene oxide thin film fabricated by layer-by-layer with covalent anchoring on flexible substrate", *Sensors Actuators, B Chem.*, vol. 200, pp. 9–18, Sep. 2014.

[310] R. M. Morais, M. dos S. Klem, G. L. Nogueira, T. C. Gomes, and N. Alves, "Low Cost Humidity Sensor Based on PANI/PEDOT:PSS Printed on Paper", *IEEE Sens. J.*, vol. 18, no. 7, pp. 2647–2651, Apr. 2018.

[311] H. Andersson, A. Manuilskiy, T. Unander, C. Lidenmark, S. Forsberg, and H.-E. Nilsson, "Inkjet printed silver nanoparticle humidity sensor on paper", *IEEE Sens. J.*, vol. 12, no. 6, pp. 1901–1905, 2012.

[312] P. He, J. R. Brent, H. Ding, J. Yang, *et al.*, "Fully printed high performance humidity sensors based on two-dimensional materials", *Nanoscale*, vol. 10, no. 12, pp. 5599–5606, Mar. 2018.

[313] C. Gaspar, J. Olkkonen, S. Passoja, and M. Smolander, "Paper as Active Layer in Inkjet-Printed Capacitive Humidity Sensors", *Sensors*, vol. 17, no. 7, p. 1464, Jun. 2017.

[314] A. Rivadeneyra, J. Fernández-Salmerón, M. Agudo-Acemel, J. A. López-Villanueva, A. J. Palma, and L. F. Capitan-Vallvey, "A printed capacitive-resistive double sensor for toluene and moisture sensing", *Sensors Actuators, B Chem.*, vol. 210, pp. 542–549, 2015.

[315] A. Rivadeneyra Torres, J. Fernández-Salmerón, M. Agudo, J. A. López-villanueva, L. F. Capitan-Vallvey, and A. J. Palma, "Design and characterization of a low thermal drift capacitive humidity sensor by inkjet-printing", *Sensors Actuators, B Chem.*, vol. 195, pp. 123–131, 2014.

[316] J. F. Salmerón, A. R. Torres, J. Banqueri, M. Á. Carvajal, and M. Agudo, "Design and characterization of ink-jet and screen printed HF RFID antennas", *Proc. - 2012 4th Int. EURASIP Work. RFID Technol. RFID 2012*, pp. 119–123, 2012.

[317] A. Rivadeneyra, J. F. Salmeron, A. J. Palma, J. A. Lopez-Villanueva, M. Agudo-Acemel, and L. F. Capitan-Vallvey, "Comparative study of printed capacitive sensors", *Proc. 2015 10th Spanish Conf. Electron Devices, CDE 2015*, pp. 0–3, 2015.

[318] J. Salmerón, A. Albrecht, S. Kaffah, M. Becherer, P. Lugli, and A. Rivadeneyra, "Wireless Chipless System for Humidity Sensing", *Sensors*, vol. 18, no. 7, p. 2275, Jul. 2018.

[319] M. Loch, "Nanomaterials for hybrid organic-inorganic optoelectronic devices processed from solution", Technische Universität München, 2018.

[320] T. Haeberle, A. M. Münzer, F. Buth, J. Antonio Garrido, *et al.*, "Solution processable carbon nanotube network thin-film transistors operated in electrolytic solutions at various pH", *Appl. Phys. Lett.*, vol. 101, no. 22, p. 223101, Nov. 2012.

[321] K. Melzer, V. D. Bhatt, T. Schuster, E. Jaworska, *et al.*, "Flexible Electrolyte-Gated Ion-Selective Sensors Based on Carbon Nanotube Networks", vol. 15, no. 6, pp. 3127–3134, 2015.

[322] E. D. Minot, A. M. Janssens, I. Heller, H. A. Heering, C. Dekker, and S. G. Lemay, "Carbon nanotube biosensors: The critical role of the reference electrode", *Appl. Phys. Lett.*, vol. 91, no. 9, p. 093507, Aug. 2007.

[323] M. Waleed Shinwari, D. Zhitomirsky, I. A. Deen, P. R. Selvaganapathy, M. Jamal Deen, and D. Landheer, "Microfabricated reference electrodes and their biosensing applications", *Sensors*, vol. 10, no. 3. Molecular Diversity Preservation International, pp. 1679–1715, 02-Mar-2010.

[324] E. T. S. G. da Silva, S. Miserere, L. T. Kubota, and A. Merkoçi, "A simple on-plastic/paper inkjet-printed solid-state Ag/AgCl pseudo-reference electrode.", *Anal. Chem.*, pp. 1–11, Oct. 2014.

[325] A. Määttänen, U. Vanamo, P. Ihalainen, P. Pulkkinen, *et al.*, "A low-cost paper-based inkjet-printed platform for electrochemical analyses", *Sensors Actuators B Chem.*, vol. 177, pp. 153–162, Feb. 2013.

[326] J. Schnitker, D. Afanasenkau, B. Wolfrum, and A. Offenhäusser, "Planar reference electrodes on multielectrode arrays for electrochemical measurements of ionic currents", *Phys. Status Solidi*, vol. 210, no. 5, pp. 892–897, May 2013.

[327] S. Joshi, V. D. Bhatt, H. Wu, M. Becherer, and P. Lugli, "Flexible lactate and glucose sensors using electrolyte-gated carbon nanotube field effect transistor for non-invasive real-time monitoring", *IEEE Sens. J.*, vol. 17, no. 14, pp. 4315–4321, Jul. 2017.

[328] P. Ihalainen, F. Pettersson, M. Pesonen, T. Viitala, *et al.*, "An impedimetric study of DNA hybridization on paper-supported inkjet-printed gold electrodes", *Nanotechnology*, vol. 25, no. 9, p. 094009, Mar. 2014.

[329] N. Komuro, S. Takaki, K. Suzuki, and D. Citterio, "Inkjet printed (bio)chemical sensing devices", *Analytical and Bioanalytical Chemistry*, vol. 405, no. 17. Springer-Verlag, pp. 5785–5805, 16-Jul-2013.

[330] A. Abdelhalim, A. Falco, F. Loghin, P. Lugli, J. F. Salmeron, and A. Rivadeneyra, "Flexible NH3 sensor based on spray deposition and inkjet printing", in *Proceedings of IEEE Sensors*, 2017, pp. 1–3.

[331] A. Falco, J. F. Salmeron, F. Loghin, A. Abdelhalim, P. Lugli, and A. Rivadeneyra, "Optimization of Process Parameters for Inkjet Printing of CNT Random Networks on Flexible Substrates", *Nanotechnology, 2016 IEEE-NANO IEEE Conf. Nanoelectron.*, Aug. 2016.

[332] R. Barea, L. Boquete, M. Mazo, and E. López, "System for assisted mobility using eye movements based on electrooculography", *IEEE Trans. Neural Syst. Rehabil. Eng.*, vol. 10, no. 4, pp. 209–218, Dec. 2002.

[333] A. W. North, "Accuracy and Precision of Electro--oculographic Recording", *Invest. Ophthalmol. Vis. Sci.*, vol. 4, no. 3, pp. 343–348, Jun. 1965.

[334] W. Heide, E. Koenig, P. Trillenberg, D. Kömpf, and D. S. Zee, "Electrooculography: technical standards and applications. The International Federation of Clinical Neurophysiology.", *Electroencephalogr. Clin. Neurophysiol. Suppl.*, vol. 52, pp. 223–240, 1999.

[335] J. H. Skotte, J. K. Nøjgaard, L. V. Jørgensen, K. B. Christensen, and G. Sjøgaard, "Eye blink frequency during different computer tasks quantified by electrooculography", *Eur. J. Appl. Physiol.*, vol. 99, no. 2, pp. 113–119, Dec. 2006.

[336] R. Barea, L. Boquete, J. M. Rodriguez-Ascariz, S. Ortega, and E. López, "Sensory System for Implementing a Human—Computer Interface Based on Electrooculography", *Sensors*, vol. 11, no. 1, pp. 310–328, Dec. 2010.

[337] Y. C. Y. Chen and W. S. Newman, "A human-robot interface based on electrooculography", in *IEEE International Conference on Robotics and Automation, 2004. Proceedings. ICRA '04. 2004*, 2004, vol. 1, pp. 243–248.

[338] A. Bulling, J. A. Ward, H. Gellersen, and G. Tröster, "Robust recognition of reading activity in transit using wearable electrooculography", in *Lecture Notes in Computer Science (including subseries Lecture Notes in Artificial Intelligence and Lecture Notes in Bioinformatics)*, vol. 5013 LNCS, Springer, Berlin, Heidelberg, 2008, pp. 19–37.

[339] A. Bulling, J. A. Ward, H. Gellersen, and G. Tröster, "Eye movement analysis for activity recognition using electrooculography", *IEEE Trans. Pattern Anal. Mach. Intell.*, vol. 33, no. 4, pp. 741–753, Apr. 2011.

[340] S.-J. Woo, J.-H. Kong, D.-G. Kim, and J.-M. Kim, "A thin all-elastomeric capacitive pressure sensor array based on micro-contact printed elastic conductors", *J. Mater. Chem. C*, vol. 2, no. 22, pp. 4415–4422, May 2014.

[341] A. Eshkeiti, S. Emamian, S. G. R. Avathu, B. B. Narakathu, *et al.*, "Screen printed flexible capacitive pressure sensor", *IEEE SENSORS 2014 Proc.*, pp. 1192–1195, 2014.

[342] B. B. Narakathu, A. Eshkeiti, A. S. G. Reddy, M. Rebros, *et al.*, "A novel fully printed and flexible capacitive pressure sensor", in *Proceedings of IEEE Sensors*, 2012, pp. 1–4.

[343] David Savastano, "The Growth Of The Flexible Hybrid Electronics Market", *Printed Electronics Now*, Nov-2016.

[344] David Savastano, "Flexible Hybrid Electronics And Sensors", *Printed Electronics Now*, Nov-2017.

[345] David Savastano, "The Present And Future Of Flexible, Hybrid And Printed Electronics", *Printed Electronics Now*, Mar-2018.

[346] D. Y. Shin, Y. Lee, and C. H. Kim, "Performance characterization of screen printed radio frequency identification antennas with silver nanopaste", *Thin Solid Films*, vol. 517, no. 21, pp. 6112–6118, Sep. 2009.

[347] Q. Hirmer, A. Albrecht, M. Bobinger, M. Loch, *et al.*, "Inkjet-printed patch antennas for wireless chip-to-

chip communication on flexible substrates", in *PRIME 2017 - 13th Conference on PhD Research in Microelectronics and Electronics, Proceedings*, 2017, pp. 141–144.

[348] N. Marquardt, A. S. Taylor, N. Villar, and S. Greenberg, "Rethinking RFID", in *Proceedings of the 28th international conference on Human factors in computing systems - CHI '10*, 2010, p. 2307.

[349] R. S. Dahiya, P. Mittendorfer, M. Valle, G. Cheng, and V. J. Lumelsky, "Directions toward effective utilization of tactile skin: A review", *IEEE Sens. J.*, vol. 13, no. 11, pp. 4121–4138, 2013.

[350] G. Cheng, R. S. Dahiya, S. Member, P. Mittendorfer, and M. Valle, "Directions Toward Effective Utilization of Tactile Skin : A Review Directions Towards Effective Utilization of Tactile Skin – A Review", no. February 2016, 2013.

[351] P. Mittendorfer and G. Cheng, "Humanoid multimodal tactile-sensing modules", *IEEE Trans. Robot.*, vol. 27, no. 3, pp. 401–410, 2011.

[352] A. Schmitz, P. Maiolino, M. Maggiali, L. Natale, G. Cannata, and G. Metta, *Methods and Technologies for the Implementation of Large-Scale Robot Tactile Sensors*, vol. 27, no. 3. IEEE, 2011, pp. 389–400.

[353] P. D. Calvert, "Inkjet Printing for Materials and Devices", *Chem. Mater.*, vol. 13, pp. 3299–3305, 2001.

[354] J. Doggart, Y. Wu, and S. Zhu, "Inkjet printing narrow electrodes with", *Appl. Phys. Lett.*, vol. 94, no. 16, p. 163503, Apr. 2009.

[355] H. Meier, U. Löffelmann, D. Mager, P. J. Smith, and J. G. Korvink, "Inkjet printed, conductive, 25 µm wide silver tracks on unstructured polyimide", *Phys. status solidi*, vol. 206, no. 7, pp. 1626–1630, Jul. 2009.

[356] P. Ihalainen, A. Määttänen, J. Järnström, D. Tobjörk, R. Österbacka, and J. Peltonen, "Influence of Surface Properties of Coated Papers on Printed Electronics", *Ind. Eng. Chem. Res.*, vol. 51, no. 17, pp. 6025–6036, May 2012.

[357] J. Felba and H. Schaefer, "Materials and Technology for Conductive Microstructures", in *Nanopackaging*, 2008, pp. 239–263.

[358] J. R. Windmiller and J. Wang, "Wearable Electrochemical Sensors and Biosensors: A Review", *Electroanalysis*, vol. 25, no. 1. Wiley-Blackwell, pp. 29–46, 01-Jan-2013.

[359] S. C. Lim, S. H. Kim, Y. S. Yang, M. Y. Lee, S. Y. Nam, and J. Bin Ko, "Organic Thin-Film Transistor Using High-Resolution Screen-Printed Electrodes", *Jpn. J. Appl. Phys.*, vol. 48, no. 8, p. 081503, Aug. 2009.

[360] I. Ferrer and J. Svedin, "A 60 GHz image rejection filter manufactured using a high resolution LTCC screen printing process", in *Conference Proceedings - 33rd European Microwave Conference, EuMC 2003*, 2003, vol. 1, pp. 423–426.

[361] B. Raabe, F. Huster, M. McCann, and P. Fath, "High aspect ratio screen printed fingers", *20th EUPVSEC, Barcelona, Spain*, no. June, pp. 930–933, 2005.

[362] R. Hokari, K. Kurihara, N. Takada, J. Matsumoto, S. Matsumoto, and H. Hiroshima, "Fine and high-aspect-ratio screen printing combined with an imprinting technique", *J. Micromechanics Microengineering*, vol. 26, no. 3, p. 035005, Mar. 2016.

[363] W.-H. Chung, H.-J. Hwang, S.-H. Lee, and H.-S. Kim, "*In situ* monitoring of a flash light sintering process using silver nano-ink for producing flexible electronics", *Nanotechnology*, vol. 24, no. 3, p. 035202, Jan. 2013.

[364] H. Kang, E. Sowade, and R. R. Baumann, "Photonic sintering of inkjet printed copper oxide layer", vol. 3200, pp. 494–497, 2013.

[365] S. Chung, J. Lee, H. Song, S. Kim, J. Jeong, and Y. Hong, "Inkjet-printed stretchable silver electrode on wave structured elastomeric substrate", *Appl. Phys. Lett.*, vol. 98, no. 15, p. 153110, Apr. 2011.

[366] S. R. S. Kumar and S. Kasiviswanathan, "Transparent ITO-Mn:ITO Thin-Film Thermocouples", *IEEE Sens. J.*, vol. 9, no. 7, pp. 809–813, Jul. 2009.

[367] G. A. T. Sevilla, S. Bin Inayat, J. P. Rojas, A. M. Hussain, and M. M. Hussain, "Flexible and semi-transparent thermoelectric energy harvesters from low cost bulk silicon (100)", *Small*, vol. 9, no. 23, pp. 3916–3921, Dec. 2013.

[368] S. Duby, B. Ramsey, D. Harrison, and G. Hay, "Printed thermocouple devices", in *Proceedings of IEEE Sensors, 2004.*, pp. 1098–1101.

[369] S. Dalola, G. Faglia, E. Comini, M. Ferroni, *et al.*, "Planar Thermoelectric Generator based on Metal-Oxide Nanowires for Powering Autonomous Microsystems", *Procedia Eng.*, vol. 47, pp. 346–349, 2012.

[370] L. Bareket, L. Inzelberg, D. Rand, M. David-Pur, *et al.*, "Temporary-tattoo for long-term high fidelity biopotential recordings", *Sci. Rep.*, vol. 6, no. 1, p. 25727, Sep. 2016.

[371] A. Searle and L. Kirkup, "A direct comparison of wet, dry and insulating bioelectric recording electrodes", *Physiol. Meas.*, vol. 21, no. 2, pp. 271–283, May 2000.

List of Publications and Supervisions

1. Peer-Reviewed Journal Articles

[1] A. Albrecht, A. Rivadeneyra Torres, J. F. Salmerón, A. Abdellah, and P. Lugli, "Inkjet Printing and Photonic Sintering of Silver and Copper Oxide NPs for Ultra-Low-Cost Conductive Patterns", *J. Mater. Chem. C*, Mar. 2016.

[2] A. Albrecht, F. Loghin, J. F. Salmerón, M. Bobinger, M. Becherer A. Falco, P. Lugli, and A. Rivadeneyra, "Scalable deposition of nanomaterial-based temperature sensors for transparent and pervasive electronics", *Journal of Sensors*, accepted for publication in August 2018.

[3] S. El-Molla, A. Albrecht, E. Cagatay, P. Mittendorfer, G. Cheng, P. Lugli, J. F. Salmerón, and A. Almudena, "Integration of a Thin Film PDMS-Based Capacitive Sensor for Tactile Sensing in an Electronic Skin", *Journal of Sensors*, vol. 2016, 2016.

[4] F.J. Romero, A. Salinas-Castillo, A. Rivadeneyra, A. Albrecht, A. Godoy, D.P. Morales, N. Rodriguez, "In-Depth Study of Laser Diode Ablation of Kapton Polyimide for Flexible Conductive Substrates", *Nanomaterials*, vol. 8, no. 7, p. 517, Jul. 2018.

[5] J. F. Salmeron, A. Albrecht, S. Kaffah, M. Becherer, P. Lugli, A. Rivadeneyra, "Wireless chipless system for humidity sensing", *J. Sensors*, vol. 2018, Jul. 2018, 2275

[6] M. Bobinger, M. Haider, Y. Goliya, A. Albrecht, J. Russer, M. Becherer, P. Lugli, and A. Rivadeneyra, "On the Sintering of Solution-based Silver Nanoparticle Thin-films for Sprayed and Flexible Antennas", *Nanotechnology*, accepted in September 2018.

[7] F. Loghin, A. Falco, A. Albrecht, J. F. Salmerón, M. Becherer, P. Lugli, and A. Rivadeneyra, "A handwriting method for low-cost gas sensors", *ACS Applied Materials & Interfaces*, accepted in September 2018, 10.1021/acsami.8b08050

2. Peer-Reviewed Conference Proceedings

[8] A. Albrecht, "Ultra-Low-Cost and Rapid Production of Inkjet-Printed Conductive Patterns using Silver Inks and Copper Oxide Inks", in *Printing Future Days 2015: Proceedings of the 6th International Scientific Conference on Print and Media Technology for Junior Scientists and PhD Students*, 2015, pp. 19–24.

[9] A. Albrecht, M. Bobinger, J. B. Calia, A. Falco, F. Loghin, M. Becherer, and P. Lugli, "Transparent Thermocouples based on Spray-coated Nanocomposites", *2017 IEEE SENSORS*, pp. 4–6, Oct. 2017.

[10] A. Albrecht, M. Trautmann, M. Becherer, P. Lugli, and A. Rivadeneyra, "Multi-Layer Printed Shear Force Sensor on Flexible Substrates", in *ALLSENSORS 2018, The Third International Conference on Advances in Sensors, Actuators, Metering and Sensing*, 2018, pp. 70–75.

[11] P. Lugli, A. Abdellah, A. Abdelhalim, A. Albrecht, M. Becherer, E. Cagatay, S. Colasanti, F. Falco, F. Loghin, S. El-Molla, J. F. Salmeron, and A. Rivadeneyra, "Fabrication, characterization and modeling of flexible electronic components based on CNT networks", in *Proceedings - IEEE International Symposium on Circuits and Systems*, 2016, vol. 2016–July, pp. 1362–1365.

[12] M. Bobinger, V. Dergianlis, A. Albrecht, M. Haider, Q. Hirmer, M. Becherer, and P. Lugli, "Solution processing of silver nanowires for transparent heaters and flexible electronics". in *PRIME 2017 - 13th Conference on PhD Research in Microelectronics and Electronics, Proceedings*, 2017, pp. 141–144.

[13] Q. Hirmer, A. Albrecht, M. Bobinger, M. Loch, M. Haider; J. A. Russer, M. Becherer, and P. Lugli, "Inkjet-printed patch antennas for wireless chip-to-chip communication on flexible substrates", in *PRIME 2017 - 13th Conference on PhD Research in Microelectronics and Electronics, Proceedings*, 2017, pp. 141–144.

[14] J. F. Salmerón, A. Albrecht, S. Kaffah, M. Becherer, P. Lugli, and A. Rivadeneyra, "Wireless Printed System for Humidity Monitoring", in *ALLSENSORS 2018, The Third International Conference on Advances in Sensors, Actuators, Metering and Sensing*, 2018, pp. 70–75.

[15] P. La Torraca, Y. Ricci, A. Albrecht, M. Bobinger, P. Pavan, M. Becherer, P. Lugli, and L. Larcher, "Printed Technology Solutions for Audio Transducers", in *2018 IEEE 18th International Conference in Nanotechnology, July 2018*

3. Submissions to Peer Reviewed Journals and Conferences

[16] B. Cruz, A. Albrecht, "Inkjet printing of metal nanoparticles for green UHF RFID tags", *Kleinheubacher Tagung 2018,* accepted in August 2018

[17] A. Albrecht, M. Bobinger, M. Becherer, G. Cheng, P. Lugli, and A. Rivadeneyra, "Over-Stretching Tolerant Conductors on Rubber Films by Inkjet-Printing Silver Nanoparticles for Wearables". *J. Mater. Chem. C*, submitted in July 2018.

[18] A. Albrecht, M. Trautmann, M. Becherer, P. Lugli, and A. Rivadeneyra, "Inkjet-Printed Three-Axial Force Sensor on Flexible Substrates", *Journal of Sensors,* submitted in August 2018.

[19] A. Albrecht, J. F. Salmerón, M. Becherer, P. Lugli, and A. Rivadeneyra, "Screen-printed capacitive pressure sensors with high sensitivity and accuracy on flexible substrates", ready to submit in August 2018

4. Conference Talks without Proceedings

[20] A. Albrecht, "KEYNOTE: Printed Sensors for the Internet of Things", in *Advanced Functional & Industrial Printing 2016*, 2016.

[21] A. Albrecht, Almudena Rivadeneyra-Torres, and Gordon Cheng, Paolo Lugli, "Capacitive Force Sensors for an Artificial Skin", in *LOPEC 2017 München*, 2017.

5. Selected Poster Contributions

[22] A. Albrecht, A. Rivadeneyra, J. F. Salmeron, A. Abdellah, and P. Lugli, "Inkjet Printing and Photonic Sintering of Silver and Copper Oxide NPs for Ultra-Low-Cost Conductive Patterns", in *LOPEC 2016*, 2016, Munich, Germany. **Best Poster Award**

[23] A. Albrecht, A. Rivadeneyra, J. F. Salmerón, M. Bobinger, A. Falco, P. Lugli, and M. Becherer, "A Sustainable Production of Electronic Devices for the Internet of Things by Inkjet and Screen Printing", in *International Workshop on "Internet of Things: sustainability and energy awareness"*, Free University of Bozen-Bolzano, unibz, 2017, Bozen-Bolzano, Italy.

[24] A. Albrecht, A. Rivadeneyra, J. F. Salmerón, M. Bobinger, A. Falco, P. Lugli, and M. Becherer, "Inkjet and Screen Printing for an Environmental-Friendly Production of Electronic Devices". In *7. MSE Kolloquium 2017 Highlights in Energy Research, Munich School of Engineering TUM MSE*, 2017, München Garching, Germany.

[25] A. Albrecht, A. Rivadeneyra, M. Becherer, and P. Lugli, "Inkjet-Printing, Screen-Printing, and Intense Pulsed Light Sintering for Flexible Hybrid Sensor Systems", in *LOPEC 2018*, 2018, Munich, Germany.

[26] A. Albrecht, A. Rivadeneyra, J. F. Salmerón, M. Bobinger, A. Falco, P. Lugli, and M. Becherer, "Production of Smart Sensor Systems for Distributed Sensing by Printing Techniques". In *8. MSE Kolloquium 2018 Advances in Energy Transition, Munich School of Engineering TUM MSE*, 2018, München Garching, Germany.

[27] A. Ivanovskaia, A. Albrecht, A. Rivadeneyra, and M. Becherer, "Structured Electrodes and Dielectrics by Multilayer Screen Printing". in *International Workshop on "Internet of Things: sustainability and energy awareness",* Free University of Bozen-Bolzano, unibz, 2017, Bozen-Bolzano, Italy.

[28] M. Bobinger, J. Mock, P. La Torraca, A. Albrecht, L. Larcher, M. Becherer, and P. Lugli, "Solution-processing and Deposition of Metal Nanowires for Transparent Heaters", in *International Workshop on "Internet of Things: sustainability and energy awareness"*, Free University of Bozen-Bolzano, unibz, 2017, Bozen-Bolzano, Italy.

[29] M. Bobinger, S. Hinterleuthner, M. Loch, A. Albrecht, M. Becherer, s. Keddis, N. Schwesinger, and P. Lugli, "Piezo- and Pyroelectric Energy Harvesting based on PVDF for Wireless Sensor Nodes". In *7. MSE Kolloquium 2017 Highlights in Energy Research, Munich School of Engineering TUM MSE*, 2017, München Garching, Germany.

[30] M. Bobinger, M. Haider, A. Albrecht, Y. Goliya, J. A. Russer, M. Becherer, and P. Lugli, "Highly conductive thin-films based on solution-processed Ag-NPs for spray-on antennas", in *DPG-Verhandlungen DS: Fachverband Dünne Schichten DS 17: Poster Session I DS 17.57: Poster B*, Deutsche Physikalische Gesellschaft DPG, 2018, Berlin, Germany.

[31] N. Isiktas, A. Ivanovskaia, M. Becherer, and A. Albrecht, "Screen-printing microstructured, dielectric films with silicone rubber for low-hysteresis pressure sensors", in *LOPEC 2018*, 2018, Munich, Germany.

[32] A. Ivanovskaia, A. Maier, F. Loghin, M. Becherer, and A. Albrecht, "High–resolution, Screen–printed Interdigitated Electrodes for Biosensors and Gas Sensors", in *LOPEC 2018*, 2018, Munich, Germany.

[33] C. Wendler, A. Rivadeneyra, M. Becherer, and A. Albrecht, "Current and Future Obstacles and Chances of Printed Electronics from a Technical and an Economical Perspective", in *LOPEC 2018*, 2018, Munich, Germany.

[34] A. Rivadeneyra, M. Haider, V. Bhatt, A. Albrecht, J. F. Salmeron, and M. Becherer, "TUMino: Modular platform for sensor networks", In *8. MSE Kolloquium 2018 Advances in Energy Transition, Munich School of Engineering TUM MSE*, 2018, München Garching, Germany.

[35] M. Bobinger, S. Hinterleuthner, M. Loch, A. Albrecht, M. Becherer, s. Keddis, N. Schwesinger, and P. Lugli, "Thermal and Mechanical Energy Harvesting based on PVDF". In *8. MSE Kolloquium 2018 Advances in Energy Transition, Munich School of Engineering TUM MSE*, 2018, München Garching, Germany.

6. Supervised Student Theses and Projects

[1] Frenkli Shoraj, *"Development of an Inkjet-Printed Circuit Board with PDMS-bases Capacitive Sensors"*, Forschungsspraxis, 2016.

[2] Meriam Trad, *"Dehnbarkeit von Silbernanopartikelfilmen auf Silikonfolie"*, Ingenieurspraxis, 2016.

[3] Mauriz Trautmann, *"Multi-Layer Printed Shear Force Sensors on Flexible Substrates"*, Bachelor Thesis, 2017.

[4] Friederike Michael, *"Construction of a Flatbed Inkjet Printer for 3D-Printed Electronics"*, Forschungspraxis, 2017.

[5] Jacopo Bonacini Calia, *"Transparent Thermocouples Based on Spray-Coated Nanocomposites – Experimental Setup and Characterizations"*, Master Thesis, 2017.

[6] Nasuh Isiktas, *"Screen-printing microstructured, dielectric films with silicone rubber for low-hysteresis pressure sensors"*, Ingenieurspraxis, 2018.

[7] Touba Jamal Khalaf, *"Photonisches Sintern von Inkjet-gedruckten Gold- und Siebgedruckten Silber-Nanopartikeln"*, Forschungspraxis, 2018.

[8] Alesia Ivanovskaia, *"Fine-line and Multilayer Screen Printing of Sensor Electrodes"*, Master Thesis, 2018.

[9] Charlotte Wendler, "*Current and Future Obstacles and Chances of Printed Electronics from a Technical and an Economical Perspective"*, Master Thesis, 2018.

[10] Paritosh Isiktas, "*Implementation of Metal and Dielectric Layers in flexible OLED devices with Roll-to-Roll Flexographic Printing"*, Master Thesis, 2018.

8 group projects in the frame of the *"Projektpraktikum Nanoelektronik und Nanotechnologie",*
6 group projects in the frame of the *"Nanoelectronics Lab"*, and
2 group projects in the frame of "*Wirtschaftliche Aspekte der Nanotechnologie*".

Appendix

A Inkjet-printed Ag-AgCl electrodes

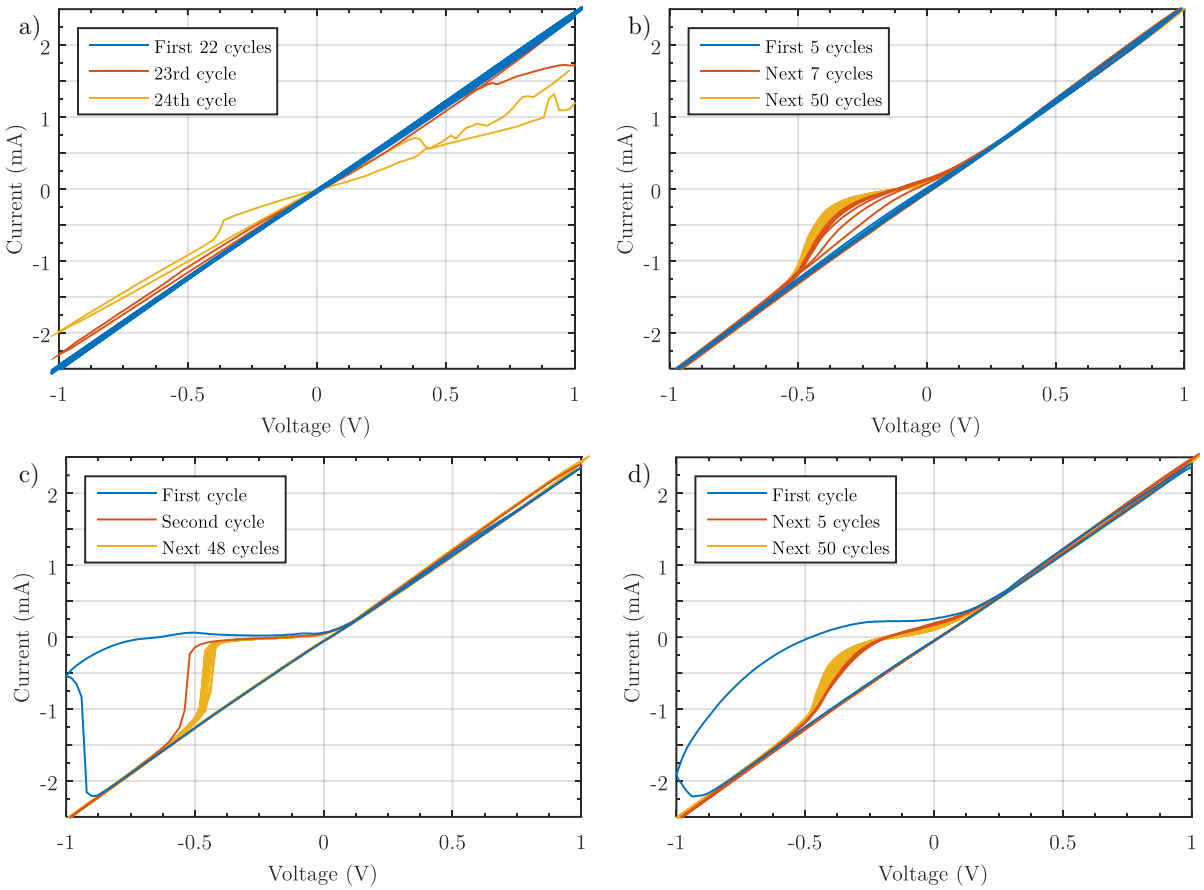

Figure A.1. Comparison between shortly chlorinated and non-chlorinated electrodes and a silver wire. a) Double printed silver electrode chlorinated for 120s dipping that is stable for 22 cycles. b) Single-printed electrode chlorinated for 20s that is stable for five cycles, then comparable to only printed silver. c) Non-chlorinated printed silver electrode shows a repeatable behaviour over more than 50 cycles. d) Simple silver wire.

Table A.1. Prepared samples and stable voltage cycles.

Dipping time	**3s**	**20s**	**60s**	**60s**	**60s**	**60s**	**120s**	**300s**
Printing	single	single	single	single	double	double	double	double
Stable cycles	0	5	8	13	13	24	22	7

B EOG Measurements

The following two figures, Figure B.1 and Figure B.2, show the EOG signals on all six electrodes and the calculated vectors for all seven movements.

Figure B.1 Complete set of EOG signals $V_{i,j}$ on six pairs of electrodes (i, j) over time in seconds during seven different movements that are indicated in the title row and were repeated five times. Each electrode pair was recorded separately, which explains the temporal shift in the repetitions. The manual separation identified the starting point of each movement and set the t=0 point there. Red and yellow marker identify the two extrema during the first 1000 samples. Red marks the first maximum or

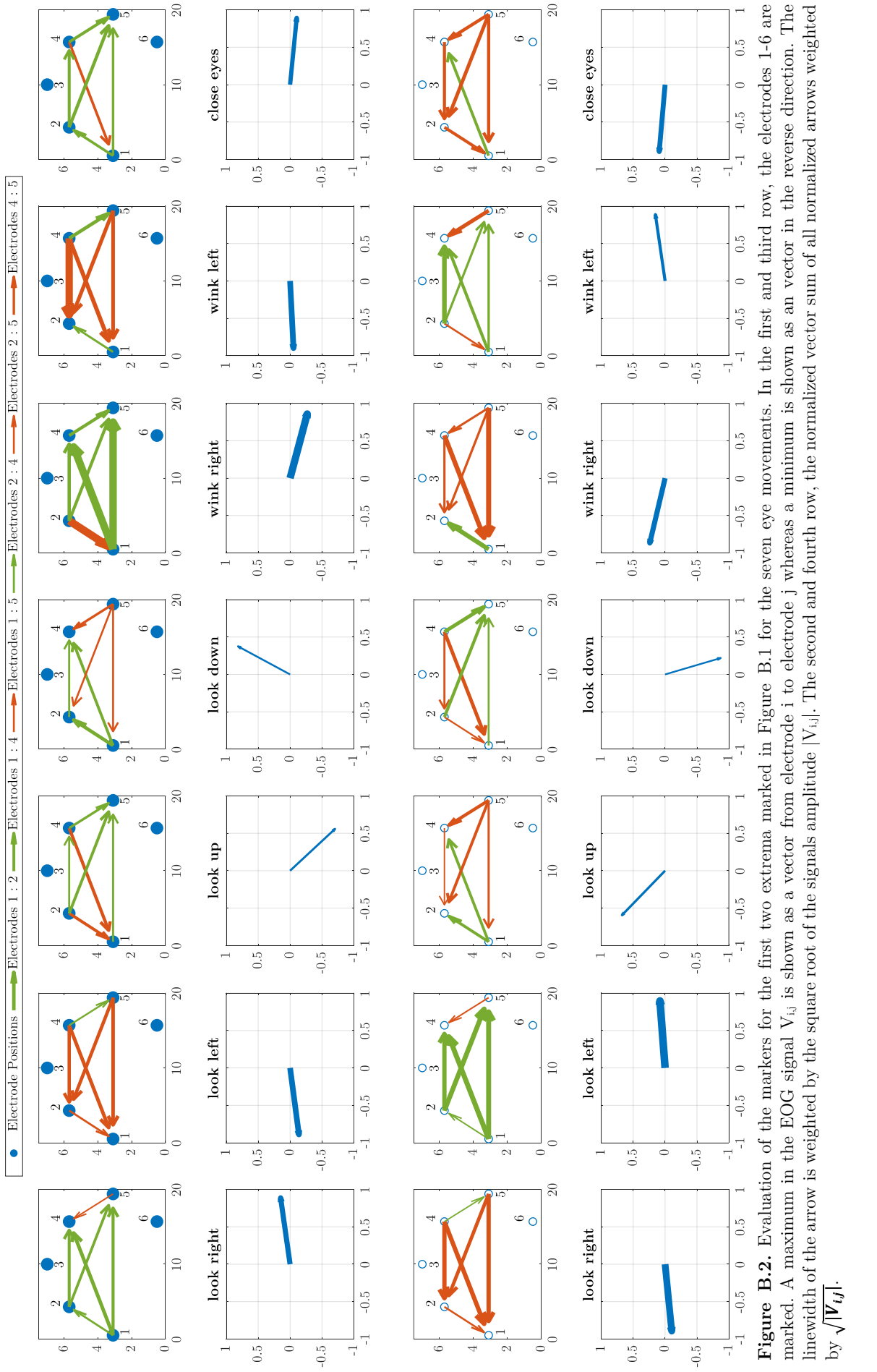

Figure B.2. Evaluation of the markers for the first two extrema marked in Figure B.1 for the seven eye movements. In the first and third row, the electrodes 1-6 are marked. A maximum in the EOG signal $V_{i,j}$ is shown as a vector from electrode i to electrode j whereas a minimum is shown as an vector in the reverse direction. The linewidth of the arrow is weighted by the square root of the signals amplitude $|V_{i,j}|$. The second and fourth row, the normalized vector sum of all normalized arrows weighted by $\sqrt{|\boldsymbol{V_{ij}}|}$.

Acknowledgement

I think I can be proud of this thesis and I could only achieve this by hard work but also by support of a few other people who I want to thank here. At the beginning is of course, my principle advisor, Prof. Paolo Lugli, who offered me this research position and supported me throughout the last three and a half years. He was not only organizing my salary but also the new labs in the ZEI in Garching where I could finish my remaining experiments. A big deal of work for these new labs was also done by my mentor, Bernhard Fabel, whom I want to thank, too. After the labs were built, not everything was running and we needed a lot of new equipment. My current legal boss, Prof. Markus Becherer, always had an open ear for our needs and tried to arrange it. I benefited also greatly from his academic knowledge and his continuous efforts to improve our infrastructure. Talking about infrastructure, I also want to thank Rosi Mittermeier for the great organization of our labs and the save working atmosphere within the hundreds of chemicals. I also thank our two secretaries, Lucia Weik and Katrin Blahetek, for their support with all administrative stuff.

I also want to thank all my office mates during the last three years, Marco Bobinger, Petar Tsenov, Marius Loch, Michael Haider, and Florin Loghin (ordered by length of stay in the office). It was a great time with you and there are still a few months left with some of you. I greatly enjoyed the ICMST conferences and will contribute at least one more talk. I hope I do not descend to the second league in our office's high score after all this writing. A great thanks goes to Michael Haider for the great network administration that makes things so convenient. I want to thank Alesia Ivanovskaia for her pressure to join social activities.

There were also some people that supported me a lot by letting me use their devices. First, there is Prof. Gordon Cheng of the Institute for Cognitive Systems that let me use their Dimatix Inkjet printer, was always curious about my work, and provided a lot of useful ideas for the further development of the artificial skin. Then, there is Prof. Ulrich Moosheimer of the Hochschule München, who gave me access to his screen printing lab, so that I could prepare my own screens at almost any time. I also want to thank his lab responsible, Helmut Schabl, for the nice welcomes, the Currywurst, and the help with any technical trouble. I also got technical support by Joachim Biegel and Markus Engel, who explained to me and helped me with a lot of technical questions for high-precision functional screen printing.

My research stay in Granada was productive and enjoyable together with Prof. Diego Pedro Morales and Prof. Encarnación Castillo Morales. Thank you for not given up with the Andalusian dialect and still try out my Spanish. In this Spanish group, I want to include my two Post-Docs, Almudena Rivadeneyra and José Fernández Salmerón, who pushed me often and made me succeed with this thesis.

One of the biggest thanks go to my parents to enabled me to go to study, travel, and become an open-minded person. A great thanks goes to my wonderful partner, Katja Körber, for all the love and the great time I had in the recent years and the design support for some of the figures.